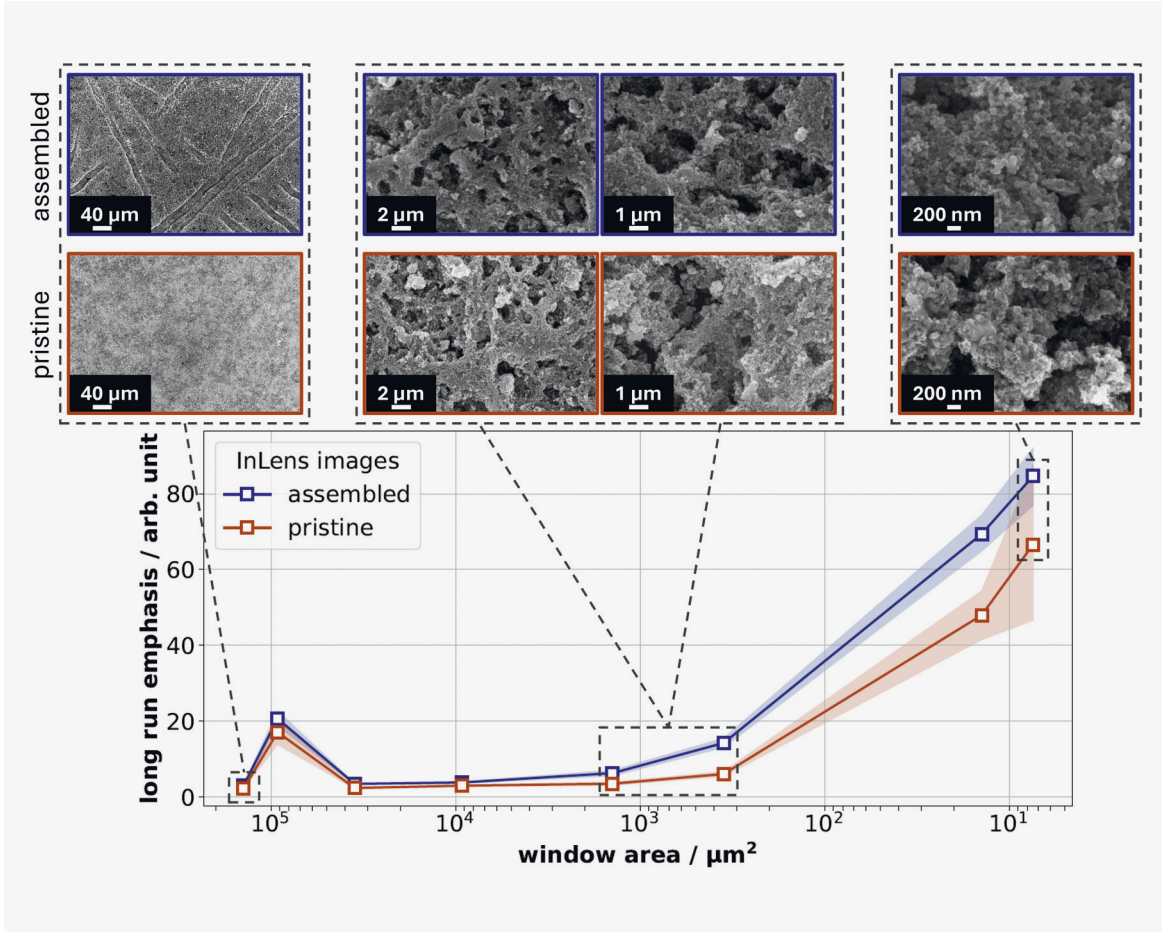

Methods for Investigating the Structure-Performance Correlation in Membrane Electrode Assemblies

Nikolai Utsch

Energie & Umwelt / Energy & Environment
Band / Volume 702
ISBN 978-3-95806-901-5

Mitglied der Helmholtz-Gemeinschaft

JÜLICH
Forschungszentrum

Schriften des Forschungszentrums Jülich
Reihe Energie & Umwelt / Energy & Environment Band / Volume 702

Forschungszentrum Jülich GmbH
Institute of Energy Technologies (IET)
Elektrochemische Verfahrenstechnik (IET-4)

Methods for Investigating the Structure-Performance Correlation in Membrane Electrode Assemblies

Nikolai Utsch

Schriften des Forschungszentrums Jülich
Reihe Energie & Umwelt / Energy & Environment Band / Volume 702

ISSN 1866-1793 ISBN 978-3-95806-901-5

Bibliografische Information der Deutschen Nationalbibliothek.
Die Deutsche Nationalbibliothek verzeichnet diese Publikation in der
Deutschen Nationalbibliografie; detaillierte Bibliografische Daten
sind im Internet über http://dnb.d-nb.de abrufbar.

Herausgeber und Vertrieb:	Forschungszentrum Jülich GmbH Zentralbibliothek, Verlag 52425 Jülich Tel.: +49 2461 61-5368 Fax: +49 2461 61-6103 zb-publikation@fz-juelich.de www.fz-juelich.de/zb
Umschlaggestaltung:	Grafische Medien, Forschungszentrum Jülich GmbH
Druck:	Grafische Medien, Forschungszentrum Jülich GmbH
Copyright:	Forschungszentrum Jülich 2026

Schriften des Forschungszentrums Jülich
Reihe Energie & Umwelt / Energy & Environment, Band / Volume 702

D 82 (Diss. RWTH Aachen University, 2025)

ISSN 1866-1793
ISBN 978-3-95806-901-5

Vollständig frei verfügbar über das Publikationsportal des Forschungszentrums Jülich (JuSER)
unter www.fz-juelich.de/zb/openaccess.

EMPOWERED AND EMPOWERING

- unkown

Kurzfassung

In dieser Arbeit werden am Beispiel der Protonenaustauschmembran-Wasserelektrolyseure umfassende Einblicke in die Zusammenhänge zwischen Morphologie, Herstellungsprozessen und elektrochemischer Leistung von Katalysatorschichten aufgezeigt. Die Verbindung von Mikroskopieverfahren mit modernen Auswertemethoden liefert eine zuverlässige Grundlage für die Charakterisierung und Weiterentwicklung der strukturellen und elektrischen Parameter der Katalysatorschicht. Die wichtigsten Ergebnisse betonen die Bedeutung der Homogenität der Oberflächentextur, die nachweislich sowohl die Leistung als auch die Lebensdauer der Elektrolyseure erheblich beeinflusst. Durch die Anpassung von Produktionsparametern wie Sprühdruck, Düsenabstand und Dispersionsformulierung wird aufgezeigt, wie die morphologischen und elektrochemischen Eigenschaften durch das ursprüngliche Katalysatorschichtdesign beeinflusst werden.

In Verbindung mit der Identifizierung starker Korrelationen zwischen physikalischen Texturdeskriptoren und aus Bildern abgeleiteten statistischen Merkmalen wird in dieser Arbeit ein neuer Ansatz zur Bewertung der Eigenschaften von Katalysatorschichten vorgestellt. Der Ansatz wird auf Rasterelektronenmikroskopie-Aufnahmen von Katalysatorschichten angewendet, beispielsweise mit variierender Beladung oder nach Langzeitversuchen. Dadurch ist eine quantitative Beschreibung entlang der Vergrößerungsskala möglich. So können Strukturen sowohl im makroskopischen Bereich der Schicht als auch im Übergang zum Katalysator-Poren-Netzwerk analysiert und objektiv bewertet werden. Darüber hinaus ermöglicht die Entwicklung einer neuartigen Vier-Linien-Sonde auf Grundlage industrieller Leiterplattentechnologie die zuverlässige Bestimmung des Schichtwiderstandes, wodurch die Einschränkungen herkömmlicher Methoden überwunden werden.

Letztlich fördert diese Arbeit das Verständnis der Rolle der Katalysatorschichtmorphologie in elektrochemischen Systemen und bietet einen Weg zur Verbesserung der Leistung, Haltbarkeit und Skalierbarkeit von Wasserelektrolyseuren.

Abstract

This work uses proton exchange membrane water electrolyzers as an example to provide a comprehensive understanding of the relationship between catalyst layer morphology, manufacturing processes, and electrochemical performance. Combining microscopy techniques with modern evaluation methods establishes a reliable foundation for characterizing and developing the catalyst layer's structural and electrical features. The most significant findings underscore the importance of surface texture homogeneity which impact the performance and lifetime of the electrolyzers. This work demonstrates how production parameters such as spray pressure, nozzle spacing, and dispersion formulation influence the morphological and electrochemical properties of catalyst layers.

The developed approach enables the evaluation of catalyst layer properties by identifying strong correlations between physical texture descriptors and statistical features derived from image analysis. Using this approach to examine scanning electron microscopy images of catalyst layers provides a quantitative description across the magnification scale. It enables the analysis and objective evaluation of structures in the macroscopic region of the layer, as well as the transition to the catalyst-pore network. Additionally, the development of a novel four-line probe based on industrial printed circuit board technology reliably determines the catalyst layer resistance, overcoming the limitations of conventional methods.

Ultimately, this work advances the understanding of the role of catalyst layer morphology in electrochemical systems, paving the way for advancements in the performance, durability, and scalability of water electrolyzers.

Dissemination Activities

During my dissertation, I contributed to several peer-reviewed publications, with others submitted or under review, and presented my research at academic conferences. A list of these contributions can be found below. The publications used within this thesis are listed in the following chapter.

List of Conferences

Prototyping Low-Loaded Iridium Electrodes - From Lab to Industrial Scale

Utsch, N. & Glüsen, A.

2024 — European Hydrogen Energy Conference, PROMET-H2 Workshop. Drastic reduction of CRM and costs in PEMWE. Approach from EU project PROMET-H2

not available

Quantifying Sheet Resistance and in-Plane Electrical Resistivity of PEM Water Electrolyzer Components

Utsch, N.; Berg, F.; Scheepers, F.; Holtwerth, S.; Shviro, M.; Lehnert, W. & Mechler, A. K.

2023 — 244th ECS Meeting, I01A - Polymer Electrolyte Fuel Cells and Electrolyzers 23 (PEFC&E23) - Diagnostics/Characterization Methods, MEA Design/ Model, MA2023-XX 1756

DOI: 10.1149/MA2023-02371756mtgabs

Impact of Loading Displacements on the Degradation Behavior of Low-Load PEM Water Electrolysis Electrodes

Utsch, N.; Jain, M.; Froning, D.; Shviro, M. & Lehnert, W.

2022 242th ECS Meeting, I07: Advanced Electrolysis Systems for Renewable Energy Conversion and Storage, MA2022-01 1751

DOI: 10.1149/MA2022-01391751mtgabs

Assessment of Catalyst Layer Quality By Image Processing and Correlation to Its Degradation Behavior in PEM Water Electrolysis

Utsch, N.; Shviro, M. & Lehnert, W.

2021 240th ECS Meeting, I01A: Polymer Electrolyte Fuel Cells & Electrolyzers 21 (PEFC&E 21) - Diagnostics/Characterization Methods, MEA Design/Model, MA2021-02 1053

DOI: 10.1149/MA2021-02361053mtgabs

Implementation Study of IrNi-Nanostructures for PEM Water Elektrolysis - From RDE to Single-Cell Testing

Utsch, N.; Shviro, M. & Carmo, M.

2020 Materials Science and Engineering Congress (MSE)

DOI: not available

List of Publications

Highly Active and Durable Anode Electrodes with Low Iridium Loading for Proton Exchange Membrane Water Electrolysis

Ambu, S. S.; Morawietz, T.; **Utsch, N.**; Kimmel, B.; Gago, A. S.; Glüsen, A.; Hosseiny, S.; Goll, M. & Friedrich, K. A.

2026 submitted

submitted

Comprehensive Analysis of the Degradation Mechanisms of Proton Exchange Membrane Water Electrolyzers with Iridium on Antimony Tin Oxide Anodes

Ambu, S. S.; **Utsch, N.**; Morawietz, T.; Retuerto, M.; Roja, S.; Usoltev, O.; Goll, M.; Sanchez, D.G.; Glüsen, A.; Gago, A. S.; Hosseiny, S.& Friedrich, K. A.

2025 Energy and Environmental Materials

10.1002/eem2.70242

Evaluation of Simplified Test Rig for High Throughput Screening of Proton Exchange Membrane Water Electrolysis Components

Berg, F.; Shviro, M.; Carmo, M., **Utsch, N.** & Müller, M.

2025 International Journal of Hydrogen Energy, 120, 385-392

10.1016/j.ijhydene.2025.03.210

Verification and Error Analysis of the Mechanical Properties of Nafion™117

Yonkova, V.; **Utsch, N.**; Borowec, J.; Eichel, R.-A.; Hausen, F.; Scheepers, F.; Brinckmann, S. & Schwaiger, R.

2024 JOM, 76, 2315-2325

10.1007/s11837-024-06485-7

Introducing titanium hydride on porous transport layer for more energy efficient water electrolysis with proton exchange membrane

Bautkinova, T.; **Utsch, N.**; Bryston, T.; Lhotka, M.; Kohoutkova, M.; Shviro, M. & Bouzek, K.

2023 Journal of Power Sources, 565, 232913

10.1016/j.jpowsour.2023.232913

Iridium - Nickel Nanoparticle-Based Aerogels for Oxygen Evolution Reaction

Park, S.; **Utsch, N.**; Carmo, M., Shviro, M. & Stolten, D.

2022 ACS Applied Nano Materials, 5, 12, 18060

10.1021/acsanm.2c04000

Author Contribution

During this work a master thesis was supervised and its use is indicated by the special quotation mark ⧫. The following publications have been included in this thesis with permission from the publishers and their use is indicated by the special quotation marks † and ‡.

Optimization of anode catalyst layer in low loaded MEAs for PEM Water Electrolysis using spray coating

Jain, M.; Supervisors: **Utsch, N.**; Shviro, M.; Schulz, P.; Wasserscheid, P.

2021 Master Thesis

- quotation mark: ⧫

Author Contributions: Jain, M.: Methodology, Investigation, Data Curation, Writing – Original Draft, Writing – Review & Editing, Visualization. Utsch, N.: Conceptualization, Methodology, Supervision, Writing – Review & Editing. Shviro, M.: Supervision, Writing – Review & Editing, Funding Acquisition. Schulz, P.: Supervision, Writing – Review & Editing. Wasserscheid, P.: Supervision

Innovative Method for Reliable Measurement of PEM Water Electrolyzer Component Resistances

Utsch, N.; Berg, F.; Scheepers, F.; Holtwerth, S.; Shviro, M.; Lehnert, W. & Mechler, A. K.

2025 Small Methods, 2401842

10.1002/smtd.202401842 quotation mark: †

Author Contributions: Utsch, N.: Conceptualization, Methodology, Software, Validation, Formal Analysis, Investigation, Data Curation, Writing – Original Draft, Writing – Review & Editing, Visualization. Berg, F.: Methodology, Investigation, Validation, Writing – Review & Editing. Scheepers, F.: Formal Analysis, Supervision, Writing – Review & Editing. Holtwerth, S.: Investigation. Shviro, M.: Supervision, Resources, Funding Acquisition, Writing – Review & Editing. Lehnert, W.: Supervision. Mechler, A. K.: Writing – Review & Editing, Supervision.

Exploring the Potential of Image-based Feature Extraction for Catalyst Layer Characterization

Utsch, N.; Froning, D.; Scheepers, F.; Jain, M.; Shviro, M.; Lehnert, W. & Mechler, A. K.

2024 not submitted

DOI: not announced quotation mark: ‡

Author Contributions: Utsch, N.: Conceptualization, Methodology, Software, Validation, Formal Analysis, Investigation, Data Curation, Writing – Original Draft, Writing – Review & Editing, Visualization. Froning, D.: Methodology, Formal Analysis, Supervision, Validation. Scheepers, F.: Formal Analysis, Supervision, Writing – Review & Editing. Jain, M.: Investigation. Shviro, M.: Supervision, Resources, Funding Acquisition, Writing – Review & Editing. Lehnert, W.: Methodology, Supervision, Validation, Writing – Review & Editing Mechler, A. K.: Writing – Review & Editing, Supervision.

Contents

1 Introduction and Motivation

Increasing energy demand correlates with deteriorating ecosystems and continues to threaten habitats of life on a planetary scale.[1,2] Renewable energies, such as wind and solar power, will become progressively more relevant by enabling a sustainable driven energy market,[2,3] expected that their share could hold 86% of worldwide electricity generation in 2050.[4] However, renewable energies are crucially connected to a successful progress in the field of energy conversion devices, such as the proton exchange membrane water electrolyzers (PEMWEs) to produce green hydrogen. The smallest known molecule can shift the fossil fuel-based energy market towards a low-emission economy, its conceivable implementation in the existing gas infrastructure promotes hydrogen as the future energy carrier.[5–7]

The PEMWE is a technology possessing attractive hydrogen production rates combined with high efficiencies aiding the effective utilization of renewable energy. Costly components, sluggish anode kinetics, and the required usage of scarce metals are still delaying the comprehensive market penetration of the PEMWE technology.[8,9] While research on the single components gained momentum in recent years, gaps in understanding their system integration are still hampering progress from the manufacturer's perspective.[10–12†]

Numerous research activities have aimed to reduce the noble metal content (i.e. iridium, platinum) used as catalyst, by boosting the activity of the anodic oxygen evolution reaction (OER).[13–15] State-of-the-art catalysts for the anode made from pure (unsupported) iridium or iridium oxide[16–18] applied with high loadings, originated from the target to develop a PEMWE with maximized performance and minimized degradation rate.[9] However, recent research results have shown that the annual iridium metal mining complicates the applied contingency for PEMWE, while it also defines the required iridium loadings and thus the iridium-related specific power.[19–22] Depending on the market share, PEMWE deployment targets can be achieved by reducing the iridium-specific power sufficiently through minimising the applied iridium loading. According to Taie et al., decarbonization of the natural gas sector by 2050 requires a 13-fold intensification of the iridium specific power (25 MW kg_{Ir}^{-1}).[23] Accounting the carbon neutrality by 2100 for the transportation sector means that the iridium loading must be re-

duced by approximately a factor of 50 until a sufficient iridium specific power is reached.[24] Research tends to focus on developing catalysts to tackle these challenges. Enormous efforts are taken to find possible solutions, leading to a variety of likely complex catalyst systems, such as iridium doped with 3d-transition metals,[25,26] iridium on advanced supports,[27–29] and bi- or multi-metallic nanostructures which aim to control the crucial iridium oxygen adsorption affinity by band-structure engineering.[25,30–32]

However, most of these catalysts are developed in small quantities at the lab scale, while their characterization is performed using idealized methods, such as the rotating disk electrode. This results in a gap between catalyst development and the real-world operating environment. The decision making in the iterative optimization process that a catalyst goes through is obscured by this gap. To guide catalyst development in the right direction, it is necessary to perform single-cell testing, an environment that is closer to the real application.[33] This requires the catalyst to be embedded in a three-dimensional body, i.e. a catalyst layer (CL). From the perspective of R&D applications, the fabrication and testing of the CL is a challenging endeavor. Significant costs are associated with the complex manufacturing of the CL and the need for sophisticated testing hardware and expertise. The CL must also be combined with other materials to form the membrane electrode assemblies (MEA), which can then be tested in a single-cell where it interacts with other components. This complex interaction continues to present challenges for catalyst development because the generated data depends not only on the catalyst itself, but also on external factors such as membrane creep. Consequently, these interactions are often overlooked or inadequately addressed in many studies, despite their significant impact on performance and degradation evaluation.

On the other hand, from an industrial point of view, reaching the gigawatt scale for PEMWE or implementing proton exchange membrane fuel cell (PEMFC) in the transportation sector requires that the production of CLs and MEAs is to be governed by industrial quality standards to ensure the reliability of the technology.[34] Unfortunately, the CL poses a significant challenge to both technologies, as their performance and durability depend on the nature of the CL produced.[35–42] The importance of understanding the relationship between electrolyser durability and catalyst integration, CL formation, and operation has been emphasized by numerous authors.[10,33,40,43,44] Aside from single-cell testing, techniques for analyzing CL properties are limited. The stochastic nature of CL morphology results in a lack of appropriate structural descriptors. Therefore, this work focuses on computational and experimental methods of describing the structure of catalysts along with their electrical and electrochemical properties.

The most frequent used methods to characterize CLs is then simply the single-cell combined with other electrochemical methods. To achieve this goal, the methods presented in this thesis have been developed along the production of the CL targeting reduced noble metal contents. Focusing on the structural part to describe CLs, image analysis has been used and correlated to surface and electrochemical properties, such as performance and durability. The structure of the CL is typically described using scanning electron microscopy (SEM) or transmission electron microscopy (TEM) images. However, these methods lack the ability to provide quantifiable outputs suitable for machine learning or artificial intelligence applications. Microscopic results are often interpreted subjectively rather than objectively. Regarding electrical properties, the literature presents several custom-made setups that frequently have pitfalls leading to erroneous conclusions due to a lack of robustness in the measurements.

This research demonstrates a pioneering approach to quantify SEM images reflecting structural information of porous electrode surfaces at different magnification scales. Regarding the electrical nature of the CLs, a novel probe has been developed to study the sheet resistance and in-plane electrical resistivity of CLs without entanglement in the single cell environment.[‡]

2 Fundamentals of PEM Water Electrolysis

Before delving into the specific approaches to improve the analytical capabilities related to CLs, this chapter will describe the theoretical aspects of water electrolysis. First, the general concepts used to describe electrochemical phenomena will be highlighted and then related to the components used in modern PEMWE cells. Finally, an overview of the current state-of-the art will be discussed with the background provided in the previous sections.

2.1 Aspects of Electrochemistry

The decomposition of water into its elements, or the water splitting reaction (R1), was first observed in 1789 by van Troostwijk and Deimann.[45] Their experiments were reproduced in the following years by several researchers, such as Pearson, Nicholson, Carlisle, Ritter and others. All of them observed gas evolution, namely hydrogen and oxygen, while introducing an electric charge into the water through the anode (R2) and the cathode (R3). They also noticed that material was deposited on the electrode during the process. However, some time passed before Faraday introduced his famous laws of electrolysis in 1834.[46]

$$2\,H_2O \longrightarrow 2\,H_2 + O_2 \qquad \textbf{water splitting reaction} \qquad \text{(R1)}$$

$$2\,H_2O \longrightarrow 4\,H^+ + O_2 + 4\,e^- \qquad \textbf{OER - anode} \qquad \text{(R2)}$$

$$4\,H^+ + 4\,e^- \longrightarrow 2\,H_2 \qquad \textbf{HER - cathode} \qquad \text{(R3)}$$

Faraday's law states that the amount of product produced is proportional to the charge transferred. The following are explanations of each half-cell reaction under standard conditions. Faraday related the charge transferred to the moles of electrons required for the chemical reaction. Thus, the so-called Faraday constant (F) was introduced, and its multiplication by the number of electrons (z) gives the total charge per mole required for the OER or hydrogen

evolution reaction (HER). However, this only expresses the total charge per mole when transferring four electrons, as in (R2), or as the (R3) half-cell reaction. It does not take into account that the transfer of charge is not always spontaneous. In the case of a non-spontaneous reaction, such as the water splitting reaction (R1). Before the charge can be transferred between different species, it must overcome a energy barrier. In the case of a non-spontaneous reaction, this energy barrier (ΔG^*) is quantified by the required change in the Gibbs free energy (ΔG°) plus the activation energy (E_a) of the reaction. Therefore, to transfer the total charge (zF) between different species of a non-spontaneous reaction, an external electromotive force must be applied. This required energy is quantified by the thermodynamic voltage (E), e.g. for the water splitting reaction (R1) is $-1.23\,\mathrm{V}$ at standard conditions. The required voltage can be obtained from the relationship in Equation 2.1. Therefore, zFE is equal to the work necessary to overcome the required change of ΔG°.

$$E^\circ_{cell} = -\frac{\Delta G^\circ}{zF} = -1.23\,\mathrm{V} \tag{2.1}$$

Figure 2.1 schematically shows an electrochemical cell and the ongoing processes involved for water splitting in an acidic environment. Each half-cell reaction takes part at an electrode, either at the anode (R2) or at the cathode (R3). These electrodes are immersed in an electrolyte that allows the transfer of charge carriers from the anode (light blue framed bar) to the cathode (dark blue framed bar). At the anode, water is split into oxygen and protons (R2), which then migrate to the cathode, where they are reduced to molecular hydrogen (R3). Both electrodes are connected to an electrical circuit to provide the necessary electromotive force from a DC power source. In Figure 2.1, the energy barrier for both half-cell reactions is shown schematically next to the respective electrodes. At the cathode, the energy barrier of reduction (h_{red}) is smaller than that of oxidation (h_{ox}). Therefore, during the HER the reduced species (S_{red}) are formed (R3) and not the oxidized species (S_{ox}). The relationships are reversed for the OER at the anode. Each half-cell reaction and its redox couple has a specific electrode potential upon contact with the electrolyte. In PEMWE, the anodic standard electrode potential (E°_{anode}) is $1.23\,\mathrm{V}$, while the cathodic standard electrode potential ($E^\circ_{cathode}$) is $0\,\mathrm{V}$. After connecting both electrodes through an electrical circuit, the reversible potential E°_{rev} can be calculated by Equation 2.2.

$$E^\circ_{rev} = E^\circ_{cathode} - E^\circ_{anode} \tag{2.2}$$

However, all these processes are critically dependent on the applied temperature and the

activity of the redox partners. The mentioned potentials refer to standard conditions and must be adjusted by the Nernst equation, which can be found in the literature.[47]

$$E = E^{\circ} + \frac{RT}{nF} \ln \left(\frac{\prod a^{\nu}_{\text{oxidation}}}{\prod a^{\nu}_{\text{reduction}}} \right) \tag{2.3}$$

Equation (2.3) is the general form of the Nernst equation, where E is the electrode potential under non-standard conditions and E° is the standard electrode potential. The factor RT represents the thermal energy, with R being the universal gas constant and T the absolute temperature in Kelvin. The logarithmic term accounts for the reaction quotient, expressed using the activities a_i of the chemical species involved, each raised to the power of their stoichiometric coefficients ν. This expression allows accurate calculation of the thermodynamic electrode potential under (non-standard) conditions.

Through the electromotive force applied by the power source, the Fermi levels (E_F) of anode and cathode are changed. If the electromotive force is smaller or equal the to the cell potential ($\leq -1.23\,\mathrm{V}$), the electrons are injected from the electrolyte into the anode. Instead, electrons are transferred from the electrode into the electrolyte at the cathode, as shown schematically in Figure 2.1.[48] To allow the electrons to start circulating along the different energy levels, the Fermi levels of the anode and cathode must be kept at an active state.[46] Ideally, this would be at a cell potential of $-1.23\,\mathrm{V}$. In reality, however, the applied electromotive force must be larger to overcome barriers that depend on several factors, such as the choice of catalyst for the electrodes, the electrolyte itself, or interfacial interactions between the resulting charges. Therefore, the Fermi level of the anode must be lowered to increase driving force of the OER (φ_{ox}) which will pull the electrons from the water molecules through the additional barriers into the electrode. At the cathode, the Fermi level must be high enough to allow the driving force of the HER (φ_{red}) to inject the electrons from the electrode through the additional barriers into the adsorbed hydrogen protons. This is only a basic and brief description of the ongoing process at the electrode interface. The additional driving force of φ_{red} and φ_{ox} is also known as the overpotential (η).

Figure 2.2 gives an overview of how different resistances (R) increase the electromotive force demanded. This additional work is represented by several overpotentials, which arise from different aspects of the cell. Reducing overpotentials is a major task in technologies such as the PEMWE. The cell potential at standard conditions E°_{cell} depends on both half-cell reactions. The dashed boxes in Figure 2.2 represent the half-cell reaction that can be described by the Bulter-Volmer equation at low current densities (J). Two important kinetic aspects derived

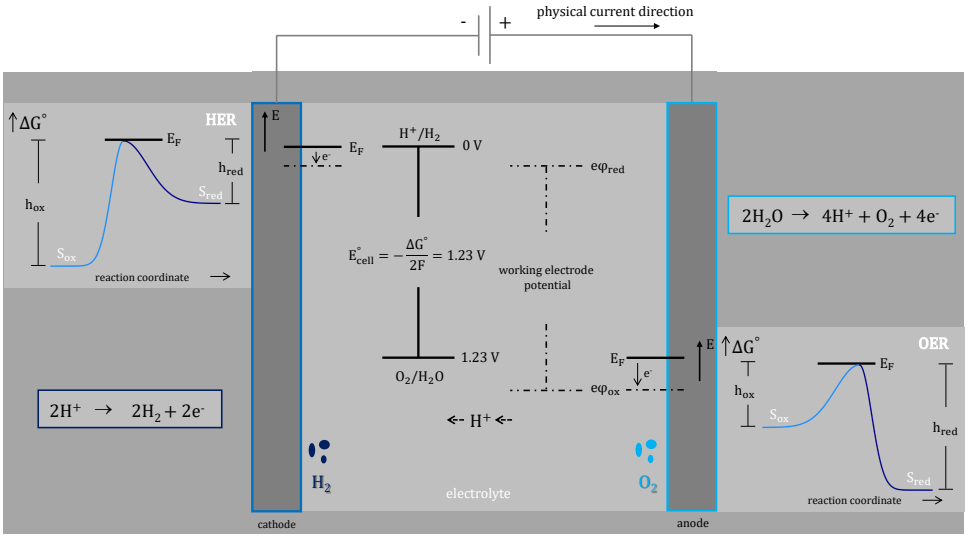

Figure 2.1. Schematic representation of the basic processes in an electrolysis cell. The dashed line represents E_F under operating load. Inspired by [46, 48]

.

from the Butler-Volmer equation are the activation overpotential (η_k) and the exchange current density (j_0). The activation overpotential is the difference between the applied potential and the equilibrium potential (E_q). E_q is the electrode potential at which the rates of the forward and reverse reactions are equal, resulting in zero net current. Although no net current flows at equilibrium, the oxidation and reduction reactions proceed at equal and opposite rates. The exchange current density (j_0) quantifies this intrinsic reaction rate. Both parameters are intrinsic measures of electrode materials and reactions. However, they are strongly influenced by the local concentration of species, temperature or pH fluctuations. Especially in a technical system, the Butler-Volmer equation is not well suited to describe the ongoing processes.[49] Other important properties of the electrode material used that affect η_k are the number of reaction sites and the catalytic activity, which is determined by material properties such as the degree of crystallinity and the d-band structure. A comparison of the anodic (R2) kinetics with the cathodic kinetics shows that the cathodic (R3) reaction is several orders of magnitude faster than the anodic reaction.

Another overpotential arises from limitations in the charge transport, such as the migration and diffusion of protons from the anode to the cathode. This ionic overpotential (η_i) primarily

results from the electrolyte's finite ionic conductivity, which causes a resistive voltage drop as ions move through the membrane or liquid phase. At the electrode-electrolyte interface, an external potential polarizes the electrode and leads to the reorganization of nearby charged species. This forms the electrochemical double layer, a complex region described by models such as the Gouy–Chapman and Stern models. The double layer itself is not responsible for mass transport, however, it influences the electrostatic environment and thus affects how ions enter or leave the electrode surface. Beyond the double layer is the diffusion layer, where concentration gradients develop due to limited ion diffusion. This can lead to concentration overpotentials, which is especially significant at high current densities when ion transport cannot keep pace with reaction rates. The electronic overpotential (η_e) is caused by the

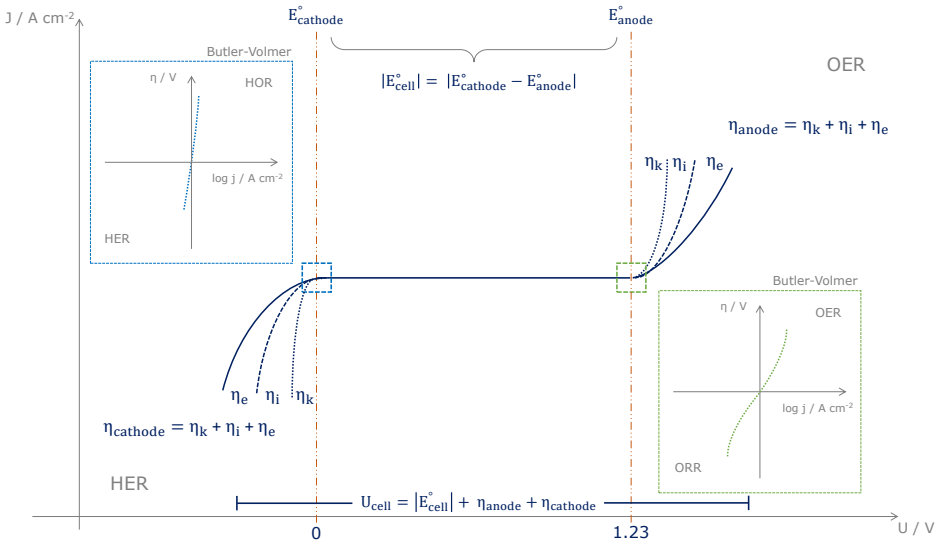

Figure 2.2. Overview of the different overpotentials inside an electrochemical cell.

electrical resistance of solid, conductive components such as electrodes, current collectors, and external circuit connections. This effect becomes increasingly significant at high current densities due to resistive (ohmic) losses in these elements. Together, η_i and η_e represent the ohmic overpotentials in the system, which arise from ionic and electrical resistive losses. All of the aforementioned loss factors contribute to the total anode (η_{anode}) or cathode ($\eta_{cathode}$) overpotential. These losses reduce the amount of species produced, thus limiting the current density. For each additional overpotential, the applied cell voltage (U_{cell}) must be increased to maintain the current density. Equation 2.4 shows that the sum of the cathode and anode

overpotentials must be added to the cell potential.

$$U_{\text{cell}} = |E^{\circ}_{\text{cell}}| + \eta_{cathode} + \eta_{anode} \tag{2.4}$$

Another key point is that degradation effects increase the overpotentials over time. This leads to a decrease in the amount of species produced. Understanding degradation mechanisms is essential to improve the long-term performance and durability of electrochemical systems. Changes in overpotential over time are usually caused by the physical and chemical degradation of cell components, such as electrodes, membranes, and interfaces.

2.2 State-of-the-Technology

The International Energy Agency (IEA) forecasts hydrogen production to reach $528\,\mathrm{Mt}$ by 2050, while the International Renewable Energy Agency (IRENA) estimates $614\,\mathrm{Mt}$ by the same year. To support this increase, the IEA targets $700\,\mathrm{GW}$ of electrolyzer capacity by 2030 and $3600\ \mathrm{GW}$ by 2050, while IRENA targets $350\,\mathrm{GW}$ by 2030 and $5000\,\mathrm{GW}$ by 2050. Achieving these ambitious objectives will require a significant annual increase in electrolyzer installations, reaching $400\,\mathrm{GW}$ per year by mid-century.[22] The PEMWEs's reliance on iridium, titanium, and platinum raises concerns regarding the stability of the supply chain. As reported by the European Commission's Raw Materials Information System, South Africa accounts for 93% of the global iridium mining capacity. Limited annual iridium production of a maximum of 7 - $8\,\mathrm{t\,yr^{-1}}$, presents challenges in meeting desired targets.[19–21,24] It is currently estimated that about 20% of the annual iridium supply, equal to $1.5\,\mathrm{t\,yr^{-1}}$, is available for PEMWE systems.[21] This change is also reflected in the cost breakdown analysis of the National Renewable Energy Laboratory (NREL) in 2019[50] and 2024[51]. In 2019, the cost distribution of a MEA was almost evenly split, with the membrane comprising one part, while the other part included platinum group metals (PGM) along with the ionomer. However, the iridium prices skyrocketed in 2021 which is reflected in the study of 2024[51] as the cost of iridium dominates the MEA manufacturing and stack costs. Assuming an annual stack production rate of $1\,\mathrm{GW\,yr^{-1}}$, the iridium cost would still account for 48% of the total stack cost. In their 2019 analysis, the whole MEA hold a 36%-47% share of the total stack cost, depending on the annual production rate for a $1\,\mathrm{MW\,yr^{-1}}$ stack. However, these studied assumed a high iridium loading of $> 2\,\mathrm{mg_{Ir}\,cm^{-2}}$.

In this context, it is reasonable that research related to PEMWE focuses on reducing the

required iridium content. Depending on the assumed scenario, several studies have estimated that the iridium-related specific power must be $< 0.10\,\mathrm{mg_{Ir}\,W^{-1}}$ or $\mathrm{t_{Ir}\,GW^{-1}}$. More concerning than performance are the ambitious degradation rate targets, such as $1.6\,\mu\mathrm{V\,h^{-1}}$ at $3\,\mathrm{A\,cm^{-2}}$ by 2030.[21] The aforementioned challenges related to tailoring the interface between the CL and the porous transport layer (PTL), implementing a variety of catalysts, improving the in-plane electrical conductivity, and understanding the impact of different load profiles on the degradation mechanism will require a thorough understanding of the nature of the CL.

Achieving these ambitious targets will not be possible without advancements in other components of PEMWE technology. In general, the development of components is led by the aspiration to reduce the amount of critical raw materials (CRMs) while lowering the corresponding costs. The main components of an PEMWE cell are the PTL, the gas diffusion layer (GDL), the membrane, and the anode and cathode CLs.[9] These components are sandwiched between the end plates and the flow field plates.[†] A schematic of the cell assembly can be found in Figure 2.3. The **end plates** are typically two stainless steel metal plates that are

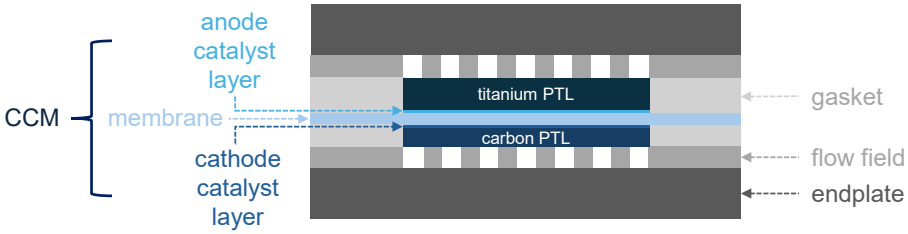

Figure 2.3. A schematic illustrating the primary components of PEMWE and their configuration within the cell assembly.

critical for mechanical compression of the stacked components. Research has shown that mechanical compression affects performance, but also hydrogen crossover from the cathode to the anode. The higher the cell compression, the higher the performance until it reaches a threshold. Simultaneously the hydrogen crossover increases. Homogeneity of compression ensures heat transfer and homogeneous contact between the components.[52,53] Compression is usually controlled by the thickness of the **gasket** relative to the thickness of the GDL and PTL. A typical gasket is made of polytetrafluorethylen (PTFE), ethylene propylene diene monomer rubber (EPDM), or Viton. Its mechanical properties, i.e., Young's modulus, affect the compression of the components. An important requirement for the gasket is that it must be an insulator, chemically inert and have high corrosion resistance.[52,54,55] If a hard-stop gasket is used on the cathode side, it is thinner than the PTL to achieve the desired compression within

the cell. Other gasket types regulate compression through material elasticity or controlled assembly torque. All components are stacked between both endplates while one **flow field** is dedicated for the anode and one for the cathode. These components act as a water supply to the cell, but also as gas channels to remove the produced gas from the cell. The shape and design of the flow field affect the thermal management of the cell, as well as the mechanical compression of other components, such as the PTL, CL, and membrane.[56] In the case of single cells, the flow field plates are called monopolar plates as the flow field pattern is integrated on one side of the plate. This distinguishes them from the bipolar plates used in PEMWE stacks, which are possessing flow fields on both sides. There are a variety of flow fields such as serpentine, pin cushion, parallel or meander type flow fields. Typically the flow fields are made out of titanium, which are coated with noble metals, such as platinum and gold.[57–60]

Most of the time, the GDL is carbon based and used on the cathode side. However, the term "GDL" originated from fuel cell research as it is often the same material. Typical brands used are Toray, Spectracarb, Freudenberg or SGL Carbon. However, in the case of PEMWE it is actually a **PTL** as the media feed is water and not gas like for the GDL in the fuel cell. Typically, titanium based PTLs are used on the anode side. In general, the PTL is a porous body made of fibers or sintered particles. Its thickness, porosity and tortuosity define the water distribution and the removal gas produced inside the CL. In addition, its geometric characteristics limit the electrical contact with the CL.[61–63] In the last decade, the main motivation to improve the components of PEMWE technology was that the required materials corresponded to high costs.[51,64–66] Therefore, the goal was to reduce the amount of material used or replace it with alternatives. With this in mind, attempts have been made to replace expensive titanium with other materials such as stainless steel,[67,68] niobium,[69] copper,[70] or graphite.[71] However, recent research has shown that the challenges associated with PEMWE cannot be solved by a single component. It is more important to design the interface between these components, such as the interface between PTL and CL. Therefore, research is also focused on the introduction of a microporous layer (MPL) between PTL and CL to increase the contact area between both to enhance the utilization of the CL.[72,73] The most commonly used catalyst for the cathode is still platinum on carbon. Different weight ratios of platinum to carbon are commonly used. On the anode, iridium-based catalysts are commonly applied. Prior to cell assembly, the membrane and CLs are combined to form a so-called MEA.[12,74,75] The **membrane** acts as an electrical insulator and ionic phase between anode and cathode. Its resistance depends strongly on the thickness and for relatively thick membranes ($> 100\,\mu\mathrm{m}$) it possesses the highest share among the overpotentials inside a PEMWE cell at higher current densities. The ionic overpotential is

directly proportional to the membrane thickness. However, the thinner the membrane, the more relevant the hydrogen crossover. Although the membrane is an attractive area of research, Nafion remains the most commonly used material. Most alternative materials have lower performance and less stability. Poisoning of the membrane by foreign cations, such as iron or nickel, or anions, such as chlorine, leads to rapid deterioration in performance. Therefore, the quality of the feed water is highly regulated. The strategy related to the membrane is to make it thinner in order to reduce the material consumption while increasing the performance of the PEMWE system. However, the hydrogen crossover becomes critical if the PEMWE stack is to be operated at differential pressure. For this purpose the cathode is usually operated at 15 to $30\,\mathrm{bar}$. The reason for pressure operation is that it reduces the number of compressor stages required for hydrogen storage.[76] Therefore, recombination CLs are studied and implemented as interlayer inside the membrane. Typically, platinum-based catalysts are used within a layer that is below $< 10\,\mu\mathrm{m}$ and effectively reduces hydrogen crossover.[77,78] A recent development related to the Nafion membrane was that the European Chemicals Agency (ECHA) planned to ban most per- and polyfluorinated alkyl substance (PFAS) materials. In 2023, the ECHA launched a public consultation on the proposed ban.[79–81] This ban would cause gaskets, membranes, and ionomers, commonly used components, to become unavailable for PEMWE systems. There are already commercially available hydrocarbon alternatives, such as Premion™ from Ionomr Innovations. Also some laboratory membranes have outperformed commercial Nafion (N115) membranes but still suffer from high degradation rates.[82]

Perhaps the most significant barrier associated with PEMWE is currently its heavy reliance on the iridium catalyst. This additional uncertainty, again related to the supply chain, puts a burden on the technology.[19,20] The anode catalyst and the CL will be discussed in Chapter 3.

3 The Production-Structure-Property Triangle

Research is tending to focus on the catalyst itself instead on the CL or catalyst integration.[10,11,83] Moreover, the current challenges emphasize the need to understand how the electrolyzer durability is connected with CL formation.[10,40,43,44] Manufacturing technologies, such as laboratory-scale ultrasonic spray coating,[39,83,84] and their effect on the properties of the CL must be compared with others that are more relevant on an industrial scale,[10] such as slot die casting,[77,85,86] or inkjet printing.[87,88‡]

The focus of this work is on ultrasonic spray coating. The chosen technique provides a versatile platform to tailor the electrode structure. The main objective of this work is to study the production-structure-property triangle (PSPT). Each vertex of the triangle represents a subject, such as production, structure, or property. The edges represent the entry to the relationship between two of these subjects. In the following, the typical manufacturing steps to produce CLs are shown and explained using the example of ultrasonic spray coating. This is followed by discussing the general CL structure and the resulting characteristics.[‡]

3.1 Aspects of Catalyst Layer Production

Each CL fabrication process begins with the dispersion formulation. The typical preparation of the dispersion is shown schematically in Figure 3.1. Milling or sieving may be used to homogenize the catalyst prior to dispersion preparation. PGM group catalysts are flammable with organic solvents or alcohols. For safety reasons, the first step is to quench the catalyst powder with a quantity of water. The mixture can then be further diluted with one or more components such as isopropanol, n-propanol, glycerin or butyl acetate. Another option is to ice the mixture to prevent evaporation of volatile solvents or to prevent heating during subsequent treatments. Typically, Nafion is added by dosing a quantity of a specific Nafion dispersion (e.g. DS2020CS, D1021, LQ-1115) into the vial containing the mixture. As an alternative to Nafion, Aquivion dispersions such as D79-25BS and D87-28BS can be used.

The dispersion is then homogenized by one or a combination of treatments such as a high shear mixer, ultrasonic bath or horn.[89,90] The dispersion is now ready to be used in a specific manufacturing process to produce the CL. Each dispersion must be specifically tailored to the materials used, but also to the manufacturing process. For example, a dispersion made for a spray-coating device is not the same as a dispersion made for slot die casting or the doctor blade. Therefore, the process steps shown in Figure 3.1 will differ depending on the route chosen. Prior to the coating process, the microstructure and macrostructure of the CL are already influenced by the prepared dispersion.[41,91–94] Analysis of ultrasonically and high-shear

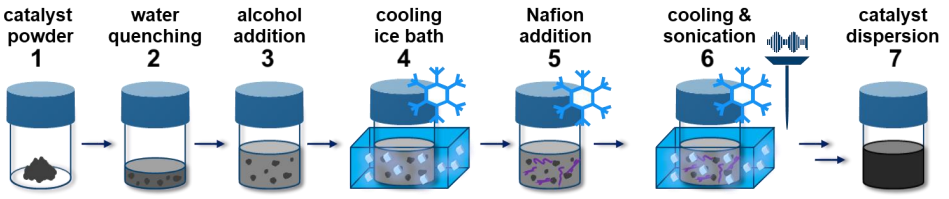

Figure 3.1. Typical process steps for dispersion formulation.

mixed Nafion dispersions showed that acoustic cavitation and high-shear mixing each played a critical role in reducing viscosity.[89,90] In another study, increasing water levels in the dispersion led to strong aggregation of Nafion ionomers.[95] The addition of alcohol to the system can induce elongation of rod-like particles through selective solvation, thereby strengthening the attractive electrostatic interaction between particles and reducing the average interparticle distance.[96] Thus, the dispersion process must successfully break up large agglomerates into ideal sizes while preventing any degradation or decomposition of the materials.[97] The complex interactions within the dispersion are much better understood in the fuel cell field. For example, the rheological properties of the dispersion are critically dependent on the weight ratios of the components and their nature. High surface area carbon exhibits higher viscosity than Vulcan dispersion due to internal pore volume and higher agglomeration. Platinum stabilizes the dispersion through electrostatic interactions, while the ionomer provides electrosteric repulsion to stabilize the aggregates. Overall, it is likely that the interaction between the ionomer and platinum, as well as the high surface area carbon, leads to flocculation of the particle aggregates.[41] During the coating process, the dispersion is spread over a specific substrate, such as a membrane, PTL or decal sheet. When the dispersion comes into contact with the substrate, the drying process begins. Again, the composition of the dispersing solvent plays a critical role. If water is enriched, it can cause cracking and ultimately delamination. This

is due to the increased surface tension and lower surface energy of the substrate. Conversely, when n-propanol predominates, the surface tension is reduced, resulting in less capillary stress and only minor cracking at the film surface.[98] However, these studies are performed for coating processes such as slot die casting or Meyer rod coating. In fact, the dispersion in the case of spray coating possess highly diluted solids (< 2 wt.%).

Ultrasonic spray coating is schematically shown in Figure 3.2. After the dispersion is made, it is filled into a precision syringe. A pump is used to feed the nozzle of the spray coating device. A specific flow rate is set and the nozzle frequency is selected. The nozzle tip oscillates at a certain frequency (i.e. $48\,\mathrm{kHz}$ or $120\,\mathrm{kHz}$) and atomizes the dispersion feed through the nozzle. The droplet size is a function of the frequency, but also depends on the dispersion quality. As can be seen in the left box of Figure 3.2, the nozzle is placed at a certain height above the substrate to be coated and the shaping pressure forms the cone of the atomized dispersion. Prior to the start of the coating, the substrate was placed onto the heated vacuum plate. The nozzle is then moved along a certain pattern, as shown in the right box of Figure 3.2. The chosen spray pattern will affect the quality of the CL. In the right box of Figure

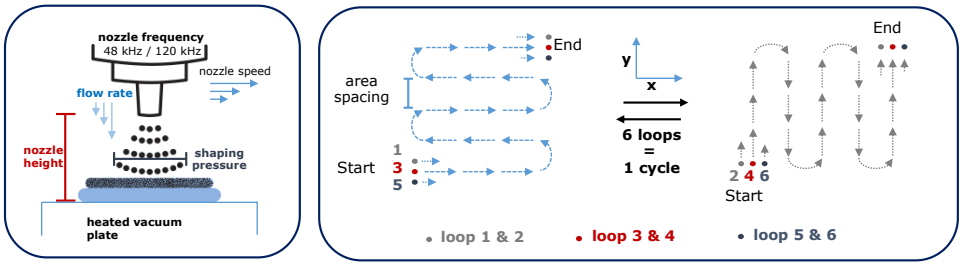

Figure 3.2. The left box shows the operating parameters of a spray coating system. The right box shows an example spray pattern.

3.2, a classic meandering spray pattern is shown. The center of the nozzle follows this path. The area spacing describes the distance between these paths. The forming pressure defines the diameter of the spray cone and therefore interacts with the area spacing. To prevent the formation of an anisotropic layer, the pattern is rotated by 90°. Typically, an offset of one third of the spacing is used per direction. This helps to avoid the formation of an uneven layer. In general, 6 loops are equal to one cycle. The number of cycles is used to adjust the loading of the electrode through the machine parameter. Depending on the respective combination of dispersion and applied machine parameter a certain CL structure is formed. However, appropriate structural descriptors to accurately describe the formed CL are needed

to better understand the relationship between production and structure.

3.2 Structure and Morphology of the Catalyst Layer

Chemistry is constantly striving to describe structure and morphology at different length scales. For example, the structure of a catalyst is typically characterized by its crystal structure and facets (e.g., (100), (111)), its elemental composition, or its surface functionalities.[99] Morphology, which is defined by particle size, shape, surface area, porosity, and pore network, plays a critical role in catalyst performance. The same characteristics apply to catalyst supports, influencing how active sites are exposed and utilized. A catalyst's activity depends not only on its composition, but also on the orientation of its crystal facets. The orientation of the facets influences surface energy and how the surface interacts with reactants. Tuning this surface energy allows for a more effective interaction with specific species undergoing conversion. Additionally, morphology affects the accessibility of the catalytic surface, determining how efficiently reactants can reach and utilize active sites. With deliberate design, morphology can be engineered to enhance selectivity toward desired reaction pathways.[100] Iridium catalysts deposited on a support, such as TiOx[27,101] or antimony tin oxide (ATO)[28], are affected by the structure of that support and vice versa. There are a number of studies that focus solely on this metal-support interaction to optimize the activity or stability of the catalytic system.[17,18,102–104] The catalyst is essential to the function of the CL, but the choice of polymer binder also profoundly influences its overall performance. Polymers, such as the Nafion ionomer, are sometimes represented by the same parameters as the catalyst, such as elemental composition. However, they are also represented by different unique features, such as degree of polymerization or viscosity.[105] The interaction between the ionomer and the catalyst and its support is critical for the CL produced.

The CL itself can be described as a catalytic system embedded in a polymer matrix. Figure 3.3 shows a schematic of the CL. A comprehensive study of CL properties must account for the multiscale nature of the underlying processes and phenomena. For instance, variations in layer thickness and the distribution of catalyst loading across the electrode are observed at the macroscopic scale. Typically, the Nafion content of a CL is given in weight percent, such as 20 wt.% of the total electrode mass.[106] The perception on the morphology changes, if the density of pure iridium ($22.65\,\mathrm{g\,cm^{-3}}$)[107] and the density of wetted Nafion at ambient pressure ($1.58\,\mathrm{g\,cm^{-3}}$)[108] is considered. Therefore, a CL with 20 wt.% Nafion means that 78% of the electrode volume is made out of Nafion and only 22% consists of iridium. This implies that

the thickness of the CL depends critically on the Nafion content used. In the literature a performance optimum has been found at 11.6 wt.% Nafion used in the anode[109] and for the cathode it should be close to 10 wt.%.[53]. However, these studies are highly dependent on the catalyst used, and higher Nafion contents are often preferable when considering other dispersion properties, such as stability and processability which depends on the selected manufacturing process. The aforementioned 11.6 wt.% refers to an iridium catalyst supported on TiO_2, while in the study related to the cathode a 60 wt.% platinum on carbon catalyst was used. The thickness of a material, as well as its pore volume and size, is affected by more than one factor.[110] In fuel cells, porosity and tortuosity are critical engineering parameter to optimize the CL.[111,112] However, in PEMWE, the swelling behavior of the Nafion ionomer makes it difficult to establish clear correlations between the pores formed during CL production and those present under operating conditions. The contact area between the PTL and the CL is influenced by surface features such as isolated islands, roughness, and waviness.

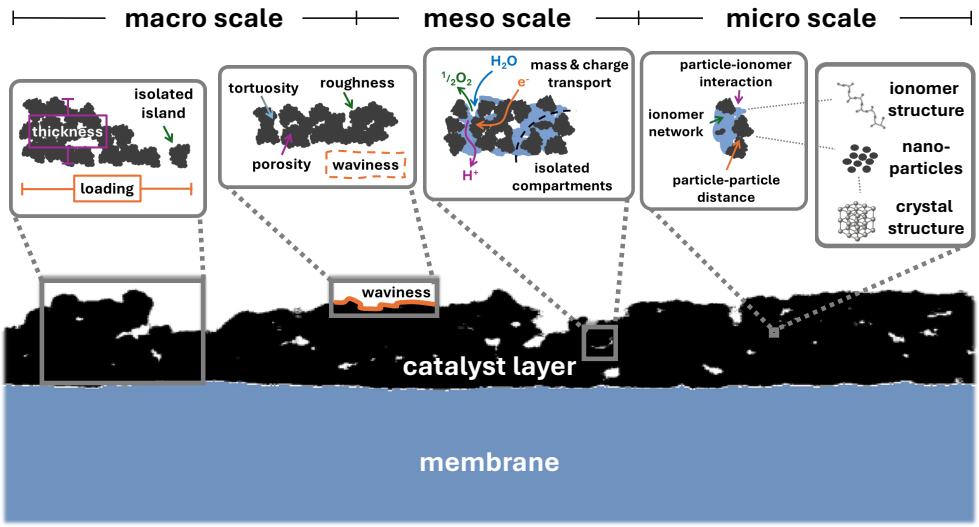

Figure 3.3. A schematic representation of the CL, highlighting some interactions and phenomena occurring at different length scales.

At the mesoscale, the transport of mass and charge is critical for the CL system and largely determines the utilization of the active material. Nafion acts as the proton conductive phase in the CL. It removes the produced hydrogen protons from the reaction site towards the membrane. More important in PEMWE is the electronic conductivity within an anode CL as

it defines the catalyst utilization.[113] At the meso and micro scale, the swelling behavior of Nafion results in a variation of the metallic conduction network of the catalyst by changing the inter-particle or inter-aggregate distance. A study by Morris et al. suggests that in the CL design, network disruptions can result in isolated aggregates, which can lead to a loss of catalyst utilization.[114] At this point also the heat transfer must be taken into account. The heat conductivity is for metals proportional to the electrical conductivity. Local variations in the composition and heat conductivity leads to hot zones which accelerate degradation.

The iridium loading used on the anode in PEMWE is in context of the PSPT frequently discussed. It has, together with the Nafion content, also a decisive influence on the thickness of the CL and thus on the contact area with the PTL. This contact area is proportional to the contact resistance (R_c) between the PTL and the CL. Moreover, the deviation in PTL thickness is in the same order of magnitude as the thickness of the CL. Typically, the CL thickness is greater using supported iridium catalysts than unsupported catalysts. The support enhances the metallic conduction network, which improves the in-plane electrical conductivity. If the loading is too low, this network is interrupted and performance deteriorates. Thus, especially at low loadings the production of the CL is critical to maintain a homogeneous and continuous phase of the metallic conducting network. In an ideal CL, the electronic conduction network is assumed to be homogeneous and continuous. Under this assumption, reducing the catalyst loading should only decrease the layer's thickness without affecting the intrinsic in-plane electrical conductivity. Therefore, if measured sheet resistance does not inversely scale with reduced loading, it implies that the conduction network is no longer behaving ideally. Specifically, this suggests that the connectivity or distribution of conductive pathways within the layer has changed, indicating an altered conduction network. The swelling of the membrane is another factor which deteriorates the metallic conduction network. Studying the electrical resistivity of the CL helps to explain effects emerging during single-cell testing while offering another brick to describe the CL microstructure and its electronic nature.[114,115]

This indicates the the CL needs to be described by more structural parameters beyond thickness, composition or loading. To correlate the manufacturing process with the formation of the CL and its properties, the CL structure must be described in greater detail. To accomplish this, characterization methods must be applied and validated. Each method has its advantages and disadvantages. The stochastic nature of the CL makes it difficult to identify clear trends, as most characterization methods examine micrometer-sized areas of square-centimeter-sized electrodes, which must then be scaled to square-meter-sized electrodes for industrial applications. Chapter 4 highlights the challenges and methods of characterizing the CL.

3.3 Structure and Related Electrochemical Properties

With low iridium loadings, the interfacial contact between the PTL and CL becomes even more crucial than in conventional electrode assemblies.[23,116–118] Rozain et al.[119] and Bernt et al.[24] observed that at a threshold value of $< 0.5\,\mathrm{mg_{Ir}\,cm^{-2}}$, the performance degraded as the layer became non-homogeneous and too thin to maintain the electrochemical activity of all reaction sites as well as its in-plane electrical conductivity. A recent study by Taie et al.[23] demonstrated that it is possible to tailor the mesoscale of low iridium loadings by optimizing the CL fabrication process. During their investigation of loadings ranging from 0.17 to $0.0035\,\mathrm{mg_{Ir}\,cm^{-2}}$, they found that the iridium loading was not affecting the Ohmic losses. A significant portion of the ohmic resistance was attributed to the membrane. That made the contribution of the CL nature to the ohmic resistance invisible. Instead, one major cause of decreased performance was attributed to the declining kinetics while reducing the loading. The decline in kinetics was ascribed to a decrease in the number of available reaction sites, which aligns with the explanation provided by Rozain et al.[119] and Bernt et al.[24] The researchers also noted a mass transport limitation for loadings lower than $\leq 0.0115\,\mathrm{mg_{Ir}\,cm^{-2}}$, which can be due to a reduction in the surface area of the CL. This reduction limits the ability of water and oxygen to be transported from the PTL pores to the CL located below the PTL land at higher current densities. Taie et al.[23] postulated that these localized mass transport limitations could be the reason for the durability issue of low loadings. Although Taie et al.[23] acknowledged the existence of a parameter linking the removal of oxygen bubbles and the distribution of reaction sites. They were unable to determine its identity or functional relationship.[‡]

According to Padgett et al.[113], in-plane electronic resistivity is identified as the predominant resistance in low-loaded $\mathrm{IrO_2}$ CL. This resistance promotes increased local overpotentials which leads to a higher concentration of oxygen evolution current at the PTL-CL interface, resulting in accelerated degradation and possible early anode failure.[113] However, a study led by Torrero et al.[120] found that the key to low iridium loading is to prioritize electronic contact with the PTL rather than improving in-plane conductivity.[120] It is likely that all of these factors together contribute to the degradation rate. Currently, there is no consensus within the scientific community on whether contact resistance or in-plane electrical resistivity is the limiting factor. Thermal management within the CL must also be considered, as thermal conductivity is proportional to electrical conductivity. Therefore, inhomogeneous current distribution would cause hot zones with a potentially higher degradation rate.[121,122] The research conducted by Möckl et al. showed an extrapolated long-term degradation rate of $1\,\mathrm{\mu V\,h^{-1}}$ for a $0.25\,\mathrm{mg_{Ir}\,cm^{-2}}$ loading, which was only slightly higher than the degradation rate ($0.25\,\mathrm{\mu V\,h^{-1}}$) reported for

the $2\,\mathrm{mg_{Ir}\,cm^{-2}}$ loading.[123] The degradation rates were determined from stack testing operated at 60°C. However, strong changes in the high frequency resistance (HFR) obscured the results, making it necessary to use HFR-corrected data to evaluate CL degradation.

It is often overlooked that the production of the CL leads to its own intrinsic properties, entangled in the interaction with specific substrates (e.g., membranes, PTLs), and their interfaces.[124–126] The CL structure is initially determined by the manufacturing method. However, performance also depends on metal loading and interactions between the catalyst and ionomer. These factors are influenced by morphology (whether homogeneous or inhomogeneous) and variations in porosity and thickness distribution.[39,115,127,128] Accessing these properties by single-cell testing yields additional impact factors such as cell compression,[52,54,55] various interfaces,[15,23,129] and electrochemical testing protocols[130–132], that also affect the results and blur the distinct interpretation of the data. Thus, optimizing and evaluating different CL designs as a MEA remains challenging and requires methods to bridge the complexity between catalyst screening, CL design, and single-cell testing results.[23,133†]

4 Characterization Methods for Catalyst Layers

This chapter is dedicated to the characterization methods that have been used to describe CLs. This work focuses on approaches to describe the morphological structure of a CL and to characterize the resistance of the CL. Microscopy is often the method of choice for the description of the morphology of the CL. More advanced characterization involves introducing computational approaches to quantitatively describe surface texture. With respect to the resistance of the CL, an overview of the available methods for its determination is given and critically discussed.

4.1 Classical Microscopy

Some works addressed the issue emerging from the interplay of the different length scales, diving from macro-structure-related properties (e.g. porosity, ionomer and catalyst distribution) towards the bottom of microstructure-related effects (e.g. catalyst-ionomer interaction, catalyst surface functionalities).[38,43,134] Thus it is common to utilize microscopy techniques such as SEM, TEM or atomic force microscopy (AFM) as the first step to access the impact of production on the structure. Several studies used SEM or TEM images to extract particle shape[135–137], particle-size distributions[138–140], pore size distributions[117,141,142] or pit formation[143–145] in corrosion studies. The later-developed AFM has significantly contributed to the understanding of surface phenomena and supports a variety of use cases. For example, AFM has been used to study the ionomer distribution inside the CL for PEMFC.[146] It has also been used to study the effect of humidity on the mechanical properties of the Nafion N117 membrane, showing that water acts as a plasticizer.[147] However, depending on the context, the observed regions of interest (ROI) or area of interest is typically only a few micrometres in size, e.g. $5\,\mu\mathrm{m}$ x $5\,\mu\mathrm{m}$.[148] On the other hand, it is possible to achieve atomic-scale resolution, i.e. $0.5\,\mathrm{nm}$.[149]

Progress has also been made in other microscopic techniques, such as SEM, confocal laser scanning microscope (CLSM), and TEM, all of which have benefited from enhanced com-

putational resources. Developments in image processing allowed advanced methodologies to apply specific algorithms for segmenting and extracting the geometric relationships represented within the images automatically while trying to avoid any biasing of the information.[37,150–152] Colliard-Granero et al.[37] demonstrated an impressive workflow utilizing several publicly available libraries, such as OpenCV[153], U-Net[154], and the StarDist model[155] to automate TEM-based particle size analysis for PEMFC. The overall schematic approach is shown in Figure 4.1, highlighting not only the computational pathway used to extract particle size distributions but also illustrating how scientific progress builds upon the integration of multiple individual contributions.

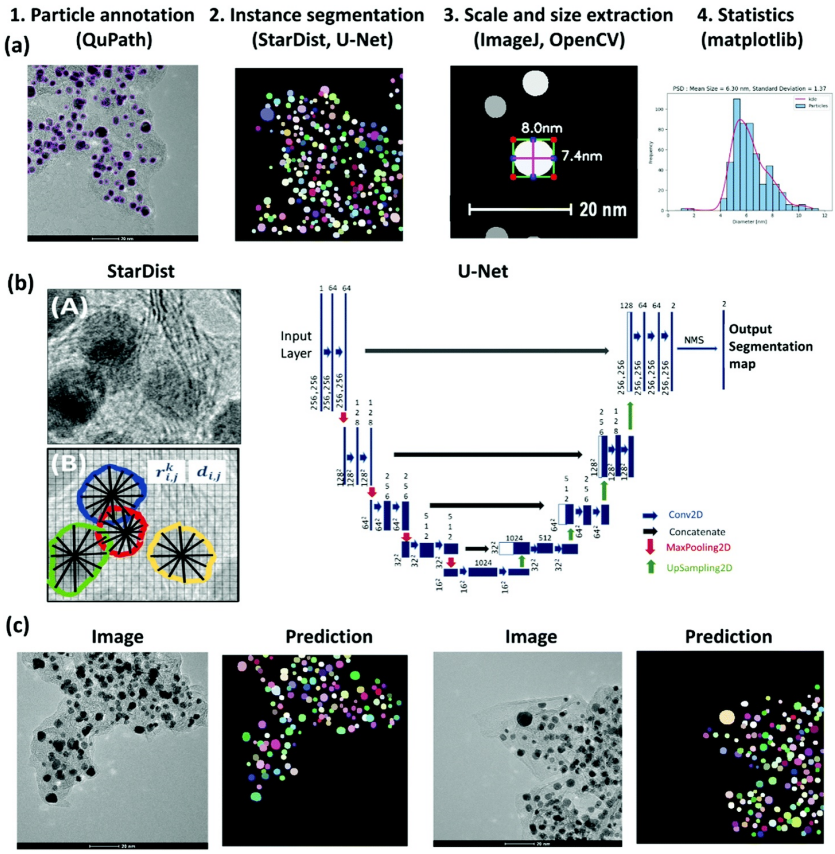

Figure 4.1. The schematic workflow developed by Colliard-Granero et al.[37] is shown in (a) and (b) illustrates the application of StarDist and U-Net to identify overlapping Pt particles on a carbon support. Reprinted with permission from the Royal Society of Chemistry 2022.

This integration improves the reliability of determining particle sizes from TEM images and paves the way for high-throughput analysis, which will be critical in the decades to come. However, applying these methods requires that the contrast between the visible components is strong enough.[37] The contrast in image processing and analysis plays a significant role for the distinguishability of objects or features within an image. In many cases, image processing techniques such as thresholding, edge detection, and segmentation rely heavily on contrast to identify and separate objects of interest from the background. On the other hand, artificial contrast enhancement is dangerous because, in the case of fine textures, this would lead to informational loss.[138‡]

In addition, studies related to SEM and TEM images lack the ability to provide a quantifiable output that could be used to apply artificial intelligence or machine learning.[156] Most SEM and TEM analyses focus on isolating particles or agglomerates rather than capturing the CL architecture, because the high structural density complicates a comprehensive assessment. This structural density arises from densely packed particles of varying sizes, irregular agglomerates, surface holes and pores, overlapping features, and multicompositional domains (e.g. Nafion, support catalysts), all of which are commonly observed in a CL. Often, microscopic results are interpreted subjectively rather than objectively. Therefore, an alternative way to describe the appearance or texture of the CL needs to be investigated.

4.2 Computational Approaches to Texture

In general, surface texture is the periodic or non-periodic variation of a pattern, with or without irregularities, fluctuating around a defined surface. The texture is the main characteristic of the appearance of a surface, contributing to its functionality.[157,158] Several methods exist to access the texture either in contact or without any contact to the surface. A variety of techniques is employed for assessing the surface texture, such as AFM to monitor surface quality of the anode[149], CLSM to study electro-active microorganism[159], analyzing coatings by SEM[160], or charge-coupled device cameras for machine monitoring.[161,162] While profile surface texture parameters (2D) are a common choice to monitor the surface height (z-axis) along an x-axis, there has been growing attention towards areal surface texture parameters (3D) for investigating functional relationships of the surface height (z-axis) in x and y direction.[163,164] Nonetheless, the suitable parameters to describe the texture may differ depending on the context and the intended use of the designed surface. For instance, the automotive and aerospace industries use different parameter sets to describe surfaces compared to the electronics industry, as each sector has distinct surface-related requirements.[158] Definition and usage of these surface texture parameters (STPs) are governed by ISO 25178 and a list of some relevant definitions can be found in Table AT.2. Selection of the set of suitable parameters remains challenging. A different approach towards texture emerged from computational imaging, classifies the textures into first-, second- or higher-ordered textures.

The first-order (FO) texture represents the intensity distribution, described by typically used statistics to describe distributions, such as the skewness, variance or kurtosis.[165] These statistical measures are commonly applied to describe gray levels occurring in images or also for surface height distributions. The variance (σ^2) quantifies the dispersion of values around the mean, indicating the degree to which values deviate from the average. Skewness measures the asymmetry of the distribution, showing whether the data are biased toward higher or lower values. Kurtosis describes the peakedness or flatness of the distribution, indicating the presence of outliers and how much the distribution differs from a normal distribution. Figure 4.2 shows several simulated surface profiles and their corresponding height distributions. These features are reflected by skewness and kurtosis. Negative skewness (Figure 4.2a) may indicate etched or corroded surfaces with deeper valleys. Positive skewness, on the other hand, can result from particulate buildup in coatings or peaks on surfaces caused by deposition processes. Symmetric profiles (zero skewness) usually appear on surfaces that are uniformly polished or machined. Kurtosis (Figure 4.2b) reflects the sharpness and tail behavior of a surface profile. Low kurtosis corresponds to flatter, worn surfaces with fewer extremes, while high kurtosis reflects surfaces

with sharp features or deep pits. These variations illustrate the types of surfaces commonly encountered in machining, polishing, erosion, and coating processes. In each distribution, the mean, median, and mode are shown to demonstrate the effect of the distribution's shape on other statistical quantities. The same rules that apply to STPs also apply to FO image

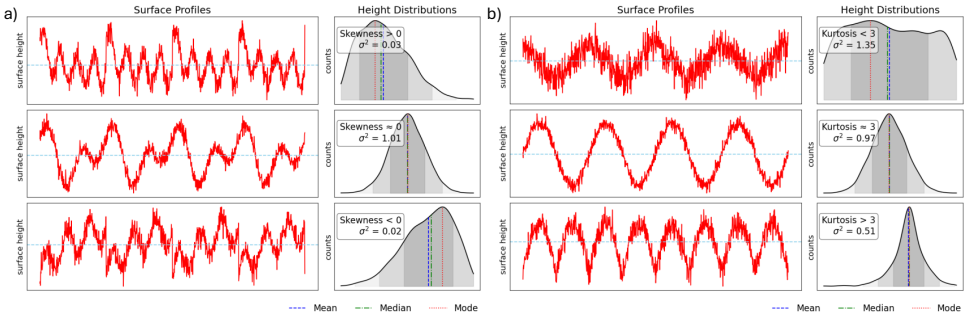

Figure 4.2. Simulated surface profiles and their corresponding height distributions illustrating statistical measures. (a) Effect of surface asymmetry on skewness, showing how the shape of the profile influences the distribution's asymmetry. (b) Effect of peakedness on kurtosis, highlighting differences in flatness or outlier presence. Mean, median, and mode are marked to demonstrate how distribution shape impacts these statistical descriptors.

features (IFs), which offers information based on the occurrence of different gray-level values, but cannot be used to quantify changes in patterns within an image.[165–167] Instead, second or higher-order texture parameters refer to the spatial relationship between pairs of pixels within an image. These relationships can be assessed using computed matrices that provide insight into the occurrence of different pixel intensity combinations. However, the method beyond the matrix construction can vary and affects the analysis. Once the matrix is computed, it becomes possible to extract various statistical measures that quantify the textural properties of the image.[168–172] Haralick's pioneering work[168] in quantitative texture analysis, particularly his introduction of the gray-level co-occurrence matrix (GLCM) method, has had a profound and lasting impact on the field.[173] His seminal publication is significant because it has been cited more than 30,000 times until 2025. It has received over 1,000 citations per year since 2011.[168] However, the GLCM method was not the only approach established in recent years. Several methods quantifying textures, like the gray-level run length matrix (GLRLM)[169], gray level size zone matrix (GLSZM)[170], neighboring gray tone difference matrix (NGTDM)[171] or the gray level dependency matrix (GLDM)[172], paved their way into the research community.

These matrices follow a certain notation to extract the neighborhood dependencies of the pixel environment.

For example, Figure 4.3 shows a surface with whitish cracks. A magnified view of the crack area reveals features such as plateaus, which could be a carbon black CL. White cracks formed during the drying process of the CL. At the plateaus boundaries, the region exhibits varying

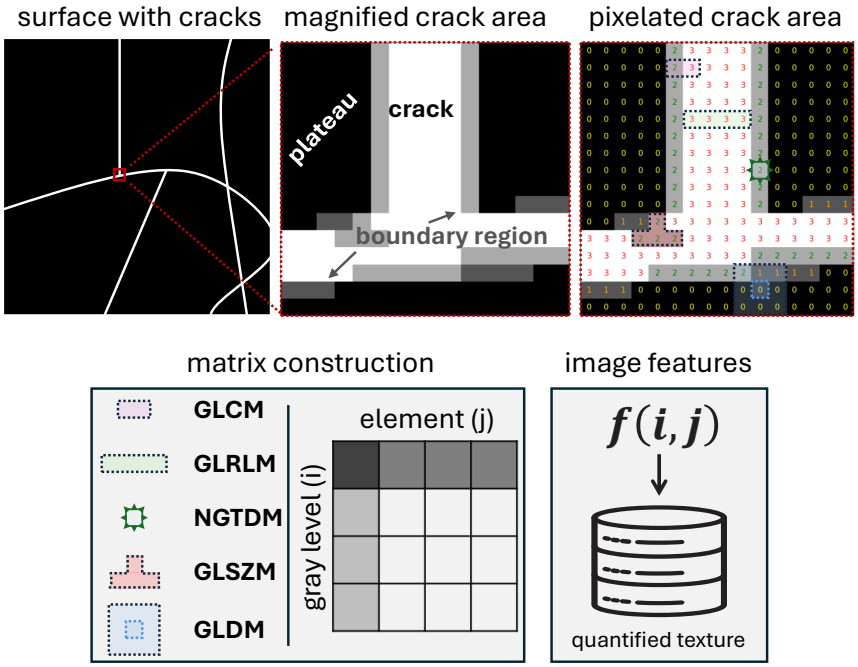

Figure 4.3. This is an example of a surface with whitish cracks, as well as a magnified view of the crack region. The plateau areas, which may consist of carbon black (CL), are surrounded by white cracks that formed during drying. The boundary regions exhibit varying heights, which are represented by different grayscale values; darker shades indicate higher elevations. For texture analysis, the pixelated crack region is modeled as a 16×16 image with 2-bit grayscale values ranging from 0 to 3. Inspired by [174].

height levels, indicated by dark and light gray shades, where darker shades represent higher level. The pixelated crack area is represented as a 16×16 image using a 2-bit grayscale color scale with values ranging from 0 to 3. Each of the matrices is built by analyzing how the gray level of a pixel relates to another element in the image at a defined spatial distance. From the matrix several statistics can be computed which are then called second- or higher

ordered IF or texture features. The GLCM provides information about the distribution of pixel pairs within an image, while the GLRLM reflects how many consecutive pixels of the same intensity (= run length) are connected in a certain direction. The GLSZM identifies regions within an image where pixels are connected and have the same gray level. The GLDM reflects the relationship between a center pixel and the surrounding pixel intensities. Similar to the GLDM, the NGTDM averages the pixel neighborhood around a pixel center.[174] The IFs, or in other words, the statistical quantities that can be calculated from these approaches, are well-documented in the literature.[174,175]

The application of IFs depends on several factors, such as the specific use case and the robustness of the features. In general, all IFs can be extracted and used to build statistical models that describe certain relationships. However, using all features is often impractical, because it significantly increases the complexity of the dataset[176]. To address this issue, dimensionality reduction is employed to eliminate redundant IFs. This is commonly achieved through correlation analysis[176], machine learning techniques[177,178], neural networks[179], or broader artificial intelligence methods[180]. Despite the use of these advanced techniques, an exploratory analysis of the extracted IFs remains essential to assess their consistency and robustness. The robustness of IFs is influenced by the image processing steps preceding feature extraction[173,181]. Moreover, some features are inherently more robust than others. For example, studies by Ericsson-Szecsenyi et al.[182] and Michalet et al.[183] have demonstrated that several IFs derived from the GLRLM, such as short run emphasis, long run emphasis, run percentage, and run length non-uniformity are among the most robust IFs.

In the case of GLRLM, run length non-uniformity reflects the similarity of run lengths within an image, thereby describing global structural characteristics. In contrast, long run emphasis quantifies the prevalence of long run lengths, with higher values indicating greater coarseness in the visible structure e.g., broader plateaus. This is illustrated in Figure 4.4a for the example of the same crack as in Figure 4.3. Here, the gray level 0 is found 19-times with a horizontal length (= run length) of 5 pixels. Similarly, white pixels (gray level value of 3) are identified corresponding to the width of the crack. Conversely, the short run emphasis may highlight valleys or pores within the CL because it captures fine textural variations. For instance, the pores depicted in Figure 4.4b exhibit short horizontal lengths (e.g. 4 pixels) within a specific gray level range (e.g., gray level of 3). The short-run emphasis assigns greater weight to features with short horizontal lengths than to those with longer lengths. It would emphasize a gray level of 3 combined with a horizontal run length of 9 less than it would a gray level of 3 combined with a horizontal run length of 4. Therefore, it highlights finer or smaller structural

features, such as small pores in the CL.

As expected, plateaus and cracks have longer and more uniform run lengths than the boundary region (Figure 4.4a). In contrast, regions containing pores (Figure 4.4b) are expected to exhibit short run lengths, often across multiple gray levels. In such cases, parameters such as short run high gray level emphasis are particularly informative, because they highlight short run lengths associated with high gray level values, revealing variations within e.g pore regions. However, before drawing such conclusions, it is essential to consider which CL features, together with their corresponding gray levels and run lengths, may be associated with small pores or fine particles and which may be associated with large pores or bulky agglomerates.

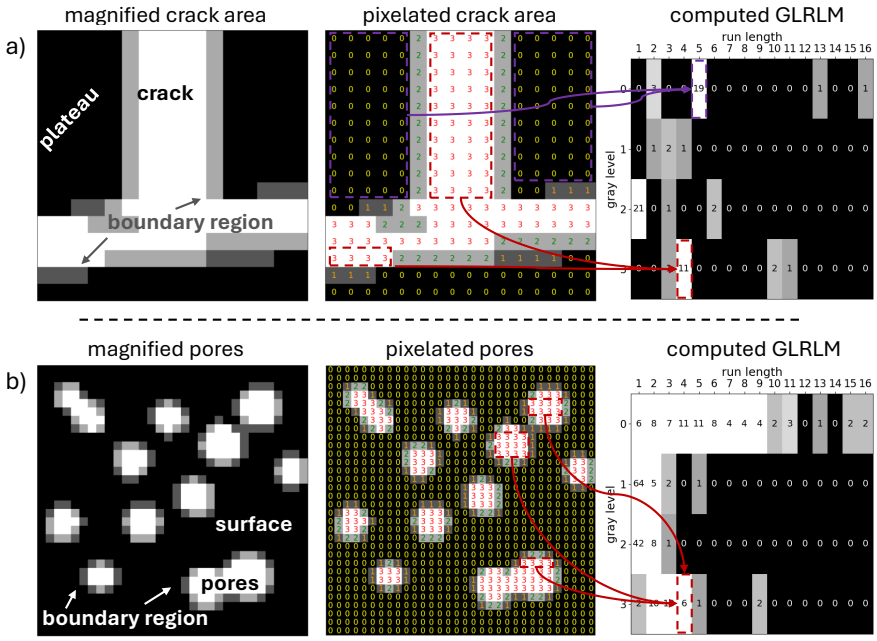

Figure 4.4. Illustration of GLRLM computation for a crack example (a) and an image with pores (b). Arrows indicate the principle of how the GLRLM is derived from the image.

In 2012, the research team around Artyushkova et al. drew a sparking pathway applying image processing of microscopy images to study the structure-to-property relationships of electrocatalysts.[184] The roughness and skewness were calculated using SEM images, and five IFs of the GLCM were utilized and computed from microscopy images. In further works focused on the PEMFC technology they studied the properties of various carbon blacks[185] and

CLs[44] regarding their corrosion behavior while connecting them to the structure observed using statistical analysis. However, relying on only five IFs derived from the GLCM limits the ability to draw definitive conclusions about the applicability of IFs in describing the CL.
Advances in computational power, growing interest in machine learning techniques, and active engagement from the scientific community have driven progress in this field. These developments have led to an expanded set of methods for deriving descriptors that could characterize the CL structure, as presented above. Technological and methodological advancements have strongly supported the growth of this research area.[186–188] These methods were applied to a wide variety of research areas, such as the terrain[189–191] or cell classification[170,192,193], visual perception[186,194–196], paleography[197,198] and tool condition monitoring[199–201]. The medical sector has benefited in the field of radiomics focusing on cancer detection using high-throughput imaging techniques.[180,202–207] To improve the reliability and accuracy of these image features, the Image Biomarker Standardization Initiative was created. The initiative enlisted the participation of 25 research teams, who worked together to standardize and reproduce 169 IFs.[208] One of the participants was the group around van Griethuysen et al. who developed the open-source platform PyRadiomics, which is utilized in this work.[175] Utilizing more mature platforms for the image processing, such as PyRadiomics[175], is advantageous because they are supported by scientific evidence, have been thoroughly tested, and are reliable. This reduces the risk of unintentional manipulation of data, which could lead to erroneous conclusions due to the malfunctioning calculation of the IFs. Although the extracted IFs ideally represent the texture present in the image, it does not mean that they have a direct correlation to the physical properties of the underlying surface. Therefore, correlation studies must be conducted first, to establish a connection between image features and physical characteristics.

Pearson Correlation and Statistical Interpretation

Calculating the Pearson correlation quantifies the strength and direction of a linear relationship between two variables. The Pearson correlation coefficient (PCC) is a statistical measure used to assess the strength and direction of the linear relationship between two continuous variables. It ranges from -1 to $+1$. Values close to ± 1 indicate a strong linear relationship, whereas values near 0 suggest little to no linear correlation. A positive coefficient implies that as one variable increases, the other tends to increase as well. In contrast, a negative coefficient indicates an inverse relationship between the variables. The PCC is defined by Equation 4.1 where x_i and y_i are the individual sample points. The terms $\bar{x}$ and $\bar{y}$ represent the sample

means of x and y, respectively. The variable n denotes the number of paired observations.

$$PCC = \frac{\sum_{i=1}^{n}(x_i - \bar{x})(y_i - \bar{y})}{\sqrt{\sum_{i=1}^{n}(x_i - \bar{x})^2}\sqrt{\sum_{i=1}^{n}(y_i - \bar{y})^2}} \tag{4.1}$$

This method is useful for identifying associations between IFs and physical characteristics because it operates on the original scale of the data. Unlike other statistical or machine learning techniques, it does not require complex transformations, such as logarithmic scaling, normalization, or dimensionality reduction techniques like principal component analysis. The Pearson correlation can be applied without altering the underlying variables. This makes it a straightforward and interpretable approach for measuring linear relationships. It allows to quantify how changes in image-derived features correspond to variations in real-world physical characteristics. The simplicity of computation and interpretation makes the PCC an accessible and transparent parameter. It is especially valuable in early-stage exploratory analyses and when communicating findings to non-specialist audiences.

However, despite its interpretability, challenges remain. Correlation does not imply a causal reationship. The reliability of the results can be affected by data quality, outliers, and limited variability in the observed features. These factors complicate the evaluation of the true significance and applicability of the calculated correlations. The actual strength of a specific correlation is controversial and depends, e.g. on the case studied or the range of observations.[209,210]

This ambiguity is illustrated by classic examples such as Anscombe's Quartet[211], the Datasaurus Dozen[212] or Simpson´s paradox[213]. Anscombe's Quartet comprises four datasets with nearly identical statistical properties, including mean, variance, and PCC, but with dramatically different graphical distributions. While the PCC remains the same, the visual patterns reveal outliers, nonlinear relationships, or clustering effects that the coefficient alone cannot capture, see Figure 4.5a-d.[211,214] The Datasaurus Dozen further illustrates this concept by presenting multiple datasets with similar summary statistics, including correlation, whose scatter plots depict vastly different shapes, such as a Tyrannosaurus (Figure 4.5e), a star, or a circle.[212,214,215] These examples emphasize the importance of visualizing data and understanding its distribution before drawing conclusions from correlation values.[176,209,210,214] Simpson's Paradox is another example of why context is crucial in correlation analysis. The Simpson's Paradox highlights the potential for trends in separate data sets to disappear or even reverse when the datasets are combined.[213,214] The PCC should not be interpreted in isolation, especially when assessing the practical relevance or underlying structure of a relationship.[176,209,210,214]

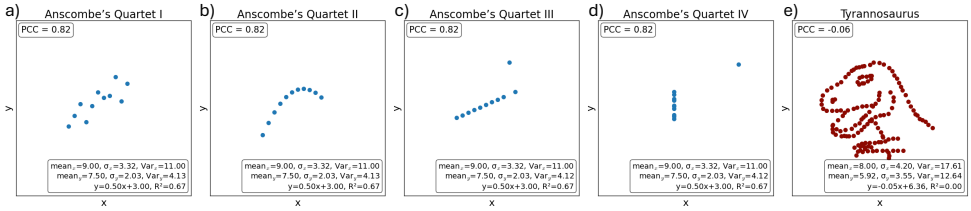

Figure 4.5. The scatterplots illustrate Anscombe's Quartet[211] datasets I-IV (a-d), which have identical summary statistics but reveal distinct distributions when visualized. The Tyrannosaurus dataset from the Datasaurus Dozen[215] (e) highlights how data with similar statistical properties can form dramatically different shapes.

Conversely, correlation analysis is essential for identifying and selecting meaningful variables for final conclusions. This is especially important when working with large, high-dimensional datasets where reducing dimensionality is critical to isolate the most informative features from a pool of largely unknown variables. For example, evaluating the pairwise correlation strength using the PCC between three known variables and 87 unknown ones yields 4,005 unique variable pairs. Extending this analysis across six different datasets results in 24,030 individual correlations to consider. Such analyses can be optimized using automated correlation filtering, threshold-based significance selection (e.g., considering only $|\mathrm{PCC}| > 0.7$), and visualization techniques, such as heat maps or clustergrams. In such cases, it is advisable to begin with simple yet effective strategies, such as prioritization, redundancy-targeted feature selection, and trend analysis, to gain initial insights.[176] These tools reduce cognitive load, allowing to focus on the most promising relationships and efficiently and scalably explore large parameter spaces.

Exploring the causality between image features and physical properties is even more challenging and beyond the scope of this work. However, the chosen approach is helpful for detecting possible connections, as it identifies correlations which could later be examined in more detail to assess potential causal relationships. This work's methodology aims to enhance the accessibility of the PSPT by studying the impact of different production variables on the formed CL structure, which can be described by surface texture parameters (STPs) and image features (IFs). These correlations may serve quality control and R&D objectives by offering deeper insights into the processes that govern CL production.

4.3 In-Plane Electrical Conductivity of Catalyst Layers

Various methods are described in the literature for determining the sheet resistance or in-plane electrical resistivity of thin films, CL, or multilayer systems.[216–219] Ahadi et al. introduced the transfer length method to study production parameters,[115] whereas other studies used this method to analyze Nafion/PEDOT-PSS mixtures,[220] iridium catalyst compositions,[221] or carbon graphitization temperature.[133] Furthermore, Nafion swelling and its impact on the in-plane electrical resistivity studied by the van-der-Pauw and four-electrode methods revealed that the expanded Nafion distorts the layer conductivity by separating the catalyst particles.[114,222] Insights into the contact resistance were mostly provided by impedance data recorded during single-cell testing and correlated to performance losses[24,223] or degradation.[123,224] From an electrode engineering perspective, these methods are suitable, but a rapid iterative method would be advantageous for electrode improvement. Most of the methods used at present are custom-made setups with limited possibilities to be flexibly applied as a standardized method for all PEMWEcomponents (PTLs, GDLs, CLs and MEAs).† Figure 4.6 provides schematic representations of four main techniques used in literature to evaluate the resistivity of materials, such as the the four-point method, the van der Pauw method, the transfer length method, and electrochemical impedance spectroscopy (EIS). The four-point method (Figure 4.6a) is

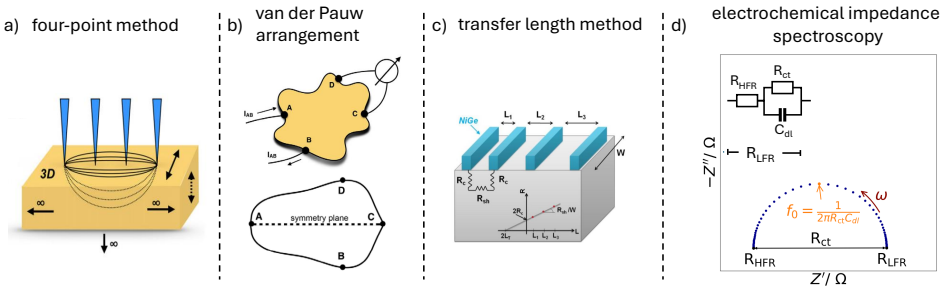

Figure 4.6. Overview of methods for measuring resistances: (a) Four-point probe method with four probes contacted to a 3D surface or alternative the probes are contacted to the sample following the van der Pauw method (b). In (c) the transfer length method is shown with blue probes contacted to a sample at different lengths. In (d) the EIS measurement is represented by a -Nyquist Plot and the Randles circuit at the top left. The real part of the impedance (Z') represents Ohmic components and is plotted on the x-axis. The imaginary part (Z'') represents capacitive or inductive behavior and is plotted on the y-axis. The figures from (a) and (b) are reprinted with permission from [216] while (c) is reprinted with permission from [225].

one of the most commonly used techniques to determine the resistance of materials. In this method, current is applied through the outer two probes, and voltage is measured across the inner two, which is then used to calculate the electrical resistance. From Ohm's law, the electrical resistance R of a material is defined as the ratio of the voltage V applied across it to the resulting current I, i.e., $R = \frac{V}{I}$. The conductivity σ is a measure of a material's intrinsic ability to conduct electric current. Its inverse is the resistivity ρ, where $\rho = R \cdot \frac{A}{L}$ for a homogeneous conductor of cross-sectional area A and length L. The four-point method effectively excludes the influence of contact resistance from the measurement. Although this method provides reliable electrical characterization, careful control of contact force and probe depth is necessary to prevent surface damage or inconsistencies. Additionally, the method's spatial resolution is limited, and it does not account for heterogeneity across the sample.[226] Instead, the four-line probe adaptation of the commonly-used four-point method allows pressure control, aiding in the adjustment of the contact between specimen and probe while being a robust method with an appropriate signal-to-noise ratio.[226,227†]

The van der Pauw method (Figure 4.6b) is also a four-point technique, but it differs from the classical linear four-point probe configuration in its geometry and application. The van der Pauw method is designed for samples with an arbitrary geometry, uniform thickness, and uniform resistivity. By placing four contacts on the periphery of a thin, flat sample, the resistivity can be calculated from multiple voltage and current pair measurements. However, this method assumes ideal conditions, such as an absence of surface defects and homogeneous material properties, which are not met in practical CLs or MEAs. Therefore, deviations from these assumptions can lead to significant measurement errors.[216†]

The transfer length method (Figure 4.6c) separates contact resistance and in-plane resistivity by analyzing total resistance as it varies with the distance between current-collecting electrodes. A linear fit of resistance versus spacing (L) allows one to extract both the contact resistance (from the y-intercept) and the resistance (from the slope). However, the transfer length method is highly sensitive to the exact placement and alignment of the electrodes. Any displacement or inconsistency can severely affect measurement accuracy. Additionally, the method relies on reproducibility in electrode fabrication and mechanical positioning.[228] Moreover, another point often neglected by the presented methods is the accurate determination of the thickness distribution, suggesting a uniform layer, which describes the ideal not the real case. However, a heterogeneous thickness distribution would lead to an over- or underestimation of in-plane electrical resistivity.[†]

EIS characterizes the frequency-dependent response of an electrochemical system by applying a small-amplitude sinusoidal voltage or current over a wide range of angular frequencies $\omega = 2\pi f$. The resulting response allows for the calculation of the system's complex impedance $Z(\omega)$, which reflects the interplay of resistive, capacitive, and diffusive elements within the cell. A common way to interpret EIS data is through equivalent circuit models, with the Randles circuit serving as a fundamental example or more advanced models such as the transmission line model.[229] The Randles circuit consists of a resistance (R_{HFR})in series with a parallel combination of a double-layer capacitance (C_{dl}) and a charge transfer resistance (R_{ct}).[229] The high-frequency intercept of the Nyquist plot corresponds to R_{HFR}, representing ohmic losses from the membrane, electrolyte, and electronic conductivity. At lower frequencies, the capacitive branch is no longer shorted, and the impedance reflects the combined contribution of both R_{HFR} and R_{ct}. In total this gives the low frequency resistance (R_{LFR}). The charge transfer resistance R_{ct} provides direct insight into the kinetics of interfacial electrochemical reactions. Each element in the circuit has a characteristic frequency (f_0), at which its contribution to the impedance is most pronounced. In the Randles circuit, this corresponds to the frequency at which the capacitive C_{dl} and resistive effects of the parallel branch are balanced. By analyzing the shape and features of the EIS spectrum presented as Nyquist (Figure 4.6d) or Bode plots distinct physical processes such as ionic conduction, interfacial charge transfer, and mass transport can be deconvoluted and quantified.[229] Nevertheless, certain challenges are inherent to the application of EIS. For example, the physical models required to fit the data can be difficult to apply to complex structures with irregular domains. These models often must be tailored to specific applications, which limits their general applicability. Additionally, EIS measurements can be time-consuming and sensitive to noise.

5 Research Questions and Approach

This chapter presents the key research questions that drive the exploration of CL characterization. These questions are based on existing knowledge gaps and challenges identified in the literature regarding the structure and electrical properties of CL. Microscopy is often used to characterize the structure of a CL, but it lacks quantitative capabilities and therefore limits the ability to compare results across studies and the potential for comprehensive structural assessment. Methods to describe the in-plane electrical resistivity suffer from limited spatial resolution and assumptions that may not hold in heterogeneous or layered materials. Overall, limited characterization of the CL hampers its iterative optimization and effective implementation within technical PEMWE systems. However, significant advancements are required to meet future technological demands.
The primary goal of this research is to establish a methodology to connect the production with the resulting structure and its physical properties of CLs, with a particular focus on surface texture and in-plane electrical conductivity. Therefore, the key research question addressed in this study is:

How can production parameters be systematically correlated to the morphology, electrical properties and electrochemical performance of CLs, and what interactions influence surface texture and in-plane electrical conductivity?

This thesis aims to bridge the gap between production processes and the electrochemical performance of CLs by exploring the interplay between morphological characteristics and their physical properties. The following sub-questions are formulated, each targeting specific aspects of the CL's characterization. A key area of focus is the utilization of image-extracted texture descriptors for the characterization of CLs.

-Q1- What are the key morphological features of CLs and how do these features affect the electrochemical performance of PEMWE?
-Q2- How can advanced microscopy techniques, such as SEM or CLSM, be integrated with computational tools to provide a more objective and quantitative description of CL morphology?
-Q3- How does the surface texture correlate with the manufacturing process and the electrochemical performance of the CL in PEMWE?

One sub-question is directed towards determining the extent to which statistical image features can be relied upon to accurately capture and represent the texture of the CL, given the inherent uncertainty associated with their precision. Another sub-question addresses the characterization of texture across different length scales. This investigation aims to understand how surface texture affects the functionality of the CL. Additionally, the study explores the influence of production processes, catalyst loading, and ionomer content to better understand the relationship between CL texture and electrochemical performance.

-Q4- How strong is the correlation between physical texture descriptors of the CL and statistical features extracted from images?
-Q5- In what ways does the CL's surface texture, including its scale-dependent variations, impact electrochemical performance, and how are these effects influenced by production methods, catalyst loading, and ionomer content?

In addition to describing the CL structure through image processing, understanding the in-plane electrical conductivity and resistance as a function of catalyst loading is essential. Emerging questions include:

-Q6- How can the in-plane electrical conductivity of CLs be reliably determined?
-Q7- What is the relationship between the in-plane electrical conductivity of the CL and the catalyst loading?

Finally, this thesis investigates how surface texture parameters and electrical conductivity measurements can be linked to enhance the understanding of structure-property relationships in CLs. Based on these questions, the following hypotheses are proposed:

-H1- Optimization of production parameters will result in a CL with improved homogeneity, leading to reduced errors measured by texture parameters and electrochemical testing.

-H2- Advanced computational image analysis techniques can provide more accurate, quantitative and objective characterization of CL morphology and surface texture compared to traditional microscopy.

-H3- There is a correlation between CL surface texture and the measured electrochemical performance of the CL.

-H4- Determining the in-plane electrical conductivity with an appropriate method provides reliable and reproducible data for CL optimization.

These hypotheses will be tested using a combination of microscopy, computational imaging, electrical conductivity measurements, and statistical analysis. The study aims to deepen the understanding of structure-property relationships in CLs and contribute to the development of optimized materials for PEMWE.

In **Chapter 6**, the methodological framework is outlined, detailing the data acquisition process and the techniques used to explore the relationship between production parameters, structure, and performance. The production requirements for homogeneous CLs are discussed, along with an overview of the techniques employed to characterize the texture, thickness, and material distribution of the CLs. Additionally, the evaluation of electrochemical properties through single-cell testing, sheet resistance measurements, and in-plane electrical conductivity is explained. The chapter also presents the correlation study that links production parameters with structural and performance data, providing insight into how these interactions affect the CLs properties. **Chapter 7** examines how production variables influence the microstructure, material distribution, and performance of the CLs. It explores the impact of factors such as iridium loading and Nafion content on CL properties, while also addressing the challenges of imaging these structures. This chapter further outlines the steps taken to correlate production variables with the structural properties of the CLs. In **Chapter 8**, the focus shifts to linking electrode structure to performance, starting with the characterization of benchmark electrodes, particularly those with low iridium loading. The effects of cell assembly on the microstructure are analyzed, and the impact of CL thickness on resistivity is explored. Finally, **Chapter 9** revisits the research questions introduced earlier and analyzes them in the context of the data collected and discussed in the previous chapters. **Chapter 10**, finally provides an outlook on future directions and potential applications of the findings.

6 Methodology

This thesis focuses on establishing a connection between the catalyst layer (CL) production process, its structural characteristics, and the resulting properties. Correlating the CLs structure with its properties requires ensuring the production method yields a uniform, reproducible CL structure. Once the production process is well understood, one can examine the correlation between the macroscale, mesoscale, and microscale features of the CL systematically to assess the influence of the production process on the final structure. The generated datasets enable the correlation of meaningful physical [surface texture parameters (STPs)] and statistical descriptors [image features (IFs)], revealing consistent conclusions from both perspectives. The identified descriptors can be used to monitor structural evolution across scales and establish correlations between structure and performance. Therefore, the developed methodological workflow for establishing this comprehensive connection is visualized in Figure 6.1 and comprises four main stages. These are briefly summarized in the following and more extensively discussed in the next sections.

The first stage, **Data Acquisition**, involves using an ultrasonic spray-coater and a confocal laser scanning microscope (CLSM). A total of 89 CLs were fabricated using the spray-coater and were then systematically grouped into six different datasets based on the defined parameter study. Layer digitization was carried out by measuring the optical density of the entire CL to evaluate the uniformity of the loading distribution, highlighting the effects of various production parameters on CL homogeneity. Next, the samples were analyzed using a CLSM, which produces intensity-based microscopy images and height maps. From the latter, 19 STPs were extracted to quantitatively describe the microstructure of the produced CL. All relevant devices, materials, further components and production processes are specified in Chapter 6.1. In the second stage of the workflow, the **Correlation Study**, two main phases were carried out: Data Processing and Parameter Space Reduction. In the first phase, the STPs from the CLSM are transferred into an appropriate data structure, and the intensity images are processed with the *PyRadiomics* library to extract the IFs. Pearson correlation analysis was then applied to detect linear relationships between the extracted STPs. This analysis identified

three representative STPs that effectively characterized the entire parameter set. Additionally, 87 IFs were extracted using the open-source platform PyRadiomics.[175] In the second phase, the selected STPs were correlated with the extracted IFs by calculating the Pearson correlation coefficient (PCC) for each parameter combination. To reduce the parameter space, a combination of strategies was employed to prioritize and eliminate redundant IF. This two-step process established a link between the physical STPs and the statistical IFs.

The third stage involved a detailed analysis of the **Production-Structure Relationship** for CLs, considering optical density measurements, STPs, and IFs. This framework was used to evaluate the feasibility of using IFs for CL texture quantification. To validate the viability of this method, production variables must lead to consistent and measurable structural trends in the CL, as determined by both STPs and IFs analyses. Based on insights from this stage, five benchmark electrodes with distinct loading distributions were designed. The first benchmark electrode was used to study how Nafion content, heat treatment, and iridium loading affect the structure of the CL. This study aimed to improve understanding of how IFs describe CL texture. Additionally the description of the CL was extended by using image processing to extract the thickness distribution of the CL. The CL structure was characterized across the entire magnification scale accessible through the SEM, which primarily covers the mesoscale and microscale. At each magnification level, IFs were calculated to describe the structure at those scales.

This scale-dependent analysis marked the transition from the third to the fourth stage. For simplicity and clearer visualization of the workflow, this analysis is shown in Figure 6.1 as part of the fourth stage, which focuses on the **Structure–Property Relationship**. The final stage investigated how structural features influence the electrochemical and electrical performance of CL. Single-cell testing of five benchmark electrodes included performance and durability evaluations to study the effects of non-uniform iridium loading on degradation behavior. Before and after testing, samples were imaged using SEM. IFs were extracted from images taken at various magnifications, which enabled tracking of structural changes at specific length scales. Electrochemical data were then analyzed to extract key performance indicators, which were correlated with the previously calculated IFs. This correlation provided insight into the structure-property relationship by linking CLs texture, as described by IFs, to electrochemical behavior.

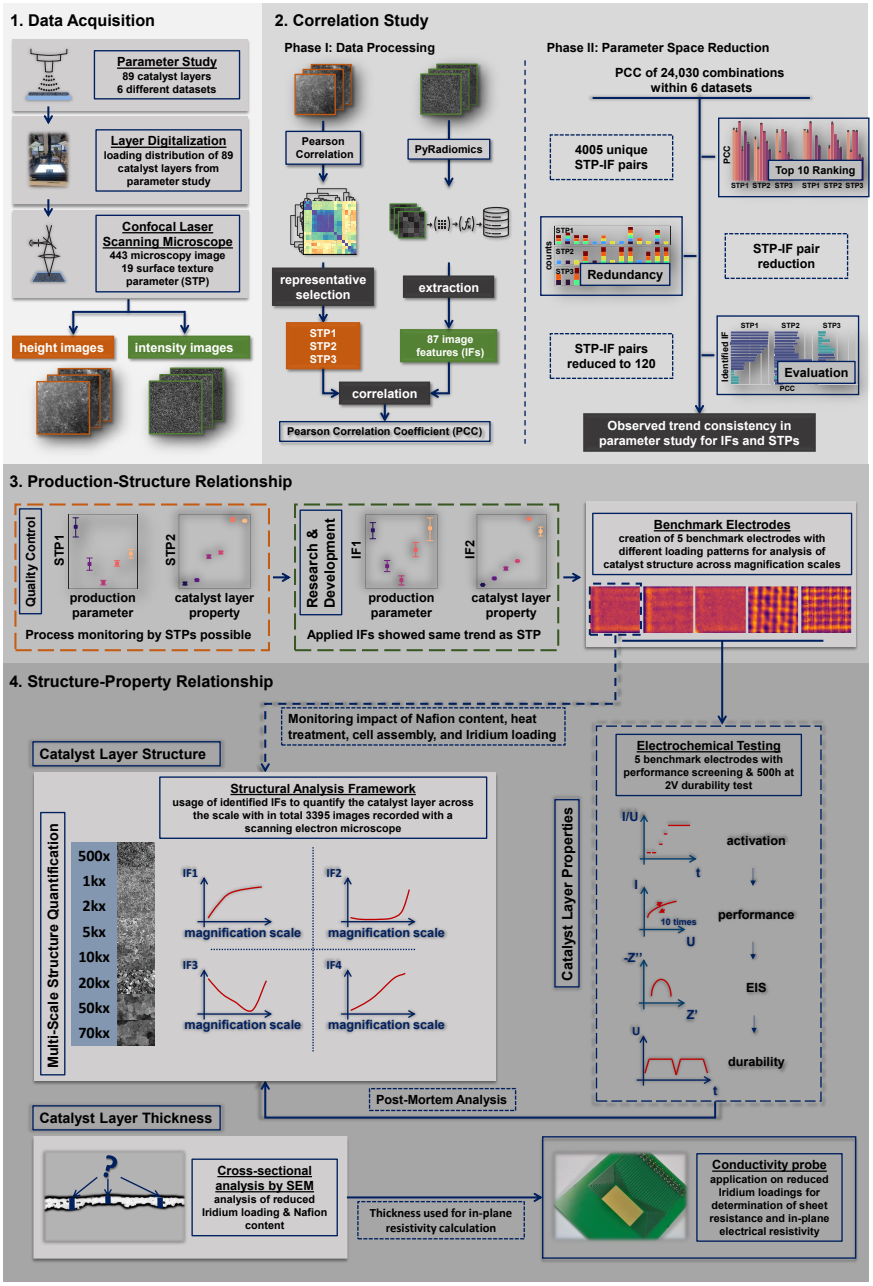

Figure 6.1. Workflow of the developed methodology for correlating statistical image features with physical surface texture parameters across multiple stages, from data acquisition to structure-property analysis.

In order to access the electrical properties of catalyst loadings, this work presents a four-line probe with ten different spatial resolutions ranging from 250 µm to 2500 µm, pressure control, and the possibility of monitoring the local electrical resistances multiple times within a total area of 11 mm x 20 mm. Initially, the concept was validated by using a commercially-available reference specimen with defined sheet resistivity, whereas the probe was factory-made. This work demonstrates its applicability by determining the in-plane electrical resistivity for a titanium-PTL, GDL, and CL. For enhanced accuracy regarding the CL in-plane electrical resistivity, open-source image-processing techniques are used to obtain the thickness distribution from CLs coated onto a membrane.[†]

6.1 Data Acquisition

This section details the materials, manufacturing processes, and analytical capabilities used to develop the characterization methods, along with their theoretical and technical background.

6.1.1 Production - Requirements for Homogeneous Catalyst Layers

Catalyst Layer Production. Initially, the dispersion production started with adding the iridium oxide catalyst (Premion, Alfa Aesar) into a 100 mL laboratory bottle. Deionized water (Milli-Q, Merck Millipore) was added, followed by n-propanol (Merck). The catalyst concentration was 3.3 $\mathrm{mg\,mL^{-1}}$ for all datasets. The dispersion was ice-cooled for 5 min prior to the addition of the water-based Nafion dispersion (D1021, Ion Power) and subsequently treated with an ultrasonic horn while maintained in the ice bath. The CLs were produced using an ultrasonic spray-coating system (ExactaCoat, Sono-Tek) with an integrated AccuMist nozzle operating at 48 kHz. The dispersion was injected by syringes (25 mL, Hamilton) and a syringe pump (Sono-Tek), which was operated with the ExactaCoat software. The temperature of the heated vacuum plate was 90°C. The loading of the CLs was controlled by spraying on a 6 mm thick borosilicate glass (60 mm x 60 mm) and weighing with a balance (AG204, Mettler Toledo). The CLs were sprayed directly onto an N117 membrane (Chemours).[†]

The cathodic catalyst layer (CCL) dispersion was made similarly. The dispersion consisted of a mixture with a catalyst concentration of 2.4 $\mathrm{mg\,mL^{-1}}$, 33 wt.% n-propanol (Merck), 67wt.% deionized water (Milli-Q, Merck Millipore), while for the CCL used an isopropanol-based Nafion dispersion (LQ-1115, Ion Power) was used. The loading was $0.087 \pm 0.018\,\mathrm{mg_{Pt}\,cm^{-2}}$ using 20 wt.% platinum on carbon (HISPEC3000, Johnson Matthey). Since the CCL was not the

main subject of this work, the machine parameters were left at default. Thus, the flow rate was set to $0.3\,\mathrm{mL\,min^{-1}}$, the gas pressure was $7\,\mathrm{kPa}$, and the nozzle distance was $50\,\mathrm{mm}$. The heated vacuum plate was set to 80°C.

Parameter Study. The standard production variables are found in Table 6.1, while the blue boxes show the production variables that were varied in the respective dataset. The presented parameter study consisted of four datasets focusing on the production variables and two which focused on the CL property. To investigate the impact of different production variables, one

Table 6.1. Overview of the main production variables chosen per dataset.

	variables	pressure	nozzle height	flow rate	alcohol content	Nafion content	loading
		Pa	mm	mL min^{-1}	wt. %	wt.%	mg_{Ir} cm^{-2}
datasets	pressure	1034-55160	40	0.2	67	11	0.2
	nozzle height	10342	10-60	0.2	67	11	0.2
	flow rate	10342	40	0.1 - 0.8	67	11	0.2
	alcohol content	10342	40	0.2	33-91	11	0.2
	Nafion content	10342	40	0.2	67	5-30	0.2
	loading	10342	40	0.2	67	11	0.05 - 1.00

dataset focuses on the alcohol content of the dispersion. The other datasets focused on spray parameters, such as the gas pressure adjusted by the nitrogen gas supply or the nozzle height, which measures the distance of the nozzle tip to the vacuum plate. The nitrogen gas supply serves as both the carrier gas and the shaping gas. The flow rate is a key process variable because it determines the amount of material delivered over time. This affects both the coating thickness and the total production time. The presented datasets refer to typical input variables of a CL fabrication process. The dispersion ("alcohol content") is processed by adjusting machine parameters ("gas pressure", "nozzle height", "flow rate"), interacting with each other and consequently affect the resulting CL properties. Some CL properties ("Nafion content", "iridium loading") are output variables, which are conceptualized at the beginning of production. On the other hand, the Nafion content and the catalyst could be accounted

to the input variables because they both relate to dispersion. Both influence the dispersion stability and interact with the solvent ratio and each other. This work focuses on the CL texture. Therefore, the Nafion content and iridium loading are considered output variables and CL properties. Further CL properties emerge from the entanglements between input and output variables.

6.1.2 Visualization of the Catalyst Loading Distribution

Reducing the iridium loading below $0.3\,\mathrm{mg_{Ir}\,cm^{-2}}$ while using an unsupported catalyst makes the CL transparent. This was used to analyze the catalyst loading distribution in relation to different production variables. The CL were applied to an N117 membrane as described in Section 6.1.1. The CL was then fixed in a metal frame and placed on a table with a light source underneath, (Figure 6.2). A camera (D3100, Nikon) was used to take photographs of the CL. Images were acquired at resolutions ranging from 2585 × 2657 px to 2832 × 2695 px (6.87–7.63 MP), with aspect ratios between 0.97 and 1.05, indicating a near-square format. Image processing was performed on the captured image.

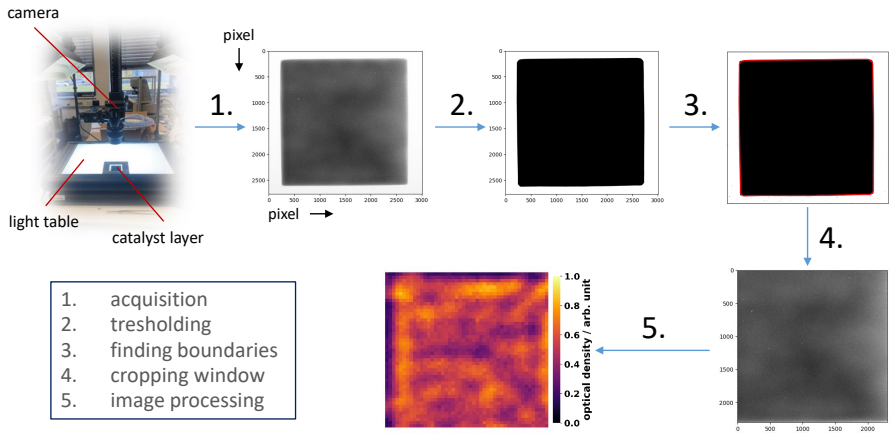

Figure 6.2. A camera-based optical imaging method was used to measure optical density and visualize the loading distribution of a CL with $0.2\,\mathrm{mg_{Ir}\,cm^{-2}}$ fabricated using the default process parameters employed prior to this thesis.

Thresholding is an image processing technique that converts grayscale images into binary images by applying an intensity threshold that segments pixels into foreground and background.

This method was used to define the boundaries of the CL, followed by its crop-out from the image for further analysis. A simple linear iterative clustering (SLIC) algorithm was then used to create a color map and reduce noise within the image. The SLIC algorithm was applied to segment the image into superpixels to enhance image clarity and reduce noise. This grouping process identified pixels similar in color and spatial proximity, generating a color map.[230–232] Bright areas of the resulting image correspond to areas of lower loading, while dark areas correspond to higher material concentration. This was then evaluated to describe the effect of production variables on the load distribution.

6.1.3 Characterization by Confocal Laser Scanning Microscopy

The characterization was carried out with a confocal laser scanning microscope (LEXT OLS4000, Olympus) possessing a height resolution of 10 nm and an x-y resolution of 120 nm. The utilized objective lens was the MPLAPON100XLEXT with (129x129) $\mu\mathrm{m}$ field of view at a working distance of 0.35 mm. Each CL was fixed onto a disassembled hard disk drive that had a uniform surface and thickness (25 mm). For fixation a 190 $\mu\mathrm{m}$ thick double-sided adhesive tape (VHB™GPT-020F50, 3M™) was used. Every sample was measured at five different locations. An exemplary schematic of the probing locations on the CLs is presented in Figure AF.1. The arrangement consisted of three equidistant point on a diagonal, with one location placed in the middle of the sample. The other two measurements were taken perpendicular to the initial three measurements, with one placed at the outer corner and the other positioned between that corner and the remaining three measurements. It was assumed that the symmetry of the square CL would not require additional measurements.
Based on this probing, it is defined that inhomogeneous CLs have higher deviations of a certain surface texture parameter (STP) than homogeneous CLs. However, the target range for the presented surface texture parameter has not been defined.

The CLSM operates by focusing a 405 nm laser beam onto a point on the surface of a specimen. The reflected or emitted light is then collected through a spatial pinhole, which is optically aligned with the focal point. This configuration eliminates out-of-focus light, producing high-resolution optical sections. This configuration minimizes the amount of out-of-focus light and therefore reduces the impact of noise. The system constructs a three-dimensional dataset by scanning the laser laterally across the sample and incrementally moving the focus in the vertical (z) direction.[233,234]
Intensity and height images are typically generated during the measurement process. Inten-

sity images record the amount of light reflected or emitted from each point on the sample's surface. They provide contrast based on the specimen's reflectivity. These images reveal surface features with varying optical properties and are useful for distinguishing different material phases or structures.[233, 235]
A height image is derived from the z-position at which the maximum intensity is detected for each lateral point. It provides precise measurements of the sample surface topography. Together, these two types of images offer complementary information. The intensity image reveals material or structural contrasts, while the height image maps the actual three-dimensional surface morphology. Both are essential for comprehensive surface analysis.[234–236]

For all measurements, the brightness was kept constant for all CL samples, while the number of z-stack steps (focal planes) and the step width (vertical distance between planes) were adjusted according to the specimen studied. The 2D laser intensity image was exported as a tagged image file (tif) in a square format of 1024x1024 pixels and as a 24-bit grayscale image. The LEXT software was used to adjust the measurement, requiring a cut-off value to be set prior to applying Gaussian filtering, which was used to reduce noise. Preliminary experiments indicated that after adjusting the surface level, a cut-off value of $25\,\mu\mathrm{m}$ provided the best results for the Gaussian filter, which was then applied to all specimen.

6.2 Correlation Study

This chapter outlines the statistical and computational framework used during the second stage (Figure 6.1) to explore potential relationships between image-derived features (IFs) and physical surface texture parameters (STPs). The goal is to identify and quantify linear associations that reveal how production variables influence the morphology of the CL, as captured through imaging and surface metrology. The Pearson correlation coefficient (PCC) is the primary metric because it is simple, interpretable, and effective at measuring the strength and direction of linear relationships between continuous variables. The chapter is divided into two main phases: data processing and parameter space reduction. In Phase I, standardized procedures are applied to extract relevant features and compute the full set of correlations. Phase II involves implementing dimensionality reduction strategies to extract the most meaningful combinations of variables, improve computational efficiency, and facilitate clearer interpretation. These steps together form the basis for connecting statistical image features with physically relevant surface characteristics, thereby informing quality control and research in CL manufacturing.

6.2.1 Phase I: Data Processing

In conjunction with the computed height image, the LEXT software calculated 19 STPs. The definition and classification of the obtained parameters are listed in Table AT.2. All further data processing utilized parts of the open-source Python libraries pandas[237,238], matplotlib[239], scipy[240], and seaborn[241].

Table AT.2 contains several commonly used surface textures according to ISO 25178. The data sets were merged to avoid the redundant use of STPs. The PCC was calculated for all possible combinations of STPs. A cluster map was used to visualize the dependency patterns among feature groups and three selected STPs, which were chosen to broadly represent different categories of surface characteristics. The 95% confidence interval of the calculated PCC was computed by applying the Fisher transformation.[242]

From the 2D light intensity images, 87 IFs were extracted from each image using the open-source platform *PyRadiomics*.[175] The calculated image features were derived from different matrices. In particular, 23 parameters were derived from the GLCM, 15 from the GLRLM, 15 from the GLSZM, 13 from the GLDM, four from the NGTDM, and 17 FO texture parameters.[‡]

6.2.2 Phase II: Parameter Space Reduction

Interpreting the combination of 87 IFs with 3 STPs required a smaller parameter space. To illustrate the scale of reduction, the number of unique pairwise correlations (C) among a set of n variables can be calculated as:

$$C = \binom{n}{2} = \frac{n(n-1)}{2} \tag{6.1}$$

This formula allows for estimating the correlation space depending on how many variables are included in the analysis. Using more variables significantly increases the number of pairwise combinations, highlighting the importance of reducing the parameter space. The total number of unique pairwise correlations among a set of n variables can be calculated using Equation (6.1). In this work, the reduced variable set included 87 IFs and 3 selected STPs, resulting in $n = 90$ variables. Applying the equation yields 4,005 correlations per dataset, or 24,030 total correlations across all six datasets.
If all 19 available STPs had been used instead, the number of variables would increase to $n = 106$, resulting in 5,565 correlations per dataset, and 33,390 across all datasets. This comparison illustrates the substantial increase in computational and analytical complexity that

would result from using the full set of parameters.

As part of this work, a multi-stage reduction strategy was developed to ensure a traceable and systematic selection process. First, the absolute value of the PCC was used to identify the ten strongest correlations per dataset and per STP, yielding 180 IF-STP pairs across all six datasets and three selected STPs. This initial filtering prioritized the most relevant relationships while significantly reducing the computational load and processing time.

Next, the redundancy of the selected image features was examined. Only features that appeared among the top correlations in more than one dataset were retained. This consistency-based filtering excluded features with isolated or dataset-specific importance, highlighting those with stable, cross-dataset relevance.

This refined subset of correlations, now reduced to a manageable number (120), enabled a more targeted evaluation. From this pool, it was possible to manually review and select the ten most promising IFs. These IFs were then used to determine, if similar conclusions could be drawn by substituting them for the original STP. This step provided insight into the practical potential of using statistical IFs as alternative to physical STPs. This was carried out mainly in the next stage (Figure 6.1) related to the production-structure relationship.

Key Aspects of the Correlation Study Methodology:

- → In Phase I, 19 STPs were calculated using LEXT software, and their correlations were assessed through the PCC, with a 95% confidence interval calculated using the Fisher transformation.
- → 87 IFs were extracted from intensity images recorded with the CLSM using PyRadiomics and different matrices, including GLCM, GLRLM, GLSZM, GLDM, NGTDM, and FO.
- → In Phase II, the strongest correlations between STPs and IFs were identified by analyzing the absolute PCC, reducing the number of pairs from 24,030 to 120.
- → The correlation analysis helps to examine how the IFs and STPs relate to the structural characteristics and electrochemical properties of electrode materials.

6.3 Production-Structure Relationship

The IFs will contribute only to the progress of electrode development, if they can show similar trends regarding structural characteristics as the STPs. Therefore, the datasets were evaluated, interpreted and discussed with both textural features classes during the third stage (Figure 6.1).[‡] First, the impact of the machine parameters was evaluated using the STPs and IFs. A consistent standard electrode design was used in these experiments to investigate the fundamental behavior of the IFs at scale. This also helped to minimize structural variations arising from the manufacturing process, which could otherwise obscure a clear evaluation. Subsequently, a discussion is presented on the impact of the alcohol content in the dispersion, the Nafion content within the CL, the effect of a typical heat treatment of the CL at 150°C and the effect of iridium loading on the surface characteristics. Based on this knowledge, five benchmark electrodes with distinct loading distributions were created to study the impact of CL inhomogeneity on degradation behavior for low iridium loadings, presented in the chapter related to the structure-property relationship. To enable multiscale monitoring of the CL structure, the most promising IFs were computed from SEM images acquired at varying magnifications. This approach allowed for high-resolution analysis that was not feasible to the same degree with CLSM. This was carried out for the datasets of the alcohol content, Nafion content and Iridium loading. The developed structural analysis framework was first tested during this stage and later used in the final phase to study the structure-property relationship.

6.3.1 Production of Benchmark Electrodes

The results of the parameter study were used to create a set of five benchmark electrodes. MP1 is the standard electrode design for all further experiments. MP1 was produced using machine parameters selected to achieve the most uniform loading distribution and smoothest surface. This should later be monitored and validated by STP. The primary objective of MP1 was to ensure a consistent microstructure across the entire electrode to enable the investigation of specific factors, such as cell assembly and electrochemical performance, under repeatable and controlled CL surface conditions.

In contrast, the CLs from MP2 to MP5 were designed to study variations in CL loading distribution. MP2 and MP3 were intended to yield uniform loading distributions with deliberately altered surface roughness compared to MP1, differences that should be detected through STP. MP4 and MP5, on the other hand, were designed to highlight the effects of non-uniform loading distributions. Non-uniformity can contribute to increased degradation and greater variability in

analysis because the microstructure is likely not homogeneously distributed across the CL. This structural heterogeneity may result in higher errors in interpreting IFs and reduce the reliability of the structural analysis. The applied machine parameters are listed in Table 6.2, while the dispersion processing was already explained in Section 6.1.1. When using different flow rates the loading was controlled by the number of cycles. The CL loading was controlled by spraying onto a 6 mm thick borosilicate glass substrate (60 mm × 60 mm) and measuring the mass using an analytical balance (AG204, Mettler Toledo). Each set of machine parameters was tested in five repetitions to estimate the average loading and corresponding standard deviation, as listed in the Table 6.2. After determining the exact loading, the machine parameters were used to spray the CL directly onto the N117 membrane.

Table 6.2. Machine parameter used to obtain five benchmark electrodes. MP1 continues to be used as the standard electrode for all other experiments requiring uniform loading distribution.

	variables	pressure	nozzle height	flow rate	cycles	Nafion content	loading
		kPa	mm	mL min^{-1}	-	wt.%	mg_{Ir} cm^{-2}
benchmark electrodes	MP1	10	40	0.2	17	11	0.19 ± 0.02
	MP2	1	40	0.2	17	11	0.20 ± 0.01
	MP3	10	40	0.8	4	11	0.20 ± 0.03
	MP4	10	10	0.2	17	11	0.19 ± 0.02
	MP5	10	10	0.4	8	11	0.22 ± 0.01

Summary of production-relevant aspects:

→ Key production variables, including alcohol content in the dispersion and spray parameters were systematically varied to investigate their impact on the CL texture.

→ Insights from the parameter study were used to develop five benchmark electrodes. The benchmark electrode (MP1) was set as a standard, while MP2 to MP5 were produced with controlled variations in catalyst loading to analyze the effects of these changes on layer properties.

6.3.2 Analyzing the Structure Across Scales by SEM

The CL structure was analyzed by SEM (Zeiss Gemini Ultra Plus) across the magnification scale. For each analysis, three samples were examined at five different locations along the magnification scale (500x; 1,000x; 2,000x; 5,000x; 10,000x; 20,000x; 50,000x; 70,000x). In the SEM, secondary electrons emitted from the specimen are detected, resulting in topographic contrast with excellent depth of focus. Alternatively, backscattered electrons that have undergone elastic interactions near atomic nuclei in the sample are used to generate material-dependent contrast. The in-lens or through-the-lens detector collects the secondary electrons and is surface sensitive, allowing low voltage ($500\,\mathrm{V}$ to $5\,\mathrm{kV}$) imaging for samples with a surface that degrades upon energy entry, such as Nafion ionomers. The high energy of backscattered electrons allows selective detection by the Everhart–Thornley detector, which effectively rejects low-energy secondary electrons. In the following, inlens images refer to the images taken with the secondary electrons, while angle-selective backscattered electron (AsB) refers to the images taken with the backscattered electrons.[243]

The approach proposed in this study utilizes the intensity information contained in the acquired images. Each pixel in an image reflects the intensity of the mapped area and was captured by a grayscale image with 8 bits per pixel (256 gray levels). In image analysis, particularly when examining complex materials under a microscope, a pixel may not correspond exactly to a single structure (e.g., a fiber, pore, or cell). Instead, it may partially overlap multiple structures. The fractional contribution refers to the percentage of a pixel's intensity or area that belongs to a specific structure.[138] Figure 6.3 shows how this fraction varies along the magnification scale for microparticles of different sizes. The exponential decrease of this fraction from lower to higher magnification is visible and has been constructed from the data obtained with the specified SEM above. The pixel size was determined in micrometers for each magnification. Then, it was used to estimate the fractional contribution of a single pixel relative to a specified particle diameter. The study by Pyrz et al.[138] demonstrated this behavior for TEM microscopy. The effect of pixel coarseness, or image quality in general, must always be considered. This is particularly important for very small structures ($< 0.75\,\mu\mathrm{m}$), where low magnification can cause a single pixel to cover over 80% of the structure's area. Consequently, the pixel cannot accurately represent the structure, which increases the likelihood of errors in measurement or classification. Therefore, appropriate magnification and image resolution are critical for reliable analysis.[138] This dependency should be taken into account when following the approach presented in the following pages. The data shown in the Figure 6.3 assumes highly dispersed particles without contact to each other. However, for CLs, these particles are embedded in

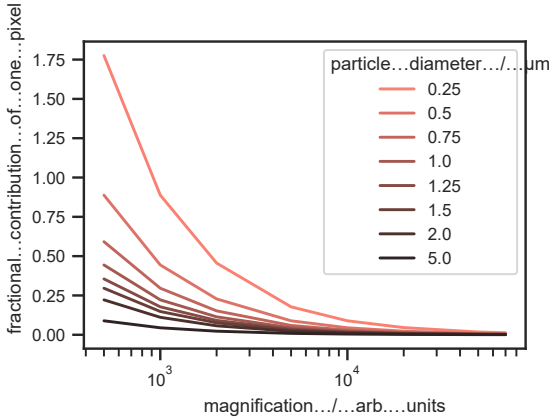

Figure 6.3. In a 1024 × 768 SEM image, the fraction of a microparticle diameter that a single pixel represents depends on the nominal magnification and varies for different particle sizes. The graph was customized for the SEM used in this thesis. Adapted from [138].

the Nafion ionomer matrix. This means that they are in close, overlapping proximity to each other. In particular, production variability, particle in-homogeneity, composition of the CL, and more make such an analysis challenging for CLs. To iteratively optimize the CL structure and enable further technological advancement, it is essential to first understand the relationship between structure and performance. As described in Chapter 3.2 and illustrated in Figure 3.3, the CL structure interacts with a variety of processes across different length scales. Therefore, descriptors are needed that can capture structural characteristics at different magnifications and that are suitable for complex mixtures, in which clear distinctions between components, such as particles, ionomer, and pores, are difficult to observe. To address this challenge, this thesis employs image features (IFs) as introduced in Chapter 4.2. Using the *PyRadiomics* platform[175], matrices describing neighborhood dependencies of pixel intensities were extracted from SEM images at different magnifications. The most promising IFs were used for further analysis. These features are classified into global and local aspects of the CL structure, with potential sublocal features corresponding to particle or agglomerate sizes and shapes. As the CL represents a stochastic texture, it is accessible only through empirical methods such as the presented approach. However, this approach focuses on data mining or identifying a descriptor for the underlying CL structure. This would make the CL structure accessible to tools such as machine learning, neural networks, or artificial intelligence. All of these tools require that the CL structure can be quantified and expressed as a numerical value. This work is a first step in this direction and is transferable to other fields involving porous electrode engineering.

6.3.3 Thickness Determination from Cross-Sections

The proposed method is similar to commonly applied approaches for obtaining the particle size distribution from microscopy images, but instead it determines the CL thickness.[244–247] The principle utilized to determine the thickness distribution from the cross-sectional AsB images is schematically shown in Figure 6.4. This study employed scikit-image, an open source image processing library available for the Python environment.[248] Analyzing cross-sectional AsB images to obtain the thickness distribution of CLs requires the conversion of pixels into a length unit (e.g. nm). Thus, the pixels of the scale were counted to obtain their lengths-per-pixel value. This value was then used to determine the thickness of the respective CL. The cross-sectional AsB images require binarization prior to evaluation. Several methods are proposed to set the threshold value, commonly to distinguish between the image background and foreground. In the case of the cross-sectional analysis, this value must differentiate between the CL and membrane. AsB images have the advantage that their contrast depends on the difference in the atomic number of the materials depicted. Thus, the anodic CL made out of iridium oxide can be easily differentiated from the Nafion membrane using the Otsu algorithm to transform the image into a binary image.[247] In this binary image, only the CL possessed a

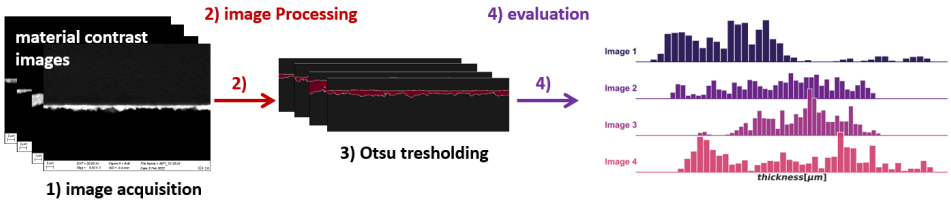

Figure 6.4. Determination of the CL thickness from cross-sections. The used material contrast images are processed by python based open-source tools.

pixel value of one. However, a CL made of 80 wt.% carbon and 20 wt.% platinum was more difficult to distinguish from the Nafion membrane due to the high carbon content in both the membrane and CLs. In this case, a multi-Otsu algorithm was used,[249] specifying several thresholds and choosing the best one by comparing different thresholds and their impact on the thickness determination. The average thickness for the presented CLs was determined using ten different images at a magnification of 10 kx. The x-direction of the image possesses a width of 1024 pixels. The accuracy of the obtained thickness distribution depends on the

number of thickness determinations per image. The thickness was determined at each of the 1024 pixels in the x-direction by summing the pixels in the y-direction. These values were then converted into the thickness by the length-per-pixel value.[†] The resulting thickness distribution can be used to derive statistical measures that characterize the CL in terms of its heterogeneity and other relevant structural features, such as average thickness, skewness, and variation.

Summary of the developed methods to characterize the CL structure:

- → Iridium loadings below $0.3\,\mathrm{mg_{Ir}\,cm^{-2}}$ makes the CL transparent, allowing analysis of loading distribution using light and image processing with algorithms like SLIC. Bright areas represent lower loading, and dark areas indicate higher material concentration.
- → CLs were characterized using a confocal laser scanning microscope (CLSM) to measure surface texture at various locations.
- → The CL structure was analyzed using SEM at various magnifications. The SEM images provides insights into the morphology of the CLs. Statistical features, including those derived from texture matrices were used to quantify both global and local texture characteristics of the CLs.
- → The thickness distribution of CLs was determined from cross-sectional SEM images using image processing techniques.

6.4 Structure-Properties Relationship

The identified IFs were further used to describe changes in the CL properties following durability testing. Prior to that, the five pristine benchmark electrodes were compared by analyzing the IFs across different magnification scales. The effect of cell assembly, including exposure to water and heat at a flow rate of $25\,\mathrm{mL\,min^{-1}}$ and a temperature of 80 °C was analyzed specifically for MP1. Then, the IFs were correlated with the extracted electrochemical performance parameters. Finally, sheet resistance and in-plane electrical resistivity were discussed as key electrical properties in the context of reduced iridium loadings using the MP1 benchmark electrode.

6.4.1 Single-Cell Testing

Single-cell testing is (often) used to test components under realistic conditions. Here, the procedure (Figure 6.5) began with an **activation process** to minimize measurement variations caused by test station conditions, initial temperature fluctuations, or material-related effects.[131] During the first two hours of this activation process, the cells were run at open circuit voltage (OCV) and the operating point of 80°C with a flow rate of $25\,\mathrm{mL\,min^{-1}}$. Subsequently, the current density was set to $0.2\,\mathrm{A\,cm^{-2}}$, followed by $1.0\,\mathrm{A\,cm^{-2}}$, each applied for $30\,\mathrm{min}$, followed by a potentiostatic operation at $1.7\,\mathrm{V}$ for eight hours. The **performance**

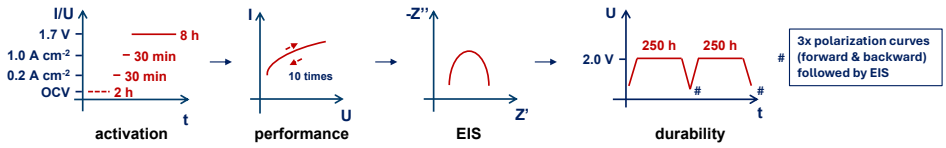

Figure 6.5. Workflow of the single-cell testing protocol applied within this work.

was evaluated by polarization curves with 5 min hold time per point, starting at $1.45\,\mathrm{V}$. From $1.45\,\mathrm{V}$ to $1.55\,\mathrm{V}$ the potential step was $0.01\,\mathrm{V}$ and then increased to $0.05\,\mathrm{V}$ for potentials $> 1.55\,\mathrm{V}$. The forward scan was terminated at a potential of $2.00\,\mathrm{V}$, followed by the reversed procedure, the backward scan. This was repeated ten times.

Electrochemical impedance spectroscopy (EIS) was carried out for each potential of the polarization curve. The frequency range was set from $100\,\mathrm{mHz}$ to $10\,\mathrm{kHz}$ and the amplitude was set to $5\,\mathrm{mV}$.[131,132] The **durability test** was started with a forward scan of a polarization curve held at $2.00\,\mathrm{V}$ for $250\,\mathrm{h}$. The durability test ended with a backward scan

as the breakout procedure. Subsequently, three polarization curves were recorded (forward & backward), followed by the EIS measurement. This was then repeated to perform a total of $500\,\mathrm{h}$ of durability testing. A similar procedure can be found in literature.[250] Data analysis was performed to extract relevant data. The Savitzky-Golay filter was applied to smooth the durability test signal. The best results were obtained using a third-order polynomial. Four window sizes were evaluated, corresponding to a period of three, six, twelve, and twenty-four hours of operation. The smoothed data were fitted with an exponential decay function to better describe the response from the single-cell testing and to facilitate its use in correlation studies, Equation 6.2.

$$J(t) = A_i \cdot e^{-x_t \cdot \lambda} + C \tag{6.2}$$

A_i denotes the initial amplitude of the curve, while C is the current density at the end of the test. λ is the decay constant, which determine the rate of decay, and x_t is the time variable. $J(t)$ describes the current density at a certain time.

6.4.2 Structure-Property Correlation

The parameters extracted from the data analysis related to the single cell tests were merged with the structural data obtained from the calculated IF of the SEM images taken. In Section 6.3.2a detailed description of the SEM image acquisition is given. Different datasets were constructed based on the similarity between the benchmark electrodes to ensure a reliable correlation between structural and electrochemical data. A total of nine datasets were defined as displayed in Table 6.3. The correlation strength was again estimated by the PCC while the PCC was also analyzed along the magnification scale of the taken SEM images, see Chapter 6.3.2.

Table 6.3. List of grouped subsets and corresponding benchmark electrodes.

Single Datasets		**Combined Datasets**	
Subset	**Benchmark Electrode**	**Subset**	**Benchmark Electrode**
subset_0	MP1	subset_1	MP1, MP2, MP3
subset_4	MP2	subset_2	MP1, MP3
subset_5	MP3	subset_3	MP1, MP4, MP5
subset_6	MP4	subset_7	MP4, MP5
subset_8	MP5	complete dataset	MP1, MP2, MP3, MP4, MP5

6.4.3 Sheet Resistance and In-Plane Electrical Conductivity

In this work, a novel developed four-line probe is presented, capable to measure at ten different spatial resolutions ranging from 250 µm to 2500 µm, pressure control, and the possibility of monitoring the local electrical resistances multiple times within a total area of 11 mm x 20 mm. Initially, the concept was validated by using a commercially-available reference specimen with defined sheet resistivity, whereas the probe was factory-made. Then the probe was used to characterize several components used in an electrolyzer, demonstrating the facile applicability. For enhanced accuracy regarding the CL in-plane electrical resistivity, the thickness determination from Chapter 6.3.3 was used to obtain the thickness distribution and average thickness from the CLs coated onto a N117 membrane. This work was partially published previously [251], as noted in Chapter: Author Contribution. Reused content from that publication is marked throughout the text with the symbol †.

Additional Materials & Characterization

Reference Specimen. For validation of the method, a commercially-available thin film of indium tin oxide (ITO) coated onto polyethylene terephthalate (PET) was employed. This well-studied material is used for a variety of electronic use cases, such as probes, or as an anode of organic light-emitting diode (OLED).[252–254] The ITO-PET was purchased from Sigma-Aldrich, with a specified sheet resistance of 300 Ω. The sheet possessed a total thickness of 178 µm, which is within the range of a Nafion N117 membrane. On the other hand, the ITO coating was only 100 nm thick, which is one order of magnitude thinner compared to the thickness of typical CLs.†

GDL and PTL Materials. Several carbon GDL materials (see Table 6.4) were used to perform a further validation of the probe. The electrical in-plane resistivity obtained from the technical specifications of the supplier is presented in Table 6.4, together with the respective thickness of the GDL. However, the specification regarding the testing procedure is limited. Furthermore, the study was extended by characterizing a titanium–felt, which is typically used as the anodic PTL (2GDL10-0.35).†

Thickness of the Materials. To calculate the in-plane electrical resistivity, knowledge regarding the specimen thickness is necessary. In the case of the GDL and PTL materials,

Table 6.4. Summary of the data gathered from the supplier specification available. In the case of the Freudenberg HC2315, the data of the complementary H23 was used and the specific resistiv ity was calculated by taking the presented thickness into account (denoted with *).†

Material	Supplier	Thickness [µm]	In-plane electrical resistivity [x10^{-5} Ohm m]
TGP-H-120	Toray Industries	370	4.70
HC2315	Freudenberg	170	13.6*
SGL22BB	SGL Carbon	215	33.0
2GDL10-0.35	Bekaert	350	-

the thickness was obtained using a stationary thickness measurement device (DM 2010, Wolf Messtechnik GmbH). On the other hand, the CL thickness was evaluated by means of a cross-sectional analysis and SEM using a Zeiss Gemini Ultra Plus as described in Chapter 6.3.3. However, the thickness is usually determined manually without any standard procedure, which gives no insight into the distribution.†

Characterization of the Topology. The probe topology was studied using a non-contact profilometer (CT-300, cyberTECHNOLOGIES GmbH) with a lateral resolution of 0.05 µm and a step width of 5 µm.†

Compression Analysis. To measure the distribution of the force applied to the specimen, three different pressure-measuring films (Prescale, Fuji Film CMV Hoven GmbH) covering a pressure range of 0.2 MPa to 10 MPa were used. It was expected that the adjusted compression force would not be equal to the force present on the measuring field and specimen. Thus, the pressure-measuring films were placed on top of the measuring field instead of a specimen, and everything was assembled as depicted in Figure 6.6. The adjusted compression force displayed by the compression force sensor ranged from 0.5 kN to 5.0 kN.†

Experimental Set-up. An accurate measurement of the resistance requires a proper and reliable way to contact the specimen with the measuring field of the probe while controlling the pressure distribution. The probe is presented in Figure 6.6a with red lines marking the

width and length of the measuring field. The image in Figure 6.6b, taken by an optical microscope (Axio Imager.M1m, Zeiss), shows the golden traces of the measurement field, and the blue-looking solder resist. An in-house manufactured setup was developed to control the contact between the probe and specimen, as shown in Figure 6.6c. The set-up consists of a stainless steel frame with a screw perpendicular to the center of the frame bottom, which was used to adjust the compression force. The specimen and probe were sandwiched between two aluminum metal blocks machined with a tolerance of $5\,\mu\mathrm{m}$. The first block possesses a rectangular cavity in which the probe can be placed and fixated by using two screws on the side. This fixation facilitates the placement of the specimen, which was placed upside-down onto the measuring field and covered with an insulating silicon sheet with a thickness of $462 \pm 4\,\mu\mathrm{m}$. The second block placed on top of the silicon sheet prevents misalignment while having contact with the protruding border of the cavity. Adjustment of the compression was performed by tightening the screw while monitoring the force using a compression force sensor (K-14, Lorenz Messtechnik GmbH) and hand-held measuring amplifier (GM77, Lorenz Messtechnik GmbH). The ridge of the bottom block distributes the compression force uniformly onto the measuring field.[†]

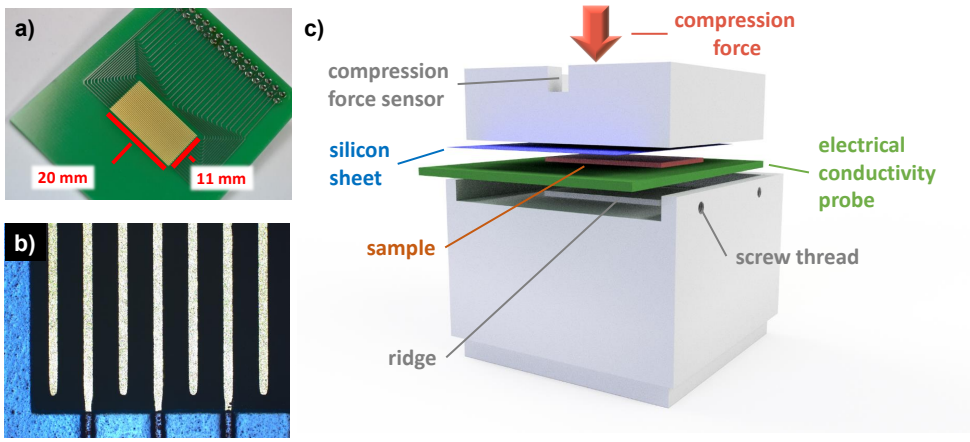

Figure 6.6. Experimental set-up to determine the in-plane electrical resistance of the PEM water electrolyzer components. The factory-made probe (a) possessed 32 traces. Each of the traces is $20\,\mathrm{mm}$ long and the area of the measuring field was $2.2\,\mathrm{cm}^2$. A close-up image obtained via optical microscopy (b) showed the blue solder resist at the border of the measuring field. The traces were $100\,\mu\mathrm{m}$ in width and $250\,\mu\mathrm{m}$ distance apart from one another. To determine the resistance, the specimen was sandwiched between the probe, a silicon sheet, and two aluminum blocks (c).

The presented experimental set-up was placed in a climate chamber (WKL64/40, Weiss Technik GmbH) to maintain 25 °C temperature and 25% relative humidity. The specimens were stored inside the climate chamber prior to usage. Before the measurement started, the compression force was adjusted 30 min in advance. The materials tested in this work were measured at a compression force of 1.00 kN first and then at 2.25 kN. Controlling of the potential/current was carried out with a battery cycler (BCS-815, BioLogic).[†]

Fabrication of the Probe To facilitate the reproducibility of the electrical resistance measurement, the probe architecture was conceptualized and ordered from Würth Elektronik GmbH & Co. KG, a specialist in printed circuit boardss (PCBs). Using PCBs as probes has the advantage that the probe production fulfills the IPC A 600 Class 2 and that further customization is possible while maintaining the quality. The material of the rigid board is a 1.55 mm-thick TG150 FR4, possessing a surface resistivity and volume resistivity ranging above 103 $\mathrm{M\Omega}$ and 103 $\mathrm{M\Omega\,cm^{-1}}$, respectively. The traces were made of copper with a final thickness of 35 $\mathrm{\mu m}$ according to the generic standard on printed board design (IPC 2221A). Additionally, the traces were coated with chemical nickel–gold to obtain a nickel thickness of 4 $\mathrm{\mu m}$ to 7 $\mathrm{\mu m}$ and 0.05 $\mathrm{\mu m}$ to 0.1 $\mathrm{\mu m}$ gold surface finishing. A solder resist (ELPEMER®SD 2467 SM-DG) was used to insulate the traces, while the area for contacting the specimen remained uncoated. The solder resist prevents short circuits during the soldering process and protects against wetting while ensuring that the specimen only has electrical contact with the measuring field. The measurement field with dimensions of 11 mm x 20 mm (Figure 6.6a) consists of 32 parallel traces with widths of 100 $\mathrm{\mu m}$, a length of 20 mm, 250 $\mathrm{\mu m}$ apart from each other, and a thickness of around 42 $\mathrm{\mu m}$. Each trace was connected to a drilled hole with an annular ring around it to solder a connection onto the probe. Then a precision socket strip (2 rows, 32 pins) was soldered onto the probe and connected this via ribbon cables to soldered 2 mm banana sockets on the other side of the cable to connect a potentiostat. Hence, each banana socket refers to a specific trace, allowing us to measure the resistance while using different equidistant configurations, made accessible by simply and quickly re-plugging the connections. The price per probe was less than €20 through ordering 15 in total. These low costs make the probe accessible to any laboratory.[†]

Measurement Method. The resistance was measured by applying voltage or current on the two outer traces (P+, P-) while sensing the response using the two inner traces (S+, S-). As an example, Figure 6.7 shows the connected traces for the 250 $\mathrm{\mu m}$ and 750 $\mathrm{\mu m}$ as

typically chosen distances. According to the corresponding configuration, the active traces were connected to the potentiostat to determine the resistance. The technical drawing of the probe shows the numbering of the 32 traces to choose the configuration of interest. According to Ohm's law, a truly Ohmic resistance is a proportional function of the voltage and current. Hence, in order to ensure the linearity of the measurement, a potential scan was performed, which increases the potential linearly in time. The potential windows set for all materials tested ranged from $0\,\mathrm{mV}$ to $5\,\mathrm{mV}$ at a scan rate of $0.5\,\mathrm{mV\,s^{-1}}$. By plotting the voltage against the measured current and performing a linear regression, the resistance (R) was obtained from the slope. For a four-line measurement, only four traces were needed, but due to the design of the probe there were 155 configurations for performing the measurement with a total of ten different equidistant distances (d) of the contacted traces, ranging from 250 to 2500 $\mu\mathrm{m}$. Using a distance of 250 $\mu\mathrm{m}$ allows to measure 29 equidistant configurations, whereas the next larger distance ($+\,250\,\mu\mathrm{m}$) reduces the number of possible configurations by three. Thus, the distance of $2500\,\mu\mathrm{m}$ can only be measured by two configurations. A detailed overview of the configurations related to the distance of interest can be found in Figure AT.1. Especially for CLs, a high locality of the resistances can be expected due to variations in thickness, loading and composition. Thus, for each distance (d) three different configurations were measured and randomly chosen across the measuring field and averaged the obtained resistances per distance.[†] Two parameters commonly used to characterize thin or thick layers are the sheet resistance (R_s) and in-plane electrical resistivity (ρ), which are proportional to the specimen thickness (t), as depicted in Equation 6.3:

$$R_s = \frac{\rho}{t} \tag{6.3}$$

However, the traditional four-point methods assume a uniform thickness, which is challenging to maintain for porous metal–polymer electrodes deposited onto a membrane, whose spatial extent is sensitive to relative humidity. Accordingly, measuring only one equidistant space between the traces remains prone to error, as it does not use the beneficial averaging effects to reduce noise. The $20\,\mathrm{mm}$ length of the traces ensures sufficient contact between the probe and specimen. Thus, in practice, the resistance (R) is measured as described above, and the averaged values are plotted against the distance (d) between the selected traces. The relationship of Equation 6.4 is used to obtain the sheet resistance by means of linear regression analysis. Equation 6.4 states that the slope is equal to the R_s of the material divided by the length of the traces (w). Any additional resistance in the circuit can arise from a variety of sources, such as contact resistance between the probe and specimen, cable resistance, and

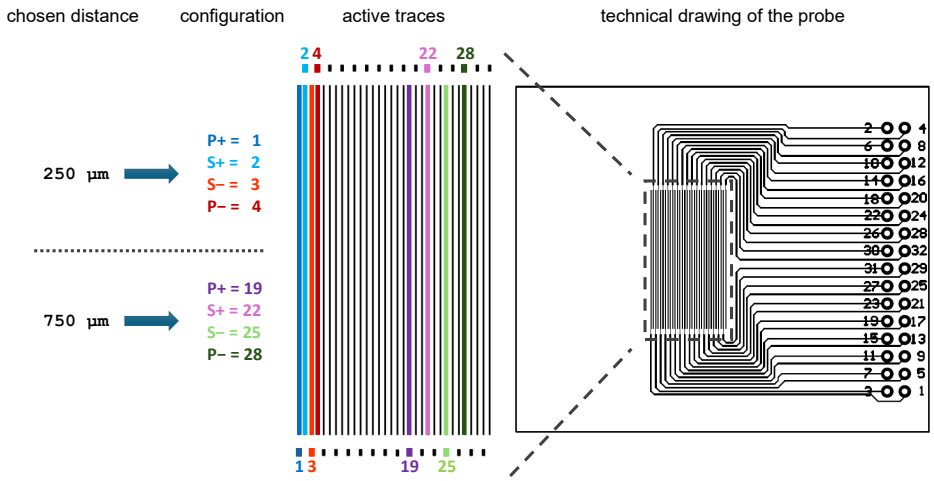

Figure 6.7. Exemplary selection of the distance of interest obtained by connecting a particular combination of traces. The selected distances were 250 µm and 750 µm. Both could be measured by a variety of combinations, as shown in Table AT.1. The outer tracks are labeled P+ and P-, whereas the inner ones are labeled S+ and S-. The 250 µm can be measured by using the traces [1, 2, 3, 4] labeled in the technical drawing of the probe. A possible configuration for measuring the 750 µm distance is [19, 22, 25, 28].

joint resistances. The collective impact of these additional resistances is represented by the y-axis intercept (R_0):

$$R = R_s \frac{d}{w} + R_0 \tag{6.4}$$

Another strength of the measurement technique is the possibility of monitoring the spatially-resolved resistances across the specimen (1D mapping). For such a measurement, all configurations at, e.g., 250 µm are tracked individually, i.e., [1, 2, 3, 4], [18, 19, 20, 21], etc., as shown in Table AT.1. Normalizing the obtained resistances by their mean value makes the fluctuation of the local resistance directly visible. To measure distances beyond 250 µm, the electron conduction pathways must be considered. The probe's measuring field in physical contact with the specimen implies that every trace is in direct contact with it. An applied current on the outer traces injects electrons into the specimen, passing through until an inner trace is reached. For distances $>$ 250 µm, not all traces are used for monitoring, but remain

in contact with the specimen. Depending on the specimen's resistivity, electrons may favor passing through additional traces or solely through the specimen, see insets in Figure 6.8 for visualization. The resistivity of the trace material (Cu) should be on the order of $10^{-8}\,\Omega\,\mathrm{m}$, whereas for CLs[114,115,133] or GDL[217] materials, it is on the order of $10^{-3}\,\Omega\,\mathrm{m}$ or $10^{-5}\,\Omega\,\mathrm{m}$. Therefore, it can be expected that for comparably high ohmic specimens, such as CLs, the electrons will pass through the additional trace instead of the specimen. The mathematical analysis and derivation of an equivalent circuit describing the electron paths and their effect on the measurement can be found in the following. In short, overestimation of the specimen resistance by ignoring the contribution of the trace width will result in an error that is orders of magnitude smaller than the measured resistance for low conductive specimen.

In the best case, the interface resistance of the copper trace and sample surface should be below $100\,\mathrm{m}\Omega$. It is likely that the electrons pass through the traces and the sample, especially if the sample and trace resistances are similar. To understand the two limiting cases more profoundly, a general mathematical expression was used (Equation 6.5) corresponding to an equivalent circuit (Figure 6.8a) representing the measurement.

$$R = N \cdot \rho_{A,m} \cdot d_m + 2R_c + R_{su} + (N-1)\frac{(2R_c + d_t \cdot \rho_{A,t}) \cdot d_t \cdot \rho_{A,m}}{(2R_c + d_t \cdot (\rho_m + \rho_{A,t}))} \tag{6.5}$$

The measured resistance (R) can be described as a serial function of the sample resistance (R_m) and the trace resistance (R_t) and needs also to account the contact resistance (R_c) between the sample and traces, as well as the resistances emerging from cables, solder joints, and others represented as R_{su} (Figure 6.5a). Assuming a constant cross-sectional area (A), the sample resistance (R_m) can be expressed as $R_m = (\rho_m/A) \cdot d_m$, where d_m is the distance (d_m = 250 µm) between the traces and $\rho_{A,m}$ is the resistivity of the material relative to the cross-sectional area. Similarly, the trace resistance (R_t) is expressed as the trace material resistivity ($\rho_{A,t}$) with a constant cross-sectional area and trace width (d_t= 100 µm). If $R_m >> R_t$, the main contribution to the measured resistance emerges from the material tested, allowing to neglect R_t. This consideration needs to be accounted in the total length (l) assumed for the evaluation of distances $d_m > 250\,\mu\mathrm{m}$, leading to two limiting cases. Equation 6.6 assumes that $R_m >> R_t$ and therefore the total length (250 - 2500 µm) is equal to the number (N) of distances between the traces. Contrary to that if $R_m << R_t$ the total length (250 - 3450 µm) needs to account the additional width of the traces ($d_t = 100\,\mu\mathrm{m}$). In this case, Equation 6.7 applies. However, these assumptions neglect possible current crowding or non-uniform contact

resistances.

$$l = N \cdot d_m \tag{6.6}$$

$$l = N \cdot d_m + (N-1) \cdot d_t \tag{6.7}$$

From the equivalent circuit and Equation 6.5 it becomes clear that if the sum of contact resistances and trace resistances is way smaller than the sample resistance, case 1 described by Equation 6.6 occurs instead of case 2 expressed by Equation 6.7. Assuming case 2 for low conductive materials would lead to high errors regarding the determined resistance. A general analysis of the error is presented in Figure 6.8b for both cases.

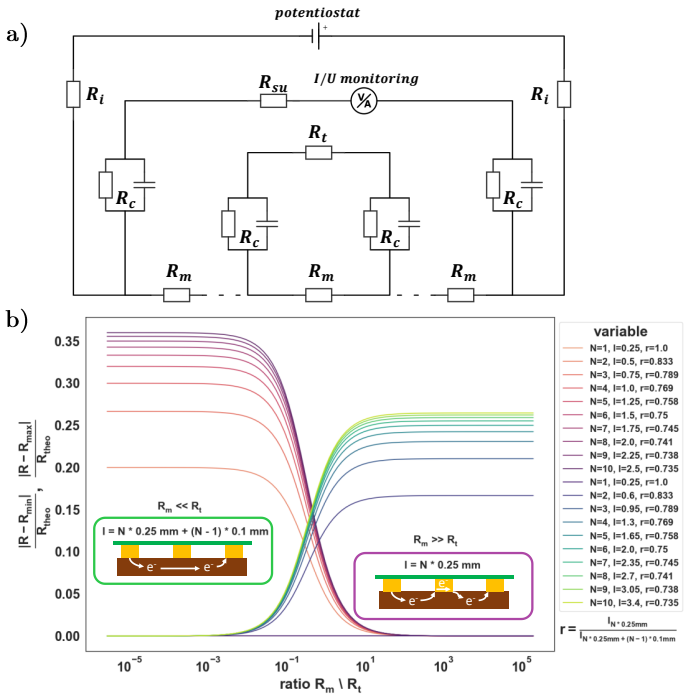

Figure 6.8. Theoretical considerations (a) regarding the equivalent circuit of the probe contacted with the sample and (b) the analysis of the deviation emerging from the assumed distance traveled by the electrons. The framed schematics in (b) represent the two cases in dependency of the ratio between sample and trace resistance. The green bar of the scheme denotes the rigid board, while the golden square represents the traces and the brown bar the sample contacted to the traces.

The deviation of the measured resistance from its theoretical value (R_{theo}) of a given sample is scaled by the minimum and maximum on the y-axis. On the x-axis, the ratio between R_m and R_t is presented. The greenish to blueish colored lines referred to case 2 with the total length calculated by equation 6.7, showing that the error increases if $R_m >> R_t$, indicating that the electrons are not flowing solely through the sample, but additionally passing through the traces. Thus, it is valid to assume case 1 and equation 6.6 for determining the resistance of low conductive materials, as can also be seen by the line represented by a magenta color code. On the other hand, it is not appropriate to assume case 1 for highly conductive samples, but case 2 would be. For case 1 the maximum error reaches a threshold of around 0.36 if $R_m << R_t$ as can be seen in Figure 6.8. Case 2 results in a maximum error at a threshold of around 0.26 for $R_m >> R_t$ which is also visible in Figure 6.8. The threshold can be explained by the geometric ratio (r) between d_m and d_t converging towards a limit at approximately 0.71. The theoretical resistance used in Figure 6.8b originated from the reference material, later used for validating the method. However, the calculation in Figure 6.8b assumed that there is no additional contact resistance between the current supply (R_i) and the sample and no resistance emerged from the set-up.[†]

Key features of the conductivity probe design:

- → The developed conductivity probe and setup involves a precise contact between the specimen and probe, with a controlled pressure distribution measured by Fuji Film analysis.
- → The data was analyzed using linear regression to determine sheet resistance, taking into account additional resistances and allowing spatial mapping of local resistance variations.
- → The measured resistance depends on the sample and trace resistances, with the contribution of the contact and trace resistances becoming significant when the sample resistance is low, but insignificant when the sample resistance is high.

7 Relationship between Production Variables and Structure

Analyzing the structure of CLs in a representative manner requires that the produced texture is uniformly distributed across the whole electrode area, in this work $17.64\,\mathrm{cm}^2$. Therefore, the impact of production variables onto the macroscopic loading distribution was analyzed first. The method to visualize the loading distribution can be found in Section 6.1.2. The impact on the microstructure was monitored by CLSM and from the intensity images extracted IFs were correlated to several STPs as described in Chapter 4 & 6. The following section presents the results related to the microstructural assessment of the CL at various magnification levels. This includes the impact of the alcohol content within the dispersion, the type of catalyst, reduced iridium loading and the Nafion content. After achieving a uniform loading distribution, the applied machine parameter (MP1) were the same for all CLs sprayed, Table 6.2.

7.1 Impact of Production Variables on the Loading Distribution

Preliminary experiments were conducted to evaluate the impact of various machine parameters and inform the design of the final parameter study. Three key parameters were found to significantly influence the quality of the produced CL. These parameters are gas pressure, nozzle height, and flow rate. However, the design of the mask used during the spray-coating process was also identified as a critical factor affecting the loading distribution. A metal mask was used to shape the CL to the desired electrode area. Initially, a $3\,\mathrm{mm}$ thick metal plate was used with a cutout having a 90° edge and the default spray parameters were set. The spray process was operated using default parameters of $20\,\mathrm{mm}$ nozzle height, $1\,\mathrm{kPa}$ gas pressure, and $0.2\,\mathrm{mL\,min^{-1}}$ flow rate. The effect of the mask edge is shown in Figure 7.1. The 90° mask edge results in an inhomogenous loading with a mixture of light and dark areas (Figure 7.1a). In Figure 7.1b the improved mask design is displayed, where the centered cutout has 45° edges

instead of 90° edges. The impact of the 45° edge mask with the default spray parameters and their effect on the macroscopic loading distribution is shown in Figure 7.1c.

The dark violet areas indicate higher iridium loading, while the bright orange areas correlate to lower loading. The 45° mask edge improved the loading distribution and leading to less noticeable dark and bright spots. Most likely, the mask edge affected the repulsion of the sprayed dispersion or interacted with the tail of the sprayed mist, which affected the average path length of the droplet. The 45° mask edge provided better performance in the single cell test, as the CL produced had a smoother and more uniform loading distribution.♦

Figure 7.1. Influence of the mask onto the loading distribution using default spray parameter.♦

The impact of classical spray parameters such as flow rate, gas pressure and nozzle height is shown in Figure 7.2 and 7.3. For all CLs shown in Figure 7.2, the nozzle distance to the membrane was set to $10\,\mathrm{mm}$ and a low gas pressure of $1\,\mathrm{kPa}$ was used in Figure 7.2a. At a flow rate of $0.2\,\mathrm{mL\,min^{-1}}$, the CL showed an alternating pattern of loading distribution. Increasing the flow rate (Figure 7.2a-c) showed that the pattern changed to a non-uniform loading distribution. This tendency increased at higher flow rates, and at a maximum flow rate of $0.8\,\mathrm{mL\,min^{-1}}$, swelling of the membrane was also observed.

Using instead a moderate gas pressure of $10\,\mathrm{kPa}$ and the same nozzle distance of $10\,\mathrm{mm}$ showed a different effect on the loading distribution when varying the flow rate. At a low flow rate the observed pattern (Figure 7.2d) in the loading distribution is similar to the pattern visible in Figure 7.2a. As the flow rate increased, this pattern changed to a more criss-cross pattern, Figure 7.2e. At a flow rate of $0.8\,\mathrm{mL\,min^{-1}}$ (Figure 7.2f) dark dots are observed indicating larger agglomerates within the CL. This demonstrates the need for improved loading distribution to study microstructural effects. Setting the nozzle height to $40\,\mathrm{mm}$ significantly improved the loading distribution. This indicates that nozzle height is one of the dominant factors in achieving uniform loading distributions. Combining this nozzle height with a constant gas pressure of $10\,\mathrm{kPa}$ resulted in uniform loading distribution as the flow rate was increased

as shown in Figure 7.3a-c. In comparison to the lower nozzle height used in the dataset presented in Figure 7.2), the loading distribution showed no pattern and was completely uniform, Figure 7.3a-c.

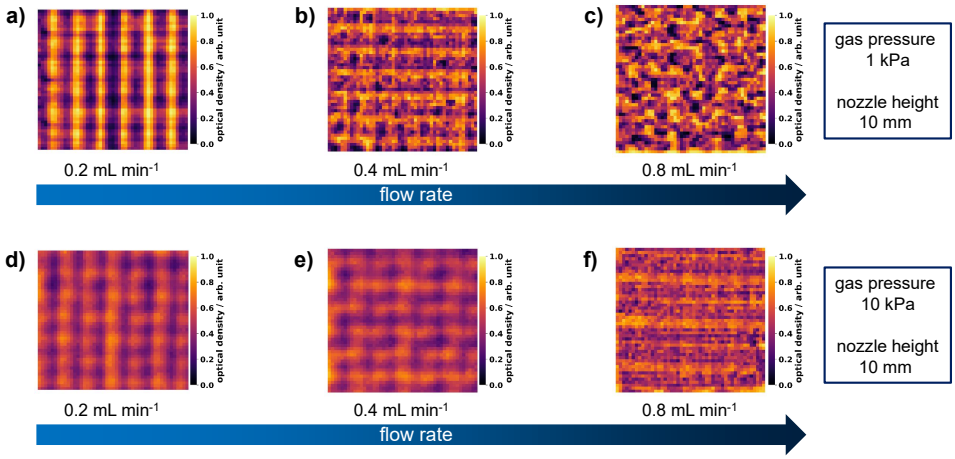

Figure 7.2. Effect of machine parameters on ultrasonic spraying at low Ir loadings. (a–c) Flow rate variation at low, constant gas pressure and nozzle height. (d–f) Increased gas pressure with varying flow rate.

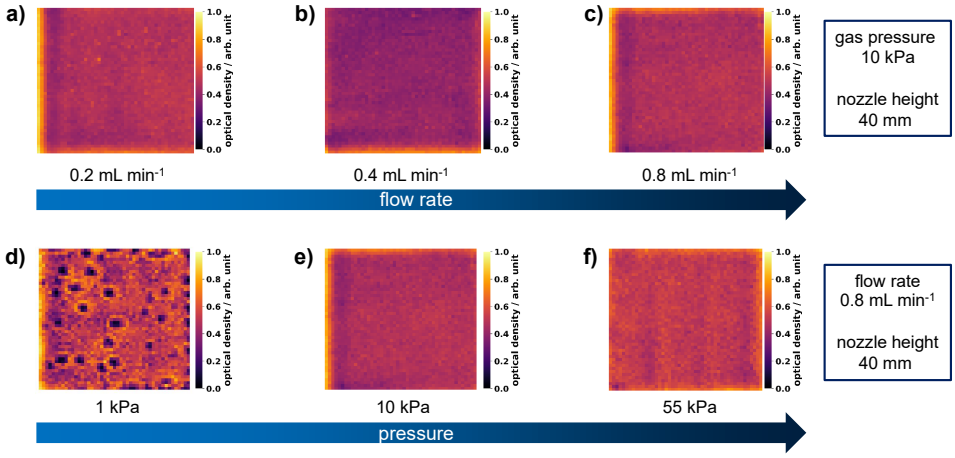

Figure 7.3. Effect of nozzle distance on loading uniformity. Greater nozzle height improves electrode loading uniformity (a–c), but optimal results depend on the combined settings of gas pressure and nozzle height (d–f).

However, the above trends have not only emphasized that nozzle height remains the most critical production variable. Rather, it highlights that there is an operating window to obtain uniform loading distributions. For example, if the gas pressure is too low (Figure 7.3d), a swelling of the membrane is observed again at high flow rate ($0.8\,\mathrm{mL\,min^{-1}}$) and thus a non-uniform loading distribution. Increasing the gas pressure led to a more uniform loading distribution, (Figure 7.3d-f). This means that if the operating window remains suitable, higher flow rates can be achieved, significantly reducing the production time of a CL. With the experiments presented, this work has shown how the loading distribution can be influenced by the operating window. An edge effect was consistently observed in nearly all analyzed CLs, likely due to interactions between the spray mist and the masking. To minimize this influence, CLs intended for electrochemical testing were sprayed over a larger area ($50\,\mathrm{mm}\times50\,\mathrm{mm}$) than the active area ($42\,\mathrm{mm}\times42\,\mathrm{mm}$) to ensure the edge region was excluded from performance measurements. Uniform loadings or uniformly distributed electrode compartments are crucial for the study of electrochemical phenomena. However, different spray parameter might still affect the microstructure.

Effects of mask design and spray parameters on CL uniformity:

- → Replacing a 90° edge with a 45° edge on the metal mask improved loading uniformity by reducing the presence of high and low loading areas due to reduced droplet repulsion and better mist distribution.
- → Higher flow rates increased loading randomness and membrane swelling, while lower rates resulted in patterned distributions at low nozzle distances.
- → Increasing gas pressure changed the heterogeneous loading pattern from ordered to criss-crossed.
- → Setting the nozzle height to 40 mm proved most effective for uniform loading. This parameter allowed consistent loading distributions over varying flow rates and gas pressures without visible patterns.
- → Uniform loading distribution was achieved within a specific operating window of flow rate, gas pressure, and nozzle height. Staying within this window allows for higher flow rates and reduced production time without sacrificing uniformity.

7.2 The Production - Structure Relationship

The influence of the production variables on the microstructure will be investigated in the following by means of confocal laser scanning microscope (CLSM). The obtained data was also used to correlate the statistical IFs with the STPs of the CL texture derived from CLSM analysis. The simultaneous discussion of the extracted STPs and computed IFs made it possible to link the stochastic IFs to physical quantities describing the surface texture of CLs.

7.2.1 Phase I: Data processing

The primary objective was to identify the STPs that can represent others based on their mutual correlation. The obtained datasets were merged at the beginning of this study part. The PCC was calculated for each possible STP combination. A $|PCC| > 0.70$ is interpreted as a very strong linear relationship between two variables. The correlation is interpreted as strong correlation if the PCC ranges between $0.50 < |PCC| \leq 0.70$.[209] Therefore, the clustermap together with the dendrogram of the PCC results (Figure 7.4) showed that the STPs can be grouped into several classes, as ISO 25178 suggested (Table AT.2). The dendrogram and clustermap analysis reveal four main groups of STPs. The level at which branches merge in the dendrogram reflects the degree of dissimilarity between surface texture parameters. Lower levels indicate greater similarity or higher correlation, while higher levels indicate greater dissimilarity.

The first group corresponds to the height parameter class extremes and comprises S_v, S_p, and S_z. Specifically, S_v represents the maximum pit depth, or the distance from the mean plane to the lowest surface point. S_p denotes the maximum peak height, which is the distance from the mean plane to the highest peak. S_z captures the maximum height, which is defined as the vertical distance between the deepest valley and the highest peak on the surface. While these parameters effectively describe extreme surface features, they are sensitive to noise and prone to outliers. They may not always accurately represent the general surface profile, particularly when measurement artifacts or irregularities are present. Consequently, none of the STPs in the first group were included in the correlation analysis.

The second group, consisting of S_{vk}, V_{vv}, S_k, V_{mc}, V_{vc}, S_q, S_a, and S_{xp}, was the largest group identified. It exhibited a minimum observed |PCC|of 0.73, with only two STPs showing |PCC| $<$ 0.93. The third group was identified as comprising S_{al}, S_{pk}, and V_{mp}, while the fourth group includes parameters that describe the general height distribution, namely S_{sk}, S_{ku}, S_{Mr1}, and S_{Mr2}.

The texture aspect ratio, S_{tr}, showed a negative correlation in all relationships, with an absolute Pearson correlation coefficient of $|\text{PCC}| = 0.22^{+0.11}_{-0.11}$, making it the most dissimilar parameter among those analyzed. This can be attributed to the fact that this parameter describes the spatial isotropy which remained relatively unchanged for all samples. In total, 100% of the CL possessed a S_{tr} value of > 0.40, while for 98% a value of > 0.70 was obtained. This indicated that all samples studied possessed a high isotropy with no directional orientation.[‡] Three representative STPs were selected based on the clustermap (Figure 7.4), and their

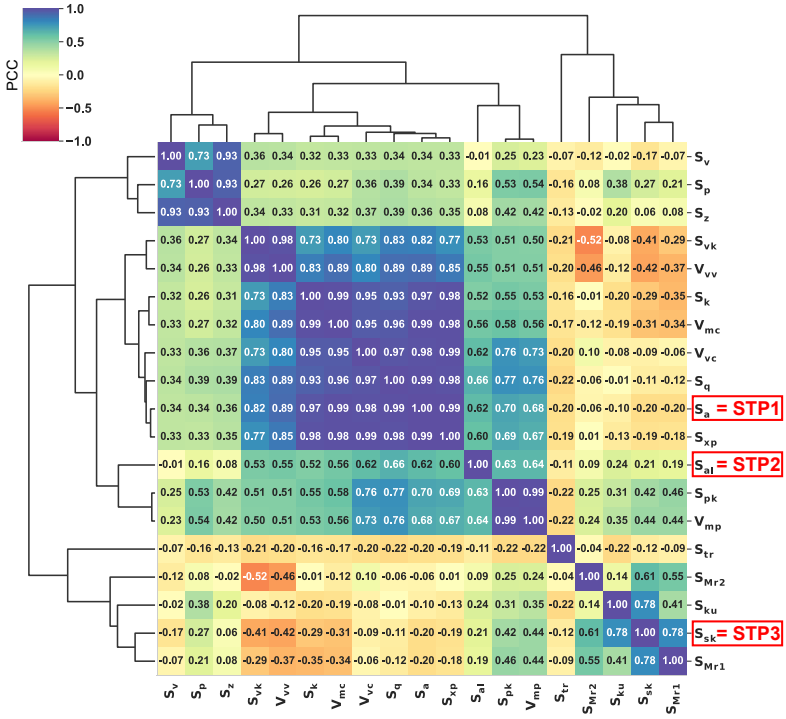

Figure 7.4. The PCC matrix is shown as a cluster map with the matrix's PCC values arranged in hierarchical order. This arrangement is shown alongside a dendrogram, which is a tree-like diagram that represents the hierarchical structure of the data.

relationship to the other STPs is presented in Figure 7.5. The arithmetical mean height (S_a), found in the second group, was chosen as first representative STP as it showed a PCC of $\geq 0.97^{+0.01}_{-0.01}$ (S_{xp}, S_q, V_{mc}, V_{vc}, S_k) in six out of nineteen combinations. Further, a very strong correlation was observed between S_a and V_{vv} (PCC $= 0.89^{+0.02}_{-0.03}$) as well as to S_{vk} (PCC $= 0.82^{+0.03}_{-0.03}$). The correlation between S_a and reduced peak height, S_{pk} (PCC $= 0.70^{+0.05}_{-0.05}$), or

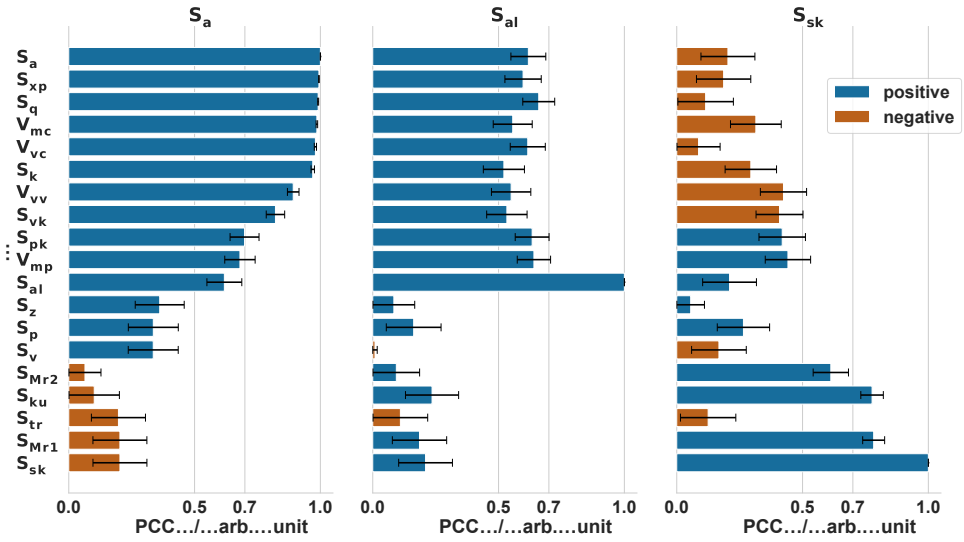

Figure 7.5. From the clustermap extracted relationships between the representative STP, noted at the top of each graph, and the corresponding STP written on the y-axis. The orange color represents the absolute value of the obtained PCC. The definition of the acronyms can be found in Table AT.2.

peak material volume, V_{mp} (PCC $= 0.68^{+0.06}_{-0.06}$), marked the boundary where S_a could be used to represent the other STPs. The reasons for these strong relationships are derived partly from mathematical relationships, e.g. root mean square height, S_q, is the square root of S_a as well as all these parameters describing the texture's height variation. Using only S_a for all applications may not be appropriate, as certain parameters could be more sensitive to particular processes. From quality control perspective of the CL production, however, it is indeed appropriate to monitor only S_a as the first quality indicator as it represents almost 50% of the STPs studied. Analyzing the computed confidence interval at a level of 95% showed that they increased with decreasing PCC. That was due to the increased variance with decreased PCC and showed why the 95% computed confidence interval was higher for the other representative STPs than for S_a.[‡]

The other two chosen representative STPs were the autocorrelation length (S_{al}) from the third group and the skewness (S_{sk}) representing the fourth group. The autocorrelation length describes the spatial surface texture and is equal to the lateral length with the fastest decay to a given value. This parameter is used to describe the contact behavior of rough surfaces or

adhesion properties.[255,256] Analysis of the PCC showed that S_{al} correlated to all parameters represented by S_a within a range of $0.52^{+0.08}_{-0.09} < PCC \leq 0.66^{+0.06}_{-0.07}$), but correlated weakly to the remaining parameters ($|PCC| = 0.24^{+0.10}_{-0.11}$) as well. Therefore, this parameter was chosen as another representative as it provides additional information on the surface texture studied.

Instead, the skewness describes the symmetry of the height distribution. The skewness correlated weakly to most of the STP ($|PCC| = 0.44^{+0.09}_{-0.09}$), except to S_{ku} (PCC $=0.78^{+0.04}_{-0.05}$), S_{Mr1} (PCC $= 0.78^{+0.05}_{-0.04}$), and S_{Mr2} (PCC $=0.61^{+0.07}_{-0.07}$).

The correlation results showed that there is a strong dependency between several surface texture parameters. The selected three STPs (S_a, S_{al}, S_{sk}) represent a large part of the parameter space. A change in these parameters would likely indicate that other parameters were also affected, so this set of parameters can be used for quality control of the catalyst surface texture and is also suitable for further correlation studies.

Results from the initial data processing step:

- → Strong correlations are defined by a threshold: |PCC| > 0.70 is considered very strong, while $0.50 <$ |PCC| ≤ 0.70 indicates a strong relationship.
- → Using a clustermap of PCC values, STPs are grouped into several classes, in line with ISO 25178 standards.
- → Three representative STPs were chosen based on correlation clusters
  - ⇀ S_a (arithmetical mean height): Captures height-based features and strongly correlates with other STPs, making it a key quality control metric.
  - ⇀ S_{al} (autocorrelation length): Describes spatial texture for contact and adhesion behaviors.
  - ⇀ S_{sk} (skewness): Indicates symmetry in height distribution, providing additional texture insight.
- → These selected STPs cover a wide parameter range, simplifying surface monitoring and quality control for CLs.

7.2.2 Phase II: Identification of Structural Descriptors

For all datasets presented in Table 6.1, the PCC was calculated between each selected STP and extracted IF. To reduce the number of IFs and to prioritize the relevant parameter set, the ten strongest correlations of the absolute PCC were selected for each dataset and STP. It became apparent that the obtained PCCs depended on the selected dataset. Averaging the absolute PCC per dataset showed that the "gas pressure" dataset had the weakest correlation with (0.49 ± 0.10), followed by the "nozzle height" dataset (0.61 ± 0.15) and the "flow rate" dataset (0.61 ± 0.15). The strongest correlations were obtained from the "iridium loading" (0.91 ± 0.06), "alcohol content" (0.78 ± 0.15) and "Nafion content" (0.70 ± 0.14) data sets. Figure AF.2a shows the averaged PCC sorted with respect to the different datasets and reference STPs and split into positive and negative correlations.[‡]

The negative PCC are shown as absolute values to facilitate comparison. After sorting the PCC, the maximum standard deviation obtained was ± 0.09 for the positive correlation between IFs and S_a in the case of the "Nafion content" dataset (0.52 ± 0.09). At the same time, this was the weakest correlation obtained for the respective dataset and the correlation between prioritized IFs and S_a. Except for this particular case, S_a correlated more strongly than S_{al} and S_{sk} with the extracted IFs for every other dataset. The strongest correlations between S_a and IFs were obtained from the "iridium loading" dataset, which showed both positive and negative correlations, with averaged PCCs of 0.96 ± 0.01. S_{al} correlated more strongly with the prioritized IFs than S_{sk} in four out of six datasets. In the Nafion content dataset, the correlation IF was stronger for S_{sk} compared to S_a and S_{al}. The strength of the correlation depended on the dataset, probably due to underlying information and dependencies within the dataset used. However, these parameters must not affect the STPs or IFs linearly. Therefore, the lower PCCs could result from a non-linear dependency within the data studied. As mentioned above, the correlation strength obtained depends on the range of observation.[210] This can also result in low correlation strength when the dataset covers only a limited range of values. Another selection factor is redundancy because it describes how versatile and robust a particular parameter is. The ten prioritized IFs per dataset were analyzed for their redundancy across all datasets examined, as shown in Figure AF.2b. In total, 38 out of 84 IFs met the requirement of being observed more than once across all datasets, reducing the parameter space by 55%. Redundancy analysis revealed that 26 IFs correlated with S_a and S_{sk}, while 22 correlated with S_{al}. Among the IFs, six parameters described the FO parameter space, while seven were derived from the GLCM, eight from the GLDM, six from the GLRLM, nine from the GLSZM,

and two from the NGTDM.‡

These numbers imply that the parameter space was reduced to 30% of the extracted GLCM features, 62% of the GLDM features, 60% of the GLSZM features, 40% of the GLRLM features, 50% of the NGTDM features, and 35% of the FO texture parameters. No tendency was observed for the correlation between the IFs and S_a. However, none of the GLCM features correlated with S_{al}, while only two of the nine GLSZM features correlated with S_{sk}. Analysis of the different datasets showed that only $GLDM9$ correlated strongly enough with S_a across all datasets and $GLRLM6$ correlated within five datasets. All other IF correlated less than across four datasets with S_{al} ($GLDM8$, $GLRLM15$, $GLRLM5$, $GLSZM12$, $GLSZM13$). Meanwhile, S_{sk} exhibited correlations with three IFs ($GLCM14$, $GLDM1$, $GLDM2$) present in three datasets at maximum. None of the extracted IFs correlated for the same dataset and simultaneously with all STPs, showing that the IFs represent different aspects of surface texture. Consequently, additional examination concentrated on the most frequently observed IFs across the datasets and their correlation with a specific STP. These parameters were then examined in more detail and compared with the other PCC values, as shown in Figure 7.6 for the "iridium loading" dataset. All other corresponding visual representations of the datasets studied can be found in the supplement from Figure AF.3 to Figure AF.7.‡ The relationship

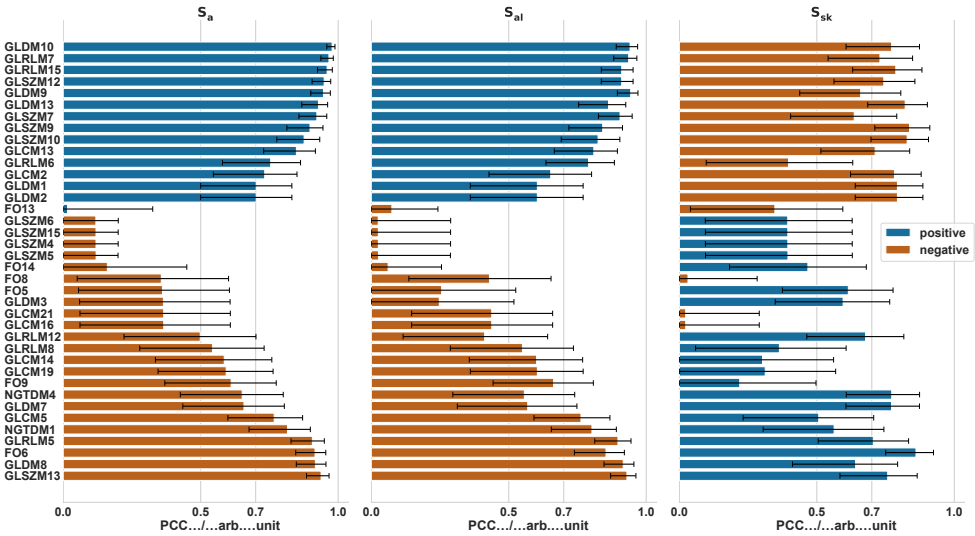

Figure 7.6. Evaluation of the correlation strength between STPs and IFs for the iridium loading dataset and the previously reduced IF parameter set.

between IFs and STPs showed a clear dependence on the specific STP, as S_{sk} showed an inverse directional dependence, unlike the other two STPs. This tendency was also observed in other data sets evaluated. Both S_a and S_{al} obtained 14 PCCs with $|PCC| > 0.80$, while the trend of the confidence interval was similar to that observed in Figure 7.6 valuating the correlation between the different STPs. The lower the PCC, the wider the confidence interval. In the case of S_{sk}, only four relationships were obtained that had a absolute PCC greater than 0.80. As explained, the respective data sets affected the correlation strength of the obtained PCCs. This made it difficult to highlight a clear tendency regarding the correlated IFs and their corresponding correlation strength. Therefore, only the selected IFs after the redundancy analysis were considered for further explanation of the datasets and an overview is given in Figure AF.2.[‡] The selected IFs from the redundancy analysis correlated in the same

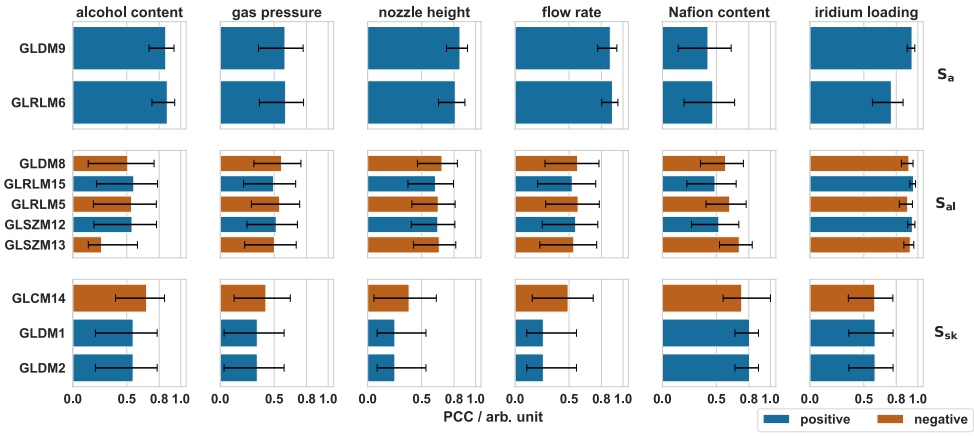

Figure 7.7. An overview of the connection between the selected STPs and IFs is provided based on the redundancy analysis conducted in Figure AF.2. The columns refer to the respective data set, while the row shows the correlation between the STP and the selected IF.

value range for each dataset and corresponding STP, while similar tendency were obtained in the 95% confidence interval. Across all datasets, the selected IFs showed correlations greater than 0.75 with each other for each STP. A table presenting the definitions and equations used in Figure 7.7 can be found in Table AT.4. Regarding S_a, long run high gray level emphasis ($GLRLM6$) describes the joint distribution of long run lengths with higher gray level values. In computer vision, a gray level run denotes a connected segment of pixels with the same gray intensity, which are consecutive and collinear. As described in Chapter 4.2, the run length itself denotes the number of pixels within the run in a particular direction.[169] If $GLRLM6$

increases, the texture possesses runs with longer length of high pixel intensities. This increase can result in a texture that appears with stronger contrasts between areas of high and low intensity. Meanwhile, large dependence high gray level emphasis ($GLDM9$) characterizes the joint distribution of large dependence with higher gray level values. The gray level dependency matrix (GLDM) represents each pixel's relationship to its neighbors at a given distance. Textures with higher values of $GLDM9$ possess an increased number of areas with high intensity values. Notably, both $GLRLM6$ and $GLDM9$ showed a robust correlation with S_a across most of the datasets. For S_{al}, four IFs were observed to have a consistent correlation strength across the datasets. Since S_a is the arithmetic mean height, the IFs correlate with the height variation within the CL surface. Therefore, increased surface roughness would be detected by increased values of the $GLDM9$ or $GLRLM6$ function. On the other hand, large dependence emphasis ($GLDM8$) and long run emphasis ($GLRLM5$) had an inverse relationship with S_{al}, indicating that when S_{al} increases, both values must decrease. $GLRLM5$ quantifies the distribution of long run lengths, where a higher value indicates the presence of long run lengths and coarser structural textures. On the other hand, $GLDM8$ assesses the distribution of large dependencies, with a higher value indicating a greater degree of dependence and more uniform textures.

Imagine a thick CL with plateaus separated by large, irregularly distributed cracks, as shown in Figure 4.3a. The whitish cracks would possess a higher pixel intensity than the smooth blackish plateaus. The wider the whitish crack, the larger $GLRLM6$ and $GLDM9$ must become, while also $GLRLM5$ must increase. Another example would consider that pixels with low-intensity values refer to valleys and pores, depending on the lateral resolution of the measurement. High intensities instead would represent grainy island-like formations or surface peaks and spikes. However, all these examples are strongly dependent on the sample acquisition. The image feature behavior could change accordingly. Interestingly, dependency entropy ($GLDM1$) and dependence non uniformity ($GLDM2$) showed the same correlation strength with S_{sk} across all the datasets analyzed, always having a correlation of 1.00 between them. These two parameters provide a measure of the similarity of pixel dependencies across the image, with a lower value indicating increased consistency and uniformity of dependencies within the image. CLs that occur smoother and flatter would possess lower $GLDM1$ and $GLDM2$ values. Instead irregular rough CL textures would exhibit higher values for both. To simplify the following explanations, the focus is on the relationship between $GLDM9$ and arithmetical mean height (S_a), $GLRLM5$ and autocorrelation length (S_{al}), and $GLDM2$ and the skewness (S_{sk}). However, it is important to note that the selection of features can

vary not only based on the dataset used, but also on factors such as signal-to-noise ratio and the acquisition used. In addition to feature selection, the extracted IFs need to be applied and should show the same trend as their counterpart.[‡]

Key results from the correlation study between surface texture and image features:

- → The "iridium loading", "alcohol content", and "Nafion content" data sets showed the strongest correlations between the classical STPs and IF, with PCC values ranging from 0.70 to 0.91.
- → The "gas pressure", "nozzle height", and "flow rate" data sets showed weaker correlations between them, with PCC values ranging from 0.49 to 0.61.
- → Redundancy analysis revealed that 38 of the 84 extracted IFs overlapped across multiple datasets, reducing the parameter space by 55%.
- → The strongest correlations with S_a were found with GLRLM6 and GLDM9, suggesting that these features effectively capture surface roughness and texture variation.
- → S_{al} and S_{sk} correlations were also examined, with inverse relationships found in some cases, such as with GLRLM5 and GLDM8.
- → Feature selection was influenced by dataset characteristics, including signal-to-noise ratio and acquisition methods.
- → Analysis confirmed that the selected statistical IFs can be used to characterize porous electrodes as they correlate with the physical quantities (STPs).

7.3 Discussion of the Production - Structure Relationship

This chapter applies the three STPs identified in the correlation study to investigate the impact of production variables on the CL structure. The preceding chapter demonstrated a strong correlation between these three STPs and specific IFs. The IFs are analyzed alongside the STPs to determine, if interpreting the STP leads to the same conclusions as analyzing the IFs. The IFs can only be considered reliable descriptors of the CL texture in future experiments, such as monitoring the CL structure across different magnification scales, if both the STPs and IFs lead to consistent conclusions. Another important aspect is that IFs enables the quantitative analysis of CLSM intensity images. This allows for more sophisticated comparisons between different samples and enhances objectivity. This is shown exemplary in Figure 7.8. The nozzle height was varied from $10\,\mathrm{mm}$ to $60\,\mathrm{mm}$, and corresponding images were acquired. A visual

comparison of these images makes it difficult to draw clear conclusions. However, applying IFs allows the objective quantification and interpretation of image data, making the underlying structural information accessible through statistical analysis, as presented in Figure 7.9g–i). To better understand and compare the influence of structural texture, three IFs were selected

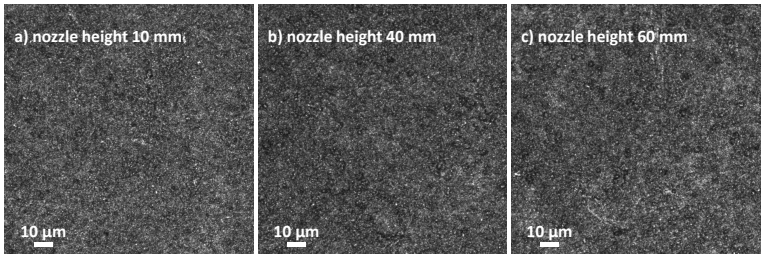

Figure 7.8. CLSM intensity images of CL surfaces at varying nozzle heights (a-c), illustrating the challenge of visual comparison and the value of using IFs for quantitative analysis.

in Chapter 7.2.2 which correlate well with the STPs S_a, S_{sk}, and S_{al}. These parameters are key descriptors of surface topography which were selected in Chapter 7.2.1. Specifically, S_a represents the arithmetic mean height, which quantifies average surface variation. S_{sk} measures skewness, indicating whether the surface has more peaks or valleys. Finally, S_{al} measures the autocorrelation length, which describes the spatial periodicity and uniformity of the surface texture.

The selected IFs used in this chapter for explanation and trend monitoring are as follows: $GLDM9$ characterizes the joint distribution of large dependencies associated with higher gray-level values. $GLDM9$ quantifies the spatial relationship of each pixel to its neighbors within a given distance with lower values tending to more homogeneity within the image. $GLRLM5$ measures the distribution of long run lengths, with higher values indicating longer sequences of similar gray levels and a coarser texture overall. Finally, $GLDM2$ assesses the similarity of pixel dependencies across the image, where lower values reflect greater consistency and uniformity in structural patterns. The selected IFs were retained after the parameter space reduction (section 7.2.2) and among the ten extracted STPs for further use and can be found in Figure 7.7.

These parameters are used to explain the impact of production variables and dispersion properties, such as the nozzle height, whose effect on the CL structure is shown in Figure 7.8. In later sections, variations in iridium loading and Nafion content are also discussed to highlight the applicability of IFs. These examples demonstrate how novel insights can be gained by

the use of IFs in characterizing structural variations. Additionally, this chapter investigates how the CL structure evolves across different magnification scales by applying statistical IFs, enabling consistent multi-scale texture characterization.

First, the datasets relating to the production variables are analyzed and displayed in Figure 7.9. This continues the discussion started in Section 7.1 by shifting the focus from macroscale observations to mesoscale and microscale observations.. The x-axis represents the production parameter studied. The doubled y-axis displays the information of the respective surface texture parameter (STP) (S_a, S_{al}, S_{sk}) together with its linked IF. Adjusting the production variables lead to variations of S_a in the range between 0.20 µm and 0.46 µm while its counterpart $GLDM9$ ranged from 1.87 to 9.48. Depending on the dataset examined, the $GLDM9$ scaled differently compared to S_a by a factor ranging from 10 to 35. The observed trends mirrored the trend observed in the analysis of S_a.
Examination of the effect of classical spray variables such as pressure, flow rate or nozzle distance showed that $GLDM9$ behaved very similarly to S_a. Surface characterization indicated that pressure resulted in minimized S_a and S_{sk} if the pressure was between 3 kPa and 10 kPa. S_{al} behaved similarly but showed a distinct minimum at 7 kPa. The flow rate showed that the higher the flow rate, the higher S_a and $GLDM9$. However, no conclusive trend could be identified for the other surface properties studied. To fully understand the relationship, it is critical to consider the flow rate in relation to pressure and nozzle distance. When the pressure was too low and the flow rate too high, the CL structure exhibited irregularities, Section 7.1. The reason was most likely that the resulting inhomogeneous spray cone distributed the dispersion non-uniformly over the membrane surface. A higher flow rate can be employed depending on the nozzle height. On the other hand, if the nozzle distance is too small, using a high flow rate can result in swelling of the non-homogeneous CLs of the membrane. When comparing the microscopy images in Figure 7.8, no clear conclusion can be drawn. However, analysis using STPs or IFs revealed that the nozzle distance influenced the arithmetical mean height (S_a), which was minimized at the greater distance of 60 mm. The S_{al} and S_{sk} obtained a clear minimum at a nozzle distance of 20 mm. The study of the associated IFs led to the same conclusion for all the production data sets presented. The relationship between all production variables studied and their effect on surface texture was not purely linear. This explains the comparatively lower PCC, but also shows that $GLDM9$, $GLRLM5$ and $GLDM2$ describe the surface texture similarly to their counterparts, even if the correlation is not linear. The recorded data also showed no linear relationship between the surface properties and the production variables. This indicates a more complex interaction between the variables studied.

Nevertheless, the interpretation of the obtained IFs leads to a similar conclusion since they show a similar behavior to their counterparts.

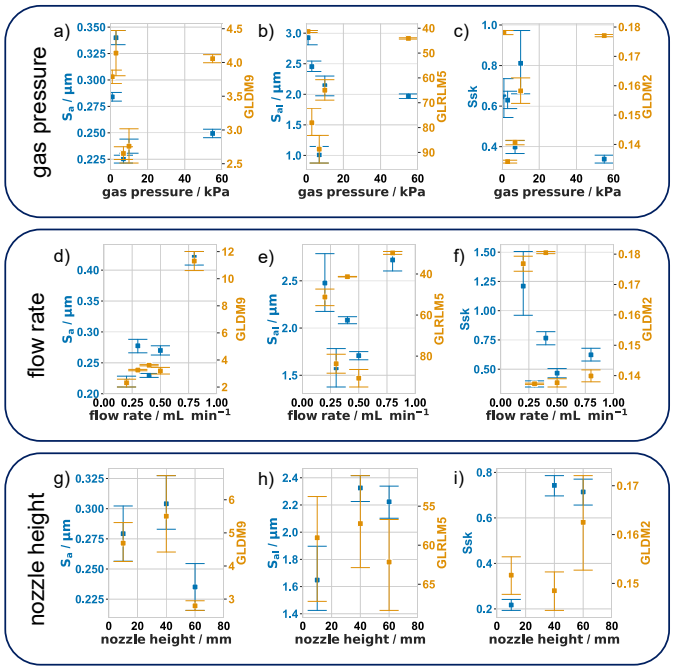

Figure 7.9. Impact of the production variables on the surface texture. The surface texture was evaluated by studying the surface texture parameter monitored by the CLSM characterization and the extracted image features of the obtained laser intensity images. The y-axis of $GLRLM5$ was inverted to facilitate the comparison to S_{al}. $GLDM9$: large dependence high gray level emphasis, $GLRLM5$: long run emphasis, $GLDM2$: dependence non-uniformity.

The alcohol content is one important property of the dispersion and is therefore crucial for the resulting CL structure. To determine whether IFs can capture the structural changes induced by varying alcohol content, the n-propanol concentration was systematically varied, and the results are presented in Figure 7.10. Adjusting the alcohol content had strong effects on the S_a and $GLDM9$. For both, S_a and $GLDM9$, the smallest value was observed at an alcohol content of 66% n-propanol.[‡] Reducing the n-propanol content of the dispersion well below the azeotropic point to 33% had a drastic effect on S_a, as the value increased from 0.26 µm to 0.46 µm, which were simultaneously the maxima of all the data sets studied. A maximum $GLRLM5$ value of 55.4 was observed at 66% n-propanol content, but the S_{al} did

not show much difference between 2.41 µm at 66% and 2.33 µm at 91% n-propanol content. S_{sk} reached its maximum of 0.71 at 66% n-propanol content, similar to $GLDM2$ which was

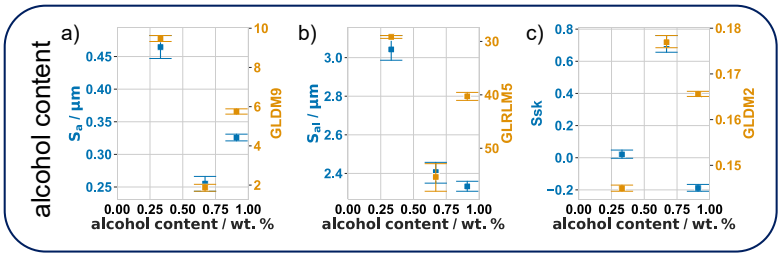

Figure 7.10. Impact of the alcohol content on the surface texture. The surface texture was evaluated by studying the surface texture parameter monitored by the CLSM characterization and the extracted image features of the obtained laser intensity images. The y-axis of $GLRLM5$ was inverted to facilitate the comparison to S_{al}. $GLDM9$: large dependence high gray level emphasis, $GLRLM5$: long run emphasis, $GLDM2$: dependence non-uniformity.

0.178. Interestingly, the skewness was comparatively high as the water/n-propanol was close to its azeotropic point at 67% n-propanol.

The reasons for this could be manifold, as the interaction between the dispersion, its processing and the resulting CL structure depends on various factors. It has been reported that for the dispersion system studied, higher n-propanol content resulted in stronger catalyst-ionomer interaction and better dispersed particles with fewer agglomerates.[42] Another study suggested that the ionomer-catalyst interaction prevents catalyst agglomeration in the dispersion.[41] This could explain why the variation in alcohol content lead to an alter CL texture. The lower the n-propanol content, the less stabilized the dispersion was. Therefore, larger agglomerates formed a rougher surface texture, indicated by higher S_a values or, inversely, by lower S_{sk} values of the CL at low n-propanol levels. High alcohol contents (91%) could lead to similar behavior, as dispersion stability is a critical and complex factor influencing the resulting CL structure.[‡]

The datasets related to the CL properties are shown in Figure 7.11. The Nafion content data set was non-linear and the PCC values for all IFs considered were below 0.50. Nevertheless, both S_a and $GLDM9$ showed that increasing Nafion content had no effect on surface roughness as long as the Nafion content was larger than 10 wt.%. One possible reason could be the lower dispersion stability, because the Nafion content affects the dispersion behavior.

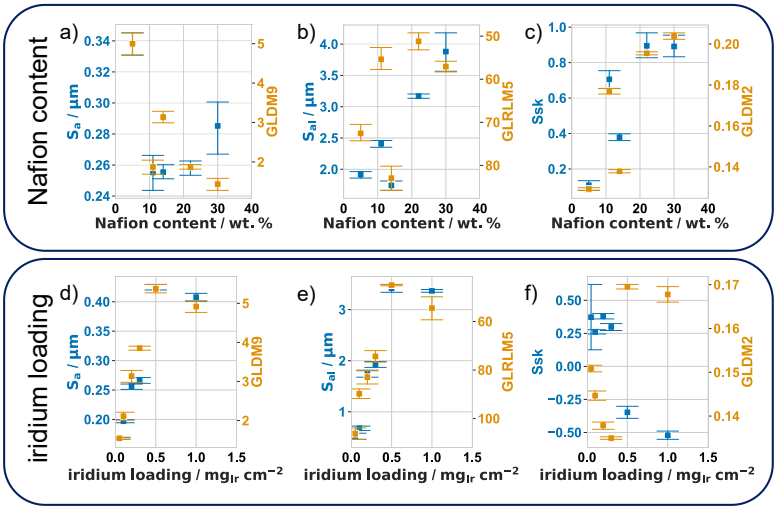

Figure 7.11. Analysis of the surface texture in dependency to basic CL properties as the Nafion content or iridium loading. The y-axis of $GLRLM5$ was inverted to facilitate the comparison to S_{al}. $GLDM9$: large dependence high gray level emphasis, $GLRLM5$: long run emphasis, $GLDM2$: dependence non-uniformity

Similar effects were observed for the alcohol content, where reduced alcohol levels led to the formation of larger agglomerates. S_{al} increased at high Nafion content, but the counterpart $GLRLM15$ behaved differently and did not show the same trend. S_{sk} and $GLDM2$ showed a similar trend, as both increased with increasing Nafion in the CL. This indicates that the surface becomes smoother as Nafion smears across it, reducing the sharpness of the emerging surface features. Sharpness may correspond to larger catalyst domains, as surface roughness (expressed by S_a) was higher for lower Nafion contents. This trend is also reflected in S_{sk}, which indicates a shift from a more symmetrical height distribution toward one where flat plateaus are more prevalent.

The "iridium loading" dataset possessed the highest PCC, i.e. the strongest correlation between the studied surface texture parameters and image features. S_a was the lowest for $0.1\,\mathrm{mg_{Ir}\,cm^{-2}}$ and increased along with the loading until $0.5\,\mathrm{mg_{Ir}\,cm^{-2}}$. Then a doubling of the loading had nearly no effect on S_a. This trend was also obtained for S_{al} and both IFs ($GLDM9$, $GLRLM6$). However, the relative impact of the roughness gets smaller as the thickness of the CL gets higher. This could indicate that a threshold was observed for loadings $> 0.5\,\mathrm{mg_{Ir}\,cm^{-2}}$, similar to the observations made by Rozain et al.[119] and Bernt et al.[24].‡

The autocorrelation length (S_{al}) and $GLRLM5$ obtained a PCC of -0.91, and the trend observed for this dataset represented this strong correlation. That emphasized the importance of underlying dataset structure while applying correlation studies.[‡]

This chapter analyzed the impact of production variables, such as alcohol content, pressure, flow rate, and nozzle distance, on surface texture parameters like arithmetical mean height (S_a) and image features like $GLDM9$. Adjusting the alcohol content significantly affected surface roughness, with lower n-propanol content leading to rougher textures due to larger agglomerates. Spray variables like pressure and flow rate also influenced S_a, revealing complex, non-linear interactions, with higher flow rates resulting in increased surface roughness. Variation in the Nafion content and iridium loading affected the surface roughness of the CL and showed that higher iridium loading resulted in rougher surfaces. It was found that IFs could serve as effective tools for analyzing CL structures, often matching the insights provided by traditional STPs.

Main takeaways of the production-structure discussion:

→ Classical spray variables such as pressure, flow rate and nozzle distance showed complex, non-linear relationships with surface properties. In particular, pressure between 3 kPa and 10 kPa resulted in minimized S_a and S_{sk}, while a nozzle distance between 20 mm and 40 mm leads to minimized S_a.

→ Flow rate also influenced surface roughness (S_a), with higher flow rates increasing S_a, but no consistent trend was observed for other STPs.

→ The smallest values for S_a and $GLDM9$ were observed at 66% n-propanol alcohol content, which had a strong effect on the surface roughness. S_a increased sharply when the n-propanol content was below or above the azeotropic point.

→ CL texture were also influenced by Nafion content and iridium loading. Nafion content had minimal effect on surface roughness below 10 wt.%. Variations in the iridium loading showed a strong impact which was monitored by STPs and IF.

→ The highest PCC values between STPs and IFs were observed for the iridium loading data set, with increasing S_a until a plateau $>0.5\,\mathrm{mg_{Ir}\,cm^{-2}}$ was reached.

→ The study confirmed that image features such as $GLDM9$, $GLRLM6$, and $GLRLM5$ are effective in analyzing the uniformity CLs and provide insights comparable to traditional STPs.

7.3.1 Analysis of the Produced Catalyst Layer Properties

In the following, the above discussion of production variables will be linked to the evolved microstructure of the CLs. The methods used to determine the thickness and to monitor the microstructure over the scale are presented in Sections 6.3.3 and 6.3.2. First, the effect of dispersion on the microstructure is discussed. Then the effects of Nafion content and iridium loading reduction on the CL microstructure are highlighted. The correlation analysis in Chapter 7.2 and the application examples in Section 7.3 demonstrate the versatility of IFs. Those initially omitted due to dimensionality reduction have also shown promising applicability after reviewing them. Despite this potential, covering all five matrices in detail is beyond the scope of this work, primarily due to the underlying mathematical complexity. Additionally, the computational robustness of the selected IFs must be taken into account. Studies by Ericsson-Szecsenyi et al.[182] and Michalet et al.[183] highlight that several features derived from the gray-level run length matrix (GLRLM), including short run emphasis, long run emphasis, run percentage, and run length non-uniformity consistently exhibit high robustness across different imaging conditions. This matrix represents the lengths of consecutive pixels that share the same intensity in specific directions within an image, see Section 4.2. Furthermore, the IFs computed from the GLRLM are relatively intuitive to interpret compared to those derived from other texture matrices, making them especially practical for applications involving structural assessment. Although the computed IFs reflect height variations similar as traditional STPs, IFs can be applied to SEM images to capture and represent surface height characteristics at various magnifications scales. Consideration of the multi-scale nature of the CL is extremely important. Several phenomena affected by the CL occur only at defined length scales (see Section 3.2 and Figure 3.3), highlighting the need for scale-aware structural analysis. A detailed description of this approach can be found in section 4.2, in the *PyRadiomics* documentation[175] and in the literature.[169,257].

7.3.1.1 Impact of the Alcohol Content on the Microstructure

Variation of the alcohol content, i.e. (n-propanol content) showed a V-shaped effect on S_a with a minimum at 67 wt.%. S_{al} also decreased from 33 wt.% to 67 wt.%, but only a minimal decrease from 67 wt.% to 91 wt.% was observed. Finally, S_{sk} showed a inverse behavior as S_a, with a maximum at 67 wt.%, as seen in Section 7.3 and Figure 7.10.
Figure 7.12a-c shows the quantified microstructure. Instead of the magnification, the window area is presented, which is the observed geometric surface area of the CL at the chosen

magnification. The lowest magnification of 500x corresponds to a surface area of $1.4 \cdot 10^5\,\mu m^2$, while the highest magnification of 70,000x represents a surface area of $7.4\,\mu m^2$. The run percentage is shown in figure 7.12a on the y-axis and represents a global aspect of the CL as it measures the coarseness of the texture. Higher values for the run percentage indicate a larger proportion of short runs and therefore a finer texture.[175,257] In Figure 7.12 a general trend can be observed. All CLs start with a maximum run percentage at the largest window area between 0.7 and 0.8. Its values can range between $\frac{1}{N_p} \leq x \leq 1$, where N_p is the number of pixels within the region of interest, in this case $N_p = 715077$. This implies that the obtained maximum of 0.8 is a relatively high value for the run percentage. Then a steep drop in the run percentage occurred for a window area of $3.5 \cdot 10^4\,\mu m^2$. Surprisingly, this was observed for all CLs within this work. This can maybe attributed to an interplay between image resolution and inherent surface texture, or possibly to artifacts introduced by the calculation approach. The value relaxed again to values between 0.7 and 0.8 for all CLs accessing the next larger window area of $9.2 \cdot 10^3\,\mu m^2$. Subsequently, the run percentage decreased steadily as the window area decreased. This means that the texture appears finer at lower magnifications but becomes more coarse at higher magnifications due to the increased visibility of the catalyst–pore network. Comparison of the effect of different alcohol contents showed that the 67 wt.% dispersion had

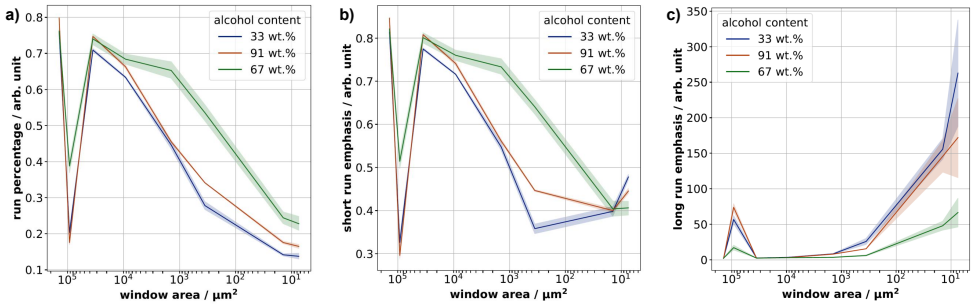

Figure 7.12. Relationship between the microstructure of the CL and the alcohol content of the dispersion. All parameters were calculated by GLRLM, including (a) run percentage, (b) short run emphasis, (c) long run emphasis. The magnification scale was replaced by the calculated window area of the taken SEM image.

the highest run percentage over the entire scale. This indicates that the surface of this CL is coarser than the other ratios. There was not much difference observed between an alcohol content of 33 wt.% and 91 wt.%. Such a non-linear trend between the three dispersions was also observed by the skewness shown in Figure 7.10, which also reached a maximum for an alcohol content of 67 wt.%. Figure 7.12b shows the short run emphasis as a measure of the

distribution of short run lengths. Small values indicate a coarser texture, while higher values indicate a finer texture. It behaves similarly to the run percentage, but describes the more locally occurring short run lengths. The only notable difference between the run percentage and short run emphasis is that at a window area of 14.1 μm^2 the short run emphasis was the same for all CLs. This may be explained by the fact that short run emphasis places greater weight on shorter run lengths. This makes it potentially more sensitive to the smallest features in an image, such as nanoparticles. Since the catalyst material remained constant throughout the experiments, the texture of very small window areas primarily reflects the intrinsic properties of the materials used. In contrast, run percentage considers all run lengths, capturing broader aspects, such as material distribution and larger-scale structural patterns. The counterpart of the short run emphasis is the long run emphasis which is more sensitive to longer run lengths, Figure 7.12c. Increasing values indicate a coarser structure. Consequently, instead of a dip at $3.5 \cdot 10^4\,\mu m^2$, a peak occurred. Interestingly, there were only small to negligible long run lengths values up to 10 μm^2, indicating finer texture and the absence of larger pores. However, from a window area of 92.3 μm^2, the CL structure becomes coarser for all samples examined. This implies that at this window area the CL structure changed from a layer system to a catalyst-pore network. However, the slope of this increase is different for the dispersion studied and could indicate an interesting electrode engineering window. In the future, this window could be used to monitor the design of the CL in an iterative optimization using IFs as feedback tool.

Linking production variables to microstructure:

- → Impact of the alcohol content:
  - ⇀ Variation of the n-propanol content showed a V-shaped effect on S_a.
  - ⇀ S_{al} increased below 67 wt.% but remained similar at 67 wt.% and 91 wt.%.
  - ⇀ S_{sk} showed similar behavior between alcohol contents of 33 wt.% and 91 wt.%.
- → SEM Image Analysis:
  - ⇀ The run percentage, which measures texture coarseness, was observed to decrease steeply for a window area of $3.5 \cdot 10^4\,\mu m^2$ for all CLs.
  - ⇀ Higher run percentages indicate a finer texture, and the maximum run percentage was observed for the CL with 67 wt.% alcohol content
  - ⇀ The short run emphasis (Figure 7.12b) and long run emphasis (Figure 7.12c) further clarified the local surface features, with peaks and dips indicating changes in the structural texture at different magnifications.

7.3.2 The Nafion Matrix and Its Influence

The Nafion content is an essential property of the CL that is chosen with the dispersion made. As mentioned in Section 3.2, the Nafion backbone has a larger volume fraction than the iridium catalyst. Therefore, it is expected that the CL structure will also depend on the chosen Nafion content. The application of the IFs and their comparison with the previously discussed data serve to verify whether the gathered results are internally consistent and well-aligned across the different analyses presented. Furthermore, the application of IFs will contribute to a deeper understanding of their behavior when used as structural descriptors.

7.3.2.1 Relationship between Nafion Content and Microstructure

In Figure 7.13 the microstructure of the CL is again analyzed by SEM. Since the run percentage showed the same tendency as the short run length (Figure 7.13b), it was replaced by the run entropy shown in Figure 7.13a. The run entropy describes the uncertainty or randomness of the gray levels and run lengths distributed within an image. Higher values indicate an increased heterogeneity in the texture.[175,257] Again, the aforementioned peak/dip occurred in the same window region within this dataset. The texture heterogeneity (run entropy) steadily increased from a value of about 4.75 at $9.2 \cdot 10^3\,\mu m^2$ to $>$ 6 at $14.1\,\mu m^2$ for all CLs. Distinguishing

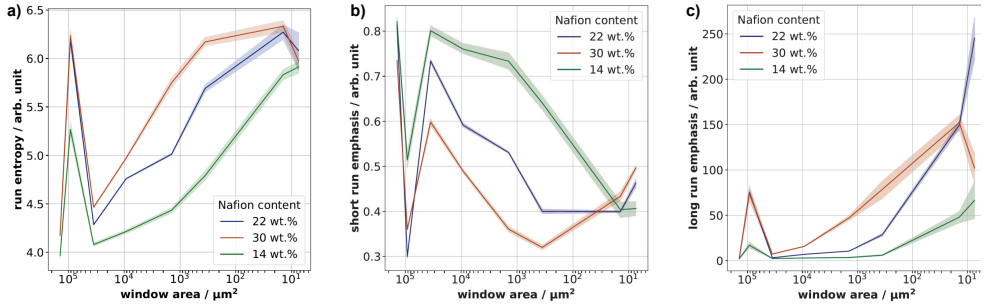

Figure 7.13. Relationship between the microstructure of the CL and the alcohol content of the dispersion. All parameters were calculated by GLRLM, including (a) run entropy, (b) short run emphasis, (c) long run emphasis. The magnification scale was replaced by the calculated window area of the taken SEM image.

between the Nafion content and the quantified texture shows that the higher the Nafion content, the higher the run entropy, indicating the most heterogeneous texture for a Nafion content of 30 wt.%. This behavior was also observed through S_{al} (Figure 7.11b), which

reflects the lateral periodicity of surface features. This is conceptually similar to run entropy, which measures the complexity and distribution of run lengths across an image.

This clear trend occurred in the range of a window area from $1.41 \cdot 10^3\,\mu m^2$ to $92.3\,\mu m^2$. The short run emphasis behaved inversely as expected. While the long run emphasis also showed a similar behavior as described in the discussion of the alcohol content. The onset of the increase of the long run emphasis and its behavior were slightly different from the studied alcohol contents. This implies that the increase in long run emphasis depends on the intrinsic nature of the CL, rather than being driven by a single influencing factor. However, no clear trend was observed for the Nafion content for a window area $< 353\,\mu m^2$. When investigating the Nafion content, it must be taken into account that the electron beam can cause a strong alteration of the polymer. This could explain the relatively high standard deviation seen in Figure 7.13c.

Cross-sectional analysis was used to determine the thickness of the different CLs, Figure 7.14. The different colored histograms refer to a certain Nafion content, which is written on the left side of the Figure 7.14. The dashed line represents the average thickness of the CLs,

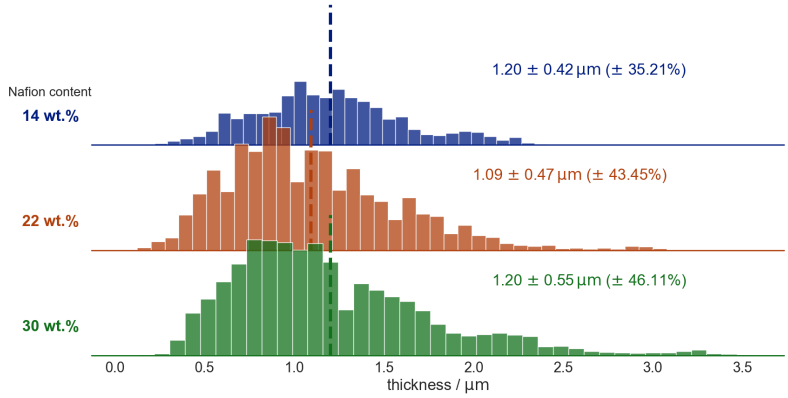

Figure 7.14. Cross-sectional analysis of the CL thickness for different Nafion contents. The dashed line shows the average thickness, the y-axis is the number of counts.

while each colored annotation refers to the Nafion content or the color used. The annotation shows the average thickness with its standard deviation. The relative standard deviation is shown in brackets. The average thickness was quite close for all CLs. However, analysis of

the relative standard deviation showed that the relative standard deviation increased as the Nafion content increased, reaching a maximum of 46% for a Nafion content of 30 wt.%. This indicates that the higher Nafion content resulted in a broader thickness distribution and thus greater heterogeneity.

In total, the analysis of the cross-sections showed a similar trend as the run entropy (Figure 7.13a) in the window area range from $1.41 \cdot 10^3\,\mu m^2$ to $92.3\,\mu m^2$. Interestingly, the 20 images for the cross-sectional analysis were taken at two magnifications. Ten images were recorded at a magnification corresponding to $1.41 \cdot 10^3\,\mu m^2$ and the other images were taken at a magnification corresponding to $353\,\mu m^2$. This indicates that the obtained data is internally consistent and aligns well across the different analyses presented.

Nafion and its impact on the microstructure:

→ Run entropy (Figure 7.13a) increased with Nafion content, peaking at 30 wt.%, indicating higher texture heterogeneity.

→ Short term and long run emphasis showed similar trends to the dispersion analysis.

→ Cross-sectional analysis (Figure 7.14) showed that higher Nafion content resulted in increased thickness variation, peaking at 46% relative standard deviation at 30 wt.%.

7.3.2.2 Alteration of the Nafion Structure and Critical Discussion of the Image Type

While varying the material composition is a straightforward method to modify the CL texture, IFs must also be capable of capturing the resulting structural changes. SEM imaging provides both InLens and AsB images, with the latter representing contrast based on the atomic number (Z) of the elements. Significant contrast differences between Nafion and iridium are expected, which could alter the image structure. These differences should also be reflected in the IFs. Therefore, this section examines how different SEM imaging modes influence the extracted features. This experiment is used to critically discuss the influence of the image type and general image properties on the microstructure evaluation. The image type influences how the gray-level neighborhood is constructed, which may, in turn, alter the resulting IF. Additionally, further IFs computed from the GLRLM are introduced. The run percentage is a global image property and the long run emphasis as an intermediate between global and local properties. The run percentage describes the entire image. Instead, long run emphasis describes an image property, the occurrence of long run lengths within an image. By this logic,

local properties are image features that describe a fragment of the image, such as the long run high gray level emphasis (GLRLM6) or the long run low gray level emphasis (GLRLM7). Both are measures of the distribution of long run lengths, but focus on either long run lengths with high or low pixel values. Other parameters focus on the short run lengths and can be found in the literature.[257]

A Nafion content of 11 wt.% was used in CL deposited on the N117 membrane. The sample was sandwiched between two metal plates and two PTFE sheets and heated for 16 minutes at 150°C in a hot press without compression. It is known that the heat treatment changes the Nafion structure inside the CL as the temperature is adjusted around the glass temperature (T_g). This increases the adhesion force between the CL and the membrane, while preventing delamination. Therefore, the induced change in the Nafion structure should cause changes in the microstructure of the CL. Two samples were subjected to the heat treatment and compared with five different untreated samples.

The analysis made was based on the calculation of inlens images, the typical image used from SEM analysis. The run percentage and the long run emphasis are shown in Figure AF.8. Similar to the previous discussion, both parameters start to differ for a window area $< 1.41 \cdot 10^3\,\mu\mathrm{m}^2$. For smaller window areas, the heat treatment showed larger values compared to the untreated sample, while the opposite was the case for the long run emphasis. In Figure 7.15 the long run high gray level emphasis and the long run low gray level emphasis is shown for AsB and inlens images. As can be observed, the scaling of both parameters was significantly affected by the image type. In addition, the difference between treated and untreated samples became larger in both cases. However, at the current state of research in describing the CL structure with IFs, a firm conclusion could be dangerous. At this stage, it is highly likely that IFs can accurately describe the CL structure and monitor various influencing factors. However, potential sources of error, particularly those related to image acquisition and processing, may still be undetected. Because CL images are the result of extensive processing, the acquisition history of these images must be carefully considered in such analyses. More materials need to be studied or some properties need to be modified in a defined way to gain deeper knowledge. Nevertheless, it is remarkable how small the deviation was for some parameters, even though they were measured five times at different locations across the scale. This could be due to the fact that each image contains 786,432 pixels. This large number of data points may contribute to statistical stability and robustness in the extracted IFs, effectively averaging out local variations and minimizing the influence of random noise. The trend remained the same for the calculation of both parameters from AsB images. In the case of the heat treatment, however, both types of images led to the same conclusion. Therefore, it can be concluded that

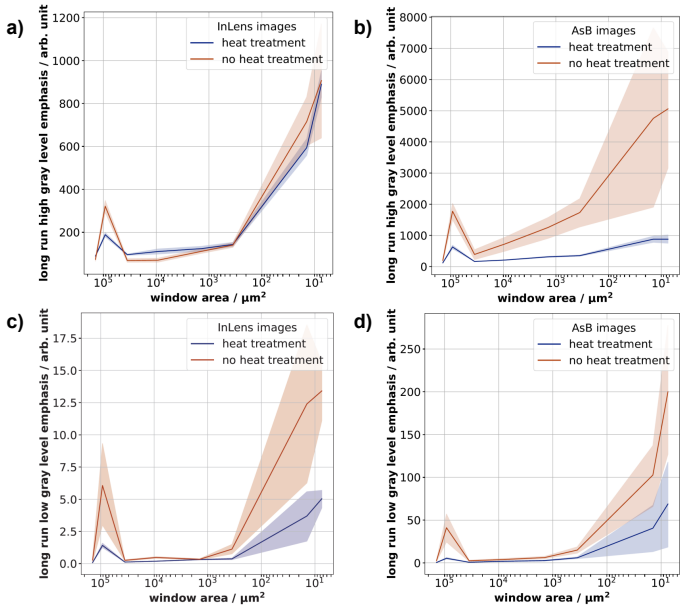

Figure 7.15. Analysis of microstructural changes induced by the heat treatment of the CL at 150°C. While in a and c the inlens images are used to calculate the long run high gray level emphasis and long run low gray level emphasis. In b and d the AsB images are used instead.

the surface of the CL becomes smoother and finer by the heat treatment. While the difference between differently manufactured samples can be clearly observed by the quantitative analysis which is required to detect these variations. It is always necessary to check whether it makes sense to use images from different sources and how the image is constructed. The chapter concludes with a discussion of iridium loading and its effect on the microstructure.

Effect of heat treatment on CL microstructure:

→ Run percentage & long run emphasis indicated a smoother surface post-treatment.

→ Image type influenced parameter scaling, but led to the same conclusion.

→ Local features such as long term high/low gray level emphasis showed reduced heterogeneity in the heat treated sample.

→ The heat treatment probably reorganized the Nafion ionomer and smoothed the CL.

→ Caution should be taken when using image features for structural analysis due to variability in image types and acquisition parameters.

7.3.3 Analysis of Reduced Iridium Loadings

This section addresses the impact of reduced iridium loading on the heterogeneity of the CL. This represents a current research question[24,258], investigated here using image processing techniques applied to cross-sectional images in combination with IFs. Thus IFs are employed as analytical tools to provide insight into an open scientific issue. The related discussion introduced in Section 7.3 is extended here by focusing on structural heterogeneity.

Using the run entropy (Figure 7.16a) to describe the heterogeneity of the CL showed that the microstructure of the 1.0 $\mathrm{mg_{Ir}\,cm^{-2}}$ and 0.5 $\mathrm{mg_{Ir}\,cm^{-2}}$ loadings behaved nearly identical over the scale. The heterogeneity was reduced for lower loadings at a window area of $9.2 \cdot 10^3\,\mu\mathrm{m}^2$ and in general for a loading of 0.2 $\mathrm{mg_{Ir}\,cm^{-2}}$ over the scale, while the lowest loading showed no clear behavior. The long run high gray level emphasis ($GLRLM6$) described for AsB and inlens images (Figure 7.16b, c) showed at a window area of $3.5 \cdot 10^4\,\mu\mathrm{m}^2$ an increasing value with decreasing loading. This indicates a pronounced change in the layer at this scale with loading reduction, which could be due to changes in thickness or the emergence of uncovered areas when the loading is reduced. Reduced loadings in the AsB image showed a strong difference in the small window area with the largest scatter for the lowest loading. These

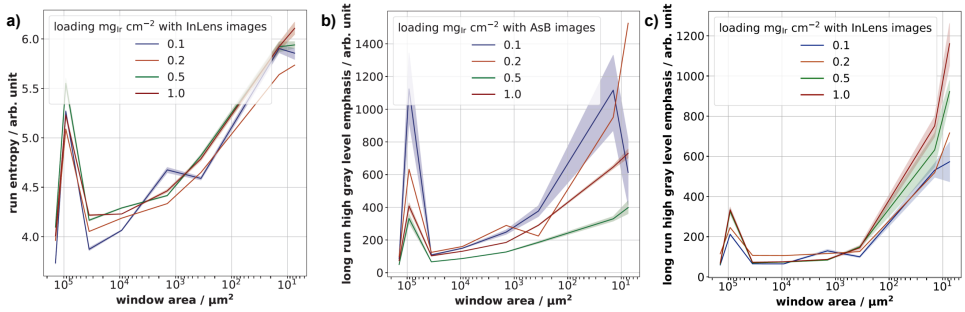

Figure 7.16. Discussion of the effect of the loading reduction on the CL microstructure.

results were correlated with the cross-sectional analysis in Figure 7.17 below. Reducing the iridium loading reduced the thickness of CL from 5.39 µm $\pm$ 0.88 µm at 1.0 $\mathrm{mg_{Ir}\,cm^{-2}}$ to 0.67 µm $\pm$ 0.33 µm at 0.1 $\mathrm{mg_{Ir}\,cm^{-2}}$. While the absolute standard deviation decreased with lower iridium loading, the relative standard deviation increased. This tendency may explain why the run entropy was comparably reduced for the lower loadings and why the heterogeneity was comparably reduced for the lower loadings. For the calculation of the run entropy, top view images were used where only the layer surface was visible. The absolute standard deviation

was higher for high loadings. By looking at the surface only, the height difference should lead to a greater contrast within the image, which affects the heterogeneity and therefore the run entropy. This behavior also occurred when examining the different loadings with the CLSM, Section 7.3. The aforementioned arithmetic mean height (S_a) and autocorrelation length (S_{al}) also showed increased values with higher loadings. Therefore, the image feature represents the same information and the run entropy could be used to describe the heterogeneity of the CL. This highlights that the correlation study revealed strong correlations and that the reviewed data remained consistent. It further demonstrates that IFs can generally be used reliably to describe the CL texture.

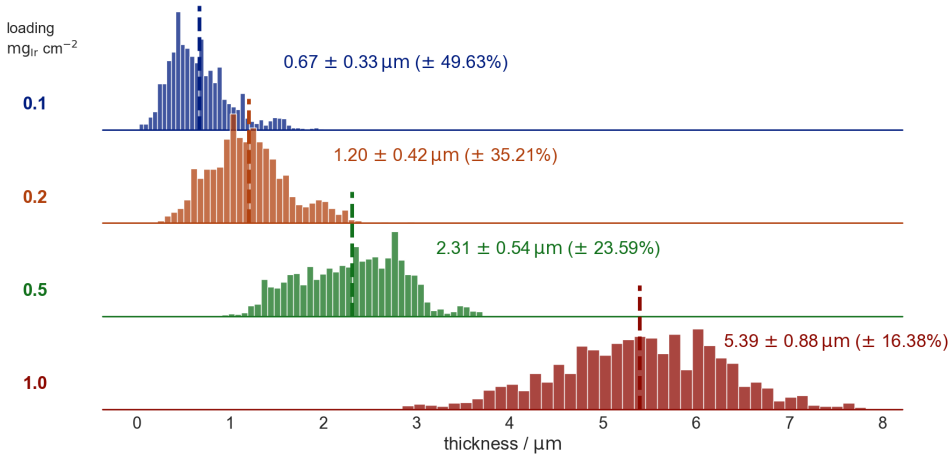

Figure 7.17. Cross-sectional analysis of the CL thickness for different iridium loadings. Dashed lines indicating the average thickness as well as the absolute and the relative standard deviation

Effect of iridium loading on CL heterogeneity:

→ At a window area of $3.5 \cdot 10^4\,\mu m^2$, long run high gray level emphasis increased with decreasing loading, indicating structural changes in the layer.

→ The run entropy, used to describe heterogeneity, correlated with physical texture parameters (S_a & S_{al}) and showed also increased values at higher loadings.

→ The analysis showed that image features effectively capture the CL texture, allowing accurate monitoring of structural changes over scales.

Chapter Summary. In this chapter, the influence of the spray variables on the macroscopic loading distribution was analyzed and improved by a parameter study, which lead to the creation of the standard electrode (MP1). In this context, the data obtained by the CLSM were used to study the correlation between statistical image features and physical surface texture parameters. The knowledge gained allowed to produce CL with uniform loading distribution and thus to study the effect of different production variables on the microstructure of the CL as a function of scale. Therefore it is postulated that the catalyst-pore network is visible for a window area $< 353\,\mu\mathrm{m}^2$. The peak at $3.5 \cdot 10^4\,\mu\mathrm{m}^2$ occurred for all samples studied and is perhaps a superposition between resolution and texture, or it could depend on the calculation. The peak also occurred for other matrices, such as the GLCM. Moreover, this work demonstrates that the IFs describe the CL texture appropriately. As a result, the structure of the CL has become accessible at multiple scales, enabling the monitoring and precise correlation of structural alterations induced by various production variables. This deeper understanding allows a more accurate assessment of how these factors influence the CL nature. By integrating imaging features at different length scales with well-defined testing protocols, the production process can be systematically optimized to achieve the desired microstructural properties, ensuring consistent and improved functionality of CLs in various applications. In addition, this approach enables a comprehensive characterization of the impact of electrochemical testing on the CL structure at different length scales.

8 Accessing the Missing Link between Electrode Structure and Performance

The insights gained in the previous chapter were applied to design several benchmark electrodes, as described in Section 6.1.1. Three of these electrodes were designed to exhibit a uniform loading distribution, while two were intended to have a non-uniform distribution. Additionally, one electrode was produced with a high flow rate, aiming for a fourfold reduction in production time, while maintaining a high degree of uniformity, to assess the potential for accelerating the manufacturing process. It was expected that the non-uniform electrodes would exhibit higher degradation rates during durability testing compared to the uniform electrodes. The main objective of this chapter is to explore the structure–property relationship at the edge of the production-structure-property triangle (PSPT) by applying IFs derived from the GLRLM. This is achieved by using a custom-designed probe to measure the sheet resistance of CLs with reduced iridium loading. Image processing is used to extract the CLs thickness which is then used to calculate the in-plane electrical resistivity. All methods employed in this analysis were developed as part of this thesis.
The effect of the material distribution was studied first, and then the influence of the cell assembly on the microstructure was analyzed for the standard electrode (MP1). This was extended by performance and durability tests in single cells for all five benchmark electrodes. The degradation was then correlated to the extracted IFs, highlighting further applicability of the presented method. At the end of the first section, the current limitations are discussed again by applying another correlation study between image features and extracted electrochemical data.

Finally, the method to study the sheet resistance and thus the PSPT is presented. The probe was first characterized and then validated before studying components typically used in PEMWE, such as GDL, PTL and CLs. The chapter concludes by relating the CL structure of reduced iridium loadings (discussed in 7.3.3) to the electrical properties accessed by the probe.

8.1 Characterization of Benchmark Electrodes

Characterization was performed by first applying using the layer digitization process described in chapter 6.1.2 and Figure 6.2. This method allowed us to measure the optical density, which was then used to visualize the CLs loading distribution. The resulting microstructure was then discussed together with the single-cell test results. However, if the CL exhibits a non-uniform loading distribution or macroscopic structural heterogeneity, it is expected that the analysis of its microstructure will likely be obscured because the CLs representative structure cannot be clearly interpreted.

8.1.1 Production - Low Iridium Loaded Benchmark Electrodes

Table 6.2 lists the parameters used to create the loading distribution shown in Figure 8.1. The five benchmark electrodes were divided into two groups. MP1 to MP3 refer to the group of macroscopically homogeneous samples. While MP4 and MP5 were classified as inhomogeneous CLs with different artifacts. MP5 had additional artifacts of small visible chunks of agglomerates in comparison to MP4.

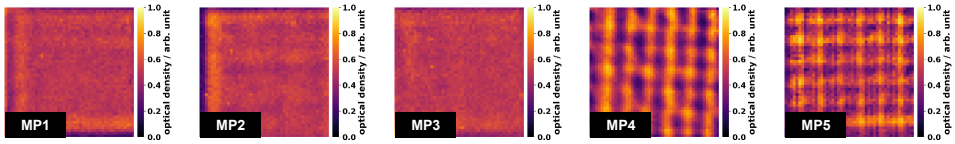

Figure 8.1. Fabrication of benchmark CLs with a loading of 0.2 $\mathrm{mg_{Ir}\,cm^{-2}}$ and an ultrasonic spray-device (top right). Classified into two groups, macroscopically homogeneous (MP1, MP2, MP3) and inhomogeneous (MP4, MP5) CLs.

Applying the developed analysis by CLSM revealed that the STP differed for the benchmark CLs. MP1 had the lowest values obtained for all STP ($S_a = 0.256 \pm 0.053\,\mu\mathrm{m}, S_{al} = 1.557 \pm 0.128\,\mu\mathrm{m}, S_{sk} = 0.245 \pm 0.318$), which implies that the previous work (section 7.2) led to the successful formation of a smoothed CL texture. MP2 ($S_a = 0.312 \pm 0.011\,\mu\mathrm{m}, S_{al} = 1.732 \pm 0.075\,\mu\mathrm{m}, S_{sk} = 0.415 \pm 0.070$) showed the second highest S_{sk}. Instead, MP3 ($S_a = 0.363 \pm 0.013\,\mu\mathrm{m}, S_{al} = 2.155 \pm 0.058\,\mu\mathrm{m}, S_{sk} = 0.861 \pm 0.124$) showed the highest S_a, S_{al} and S_{sk} among all measured samples. This demonstrates that different production variables can result in the same observable macrostructure while producing distinct microstructural characteristics. Conversely, this implies that CLs with a heterogeneous macrostructure may exhibit various

distinct microstructural characteristics. This is particularly important when using techniques with limited observation windows, such as CLSM, SEM, AFM, or TEM. Consequently, a large number of measurements is required to adequately capture the inherent variability and ensure that the sampled regions are representative of the specimen as a whole. Insufficient sampling increases the risk of misinterpretation because conclusions may be based on localized features that do not accurately reflect the full complexity of the CL. The macroscopic heterogeneous

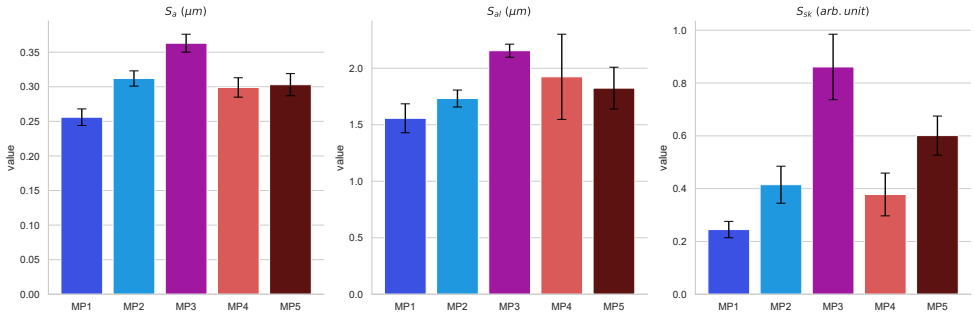

Figure 8.2. STP (S_a, S_{al}, and S_{sk}) for samples MP1–MP5 are shown with their respective standard deviations.

MP4 ($S_a = 0.299 \pm 0.014\,\mu\text{m}, S_{al} = 1.924\,\mu\text{m} \pm 0.377, S_{sk} = 0.378 \pm 0.081$) and MP5 ($S_a = 0.303 \pm 0.016\,\mu\text{m}, S_{al} = 1.824 \pm 0.185\,\mu\text{m}, S_{sk} = 0.601 \pm 0.074$) obtained similar values in all parameters except the S_{sk}, which was about 1.6 times higher in the case of MP5, indicating a comparatively stronger asymmetry in the height distribution. This fits well with the visualizations shown in Figure 8.1. In Figure 8.2, the STPs for the benchmark electrodes are shown and their values, including the standard deviations, are discussed in the following. The standard deviation of the S_a showed that most of the obtained values were close to each other. MP1 exhibited an S_a value that was in average $0.049 \pm 0.005\,\mu\text{m}$ lower than that of MP2 to MP4, and even $0.107\,\mu\text{m}$ lower compared to MP5. In contrast, MP2 to MP4 showed an average S_a of $0.058 \pm 0.005\,\mu\text{m}$ lower than MP5. However, it is unclear whether taking five measurements per electrode from three specimens of the same type adequately characterizes MP4 and MP5. This underscores the importance of first achieving a homogeneous macrostructure to ensure a reliable microstructural analysis.

The analysis of the image features again led to the same conclusion as the STPs, Figure 8.3. The least heterogeneous sample identified by the run entropy (Figure 8.3a) was MP1, which had the lowest values in a window area between $9234\,\mu\text{m}^2$ and $353\,\mu\text{m}^2$. It is difficult to examine a clear trend, but in a window area between $1412\,\mu\text{m}^2$ and $353\,\mu\text{m}^2$ the greatest

heterogeneity was obtained for MP4, which was expected by considering the heterogeneous loading distribution visible in Figure 8.1. However, it must be clarified that the probed window area represents only a tiny aspect of the CL. Even the largest window area of $1.41 \cdot 10^5\,\mu m^2$

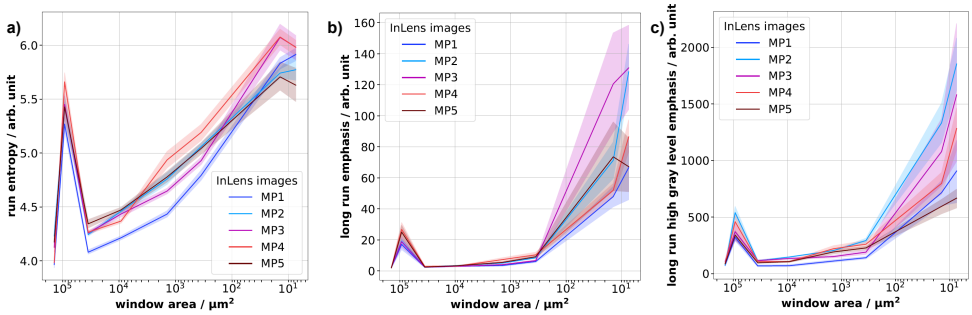

Figure 8.3. Analysis of the benchmark CLs across the scale by extracting image features from inlens images.

($0.0014\,cm^2$) represents only 0.01% of the CL surface. Therefore, this still limits the comprehensive analysis of the CL microstructure and the conclusions that can be drawn. For the other two parameters shown in Figure 8.3b & 8.3c this makes it impossible to show a clear trend. The production variables of the spray coater appear to have a less pronounced influence on the microstructure compared to the effects observed when varying the alcohol content (see Section 7.3.1.1). However, the analysis of the STPs revealed that MP1 had the smoothest microstructure, a finding that is also reflected by the corresponding IFs. In the small window region ($< 353\,\mu m^2$) of figure 8.3b MP3 showed the highest coarseness but also the highest standard deviation. This is consistent with the conclusion drawn from the analysis of the surface texture parameters.

8.1.2 Structure - Impact of the Cell Assembly on the Microstructure Across the Scale

The effect of the required cell assembly was studied to distinguish this irreversible deformation from the electrochemically modified CL texture. Thus, the CL related to MP1 was used to characterize the effect of the general conditions (80°C, $25\,\mathrm{mL\,min^{-1}}$) without the application of DC current. As expected, the cell assembly resulted in increased heterogeneity (run entropy) of the CL across the scale, Figure 8.4a.

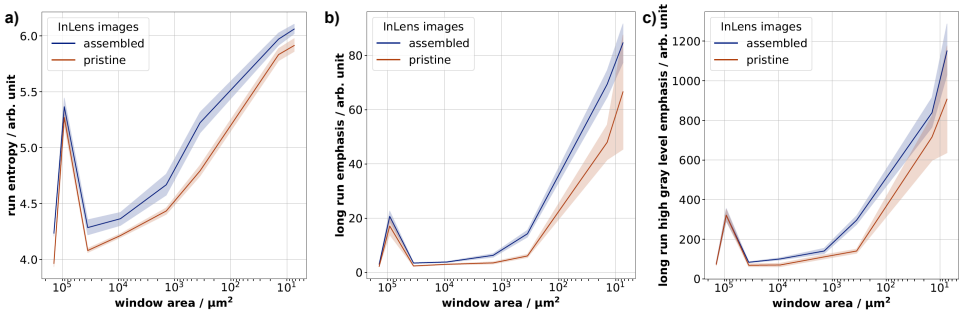

Figure 8.4. Characterization of the altered CL structure upon single-cell assembly.

The coarseness (long-run entropy, Figure 8.4b) increased as expected, with a stronger effect in the smaller window area ($1.41 \cdot 10^3\,\mu\mathrm{m}^2$) compared to the pristine CL, resulting in greater texture heterogeneity. The same was observed for the long run high gray level emphasis in Figure 8.4c. Thus, the cell assembly and operating conditions directly alter the CL structure.

Considering the run entropy, a IF decribing the global CL structure, reflects that the PTL imprint in the CL is visible at lower window areas. However, at higher window areas the PTL imprint is not recognizable anymore but the structure remains altered as visible by the run entropy. Depending on where on the CL the SEM image was taken, the window area will show the CL below the PTL fiber or the CL which intruded in the PTL. Besides this mechanical deformation, the impact of water flow and temperature on the CL structure becomes visible, influencing the structure as reflected in the run entropy. However, the PTL imprint is clearly visible for window areas $> 1.41 \cdot 10^3\,\mu\mathrm{m}^2$ but not recognizes by the local IFs long run emphasis or long run high gray level emphasis. This is highlighted in Figure 8.5 for the long run emphasis. The long-run emphasis is more sensitive to changes at higher magnifications, or smaller window areas, reflecting local variations in the CL structure. Especially, at window

areas $< 1.41 \cdot 10^3\,\mu m^2$ the advantage of the presented method becomes clear. For human perceptions its difficult to distinguish between the structures visible at this window area, but by analyzing the pixel values and their neighborhood through the presented method, it becomes possible to quantify and visualize the difference understandable for the human perception.

The region of the CL captured in the SEM image significantly influences the observed structure. The window area may capture either the CL beneath a PTL fiber or the CL that has intruded into the PTL pore. Figure 8.5 illustrates this limitation using long run emphasis as an example. The long run emphasis is notably more sensitive to structural changes at higher magnifications, or smaller window areas, where it captures local variations in the CL.

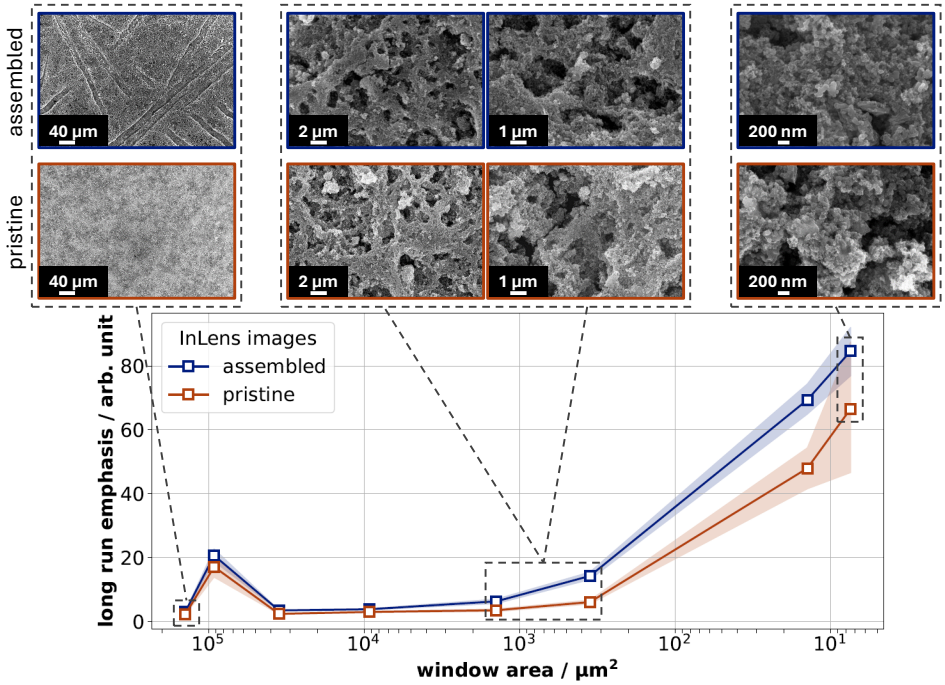

Figure 8.5. To illustrate the comparison between a visual inspection and a quantitative analysis of the CL structure, an example is presented. The quantitative analysis used long run emphasis as a IF to characterize structural changes resulting from single-cell assembly.

At window areas $< 1.41 \cdot 10^3\,\mu m^2$, the strength of the presented method is especially evident. Without quantitative image analysis, it is challenging for human perception to distinguish these subtle structural differences. The presented method transforms imperceptible variations into

quantifiable and interpretable data by evaluating pixel intensities and their spatial relationships. Conventional methods, such as visually interpreting SEM images, are limited and can lead to incorrect conclusions.

Effect of production and cell assembly:

→ MP1 (homogeneous) had the smoothest texture, while MP3 (highest S_a) had the roughest surface, which was consistent with the surface texture data.

→ Image analysis supported these findings, with MP1 being the least heterogeneous and MP4 showing the most heterogeneity in smaller window areas.

→ Cell assembly increased CL heterogeneity and coarseness.

8.1.3 Property - Performance and Durability

The produced benchmark CLs were characterized by single cell testing as described in section 6.4.1. Figure 8.6 shows the performance results extracted from the polarization curves. The current densities shown in Figure 8.6 were obtained at three cell voltages [a) 2.0 V, b) 1.7 V, c) 1.5 V]. The current densities at the beginning of the test (0h) were obtained from the 19^{th} polarization curve. The current densities at 250 h and 500 h were obtained from the fifth polarization curve recorded after applying 2V for 250 h. The recorded polarization curves are shown in the Figure AF.9 for MP1, MP2, MP3 and in the Figure AF.10 for MP4, MP5.

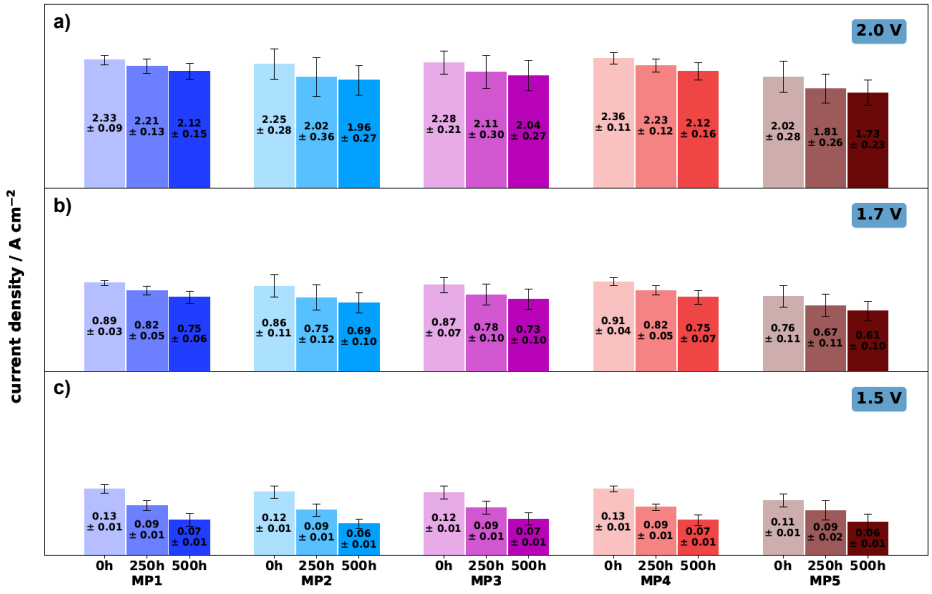

Figure 8.6. Assessment of the performance during the different stages (0 h, 250 h, 500 h) of durability testing for the benchmark electrodes.

It is apparent that the durability test affected all samples. The current density obtained at 1.5 V was initially similar for all samples and showed the same trend during the test. The differences across all benchmark electrodes were only in the range of the deviation between the measured samples. The performance loss was about 50% at a potential of 1.5 V, indicating a strong alteration of the CL kinetics. At 1.7 V MP1 to MP4 still behaved similarly. Only MP5 obtained a slightly lower initial performance of $0.76 \pm 0.11\,\mathrm{A\,cm^{-2}}$ compared to the other

benchmark electrodes. MP1 and surprisingly MP4 showed the lowest standard deviation at $1.7\,\mathrm{V}$, which was at $0\,\mathrm{h} > 50$ % lower than MP2, MP3 and MP5. However, it increased slightly after $250\,\mathrm{h}$ and $500\,\mathrm{h}$. While MP1 and MP2 showed a similar performance loss at $1.7\,\mathrm{V}$, the strongest performance decrease was observed for MP5. The same trend was observed at a cell voltage of $2.0\,\mathrm{V}$. MP5 and MP2 had the highest deviation and lowest current densities among the samples. The operation of $500\,\mathrm{h}$ at $2.0\,\mathrm{V}$ resulted in a current density loss of 9% for MP1, 10% for MP4, 11% for MP3, 13% for MP4 and 14% for MP5. This leads to the conclusion that the additional artifacts of MP5 might have caused a comparatively large performance loss, since MP4 also had an inhomogeneous loading distribution without additional material chunks.

This underscores the need for quality control in the production of CLs, especially in the case of long-term operation, as the difference increased over time. The difference at the beginning of the test was 14% between MP1 and MP5, while it was 23% at the end of the test. Therefore, it is expected that the deviation will continue to increase with longer tests. On the other hand, all low loaded CLs obtained a similarly strong performance loss in the kinetic range. This observation indicated a strong change in the CL structure, resulting in an altered interface between PTL and CL. From the cross-sectional analysis, a iridium band formation below the CL inside the membrane could be seen, Figure AF.13. This is an indication for a strong alteration of the CL structure and potentially are linked to the strong change in the kinetic region.

Therefore, the analysis was extended with EIS to get a deeper insight into the performance losses. The high frequency resistance (R_{HFR}) and the charge transfer resistance (R_{ct}) were extracted from the recorded EIS data. The Nyquist plots recorded at $1.45\,\mathrm{V}$ are shown in Figure 8.7 for MP1, MP3 and MP5. MP2 and MP4 can be found in Figure AF.14 and AF.15, respectively. For MP1, the smallest standard deviation was observed at all stages ($0\,\mathrm{h}$, $250\,\mathrm{h}$, and $500\,\mathrm{h}$) in both the real and imaginary parts of the impedance. R_{HFR} increased only slightly, especially compared to the more pronounced increase in R_{ct}, as reflected by the enlarged diameter of the semicircle. This behavior was also observed for all other benchmark electrodes. A comparison of all Nyquist plots revealed that MP1 exhibited the lowest standard deviation across all frequencies. This behavior becomes particularly pronounced after $250\,\mathrm{h}$ and $500\,\mathrm{h}$ of durability testing, highlighting that the initial homogeneity of a electrode reduces data scattering during extended tests. Figure 8.8a shows the R_{HFR} for all measured samples. Initially, MP1 and MP2 had almost identical R_{HFR} with a slightly higher deviation occurring in the case of MP1 at the beginning of the test. However, MP1 had the lowest R_{HFR} and

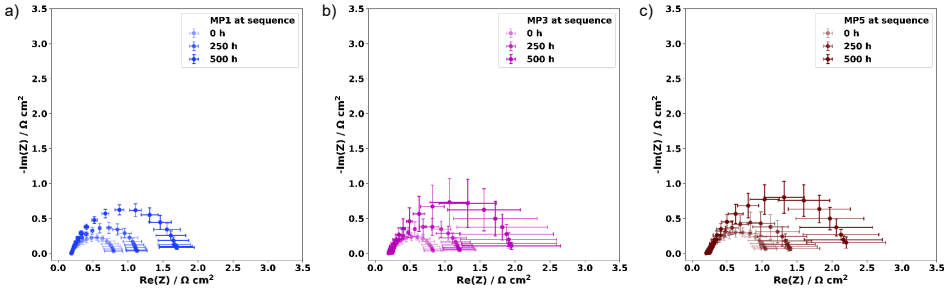

Figure 8.7. Nyquist plot recorded at 1.45 V during the durability testing for MP1, MP3 and MP5.

standard deviation after the 500 h durability test. The largest deviation was obtained by MP3 at each period of the measurement. While MP5 showed the strongest increase (20%) and largest R_{HFR} overall. This correlates well with the observation presented in Figure 8.6. The change in R_{ct} correlates with the shift in the kinetic region of the polarization curves, Figure AF.9 & AF.10. It also reflects the data presented for 1.5 V in Figure 8.6a. The R_{ct}

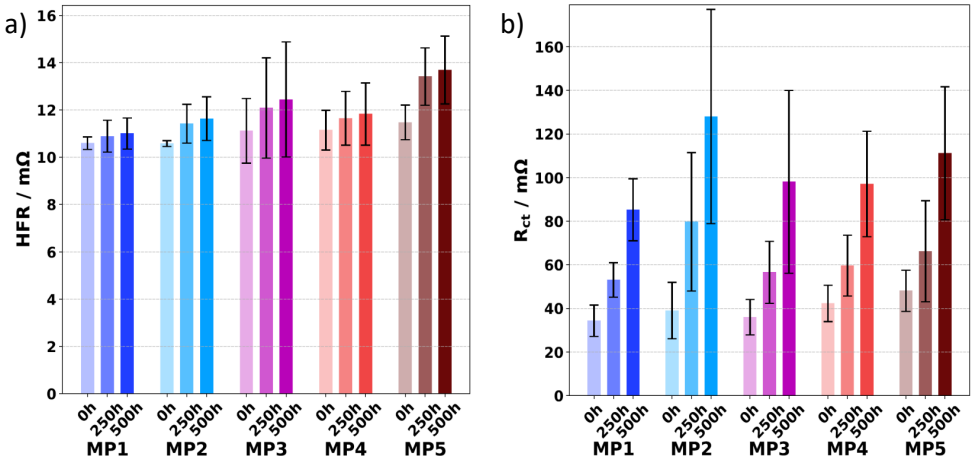

Figure 8.8. Extracted (a) high frequency resistance (R_{HFR}) and (b) charge transfer resistance R_{ct} measured at different periods of the durability test.

increased 2.5 times for MP1, again with the lowest standard deviation in all periods. MP2 had the largest R_{ct} increase of 3.3 and the largest absolute standard deviation. MP4 had the lowest R_{ct} increase with a factor of 2.3, followed by MP5 with 2.4. Overall, the data obtained

for EIS fit the data obtained from the polarization curves well. The increased R_{ct} indicated a decreased CL utilization due to an altered interface between PTL and CL.

The missing link between CL structure and performance is addressed below by re-applying SEM image analysis. The figures related to the run percentage can be found in the Appendix for MP1, MP2, MP3 and MP4, MP5 in Figure AF.11 and Figure AF.12, respectively. The pristine MP1, MP2 and MP3 (Figure AF.11) obtained a similar run percentage at the smallest window area. MP4 only showed a different run percentage at the largest window area and between $9.23 \cdot 10^3\,\mu\mathrm{m}^2$ and $353\,\mu\mathrm{m}^2$. While MP5 was the only layer that showed a comparatively lower run percentage over the entire scale. This indicates that the catalyst texture became coarser during the durability test for all samples. The long run emphasis reflected the same. Notably, MP1 (Figure 8.9a & AF.11a) and MP5 (Figure 8.10a & AF.12b)) showed an offset across the scale. Comparing the results for MP1 with the results in the previous section (Figure 8.4b)

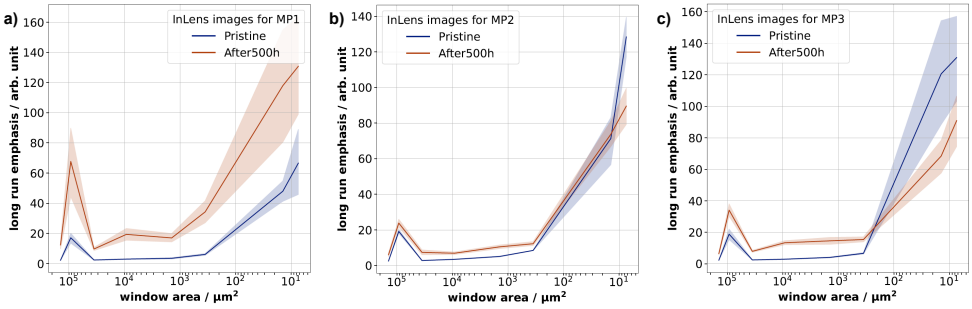

Figure 8.9. Analysis of the structural changes for MP1, MP2, and MP3 during durability testing using the long run emphasis.

regarding the cell assembly showed that the durability test significantly changed the CL texture. The cell assembly test showed that the CL texture started to differ for window areas smaller than $1412\,\mu\mathrm{m}^2$, after the durability test the CL texture differed everywhere from the pristine MP1. Thus, the image feature can be used to monitor the change of the CL texture in relation to its electrochemical nature. However, this was not so noticeable for all other benchmark catalysts. MP2 (Figure 8.9b & AF.11b) differed only slightly from its original sample in the range above $353\,\mu\mathrm{m}^2$ after testing. While MP3 showed a decrease in its coarseness for small window areas, it showed increased coarseness for window areas $> 353\,\mu\mathrm{m}^2$.

Instead, MP4 (Figure 8.10a & AF.11a) showed increased coarseness for a window area range between $9.23 \cdot 10^3\,\mu\mathrm{m}^2$ & $353\,\mu\mathrm{m}^2$, while MP5 (Figure 8.10b & AF.11b) showed a com-

plete offset across the scale. In general, a clear effect of electrochemistry is observed in the texture of the CL. However, to distinguish between specific electrochemical processes and the structural changes they cause would be speculation at this point. Considering all five

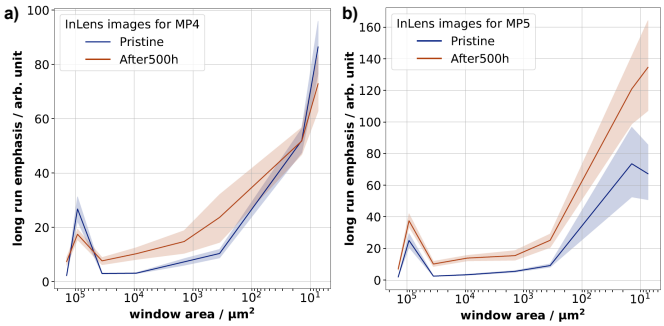

Figure 8.10. Analysis of the structural changes for the more heterogeneous MP4 and MP5 during durability testing using the long run emphasis.

benchmark electrodes (MP1 to MP5) and their structure descriptors (IFs), it is clear that the alteration of the CL structure depends on its original texture. In general, a coarser texture was observed after 500 h for all the benchmark electrodes. However, the results presented in Chapter 8.1.1 showed that the production variables already lead to distinct characteristics on the macroscopic scale. In particular, the more heterogeneous samples (MP4 & MP5) could lead to a false conclusion because their local properties at the microscale are intertwined with their macroscopic properties. Thus, the effort to create a macroscopically homogeneous CL is a crucial undertaking and necessary before studying the microscale effects. This may be the reason why the increased coarseness of the texture was the most apparent across the entire scale for MP1. On the other hand, the results presented in Chapter 8.1.2 showed that the cell assembly tendency primarily affected regions smaller than $1.41 \cdot 10^3\,\mu\mathrm{m}^2$. However, the electrochemical test affected the CL texture throughout the entire scale. Electrochemical reactions and phenomena occur at the nanoscale, but alter the texture at the microscopic scale. The presented method and the obtained results show that this can be confirmed. Most likely, the changes at high window areas ($> 9.23 \cdot 10^3\,\mu\mathrm{m}^2$), i.e. at the macroscopic scale, are not due to electrochemistry alone. Taie et al.[23] (discussed in Chapter 3.3) suggest, that gas transport through the CL could be one reason for the degradation at low loadings. The mass transport of oxygen could further result in the observed changes in the CL texture at the macroscopic scale. This could be due to the formation and detachment of gas bubbles, which may displace CL material and lead to increased coarseness, especially at high gas fluxes (i.e.,

high current densities). This also demonstrates that the presented IF were sensitive enough to detect alterations caused by durability tests across the entire scale. This level of detection is not possible with other methods that focus solely on specific window areas, such as classical SEM, AFM, or TEM. However, the presented methods can link results from macroscopic analyses, such as those from optical microscopy, CLSM, white light interferometry, and optical density measurements, with analyses conducted at the microscopic or nanoscale. These microscopic and nanoscale analyses include SEM for texture and elemental mapping via energy dispersive X-ray spectroscopy (EDX), AFM for stiffness and local conductivity, and TEM for particle shape and size. This is possible because the presented method uses IF, which correlates well with surface texture, particularly physical parameters such as height and roughness. Therefore, it is possible to correlate analyses obtained by other methods at different scales with the local domains and topography visible within the area of interest in the window. Thus, it is possible to access the missing link between CL structure and electrochemical properties by the method demonstrated, but their causal relationship is beyond the scope of this research. In summary, the presented IF-based method enables the detection of CL texture deterioration, such as coarsening and roughening, which is likely associated with reduced electrochemical performance.

Benchmark CL performance and durability:

→ Single cell testing showed that the benchmark CL behaved differently depending on the structure produced.

⇀ Structural artifacts in MP5 contributed to its performance loss, as supported by Nyquist plots and R_{HFR} values (Figure 8.8), which showed a 20% increase for MP5. In contrast, MP1 maintained the lowest R_{HFR} after 500 h, emphasizing the importance of CL quality control.

⇀ Changes in R_{ct} reflected degradation in kinetics most probably due to an altered interface between PTL and CL: MP1 had the lowest increase (2.5x), whereas MP2 showed the highest (3.3x), followed by MP5 (2.4x) and MP4 (2.3x).

⇀ The results showed that the most homogeneous (macroscale) and smoothest (microscale) electrode (MP1) exhibited the highest stability, highlighting the importance of improving electrode homogeneity prior to durability tests.

→ SEM image analysis (Figures AF.11 and AF.12) revealed significant changes in catalyst texture post-test.

⇀ The CL texture coarsened across the entire scale for all electrodes after the durability test

⇀ Electrochemical effects were observed to influence the CL texture at both the macroscale and microscale.

⇀ The IF-based method proves to be a powerful tool for detecting CL texture degradation, such as coarsening and roughening, which strongly correlates with a measurable reduction in electrochemical performance.

8.1.4 Correlation Study and the Current Limitation of the Approach

A first step in the direction of creating a link between IF and electrochemical properties is to perform correlation studies again. The use of Pearson correlation coefficient (PCC) provides a simple approach to the relationship between image feature (IF) and electrochemical properties. Several other parameters are extracted from the data as described in Section 6.4.1. As discussed in Section 7.2, the strength of the correlation depends strongly on the data set and its construction, i.e. the Pearson correlation implies that the relationship must be linear. However, it is unlikely that the relationship between electrochemistry and CL texture is linear. Nevertheless, with the lack of a suitable model, the Pearson correlation is used to evaluate if there is a possibility of a linear correlation between IFs and electrochemical properties.
The data presented thus far suggest a relationship between the parameters. However, macroscopic heterogeneity obscures definitive interpretation when it comes to more heterogeneous CLs (MP4, MP5). Therefore, the data obtained were pooled (see Table 6.3) according to their macroscopic heterogeneity into different subsets. This data stratification improves the reliability of the correlation study by reducing variability within the datasets. This enables more precise identification of underlying trends and relationships. Classifying by macroscopic heterogeneity improves the robustness of correlation studies by minimizing intra-group variability. Meanwhile, including heterogeneous samples, such as MP4 and MP5, ensures the analysis remains applicable to real-world conditions where a complete uniformity is rarely achieved. Figure 8.11 shows several correlations between structure and electrochemical property. The Pearson correlation coefficient is plotted on the y-axis, while the window area is plotted on the x-axis. The green line always refers to the full data set, while the subsets are filtered from this dataset. For example, subset eight refers to MP5 during the durability test. It contains the structural information (IFs) from the images of the pristine and post-mortem analysis, while being pooled with the electrochemical properties recorded during the durability test. Other subsets are, for example, the first (MP1, MP2, MP3), or second (MP4, MP5) benchmark electrode class, or more simply each benchmark electrode by itself. The areal R_{HFR} was correlated with the run percentage in Figure 8.11a, because the R_{HFR} showed a strong alteration during the durability test. Interestingly, not only in this particular correlation, but in all correlations shown in Figure 8.11, the window area of $3.5 \cdot 10^4\,\mu\mathrm{m}^2$ showed a strong decrease in correlation strength. This could mean that the discussed peak/decline at $3.5 \cdot 10^4\,\mu\mathrm{m}^2$ could be a technical artifact. Most of the relationships presented show either higher correlation at larger window areas or a more constant correlation strength.

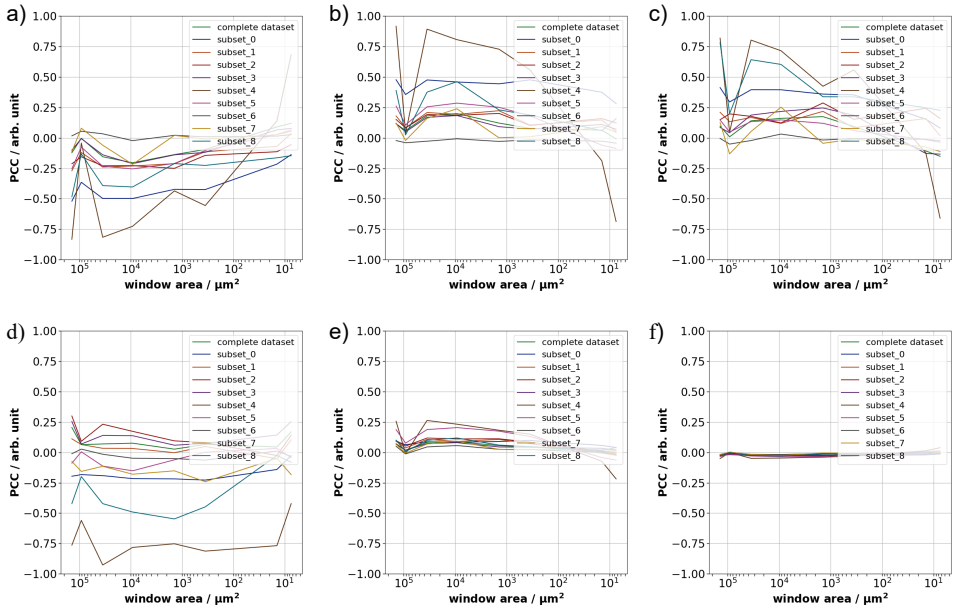

Figure 8.11. Results of the Pearson correlation study using different pooled data sets from the performance characterization of the benchmark CL and inlens images. The strength of the relationship between the areal R_{HFR} and the run percentage (a) and long run emphasis (b) is shown. The relationship between the initial current density at the beginning of the durability test and the run percentage and long run emphasis is shown in (c) and (d), respectively. While (e) shows the strength of the relationship between R_{ct} and the long run emphasis. In (f), the effect is shown when a certain parameter, such as the current density, is not pooled in the correct way, causing the correlation with the long run emphasis to be zero. The list of subset definitions can be found in Table 6.3.

However, the subset of MP5 showed a strong correlation in all data pairs in the aforementioned window range between $9.23 \cdot 10^3\,\mu\mathrm{m}^2$ & $353\,\mu\mathrm{m}^2$. Actually, when there was a stronger correlation between both variables, such as between the areal R_{HFR} and the long run emphasis (Figure 8.11b), or between the initial current density, the run percentage (Figure 8.11c) and the long run emphasis (Figure 8.11d), the correlation strength tended to be stronger in this range of window area. The R_{ct} generally showed a lower correlation strength, e.g. to the long run emphasis (Figure 8.11e), than the R_{HFR}. The reason for this could be that the R_{ct} is about one order of magnitude more scattered than the determined R_{HFR}. Such limitations from the measurement equipment during the test require special attention and must be taken

into account when performing the correlation analysis.
In Figure 8.11f, the mean current density of the whole polarization curve was correlated with the long run emphasis. The resulting correlation strength between the mean current density and the long run emphasis was close to zero over the entire scale. This demonstrates that artificially generated electrochemical properties are not correlated with the extracted IFs, thus confirming that any observed relationships are not coincidental or artificially induced. This further supports the validity of the correlations presented and indicates that a genuine relationship exists between the IFs descriptors and electrochemical performance.

This clearly shows also the current limitation of the approach. Since there is no established model for PEMWE-related CL that reflects the entire scale at once, it is difficult to evaluate the actual strength of the relationship between CL texture and electrochemical properties. As mentioned at the beginning of this work, the CL is not well represented and described, so there is no model that mimics the CL nature. Therefore, this work introduced an empirical approach to describe the CL texture. This can be used in the future to create the missing model linking the CL structure with its electrochemical properties using artificial intelligence, machine learning or classical statistics. However, this requires not only the characterization of the CL texture, but also the electrical nature such as resistance and resistivity of the CL. Therefore, more methods are needed to describe the electrical aspect CLs.

Correlation Study between CL Structure and Electrochemical Properties:

- → Correlation strength varied with the window area, suggesting a technical artifact at $3.5 \cdot 10^4\,\mu\mathrm{m}^2$.
- → MP5 showed strong correlation in smaller window areas, indicating significant interaction between structure and electrochemical properties.
- → The R_{HFR} correlated well with run entropy and long run emphasis, while R_{ct} showed lower correlation strength.
- → The lack of a definitive model for CL texture and its electrochemical properties presents a challenge.
- → Future work could use artificial intelligence or machine learning to develop a model linking structure and properties.

8.2 Resistance and Resistivity of Catalyst Layers and Other Components

This section presents the characterization and validation of another method presented in this thesis for analyzing the CL. A specialized probe was developed to describe the electrical properties of the CL, specifically its sheet resistance and in-plane electrical resistivity. The following subsections detail the probe's design and validation. Then, the measurement concept employing the probe is applied to analyze additional PEMWE components. Lastly, the focus shifts to the CL themselves, examining how reduced catalyst loadings impact sheet resistance and in-plane resistivity. Parts of this work have been previously published[251] and were reused for the purpose of this thesis. Each paragraph that includes content from the publication is marked with a † symbol.

8.2.1 Characterization and Validation of the Probe

8.2.1.1 Probe Geometry

The probe surface was studied in detail by scanning the probe's surface with a non-contact profilometer to see the impact of the solder resist coating on the height distribution. The obtained data presented in Figure 8.12a shows a scan of the entire probe and a focused scan on the measuring field. The insulated traces covered with the solder resist protrude from the surface, with their maximum height ranging between 65 µm and 72 µm. The solder resist coated on the blank rigid board leads to heightened levels of around 40 µm to 50 µm, which is slightly higher than the in Section 6.4.3 mentioned specifications. An explanation for the increased height could be that the traces are very close to each other, increasing the thickness more strongly than expected. Analyzing the most crucial zone, the measuring field, shows that this zone exhibits a lower maximum height than the remaining probe. This can also be quantified by the averaged line profiles shown in Figure 8.12b.† The line profiles recorded perpendicular to the traces of the measuring field exhibited a bimodal distribution of the height. This bimodal distribution emerged from the low height of the 250 µm distance between the traces and the actual height of the 100 µm width traces. The average height difference was 41.4 µm, which fits well to the height specification, mainly the final thickness of the copper (35 µm), with the additional nickel–gold surface finish (4–7 µm). However, the solder resist at the measuring field border showed only a mean height of 27.5 $\pm$ 1.0 µm. This indicates that the traces protruded around 14 µm with respect to the direct neighborhood,

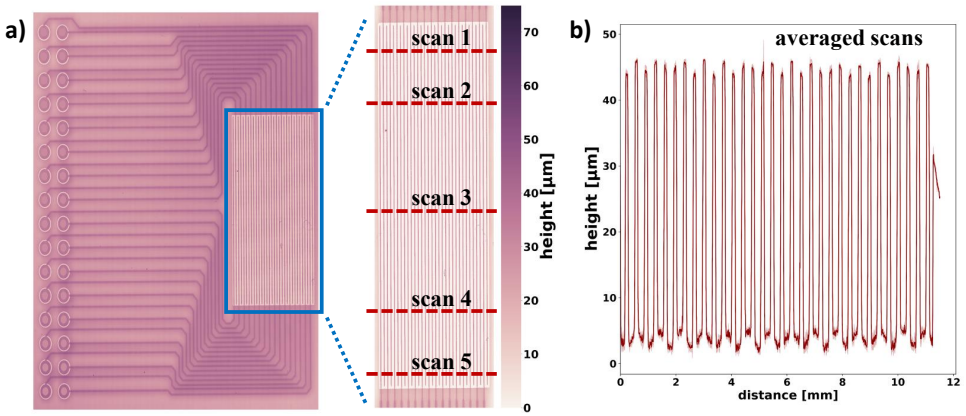

Figure 8.12. Analysis of the probe surface height distribution by non-contact profilometry: (a) Representing the entire probe surface; (b) enlarged view of the measuring field. Figure 8.12c shows several line profiles, scanned orthogonal to the traces as represented by the reddish dashed lines in (b).

whereas they were 58 µm below the maximum height of the overall probe. Thus, proper contacting of the specimen with the measuring field must be considered. Especially for the smallest trace distance (250 µm), these height variations might deteriorate the measurement, showing the non-linear behavior of the potential scan response, violating Ohm's law. To adjust for these height differences and resulting unevenness, a (462 ± 4) µm-thick silicon sheet was introduced between the specimen and stamp, ensuring proper contact between the specimen and measuring field, leading to R^2 values of > 0.99 for the recorded potential scans. The elasticity of the silicon sheet improves the pressure distribution and compensates for certain margins of error as they emerge from the stamp or probe.[†]

8.2.1.2 Compression

The contact force was studied using pressure-sensitive films at different compression forces (Figure AF.16). The mean pressure applied to the measurement field was 0.35 MPa at an adjusted compression force of 0.50 kN (Figure AF.16a). Increasing the compression force led to a linear increase of the distributed pressure for the compression forces > 2.25 kN, with a qualitative analysis showing no visual differences regarding the pressure distribution (Figure AF.16d). All further experiments were carried out at a compression force of 1.00 kN and 2.25 kN, which correlates with a mean pressure of 0.78 MPa and 1.94 MPa, respectively.

Analyzing the pressure distribution indicated that the compression force of 1.00 kN (Figure AF.16b) is still insufficient to ensure proper electrical contact between the specimen and measuring field. Allowing a suitable compression force to be sought leads to minimized errors and fluctuation of the local resistance.†

8.2.1.3 Probe Validation

The described method was validated with the aid of a commercially-available reference, namely a 100 nm-thick ITO layer, coated on a 180 µm-thick PET sheet and with a specified sheet resistance of 300 Ω. The dataset presented in Figure 8.13a shows the determined resistance as a function of the trace distance at a compression force of 2.25 kN.†

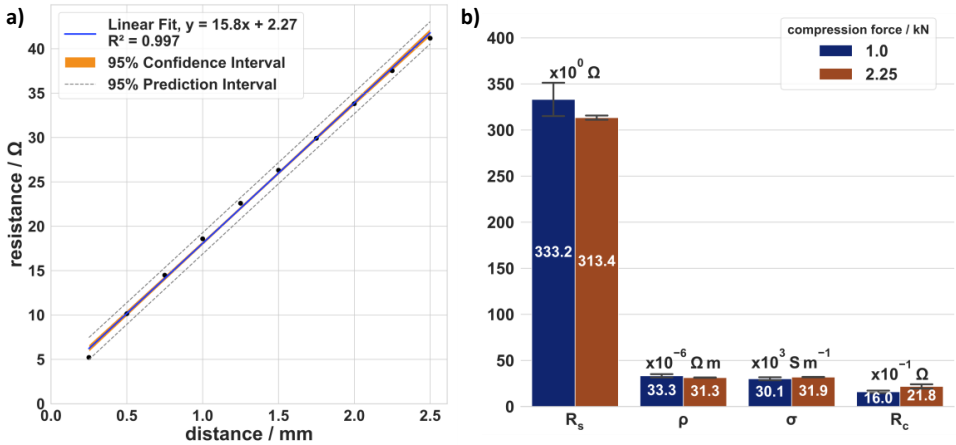

Figure 8.13. Validation results of the probe due measuring of an ITO-PET reference. The linear regression analysis in (a) shows the exemplary measurement for one sample, while (b) shows the overall result of the validation. That included four different probes, multiple measurements using one probe, and two compressions in the dataset. The in-plane electrical resistivity and electrical conductivity were calculated using the specified thickness of 100 nm.

The 95% confidence interval is shaded in orange while the 95% prediction intervals showed that the data is scattering within these limits. The coefficient of determination (R^2) was > 0.99 for all performed potential scan measurements at all distances measured. The standard error of the regression slope was 0.43 $\Omega\,\mathrm{mm}^{-1}$ at 1.00 kN and 0.37 $\Omega\,\mathrm{mm}^{-1}$ at a compression force of 2.25 kN. The resulting sheet resistance, together with the calculated in-plane resistivity and conductivity, can be found in Figure 8.13b for 1.00 kN and 2.25 kN. At a compression

force of 1.00 kN and 2.25 kN, the averaged ITO–PET sheet resistances were (333.2 $\pm$ 25.7) Ω and (313.4 $\pm$ 5.4) Ω, which differs from the reported resistance of the reference by less than 12% and 7%, respectively. The calculated in-plane electrical resistivity was (33.3 $\pm$ 0.6) $\mu\Omega\,\mathrm{m}$, whereas the in-plane conductivity was (30.1 $\pm$ 0.6) $\mathrm{kS\,m^{-1}}$. These values were in a typical range for the material but it is assumed that the thickness was uniform throughout the sheet. However, when the thickness of porous electrodes is non-uniform, both parameters are prone to error.[†]

The y-intercept represents a series of resistors that were invariably measured and consisted, among others, of the cable resistances, contact resistances, and variation in the solder joints. However, the elements of the resistor series were kept constant. Therefore, a change in the y-intercept corresponds to an altered contact resistance (R_c) between the probe and specimen. The contact resistance (Figure 8.13b) was (1.6 $\pm$ 0.2) Ω at 1.00 kN and increased to (2.2 $\pm$ 0.6) Ω at 2.25 kN with increased compression force. The deviation from 1 to 2.25 kN is in the range of the respective error. However, the absolute error decreased by half as the compression force increased. As a result, the relative standard deviation decreased from 34% to 22% and the standard error decreased from 0.67 Ω to 0.62 Ω with respect to the intercept. However, convolving and interpreting the contact resistance remains challenging and error-prone. Instead, spatial analysis of the specimen could further narrow this gap and improve understanding of the contact between the specimen and measuring field. Two distances of the probe were used for the 1D mapping, which were d = 250 $\mu\mathrm{m}$ and d = 2250 $\mu\mathrm{m}$, with 29 and 5 equidistant configurations, respectively.[†]

The 1D mapping, presented in Figure 8.14, was used to gain more insights regarding the homogeneity of the electrical contact between the specimen and measuring field. The x-scale represents the location on the specimen, starting from the right end of the measurement field and progressing towards the center of the probe (refer to Figure AF.16a). The x-coordinate represents the midpoint between the traces used for the measurement. The values on the y-axis represent the deviation between the mean and measured resistance at the specified distance, whereas the shaded area indicates the standard deviation. Figure 8.14 presents 1D mapping for the distances 250 $\mu\mathrm{m}$ (Figure 8.14a, b) and 2250 $\mu\mathrm{m}$ (Figure 8.14c, d) at two different compression forces (1.00 kN, 2.25 kN). The resistance exhibited a higher standard deviation on the side of the probe where the pads are located. This behavior can be explained by the protruding height of the solder resist coating and the number of traces present in this region, which lead to a non-uniform contact area between the measurement traces and specimen. Increasing the compression force to 2.25 kN reduced this effect markedly. The

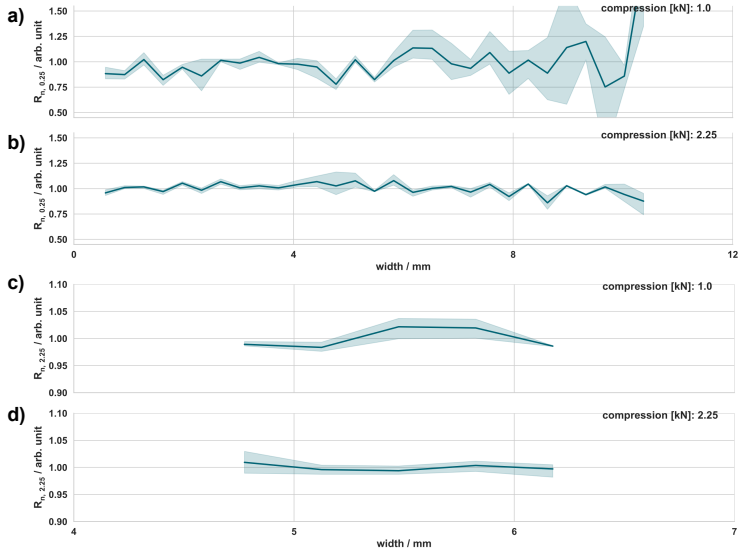

Figure 8.14. Mapping results of the reference specimen at two compressions and distances (a, b) 0.25 mm and (c, d) 2.25 mm. The compression force was varied for both distances and set to 1.00 kNN (a, c) and 2.25 kN (b, d). R_n is the resistance normalized by the average resistance measured for each distance

standard deviation of the measured resistance decreased from 28% to 6% and, in turn, the variation around the median along the width of the measurement field decreased significantly. This was due to a more uniform contact area, ensured by the compression force and silicon sheet, which reduced misalignment between specimen and probe, Figure AF.16. The relative standard deviation was remarkably lower for a distance of 2250 µm, i.e. it decreased from 2% to 1% with increased compression force. From this, it can be concluded that the more locally the measurement is taken, the more error-prone it becomes, showing greater scatter, which could be due to local inhomogeneities of the probe, specimen, or contact issues between them..[†]

After properly contacting the specimen, ensuring linearity, it is possible using the presented method to measure the local resistance fluctuation. However, the mechanical behavior during compression or local inhomogeneities of the specimen must always be considered. It was possible to determine the sheet resistance of the commercial ITO–PET reference with less than 7% error at a compression force of 2.25 kN, which proved that the proposed method

worked and is an option to be utilized for other materials. For future probe designs, the trace pathway should be rearranged and be more spatially separated from the measuring field.[†]

Validation of the Developed Probe

→ Non-contact profilometry revealed variations in height distribution due to the solder resist coating.

→ The traces covered by the solder resist protruded 65-72 µm, while the resist on the rigid board protruded 40-50 µm.

→ A silicon film (462 µm thick) was added to ensure proper contact and eliminate measurement errors, resulting in $R^2 > 0.99$.

→ Pressure-sensitive films showed that compression forces greater than 2.25 kN resulted in uniform pressure distribution.

→ At 1.00 kN, the pressure was insufficient to ensure reliable electrical contact, highlighting the importance of proper compression force.

→ Validation with an ITO-PET reference showed less than 12% error at 1.00 kN compression and less than 7% at 2.25 kN.

→ Increased compression resulted in more uniform electrical contact and minimized standard deviation in resistance measurements.

→ 1D mapping of the resistance at different distances further confirmed the relationship between compression and measurement reliability.

8.2.2 Determination of the Thickness for PEMWE Components and Catalyst Layers

Before calculating the in-plane electrical resistivity from the sheet resistance, the thickness of the specimen must be determined. The thicknesses of the GDLs and the PTL were determined by measuring at least three specimens five times with a stationary thickness-measuring device. The paper-type GDL from Toray, TGP-H-120, possessed a mean thickness of $(360 \pm 4)\,\mu\mathrm{m}$. The thickness obtained from the microporous side of the SGL22BB was $(197 \pm 2)\,\mu\mathrm{m}$, whereas it was $(194 \pm 2)\,\mu\mathrm{m}$ in the case of the woven HC2315. The titanium-based PTL possessed a thickness of $(358 \pm 6)\,\mu\mathrm{m}$. All specimens showed a relative standard deviation (RSD)below 2%. Image processing was used to obtain the thickness distribution from the CLs, as presented in Figure AF.17 and Figure 8.15. The thickness of the anodic catalyst layer (ACL) was $(2.3 \pm 0.54)\,\mu\mathrm{m}$ with 23% RSD while possessing a metal loading nearly five time higher than the

cathodic catalyst layer (CCL). The CCL possessed an average thickness of $(7.5 \pm 1.2)\,\mu\mathrm{m}$ and a comparably lower RSD (16%).† In the case of the ACL, the minimum thickness was

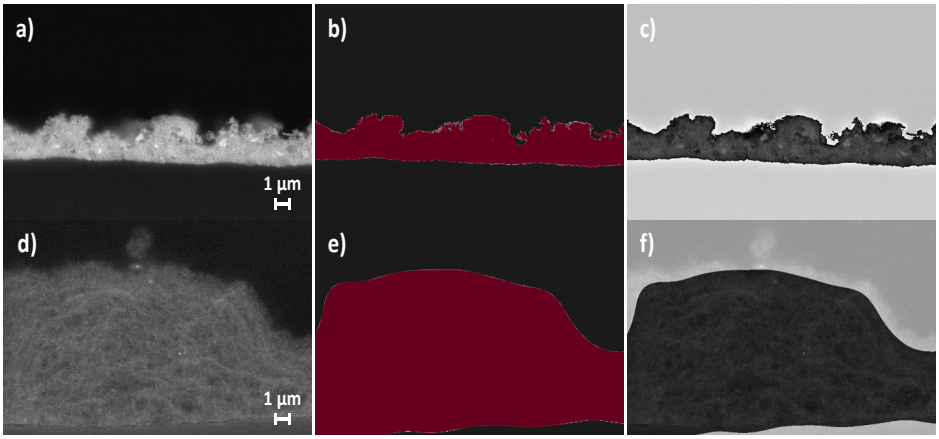

Figure 8.15. Analysis of the cross-sections for the ACL (a–c) and CCL (d–f). Image processing of the cropped raw cross-sections (a, d) leads to the extracted binary image determining the thickness (b, e) and the equally weighted image composition to inspect the image processing quality (c, f).

0.91 µm, and the maximum was 3.71 µm, whereas the 25% percentile was at 1.89 µm and the 75% percentile at 2.73 µm. Instead, the cathode possessed a broader distribution with a minimum and maximum thickness of 4.73 µm and 11.0 µm, respectively. The 25% percentile was at 6.71 µm and the 75% percentile was at 8.47 µm for the cathode. The distribution and related statistics visualized that the CLs are films with a non-uniform thickness distribution. This must be considered when determining the in-plane electrical resistance of CLs and calls for robust, empirical methods to overcome the limitations of the existing measurement methods.†

8.2.3 Resistance and Resistivity of Water Electrolyzer Components

8.2.3.1 GDL and PTL materials

The comprehensive technical specification of GDL materials demonstrates that these materials are well-studied and comparable to PTL and CLs. Thus, to extend the validation of the probe, three GDL materials were applied to determine the electrical in-plane resistivity. The results presented in Figure 8.16 were compared to the technical specifications listed in Table 6.4. Each

GDL material has its own column in Figure 8.16, but a common y-axis to facilitate comparison. The x-axis of each column represents the set of parameters relevant to the discussion (sheet resistance, in-plane resistivity and conductivity, contact resistance). The in-plane resistivity was calculated using the previously determined thickness of the respective specimen measured. For all specimens, in Figure 8.16, the standard error of the slope was below 5 $\mathrm{m\Omega\,mm^{-1}}$.†

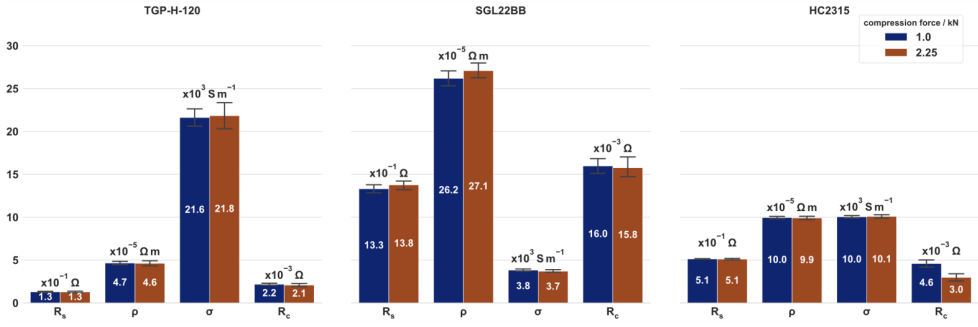

Figure 8.16. Determination of the parameter set for typical carbon-based GDL materials from three different suppliers. The presented parameter set contains the sheet resistance (R_s), in-plane resistivity (ρ), conductivity (σ), and contact resistance (R_c).

Linear regression led to R^2 values $>$ 0.99, except for the TGP-H-120, which possessed an $R^2 > 0.97$ and $R^2 > 0.94$ at a compression force of 1.00 kN and 2.25 kN, respectively. One explanation could be that this behavior was due to the mechanical properties of the TGP-H-120. Applying a lower compression force or thicker silicon sheet reduces this effect. However, TGP-H-120 possessed the lowest in-plane resistivity and deviation from the reference value provided by the technical specification. The highest in-plane electrical resistivity was measured for SGL22BB, which deviated -18% from the provided value. The largest difference between the determined and specified value occurred for the HC2315, at around -36%. However, the technical specifications were limited in providing information regarding the method and conditions used. Nothing was specified in the case of the TGP-H-120. The in-plane resistivity of SGL22BB was determined by applying the van-der-Pauw method, and an internal standard procedure was utilized for HC2315. The difference could also have originated from differences in the thickness, as the compression load affects the thickness of the GDL materials and, therefore, the in-plane electrical resistivity.[217,259] The contact resistance between the specimen and probe was similar among the materials tested.†

The resistance determination of the titanium PTL had to be adjusted because of its comparably high electrical conductivity. This was due to the limited measurement window of the low potentials ($< 40\,\mu\mathrm{V}$) that occurred and the final copper thickness of the probe's traces, which limited the maximal current to around $400\,\mathrm{mA}$. Therefore, the PTL resistances was determined differently from the previous data but still used linear regression to determine the resistance for each distance. The applied currents ranged from $300\,\mathrm{mA}$ to $400\,\mathrm{mA}$ to keep the potential as high as possible instead of measuring between $0\,\mathrm{mV}$ and $5\,\mathrm{mV}$. Thus, the sheet resistance presented in Figure AF.18 scattered the most, although, as expected, it was also the lowest determined within this study. The sheet resistance of $(3.8 \pm 1.4)\,\mathrm{m\Omega}$ was thirty times smaller than that of the GDL materials, whereas the in-plane electrical resistivity was in the typical dimension of metals ($10^{-6}\,\Omega\,\mathrm{m}$). However, R^2 was sometimes lower than < 0.34, which clearly showed the current limitations of the method regarding highly conductive specimens. Using increased distances or thicker traces could improve the result, allowing a broader operation window. On the other hand, electrical testing must be adapted to reduce the noise within the measurement. From a scientific point of view, accessing the in-plane resistivity of metallic porous transport layers with a more accurate method is still of great interest. The crucial interface between the PTL or coated PTL and CL still requires more attention. However, the material's resistivity is, from a technological point of view, not the limiting component in an electrolyzer.[†]

8.2.3.2 Catalyst Layers

This method aimed to characterize the resistance of CLs coated onto membranes for proton exchange membrane (PEM) water electrolysis. Therefore, two different CLs were characterized, representing a typical system for the anode (ACL) or cathode (CCL). A comparison (Figure 8.17) was made for both CLs. The ACL (Figure 8.17a) possessed a sheet resistance of $(13.6 \pm 0.9)\,\mathrm{k\Omega}$ at a compression force of 1.00 kN and $(12.9 \pm 3)\,\mathrm{k\Omega}$ after increasing the compression force to $2.25\,\mathrm{kN}$. However, the RSD rose from 6% to 23% with increased compression force, which could indicate that the CL deforms with increased compression force, deteriorating the in-plane connectivity between the particles. The inverse was the case for the CCL (Figure 8.17b), which could be attributed to differences in the contact between the respective CL and the probe traces. The CCLs showed a remarkably lower sheet resistance of $(629 \pm 4)\,\Omega$ at a $2.25\,\mathrm{kN}$ compression. In both cases, R^2 was > 0.99, whereas the standard error was below $9\,\Omega\,\mathrm{mm^{-1}}$ for the ACL and smaller than $1\,\Omega\,\mathrm{mm^{-1}}$ for the CCL.[†] The in-plane electrical resistance obtained for the anode and cathode was in the range of $10^{-3}\,\Omega\,\mathrm{m}$ and similar to

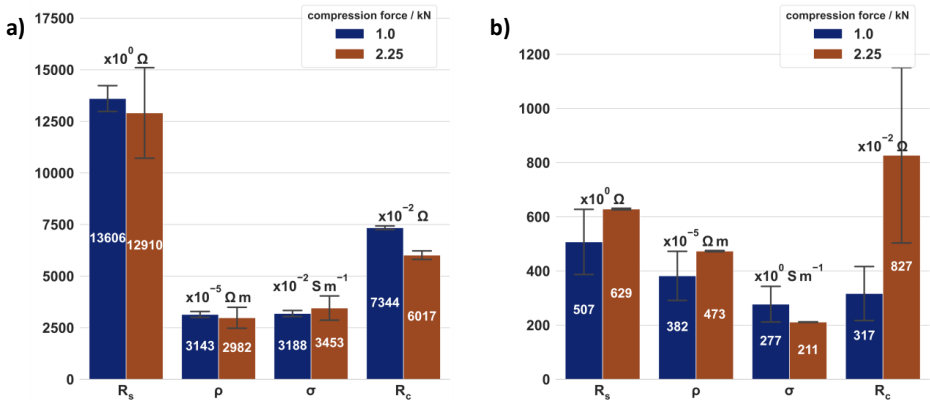

Figure 8.17. Comparison of the ACL and CCL in (a) and (b), respectively. The anodic CL possessed a loading of 0.46 $\mathrm{mg_{Ir}\,cm^{-2}}$ and an average thickness of (2.31 $\pm$ 0.54) µm, whereas the thickness of the lower loaded cathode (0.087 $\mathrm{mg\,mg_{Pt}\,cm^{-2}}$) was (7.53 $\pm$ 1.2) µm.

values already presented in the literature.[115,133] This underscores the urgent need to optimize the CLs-PTL interface and develop microporous transport layers tailored to the anode, since its high sheet resistance suggests a significant barrier to in-plane electron transport toward the reaction sites. Another strategy to improve the performance of CLs is the utilization of highly conductive supports or advanced catalyst designs. However, considering the 25% and 75% percentile of the thickness distribution for both CLs, the in-plane electrical resistivity could vary. For the CCL, the resistivity calculated with the 25% percentile would be 11% less than that calculated with the average thickness. In the case of the 75% percentile, ρ would be 13% greater. Therefore, it is evident that the determined thickness has a strong influence on the in-plane resistivity. As a result, it is recommended to use sheet resistance instead, as a more reliable descriptor of the electronic properties of the CLs. The values of the contact resistance displayed in Figure 8.17 for both CLs showed that the CCL obtained a factor of ten lower contact resistance than the ACL. However, it is only possible to represent this as a comparison between these two specimens, as the same probe and cables, etc. were used. Figure AF.19 presents the mapping for both CLs showing again that the increased distance led to lower deviation in the resistance. †

At adjusted compression forces and a distance of 0.25 µm, the ACL had 25% and 75% quantile values ranging around 0.89 and 1.08, respectively, whereas the CCL had corresponding values of about 0.95 and 1.05. As the distance increased, the resistance deviation for both CLs decreased, with 25% and 75% quantile values ranging around 0.98 and 1.02. However, it is

not yet possible to draw a definitive conclusion about the impact of compression force and probe–CLs interaction. Compression seems to have less influence on the resistance fluctuation compared to the reference shown before, most likely because the PET-supported reference has different mechanical properties than the membrane. Moreover, the reference ITO coating was 100 nm-thick, while both CLs possessed a thickness greater than 1 µm. Thus, the fluctuation visible in Figure AF.19a and AF.19b could be caused by deviations in the thickness, loading displacements or different local ionomer concentrations. However, such a profound analysis would require measuring different conceptualized CLs with variations in their composition and production. From the insights gained, it is expected that the sheet resistance offers the more suitable engineering parameter because it possesses the advantage that the thickness does not need to be known, which reduces the uncertainty and error propagation in comparison to the in-plane resistivity.[†]

Impact of Reduced Iridium Loadings

As shown in Section 7.3, the production of the CL resulted in different CL textures. In addition, the reduction of the iridium loading led to a decrease in the arithmetic mean height (S_a) and thickness. In Figure 8.18 the results from the characterization of different loadings with the probe are presented (similarly to the sections above). The need to reduce the iridium loading is often discussed in the scientific community. However, so far it has only been postulated that the in-plane resistivity or conductivity decreases with reduced iridium loading.[23,24,123,258] With the methods presented here, the effect of loading reduction has been described more precisely in terms of structure and, with the probe presented here, also in terms of electrical properties. The thickness determined to calculate the resistivity/conductivity has already been presented in Section 7.3.3 and Figure 7.17. Reducing the iridium loading decreased the CL thickness from (5.39 ± 0.88) µm at 1.0 $\mathrm{mg_{Ir}\,cm^{-2}}$ to (0.67 ± 0.33) µm at 0.1 $\mathrm{mg_{Ir}\,cm^{-2}}$. While the absolute standard deviation decreased with lower loading, the relative standard deviation increased.

It is evident that the sheet resistance doubles when comparing an iridium loading of (0.97 ± 0.03) $\mathrm{mg_{Ir}\,cm^{-2}}$ with (0.20 ± 0.03) $\mathrm{mg_{Ir}\,cm^{-2}}$, but is not strongly affected by halving the iridium loading to (0.46 ± 0.01) $\mathrm{mg_{Ir}\,cm^{-2}}$. However, the in-plane electrical resistivity decreased with decreasing iridium loading or, conversely, the conductivity increased with decreasing iridium loading.

This is controversial to published studies, which on the other hand have never quantified the thickness to this extent as was presented. Another interesting parameter was derived from

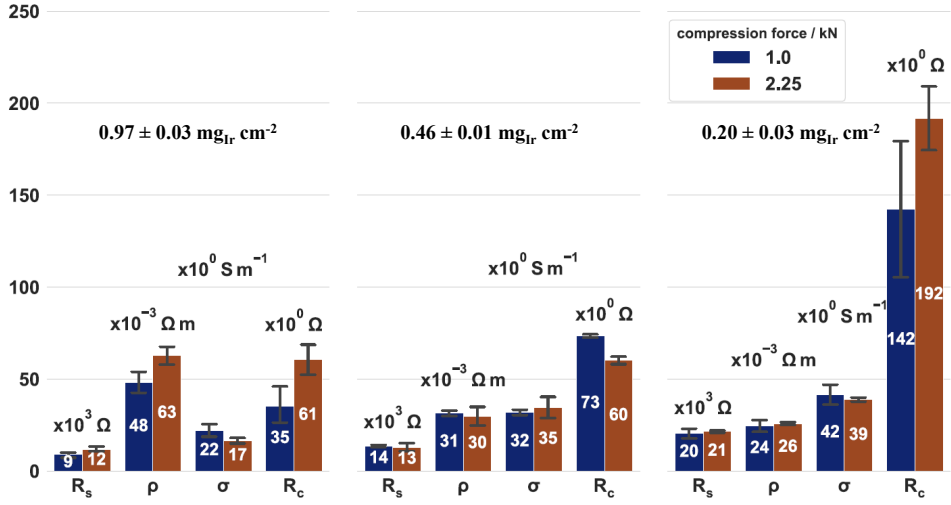

Figure 8.18. Study on the effect of the iridium loading reduction for three different loadings. The presented parameter set contains the sheet resistance (R_s), in-plane resistivity (ρ), conductivity (σ), and contact resistance (R_c). The studied loadings were $(0.97 \pm 0.03)\,\mathrm{mg_{Ir}\,cm^{-2}}$, $(0.46 \pm 0.01)\,\mathrm{mg_{Ir}\,cm^{-2}}$, and $(0.20 \pm 0.03)\,\mathrm{mg_{Ir}\,cm^{-2}}$.

the y-intercept, which was interpreted, under certain assumptions, as the contact resistance between the probe and the sample. The contact resistance was more than tripled when the loading was reduced from $(0.97 \pm 0.03)\,\mathrm{mg_{Ir}\,cm^{-2}}$ to $(0.20 \pm 0.03)\,\mathrm{mg_{Ir}\,cm^{-2}}$. Considering the increase in sheet and contact resistance with reduced iridium loading, alongside a decrease in in-plane resistivity, the following conclusion can be drawn. To maintain constant resistivity, halving the CL thickness requires doubling the sheet resistance. The data further suggest that a low-iridium CL with uniform thickness, narrow distribution, and good contact quality could outperform a highly loaded CL with similar structural characteristics in terms of current density. However, since this performance is currently not observed, the limiting factor lies in the fabrication quality of the CL, not the reduced iridium content itself.

Characterization of the Electrical Properties of Catalyst Layers:

→ Comparison of ACL and CCL (Figure 8.17):
- ⇀ ACL had a sheet resistance of $(13.6 \pm 0.9)\,\mathrm{k\Omega}$ at $1.00\,\mathrm{kN}$, which dropped to $(12.9 \pm 3)\,\mathrm{k\Omega}$ at $2.25\,\mathrm{kN}$ with an increase in RSD from 6% to 23%.
- ⇀ CCL demonstrated significantly lower sheet resistance, $(629 \pm 4)\,\Omega$ at $2.25\,\mathrm{kN}$.
- ⇀ For CCL, resistivity calculated with the 25% percentile of thickness was 11% lower than the resistivity calculated with average thickness, whereas the 75% percentile resulted in 13% higher resistivity.
- ⇀ This demonstrates that thickness significantly impacts in-plane resistivity, underscoring the recommendation to use sheet resistance as a more stable parameter to characterize the electronic nature of CLs.
- ⇀ Contact resistance for CCL was a factor of ten lower than that for ACL (Figure 8.17).

→ Reducing iridium loading in ACL doubled the sheet resistance from 0.97 to $0.20\,\mathrm{mg_{Ir}\,cm^{-2}}$.
- ⇀ In-plane electrical resistivity decreased with reduced iridium, contrary to prior studies but accounted for here due to precise thickness measurements.
- ⇀ The y-intercept provided an estimate for contact resistance, which more than tripled with lower iridium loadings.
- ⇀ Sheet resistance is a more reliable engineering parameter, as it reduces error by not requiring thickness data.
- ⇀ A lower iridium CL with uniform thickness and optimal contact may yield better current densities than higher-loaded layers.
- ⇀ Production methods, not iridium quantity, are critical for performance improvements.

9 Discussion

In this chapter, the study's research questions and hypotheses are revisited in light of the key findings. Each question is addressed, offering insights into the morphological and electrochemical properties of CLs in PEM water electrolyzers. The questions (Q1-Q7) and hypotheses (H1–H4), initially introduced in Chapter 5 "Research Questions and Approach", are critically evaluated based on the experimental outcomes and literature.

-Q1- What are the key morphological features of CLs and how do these features affect the electrochemical performance of PEMWE?

The CL morphology, including texture, thickness and heterogeneity, significantly affected the electrochemical performance and durability of PEM water electrolyzers. Homogeneous CLs, such as MP1, exhibited less resistance increase and texture coarsening over time, resulting in better long-term performance and less data scattering. In contrast, higher texture heterogeneity (as seen in MP3 and MP5) leads to poorer stability, higher resistance, and faster degradation under operating conditions. These results highlight the importance of controlling the morphological characteristics of CLs, particularly for optimizing the electrochemical performance and increasing the durability of PEM water electrolyzers.

-Q2- How can advanced microscopy techniques, such as SEM or CLSM, be integrated with computational tools to provide a more objective and quantitative description of CL morphology?

Advanced microscopy techniques such as scanning electron microscopy (SEM) and confocal laser scanning microscope (CLSM), combined with computational tools, provide a highly objective and quantitative approach to characterize the morphology of CLs in PEM water electrolyzers. The integration of these methods provided valuable insights into the microstructure, texture and distribution of materials within the CL. Computational tools, including texture analysis algorithms and statistical methods, were applied to the SEM and CLSM images to

quantify the CL texture. The extracted features, such as run percentage, short and long run emphasis, monitored the transition from layered (macro-) to catalyst pore network (micro-) structures and provided quantitative measures of surface texture, coarseness, and microstructural evolution at different scales. These metrics allowed detailed, objective analysis of how changes in morphology, such as increased porosity or surface roughness, affected the electrochemical behavior of the CL. The integration of these techniques also facilitated the tracking of microstructural changes over time, particularly under different electrochemical durability testing. For example, feature extracted from SEM images revealed texture coarsening, and computational analysis highlighted how this change correlated with performance degradation, such as increased resistance or lower catalyst activity.

-Q3- How does the surface texture correlate with the manufacturing process and the electrochemical performance of the CL in PEMWE?

The relationship between surface texture, manufacturing processes, and electrochemical performance of CLs in PEM water electrolyzers was investigated through a series of manufacturing adjustments and electrochemical tests. The results showed that modifying production variables significantly affected the surface texture, which in turn affected the electrochemical behavior of the CLs. Key findings include the ability to tailor the arithmetic mean height (S_a) between $0.20\,\mu\mathrm{m}$ and $0.46\,\mu\mathrm{m}$ by adjusting production parameters such as spray pressure, flow rate and nozzle spacing. Surface roughness, as indicated by S_a, was strongly influenced by the alcohol content of the solvent. For example, at 66 wt.% n-propanol alcohol content, the resulting S_a was minimized. Reducing the alcohol content below the azeotropic point (33 wt.%) caused a drastic increase in S_a, highlighting the sensitivity of surface texture to solvent composition. The study also showed that classical spray variables such as pressure, flow rate and nozzle distance have complex, non-linear relationships with surface properties. In particular, pressure between $3\,\mathrm{kPa}$ and $10\,\mathrm{kPa}$ minimized S_a and skewness (S_{sk}), while nozzle distance between $20\,\mathrm{mm}$ and $40\,\mathrm{mm}$ helped minimize S_a. Furthermore, Nafion content had minimal effect on surface roughness as long as it exceeded 10 wt.%, while iridium loading was found to have the most significant effect on surface texture. A strong correlation was observed between iridium loading and S_a, with S_a increasing with the loading until it plateaued at $0.5\,\mathrm{mg_{Ir}\,cm^{-2}}$, indicating a threshold beyond which further increases in loading did not significantly affect surface texture. Electrochemical tests, including polarization curve measurements, potentiostatic operation, and EIS analysis, showed that these changes in surface texture affected the performance of the CL. The electrochemical performance of the CLs correlated with surface

texture characteristics, with image-based texture parameters such as large dependence high gray level emphasis ($GLDM9$), long run high gray level emphasis ($GLRLM6$), and long run emphasis ($GLRLM5$) providing valuable insight into catalyst uniformity, similar to traditional texture metrics such as S_a and S_{sk}. These results confirm the importance of controlling the surface texture during the manufacturing process to optimize the electrochemical performance and durability of the CL in PEM water electrolyzers.

-Q4- How strong is the correlation between physical texture descriptors of the CL and statistical features extracted from images?

The correlation study highlighted that advanced image features (IFs) extracted from microscopy images lead to the same conclusion as traditional physical surface texture parameter (STP). The results showed robust relationships between STPs such as arithmetic mean height (S_a) and specific image features such as $GLRLM6$ and $GLDM9$, particularly in datasets related to iridium loading, alcohol content, and Nafion content. High Pearson correlation coefficient (PCC) values, ranging from 0.70 to 0.91, confirm that these image-derived features effectively capture surface roughness and texture variations, providing valuable insight into the structural properties of the CL. However, weaker correlations observed in data sets containing process parameters such as gas pressure, nozzle height, and flow rate suggest that some manufacturing conditions introduce complex, non-linear dependencies and noise. The mentioned factors prevent a clear or direct relationship from being established between process inputs and CL properties. This black box cannot be transformed into a white box without progress in analytical capability. These challenges highlight the need for advanced analytical approaches to monitor CL optimization, which can then be used to create a physical model. Redundancy analysis proved effective in reducing the parameter space by consolidating overlapping features, achieving a 55% reduction while preserving the features' key descriptive capabilities. This streamlined approach improves computational efficiency and interpretability, which are essential for practical application in industrial settings or R&D applications. The study also revealed inverse relationships, such as those between autocorrelation length (S_{al}) and S_{sk} with long run emphasis ($GLRLM5$) and large dependence emphasis ($GLDM8$), indicating that the interactions between texture descriptors and image-derived features are complex and require a multivariate approach for a comprehensive understanding of CL morphology. The robustness of certain statistical features, demonstrated by their consistency across data sets, underscores their versatility in representing surface properties under varying manufacturing and structural conditions. This versatility enhances their utility in linking structural charac-

terization to electrochemical performance and durability. These results highlight the critical role of correlating physical and statistical descriptors in advancing the understanding of CL morphology and its impact on performance. By leveraging these relationships, manufacturers can improve manufacturing precision and optimize catalyst properties, ultimately improving the performance and durability of proton exchange membrane (PEM) water electrolyzers. In addition, this approach lays the groundwork for the implementation of automated, data-driven quality control systems that provide real-time monitoring and feedback during CL production.

-Q5- In what ways does the CL's surface texture, including its scale-dependent variations, impact electrochemical performance, and how are these effects influenced by production methods, catalyst loading, and ionomer content?

The surface texture and scale-dependent variations in CL morphology play a critical role in determining the electrochemical performance and durability of PEM water electrolyzers. The study revealed that production methods, catalyst loading, and ionomer content significantly influence these morphological features, which in turn affect performance metrics such as activity and durability. CL uniformity, achieved through optimized mask designs and spray parameters, was critical to improving performance/durability but also reduced the data scattering. Changes such as replacing a 90° edge with a 45° edge on the metal mask improved loading uniformity by reducing high and low loading areas, resulting in better mist distribution and droplet deposition. Similarly, specific nozzle heights and controlled flow rates ensured uniform material distribution, which mitigated random patterns and membrane swelling. The analysis of the five benchmark electrodes (MP1 to MP5) showed that the coarseness of the CL texture increased in all samples after testing. However, the production variables already introduced distinct macroscopic characteristics as highlighted in previous results. The more heterogeneous samples (MP4 and MP5) illustrated how local microscale properties are intertwined with macroscopic ones, potentially leading to misinterpretations. This finding emphasizes the importance of achieving macroscopic homogeneity in CLs as a prerequisite for isolating and studying microscale effects. In this context, MP1, the most homogeneous sample, showed the clearest coarsening effect at all scales, highlighting the importance of initial texture uniformity. Furthermore, the study found that cell assembly only affected regions below $\sim 1.5 \cdot 10^3\,\mu\mathrm{m}^2$, while electrochemical testing altered the CL texture across the entire scale. This observation is consistent with the notion that electrochemical reactions, which occur primarily at the nanoscale, induce changes that are visible at the microscopic scale. While the presented methodology confirmed the sensitivity of image features to detect these changes, it also suggested that macroscopic scale

changes, especially at large window areas of above $\sim 1.5 \cdot 10^3\,\mu m^2$, may not be solely due to electrochemical effects.

-Q6- How can the in-plane electrical conductivity of CLs be reliably determined?

Existing methods for assessing in-plane electrical conductivity, such as the transfer length method, van-der-Pauw technique, and traditional four-point probe setups, face limitations like sensitivity to contact pressure, electrode depth, and assumptions of uniform resistivity and thickness. These factors often compromise measurement reproducibility and spatial resolution.
To overcome these challenges, a novel four-line probe based on printed circuit boards (PCB) technology was developed, ensuring standardized production, customization potential, and controlled pressure distribution. This setup enables precise contact between probe and sample while allowing spatial mapping of resistance variations through linear regression analysis. Results show that resistance measurements depend on both sample and trace resistances, with contact effects significant at low resistances but negligible at higher values. This method offers a reliable, reproducible, and detailed approach to characterizing the electrical properties of CLs in proton exchange membrane (PEM) water electrolyzers.

-Q7- What is the relationship between the in-plane electrical conductivity of the CL and the catalyst loading?

Lower iridium loadings showed a complex interplay between sheet resistance, in-plane resistivity, and structural properties. While a fivefold reduction in loading doubled the sheet resistance, in-plane resistivity decreased. This observation differs from previous studies where lower loadings were typically associated with higher resistivity, underscoring the importance of accurate thickness measurements for accurate interpretation of conductivity trends. Structural changes at reduced loadings were evident from cross-sectional analysis, which showed a significant decrease in CL thickness from $5.39\,\mu m$ to $1.20\,\mu m$. While the absolute standard deviation decreased with decreasing loading, the relative standard deviation showed the opposite trend, emphasizing that thickness variation must always be discussed in this context.

Addressing the research questions provided critical insight into the methods and factors influencing CL properties. Based on these findings, the hypotheses were evaluated to determine their validity in the context of the study objectives.

-H1- Optimization of production parameters will result in a CL with improved homogeneity, leading to reduced errors measured by texture parameters and electrochemical testing.

Considering Q1, Q3, and Q5, the results show that production optimizations, such as adjusting spray parameters and solvent composition, significantly improved uniformity and electrochemical performance. CLs with more uniform textures, such as MP1, showed better stability and lower resistance over time, supporting the hypothesis. In addition, while texture variations affected the electrochemical performance, optimization of the manufacturing methods allowed better control of these variations, reducing measurement errors and improving the homogeneity of the CLs. Therefore, based on the results, the hypothesis is valid.

-H2- Advanced computational image analysis techniques can provide more accurate and objective characterization of CL morphology and surface texture compared to traditional microscopy.

The integration of advanced imaging techniques, such as SEM and CLSM, with computational image analysis allowed for a thorough and quantitative evaluation of CL texture. These techniques allow for the precise evaluation of important morphological features, such as coarseness, roughness, and topographical heterogeneity. These features were monitored and identified as critical indicators of degradation processes, although they had previously been used primarily to describe the effects of the manufacturing process on CL texture. The IF-based approach enabled the quantification of microscopy images, facilitating a holistic interpretation that would not be achievable through visual inspection alone. The presented IF-based approach was sensitive enough to detect changes induced by durability tests across macroscopic and microscopic scales. Unlike conventional microscopy methods, which focus on certain window areas of interest (e.g., classical SEM, AFM, or TEM), the approach using IF enables a global, spatially resolved evaluation of the CL structure. This allowed for the detection of texture deterioration, such as coarsening and roughening, induced by electrochemical testing. This deterioration is potentially linked to gas bubble formation and subsequent material displacement.
Furthermore, this approach correlated macroscopic and microscopic analyses by linking global surface metrics to localized domains using different IF techniques. This multiscale correlation provides a more complete and objective understanding of CL morphology than traditional methods alone. It can also connect methods specialized to certain scales, such as the macroscale and nanoscale. For example, IF-based descriptors could be used with optical microscopy, SEM,

CLSM, optical density, or white light interferometry at the macroscale and linked to techniques that accurately describe the nanoscale, such as AFM or TEM. Thus, the presented method of using statistical image features would bridge the gap between scales.
In summary, these results demonstrate that advanced computational image analysis techniques significantly improve the accuracy, objectivity, and scale integration of CL morphology characterization. These results confirm the validity of Hypothesis H2.

-H3- There is a correlation between surface texture and the electrochemical performance of the CL.

Hypothesis H3, is generally supported, but with some nuances. The data suggest that the strength and clarity of the correlation depend heavily on the structure and composition of the dataset. Strong correlations were observed in datasets where IF-based descriptors and texture deterioration induced by operational processes exhibited linear behavior, such as between long run emphasis and R_{HFR}. However, when certain electrochemical performance descriptors, such as R_{ct}, showed high variability, the strength of the observed correlation decreased, primarily due to increased data dispersion. These IF-based CL texture features emerged as reliable indicators of electrochemical degradation.
However, in datasets with more complex or nonlinear characteristics, the correlation between surface texture and electrochemical performance was notably weaker. This variability highlights the importance of controlled experimental design, macroscopic electrode structure homogeneity, and feature selection when evaluating structure-function relationships in CLs. Furthermore, the results reveal a critical limitation: the absence of an established multiscale model for PEMWE-related CLs. Without such a model, it is difficult to quantitatively evaluate the true strength and nature of the structure-performance relationship. As previously mentioned, current descriptions of CL structure are incomplete, which limits the ability to generalize or mechanistically explain observed correlations. To address this gap, the study introduces an empirical framework based on image-derived texture analysis. While not yet predictive, this framework can serve as a basis to build future CL models and data analysis methods that leverage artificial intelligence, machine learning, or classical statistical approaches. In conclusion, Hypothesis H3 is supported by the evidence, particularly in well-characterized contexts. However, the observed correlation is conditional, and its broader applicability depends on future advances in CL research.

-H4- In-plane electrical conductivity measurements can be standardized to provide reliable and reproducible data for CL optimization.

The introduced four-line probe method overcomes the limitations of traditional techniques and provides more accurate and standardized measurements for CL optimization. The observed complexities in sheet resistance data are primarily related to variations in CL thickness, especially at lower iridium loadings. Once these variations were accounted for, the method provided consistent and reliable insights into the electrical properties of the CLs. As a result, hypothesis H4 is largely validated, although thickness variations must be carefully considered in in-plane conductivity/resistivity interpretations. The findings indicate that sheet resistance serves as a more practical and reliable engineering parameter, as it eliminates the need for precise thickness measurements and thereby minimizes uncertainty and the potential for error propagation associated with in-plane resistivity calculations.

In summary, the study's findings comprehensively address the research questions and confirm the validity of the hypotheses, contributing significantly to the understanding of CL morphology, texture, and their impact on electrochemical performance and durability. The image-based approach to quantify and evaluate electrode texture offers a more precise methodology, which refines existing analytical capabilities. Moreover, the developed probe has been utilized to directly assess local electrical properties. The presented methodologies facilitate the optimization of electrochemical devices.

10 Conclusion & Outlook

Conclusion. This thesis makes a significant contribution to the characterization and analysis of CLs, with a particular focus on both morphological and electrical properties. By employing image-based feature extraction from classical microscopy techniques, the study effectively expanded the comprehension of the production-structure-property triangle in CLs. In conclusion, three critical surface texture parameters—arithmetic mean height (S_a), autocorrelation length (S_{al}), and skewness (S_{sk})—are identified as key indicators for quality control. These parameters correlate with a comprehensive set of 84 image-derived features, which is further refined to improve analytical precision and relevance. By employing advanced imaging techniques and integrating them with computational analysis, it is possible to achieve precise characterization and quantification of structural features, such as thickness distribution and surface texture of CLs. This detailed framework facilitates an understanding of the critical interplay between the morphology, electrical properties, and manufacturing processes of CLs in PEM water electrolyzers. These parameters enable the monitoring of structural alterations in the CL resulting from electrochemical or related processes, and they also facilitate the integration of macroscale and microscale observations.

Furthermore, the implementation of an empirical methodology for sheet resistance assessment through the utilization of sophisticated PCB technology enables the precise and reproducible characterization of porous electrodes, including those comprising CLs and GDL materials. This method, validated with both commercial and experimental samples, offers a reliable alternative to conventional techniques, delivering high spatial resolution and applicability across a range of materials. Furthermore, the study addressed the challenges of non-uniform CL morphologies by integrating SEM-based thickness distribution analysis, thereby demonstrating the superiority of sheet resistance as an engineering parameter. The innovative methodologies developed herein significantly enhance the analytical capabilities available for CL research, thereby providing a solid foundation for further exploration of CL performance and paving the way for more efficient and scalable electrochemical systems.

In conclusion, this study establishes the foundation for the development of a unified platform

for CL characterization, integrating advanced imaging, empirical measurements, and computational tools. These endeavors will facilitate the advancement of more efficient fuel cells and electrolyzers, thereby contributing to the global transition towards sustainable energy systems.

Outlook Building on these findings, future research could focus on broadening the application of image-based feature extraction to other microscopy techniques, such as atomic force microscopy or X-ray computed tomography. This would enable deeper insights into the multi-scale properties of CLs, particularly in their interaction with other system components like membranes and transport layers.

The integration of artificial intelligence and machine learning into the analytical pipeline represents a promising avenue for further research. By incorporating these tools, researchers could develop predictive models that link production parameters directly to performance outcomes. Additionally, the expansion of the use of statistical image features to characterize alternative CL concepts could further strengthen the understanding of porous electrode behavior across scales.

Moreover, the PCB-based measurement tool has significant potential for further development. Partial automation of the measurement process has already been implemented, which enables high-throughput testing and demonstrates the feasibility of scaling the method. Future iterations could include designs that mitigate the impact of connecting traces and explore high-throughput testing capabilities for industrial applications. Adapting this method to study sheet resistance in new electrode designs, including those for next-generation batteries and supercapacitors, could extend its utility.

Bibliography

[1] A. T. Dangerman and H. J. Schellnhuber, Proc Natl Acad Sci U S A, (**2013**), 110, 7, E549–58, DOI: 10.1073/pnas.1219791110.

[2] Hans Joachim Schellnhuber, Stefan Rahmstorf, and Ricarda Winkelmann, Nature Climate Change, (**2016**), 6, 7, pp. 649–653, DOI: 10.1038/nclimate3013.

[3] T. W. Brown, T. Bischof-Niemz, K. Blok, C. Breyer, H. Lund, and B. V. Mathiesen, Renewable and Sustainable Energy Reviews, (**2018**), 92, pp. 834–847, DOI: 10.1016/j.rser.2018.04.113.

[4] IRENA. *Global energy transformation: A roadmap to 2050 (2019 edition)*. Abu Dhabi: International Renewable Energy Agency, 2019. ISBN: 978-92-9260-120-1.

[5] Domenico Ferrero, Martina Gamba, Andrea Lanzini, and Massimo Santarelli, Energy Procedia, (**2016**), 101, pp. 50–57, DOI: 10.1016/j.egypro.2016.11.007.

[6] Christina Wulf, Jochen Linßen, and Petra Zapp, Energy Procedia, (**2018**), 12th International Renewable Energy Storage Conference, IRES 2018, 155, pp. 367–378, DOI: 10.1016/j.egypro.2018.11.041.

[7] International Energy Agency, International Renewable Energy Agency, and United Nations Climate Change. *The Breakthrough Agenda Report 2022: Accelerating Sector Transitions Through Stronger International Collaboration*. OECD, Oct. 13, 2022. ISBN: 978-92-64-43740-1. DOI: 10.1787/692cdb6b-en.

[8] Christoph Rakousky, Meital Shviro, Marcelo Carmo, and Detlef Stolten, Electrochimica Acta, (**2019**), 302, pp. 472–477, DOI: 10.1016/j.electacta.2018.11.141.

[9] Marcelo Carmo, David L. Fritz, Jürgen Mergel, and Detlef Stolten, Int. J. of Hydrogen Energy, (**2013**), 38, 12, pp. 4901–4934, DOI: 10.1016/j.ijhydene.2013.01.151.

[10] Shaun M Alia, Current Opinion in Chemical Engineering, (**2021**), 33, p. 100703, DOI: 10.1016/j.coche.2021.100703.

[11] Katherine Ayers, Current Opinion in Chemical Engineering, (**2021**), 33, DOI: 10.1016/j.coche.2021.100719.

[12] Fabian Scheepers, Markus Stähler, Andrea Stähler, Edward Rauls, Martin Müller, Marcelo Carmo, and Werner Lehnert, Energies, (**2020**), 13, 3, DOI: 10.3390/en13030612.

[13] B. You and Y. Sun, Acc Chem Res, (**2018**), 51, 7, pp. 1571–1580, DOI: 10.1021/acs.accounts.8b00002.

[14] J. Peron, M. Faustini, Marion Giraud, Jacques Rozière, Deborah Jones, C. Boissière, and C. Tard, ECS Transactions, (**2017**), 80, pp. 1077–1084, DOI: 10.1149/08008.1077ecst.

[15] K. Ayers, N. Danilovic, R. Ouimet, M. Carmo, B. Pivovar, and M. Bornstein, Annu Rev Chem Biomol Eng, (**2019**), 10, pp. 219–239, DOI: 10.1146/annurev-chembioeng-060718-030241.

[16] F. Lv, J. Feng, K. Wang, Z. Dou, W. Zhang, J. Zhou, C. Yang, M. Luo, Y. Yang, Y. Li, P. Gao, and S. Guo, ACS Cent Sci, (**2018**), 4, 9, pp. 1244–1252, DOI: 10.1021/acscentsci.8b00426.

[17] Serhiy Cherevko, Simon Geiger, Olga Kasian, Andrea Mingers, and Karl J. J. Mayrhofer, Journal of Electroanalytical Chemistry, (**2016**), 774, pp. 102–110, DOI: 10.1016/j.jelechem.2016.05.015.

[18] Serhiy Cherevko, Simon Geiger, Olga Kasian, Andrea Mingers, and Karl J. J. Mayrhofer, Journal of Electroanalytical Chemistry, (**2016**), 773, pp. 69–78, DOI: 10.1016/j.jelechem.2016.04.033.

[19] Ugljesa Babic, Michel Suermann, Felix N. Büchi, Lorenz Gubler, and Thomas J. Schmidt, J. Electrochem. Soc. (**2017**), 164, 4, F387–F399, DOI: 10.1149/2.1441704jes.

[20] Christine Minke, Michel Suermann, Boris Bensmann, and Richard Hanke-Rauschenbach, Int. J. of Hydrogen Energy, (**2021**), 46, 46, pp. 23581–23590, DOI: 10.1016/j.ijhydene.2021.04.174.

[21] Mark Clapp, Christopher M. Zalitis, and Margery Ryan, Catalysis Today, (**2023**), 420, p. 114140, DOI: 10.1016/j.cattod.2023.114140.

[22] Erik Eikeng, Ashkan Makhsoos, and Bruno G. Pollet, International Journal of Hydrogen Energy, (**2024**), 71, pp. 433–464, DOI: 10.1016/j.ijhydene.2024.05.096.

[23] Zachary Taie, Xiong Peng, Devashish Kulkarni, Iryna V. Zenyuk, Adam Z. Weber, Christopher Hagen, and Nemanja Danilovic, ACS Appl. Mater. Interfaces, (**2020**), 12, 47, pp. 52701–52712, DOI: 10.1021/acsami.0c15687.

[24] Maximilian Bernt, Armin Siebel, and Hubert A. Gasteiger, J. Electrochem. Soc. (**2018**), 165, 5, F305–F314, DOI: 10.1149/2.0641805jes.

[25] J. Lim, S. Yang, C. Kim, C. W. Roh, Y. Kwon, Y. T. Kim, and H. Lee, Chem Commun (Camb), (**2016**), 52, 32, pp. 5641–4, DOI: 10.1039/c6cc00053c.

[26] H. N. Nong, H. S. Oh, T. Reier, E. Willinger, M. G. Willinger, V. Petkov, D. Teschner, and P. Strasser, Angew Chem Int Ed Engl, (**2015**), 54, 10, pp. 2975–9, DOI: 10.1002/anie.201411072.

[27] Daniel Böhm, Michael Beetz, Christian Gebauer, Maximilian Bernt, Jonas Schröter, Matthias Kornherr, Florian Zoller, Thomas Bein, and Dina Fattakhova-Rohlfing, Applied Materials Today, (**2021**), 24, DOI: 10.1016/j.apmt.2021.101134.

[28] Alexandra Hartig-Weiss, Melanie Miller, Hans Beyer, Alexander Schmitt, Armin Siebel, Anna T. S. Freiberg, Hubert A. Gasteiger, and Hany A. El-Sayed, ACS Applied Nano Materials, (**2020**), 3, 3, pp. 2185–2196, DOI: 10.1021/acsanm.9b02230.

[29] Jahowa Islam, Sang-Kyung Kim, Hyun-Seok Cho, Min-Joong Kim, Won-Chul Cho, and Chang-Hee Kim, Electrochemistry Communications, (**2020**), 121, DOI: 10.1016/j.elecom.2020.106877.

[30] Taehyun Kwon, Hyeyoun Hwang, Young Jin Sa, Jongsik Park, Hionsuck Baik, Sang Hoon Joo, and Kwangyeol Lee, Advanced Functional Materials, (**2017**), 27, 7, DOI: 10.1002/adfm.201604688.

[31] Zhifan Chen, Hongbin Zhao, Jiujun Zhang, and Jiaqiang Xu, Science China Materials, (**2016**), 60, 2, pp. 119–130, DOI: 10.1007/s40843-016-5134-5.

[32] Jongsik Park, Songa Choi, Aram Oh, Haneul Jin, Jinwhan Joo, Hionsuck Baik, and Kwangyeol Lee, Nanoscale Horizons, (**2019**), 4, 3, pp. 727–734, DOI: 10.1039/c8nh00520f.

[33] Daniel Siegmund, Sebastian Metz, Volker Peinecke, Terence E. Warner, Carsten Cremers, Anna Grevé, Tom Smolinka, Doris Segets, and Ulf-Peter Apfel, JACS Au, (**2021**), 1, 5, pp. 527–535, DOI: 10.1021/jacsau.1c00092.

[34] Xiao-Zi Yuan, Christine Nayoze-Coynel, Nima Shaigan, David Fisher, Nana Zhao, Nada Zamel, Pawel Gazdzicki, Michael Ulsh, Kaspar Andreas Friedrich, Francois Girard, and Ulf Groos, Journal of Power Sources, (**2021**), 491, DOI: 10.1016/j.jpowsour.2021.229540.

[35] Rod Borup, Jeremy Meyers, Bryan Pivovar, Yu Seung Kim, Rangachary Mukundan, Nancy Garland, Deborah Myers, Mahlon Wilson, Fernando Garzon, David Wood, Piotr Zelenay, Karren More, Ken Stroh, Tom Zawodzinski, James Boncella, James E. McGrath, Minoru Inaba, Kenji Miyatake, Michio Hori, Kenichiro Ota, Zempachi Ogumi, Seizo Miyata, Atsushi Nishikata, Zyun Siroma, Yoshiharu Uchimoto, Kazuaki Yasuda, Ken-ichi Kimijima, and Norio Iwashita, Chem. Rev. (**2007**), 107, 10, pp. 3904–3951, DOI: 10.1021/cr0501821.

[36] Patrick Schneider, Mariah Batool, Andres O. Godoy, Rajveer Singh, Dietmar Gerteisen, Jasna Jankovic, and Nada Zamel, J. Electrochem. Soc. (**2023**), 170, 2, p. 024506, DOI: 10.1149/1945-7111/acb8df.

[37] André Colliard-Granero, Mariah Batool, Jasna Jankovic, Jenia Jitsev, Michael H. Eikerling, Kourosh Malek, and Mohammad J. Eslamibidgoli, Nanoscale, (**2022**), 14, 1, pp. 10–18, DOI: 10.1039/D1NR06435E.

[38] Jasna Jankovic, Shawn Zhang, Andreas Putz, Madhu S. Saha, and Darija Susac, J. Mater. Res. (**2019**), 34, 4, pp. 579–591, DOI: 10.1557/jmr.2018.458.

[39] Shaun M. Alia, Kimberly S. Reeves, Jefferey S. Baxter, and David A. Cullen, J. Electrochem. Soc. (**2020**), 167, 14, p. 144512, DOI: 10.1149/1945-7111/abc746.

[40] Chuyen Van Pham, Daniel Escalera-López, Karl Mayrhofer, Serhiy Cherevko, and Simon Thiele, Adv. Energy Mater. (**2021**), 11, 44, p. 2101998, DOI: 10.1002/aenm.202101998.

[41] Sunilkumar Khandavalli, Jae Hyung Park, Nancy N. Kariuki, Deborah J. Myers, Jonathan J. Stickel, Katherine Hurst, K. C. Neyerlin, Michael Ulsh, and Scott A. Mauger, ACS Appl. Mater. Interfaces, (**2018**), 10, 50, pp. 43610–43622, DOI: 10.1021/acsami.8b15039.

[42] Luigi Osmieri, Guanxiong Wang, Firat C. Cetinbas, Sunilkumar Khandavalli, Jaehyung Park, Samantha Medina, Scott A. Mauger, Michael Ulsh, Svitlana Pylypenko, Deborah J. Myers, and K.C. Neyerlin, Nano Energy, (**2020**), 75, p. 104943, DOI: 10.1016/j.nanoen.2020.104943.

[43] Sarah F. Zaccarine, Meital Shviro, Johanna Nelson Weker, Michael J. Dzara, Jayson Foster, Marcelo Carmo, and Svitlana Pylypenko, J. Electrochem. Soc. (**2022**), 169, 6, p. 064502, DOI: 10.1149/1945-7111/ac7258.

[44] Kateryna Artyushkova, Plamen Atanassov, Monica Dutta, Silvia Wessel, and Vesna Colbow, Journal of Power Sources, (**2015**), 284, pp. 631–641, DOI: 10.1016/j.jpowsour.2015.02.135.

[45] S. Trasatti, Journal of Electroanalytical Chemistry, (**1999**), 476, pp. 90–91, DOI: https://doi.org/10.1016/S0022-0728(99)00364-2.

[46] Tom Smolinka and Jurgen Garche. *Electrochemical Power Sources: Fundamentals, Systems, and Applications: Hydrogen Production by Water Electrolysis*. Elsevier, 2021. ISBN: 978-0-12-819424-9.

[47] Piero Zanello and Neil G. Connelly. *Inorganic Electrochemistry*. The Royal Society of Chemistry, Aug. 5, 2003. ISBN: 978-0-85404-661-4. DOI: 10.1039/9781847551146.

[48] Frank Forstmann, Enrique Díaz-Herrera, and Eusebio Juaristi. "The Fermi level in electrolytes—about electrochemical potentials at electrolyte-electrode interfaces". In: *AIP Conference Proceedings*. 2007. Vol. 979. ISSN: 0094243X. México City (México): AIP, 2008, pp. 181–194. DOI: 10.1063/1.2901841.

[49] Edmund J. F. Dickinson and Gareth Hinds, J. Electrochem. Soc. (**2019**), 166, 4, F221–F231, DOI: 10.1149/2.0361904jes.

[50] Ahmad T Mayyas, Mark F Ruth, Bryan S Pivovar, Guido Bender, and Keith B Wipke. *Manufacturing Cost Analysis for Proton Exchange Membrane Water Electrolyzers*. NREL/TP-6A20-72740, 1557965. Aug. 13, 2019, NREL/TP–6A20–72740, 1557965. DOI: 10.2172/1557965.

[51] Alex Badgett, Joe Brauch, Amogh Thatte, Rachel Rubin, Christopher Skangos, Xiaohua Wang, Rajesh Ahluwalia, Bryan Pivovar, and Mark Ruth. *Updated Manufactured Cost Analysis for Proton Exchange Membrane Water Electrolyzers*. NREL/TP–6A20-87625, 2311140, MainId:88400. Feb. 16, 2024, NREL/TP–6A20–87625, 2311140, MainId:88400. DOI: 10.2172/2311140.

[52] Markus Stähler, Andrea Stähler, Fabian Scheepers, Marcelo Carmo, Werner Lehnert, and Detlef Stolten, Int. J. of Hydrogen Energy, (**2020**), 45, 7, pp. 4008–4014, DOI: 10.1016/j.ijhydene.2019.12.016.

[53] P. Trinke, G. P. Keeley, M. Carmo, B. Bensmann, and R. Hanke-Rauschenbach, J Electrochem Soc, (**2019**), 166, 8, F465–F471, DOI: 10.1149/2.0171908jes.

[54] Elena Borgardt, Lennard Giesenberg, Marc Reska, Martin Müller, Klaus Wippermann, Manuel Langemann, Werner Lehnert, and Detlef Stolten, Int. J. of Hydrogen Energy, (**2019**), 44, 42, pp. 23556–23567, DOI: 10.1016/j.ijhydene.2019.07.075.

[55] Agate Martin, Patrick Trinke, Markus Stähler, Andrea Stähler, Fabian Scheepers, Boris Bensmann, Marcelo Carmo, Werner Lehnert, and Richard Hanke-Rauschenbach, Journal of The Electrochemical Society, (**2022**), 169, 1, DOI: 10.1149/1945-7111/ac4459.

[56] A. Hintzen, M. Stähler, and I. Friedrich, J. Electrochem. Soc. (**2025**), 172, 4, p. 044512, DOI: 10.1149/1945-7111/adcd00.

[57] A. P. Manso, F. F. Marzo, J. Barranco, X. Garikano, and M. G. Mujika, Int J Hydrogen Energ, (**2012**), 37, 20, pp. 15256–15287, DOI: 10.1016/j.ijhydene.2012.07.076.

[58] Jianhu Nie and Yitung Chen, International Journal of Hydrogen Energy, (**2010**), 35, 8, pp. 3183–3197, DOI: 10.1016/j.ijhydene.2010.01.050.

[59] S. Toghyani, E. Afshari, E. Baniasadi, and S.A. Atyabi, Electrochimica Acta, (**2018**), 267, pp. 234–245, DOI: 10.1016/j.electacta.2018.02.078.

[60] H. Ito, T. Maeda, A. Nakano, Y. Hasegawa, N. Yokoi, C. M. Hwang, M. Ishida, A. Kato, and T. Yoshida, Int J Hydrogen Energ, (**2010**), 35, 18, pp. 9550–9560, DOI: 10.1016/j.ijhydene.2010.06.103.

[61] J. K. Lee and A. Bazylak, ECS Transactions, (**2019**), 92, pp. 801–820, DOI: 10.1149/09208.0801ecst.

[62] Carl Cesar Weber, Tobias Schuler, Ruben De Bruycker, Lorenz Gubler, Felix N. Büchi, and Salvatore De Angelis, Journal of Power Sources Advances, (**2022**), 15, p. 100095, DOI: 10.1016/j.powera.2022.100095.

[63] R. Bock, H. Karoliussen, F. Seland, B. G. Pollet, M. S. Thomassen, S. Holdcroft, and O. S. Burheim, Int J Hydrogen Energ, (**2020**), 45, 2, pp. 1236–1254, DOI: 10.1016/j.ijhydene.2019.01.013.

[64] Sayed M. Saba, Martin Müller, Martin Robinius, and Detlef Stolten, Int. J. of Hydrogen Energy, (**2018**), 43, 3, pp. 1209–1223, DOI: 10.1016/j.ijhydene.2017.11.115.

[65] Ahmad Mayyas and Margaret Mann, Procedia Manufacturing, (**2019**), 33, pp. 508–515, DOI: 10.1016/j.promfg.2019.04.063.

[66] Subramani Krishnan, Vinzenz Koning, Matheus Theodorus De Groot, Arend De Groot, Paola Granados Mendoza, Martin Junginger, and Gert Jan Kramer, International Journal of Hydrogen Energy, (**2023**), 48, 83, pp. 32313–32330, DOI: 10.1016/j.ijhydene.2023.05.031.

[67] Nuria Rojas, Margarita Sánchez-Molina, Gema Sevilla, Ernesto Amores, Eluxka Almandoz, Joseba Esparza, Marlon R. Cruz Vivas, and Carles Colominas, International Journal of Hydrogen Energy, (**2021**), 46, 51, pp. 25929–25943, DOI: 10.1016/j.ijhydene.2021.03.100.

[68] Hans Becker, Edmund J. F. Dickinson, Xuekun Lu, Ulf Bexell, Sebastian Proch, Claire Moffatt, Mikael Stenström, Graham Smith, and Gareth Hinds, Energy Environ. Sci. (**2022**), 15, 6, pp. 2508–2518, DOI: 10.1039/D2EE00876A.

[69] Aldo Saul Gago, Philipp Lettenmeier, Svenja Stiber, Asif Syed Ansar, Li Wang, and Kaspar Andreas Friedrich, ECS Trans. (**2018**), 85, 13, pp. 3–13, DOI: 10.1149/08513.0003ecst.

[70] Andrea Kellenberger, Nicolae Vaszilcsin, Delia Duca, Mircea Laurentiu Dan, Narcis Duteanu, Svenja Stiber, Tobias Morawietz, Indro Biswas, Syed Asif Ansar, Pawel Gazdzicki, Florian J. Wirkert, Jeffrey Roth, Ulrich Rost, Michael Brodmann, Aldo Saul Gago, and K. Andreas Friedrich, Materials, (**2022**), 15, 5, p. 1628, DOI: 10.3390/ma15051628.

[71] Gustav Wilhelm Sievers, Kirsten Anklam, Rouven Henkel, Thorsten Hickmann, and Volker Brüser, International Journal of Hydrogen Energy, (**2019**), 44, 5, pp. 2435–2445, DOI: 10.1016/j.ijhydene.2018.12.020.

[72] Devashish Kulkarni, Ryan Ouimet, Bryan Erb, Dilworth Y. Parkinson, Hung-Ming Chang, Cliffton Wang, Andrew Smeltz, Christopher Capuano, and Iryna V. Zenyuk, ACS Appl. Mater. Interfaces, (**2023**), 15, 41, pp. 48060–48071, DOI: 10.1021/acsami.3c06899.

[73] Tobias Schuler, Carl Cesar Weber, Jacob A. Wrubel, Lorenz Gubler, Bryan Pivovar, Felix N. Büchi, and Guido Bender, Advanced Energy Materials, (**2024**), p. 2302786, DOI: 10.1002/aenm.202302786.

[74] Martin Müller, Marcelo Carmo, Andreas Glüsen, Michael Hehemann, Sayed Saba, Walter Zwaygardt, and Detlef Stolten, Int. J. of Hydrogen Energy, (**2019**), 44, 21, pp. 10147–10155, DOI: 10.1016/j.ijhydene.2019.02.139.

[75] Jakub Mališ, Petr Mazúr, Martin Paidar, Tomas Bystron, and Karel Bouzek, Int. J. of Hydrogen Energy, (**2016**), 41, 4, pp. 2177–2188, DOI: 10.1016/j.ijhydene.2015.11.102.

[76] S.A. Grigoriev, V.I. Porembskiy, S.V. Korobtsev, V.N. Fateev, F. Auprêtre, and P. Millet, International Journal of Hydrogen Energy, (**2011**), 36, 3, pp. 2721–2728, DOI: 10.1016/j.ijhydene.2010.03.058.

[77] A. Stähler, M. Stähler, F. Scheepers, W. Lehnert, and M. Carmo, J. Electrochem. Soc. (**2022**), 169, 3, p. 034522, DOI: 10.1149/1945-7111/ac5c9b.

[78] C. Klose, P. Trinke, T. Bohm, B. Bensmann, S. Vierrath, R. Hanke-Rauschenbach, and S. Thiele, J Electrochem Soc, (**2018**), 165, 16, F1271–F1277, DOI: 10.1149/2.1241814jes.

[79] Nicole Marie Brennan, Abigail Teresa Evans, Meredith Kate Fritz, Stephanie Allison Peak, and Haley Elizabeth Von Holst, IJERPH, (**2021**), 18, 20, p. 10900, DOI: 10.3390/ijerph182010900.

[80] Francesca Spyrakis and Tommaso A. Dragani, Toxics, (**2023**), 11, 9, p. 721, DOI: 10.3390/toxics11090721.

[81] Nicholas D. Tyrrell, Org. Process Res. Dev. (**2023**), 27, 8, pp. 1422–1426, DOI: 10.1021/acs.oprd.3c00199.

[82] Carolin Klose, Torben Saatkamp, Andreas Münchinger, Luca Bohn, Giorgi Titvinidze, Matthias Breitwieser, Klaus-Dieter Kreuer, and Severin Vierrath, Advanced Energy Materials, (**2020**), 10, 14, p. 1903995, DOI: 10.1002/aenm.201903995.

[83] Zhenye Kang, Zihao Fan, Fan Zhang, Zhenyu Zhang, Chao Tian, Weina Wang, Jing Li, Yijun Shen, and Xinlong Tian, Materials, (**2022**), 15, 20, p. 7209, DOI: 10.3390/ma15207209.

[84] Emily Leonard, Andrew D. Shum, Nemanja Danilovic, Christopher Capuano, Katherine E. Ayers, Lalit M Pant, Adam Z. Weber, Xianghui Xiao, Dilworth Y. Parkinson, and Iryna V. Zenyuk, Sustainable Energy & Fuels, (**2020**), 4, 2, pp. 921–931, DOI: 10.1039/c9se00364a.

[85] Markus Stähler, Andrea Stähler, Fabian Scheepers, Marcelo Carmo, and Detlef Stolten, International Journal of Hydrogen Energy, (**2019**), 44, 14, pp. 7053–7058, DOI: 10.1016/j.ijhydene.2019.02.016.

[86] Janghoon Park, Zhenye Kang, Guido Bender, Michael Ulsh, and Scott A. Mauger, Journal of Power Sources, (**2020**), 479, p. 228819, DOI: 10.1016/j.jpowsour.2020.228819.

[87] Manas Mandal, Antoni Valls, Niklas Gangnus, and Marc Secanell, J. Electrochem. Soc. (**2018**), 165, 7, F543–F552, DOI: 10.1149/2.1101807jes.

[88] Andreas Willert, Farzin Z. Tabary, Tatiana Zubkova, Paolo E. Santangelo, Marcello Romagnoli, and Reinhard R. Baumann, International Journal of Hydrogen Energy, (**2022**), 47, 48, pp. 20973–20986, DOI: 10.1016/j.ijhydene.2022.04.197.

[89] Michael Adamski, Nicolas Peressin, Steven Holdcroft, and Bruno G. Pollet, Ultrasonics Sonochemistry, (**2020**), 60, p. 104758, DOI: 10.1016/j.ultsonch.2019.104758.

[90] Shalmali Bapat, Christopher Giehl, Sebastian Kohsakowski, Volker Peinecke, Michael Schäffler, and Doris Segets, Advanced Powder Technology, (**2021**), 32, 10, pp. 3845–3859, DOI: 10.1016/j.apt.2021.08.030.

[91] S. Khandavalli, J. H. Park, N. N. Kariuki, S. F. Zaccarine, S. Pylypenko, D. J. Myers, M. Ulsh, and S. A. Mauger, ACS Appl Mater Interfaces, (**2019**), 11, 48, pp. 45068–45079, DOI: 10.1021/acsami.9b14415.

[92] Xiang Lyu, Jayson Foster, Robin Rice, Elliot Padgett, Erin B. Creel, Jianlin Li, Haoran Yu, David A. Cullen, Nancy N. Kariuki, Jae Hyung Park, Deborah J. Myers, Scott Mauger, Guido Bender, Svitlana Pylypenko, and Alexey Serov, Journal of Power Sources, (**2023**), 581, p. 233503, DOI: 10.1016/j.jpowsour.2023.233503.

[93] Sunilkumar Khandavalli, Jae Hyung Park, Nancy N. Kariuki, Deborah J. Myers, Jonathan J. Stickel, Katherine Hurst, K. C. Neyerlin, Michael Ulsh, and Scott A. Mauger, ACS Appl. Mater. Interfaces, (**2018**), 10, 50, pp. 43610–43622, DOI: 10.1021/acsami.8b15039.

[94] Amin Said Amin, Adib Caidi, Thomas Lange, Ivan Radev, Daniel John Seale Sandbeck, Wladimir Philippi, Mena-Alexander Kräenbring, Melda Öztürk, Volker Peinecke, Dietmar Lerche, Fatih Özcan, and Doris Segets, Part & Part Syst Charact, (**2024**), p. 2400069, DOI: 10.1002/ppsc.202400069.

[95] J. H. Lee, G. Doo, S. H. Kwon, S. Choi, H. T. Kim, and S. G. Lee, Sci Rep, (**2018**), 8, 1, p. 10739, DOI: 10.1038/s41598-018-28779-y.

[96] Makoto Yamaguchi, Takuro Matsunaga, Kazuki Amemiya, Akihiro Ohira, Naoki Hasegawa, Kazuhiko Shinohara, Masaki Ando, and Toshihiko Yoshida, J. Phys. Chem. B, (**2014**), p. 141210091239007, DOI: 10.1021/jp506814m.

[97] Huiyuan Liu, Linda Ney, Nada Zamel, and Xianguo Li, Applied Sciences, (**2022**), 12, 8, p. 3776, DOI: 10.3390/app12083776.

[98] F. Scheepers, A. Stahler, M. Stahler, M. Carmo, W. Lehnert, and D. Stolten, J Coat Technol Res, (**2019**), 16, 5, pp. 1213–1221, DOI: 10.1007/s11998-019-00206-5.

[99] K. A. Stoerzinger, L. Qiao, M. D. Biegalski, and Y. Shao-Horn, J Phys Chem Lett, (**2014**), 5, 10, pp. 1636–41, DOI: 10.1021/jz500610u.

[100] C. Spori, J. T. H. Kwan, A. Bonakdarpour, D. P. Wilkinson, and P. Strasser, Angew Chem Int Ed Engl, (**2017**), 56, 22, pp. 5994–6021, DOI: 10.1002/anie.201608601.

[101] Caroline Rozain, Eric Mayousse, Nicolas Guillet, and Pierre Millet, Applied Catalysis B: Environmental, (**2016**), 182, pp. 153–160, DOI: 10.1016/j.apcatb.2015.09.013.

[102] Hong Nhan Nong, Hoang Phi Tran, Camillo Spöri, Malte Klingenhof, Lorenz Frevel, Travis E. Jones, Thorsten Cottre, Bernhard Kaiser, Wolfram Jaegermann, Robert Schlögl, Detre Teschner, and Peter Strasser, Zeitschrift für Physikalische Chemie, (**2020**), 234, 5, pp. 787–812, DOI: 10.1515/zpch-2019-1460.

[103] H. S. Oh, H. N. Nong, T. Reier, M. Gliech, and P. Strasser, Chem Sci, (**2015**), 6, 6, pp. 3321–3328, DOI: 10.1039/c5sc00518c.

[104] Janis Geppert, Philipp Röse, Steffen Czioska, Daniel Escalera-López, Alexey Boubnov, Erisa Saraçi, Serhiy Cherevko, Jan-Dierk Grunwaldt, and Ulrike Krewer, J. Am. Chem. Soc. (**2022**), 144, 29, pp. 13205–13217, DOI: 10.1021/jacs.2c03561.

[105] F. Bauer, S. Denneler, and M. Willert-Porada, Journal of Polymer Science Part B: Polymer Physics, (**2005**), 43, 7, pp. 786–795, DOI: 10.1002/polb.20367.

[106] W. Xu and K. Scott, Int J Hydrogen Energ, (**2010**), 35, 21, pp. 12029–12037, DOI: 10.1016/j.ijhydene.2010.08.055.

[107] V. Monteseguro, J. A. Sans, V. Cuartero, F. Cova, Igor A. Abrikosov, W. Olovsson, C. Popescu, S. Pascarelli, G. Garbarino, H. Johan M. Jönsson, T. Irifune, and D. Errandonea, Sci Rep, (**2019**), 9, 1, p. 8940, DOI: 10.1038/s41598-019-45401-x.

[108] Lois Anne Zook and Johna Leddy, Anal. Chem. (**1996**), 68, 21, pp. 3793–3796, DOI: 10.1021/ac960604e.

[109] Maximilian Bernt and Hubert A. Gasteiger, Journal of The Electrochemical Society, (**2016**), 163, 11, F3179–F3189, DOI: 10.1149/2.0231611jes.

[110] C. Rozain, E. Mayousse, N. Guillet, and P. Millet, Appl Catal B-Environ, (**2016**), 182, pp. 123–131, DOI: 10.1016/j.apcatb.2015.09.011.

[111] Sourov Ghosh, Hidenori Ohashi, Hiroshi Tabata, Yoshiyuki Hashimasa, and Takeo Yamaguchi, Int. J. of Hydrogen Energy, (**2015**), 40, 45, pp. 15663–15671, DOI: 10.1016/j.ijhydene.2015.09.080.

[112] D. S. Hwang, C. H. Park, S. C. Yi, and Y. M. Lee, Int J Hydrogen Energ, (**2011**), 36, 16, pp. 9876–9885, DOI: 10.1016/j.ijhydene.2011.05.073.

[113] Elliot Padgett, Guido Bender, Andrew Huag, Krzysztof Lewinski, Fuxia Sun, Haoran Yu, David Cullen, Andrew Steinbach, and Shaun M Alia, J. Electrochem. Soc. (**2023**), DOI: 10.1149/1945-7111/acee25.

[114] D. R. Morris, S. P. Liu, D. Villegas Gonzalez, and J. T. Gostick, ACS Appl Mater Interfaces, (**2014**), 6, 21, pp. 18609–18, DOI: 10.1021/am503509j.

[115] Mohammad Ahadi, Mickey Tam, Jürgen Stumper, and Majid Bahrami, Int. J. of Hydrogen Energy, (**2019**), 44, 7, pp. 3603–3614, DOI: 10.1016/j.ijhydene.2018.12.016.

[116] M. Bernt, C. Schramm, J. Schröter, C. Gebauer, J. Byrknes, C. Eickes, and H. A. Gasteiger, Journal of The Electrochemical Society, (**2021**), 168, 8, DOI: 10.1149/1945-7111/ac1eb4.

[117] Julian Parra-Restrepo, Rémi Bligny, Jérôme Dillet, Sophie Didierjean, Didier Stemmelen, Christian Moyne, Alain Degiovanni, and Gaël Maranzana, International Journal of Hydrogen Energy, (**2020**), 45, 15, pp. 8094–8106, DOI: 10.1016/j.ijhydene.2020.01.100.

[118] Marian Chatenet, Bruno G. Pollet, Dario R. Dekel, Fabio Dionigi, Jonathan Deseure, Pierre Millet, Richard D. Braatz, Martin Z. Bazant, Michael Eikerling, Iain Staffell, Paul Balcombe, Yang Shao-Horn, and Helmut Schäfer, Chem. Soc. Rev. (**2022**), 51, 11, pp. 4583–4762, DOI: 10.1039/D0CS01079K.

[119] Caroline Rozain, Eric Mayousse, Nicolas Guillet, and Pierre Millet, Applied Catalysis B: Environmental, (**2016**), 182, pp. 153–160, DOI: 10.1016/j.apcatb.2015.09.013.

[120] Jorge Torrero, Tobias Morawietz, Daniel García Sanchez, Dmitry Galyamin, Maria Retuerto, Vlad Martin-Diaconescu, Sergio Rojas, José Antonio Alonso, Aldo Saul Gago, and Kaspar Andreas Friedrich, Advanced Energy Materials, (**2023**), 13, 23, p. 2204169, DOI: 10.1002/aenm.202204169.

[121] O. S. Burheim, H. N. Su, H. H. Hauge, S. Pasupathi, and B. G. Pollet, Int J Hydrogen Energ, (**2014**), 39, 17, pp. 9397–9408, DOI: 10.1016/j.ijhydene.2014.03.206.

[122] Stefania Siracusano, Stefano Trocino, Nicola Briguglio, Fabiola Pantò, and Antonino S. Aricò, Journal of Power Sources, (**2020**), 468, p. 228390, DOI: 10.1016/j.jpowsour.2020.228390.

[123] Maximilian Möckl, Matthias F. Ernst, Matthias Kornherr, Frank Allebrod, Maximilian Bernt, Jan Byrknes, Christian Eickes, Christian Gebauer, Antonina Moskovtseva, and Hubert A. Gasteiger, J. Electrochem. Soc. (**2022**), 169, 6, p. 064505, DOI: 10.1149/1945-7111/ac6d14.

[124] J. Lopata, Z. Kang, J. Young, G. Bender, J. W. Weidner, and S. Shimpalee, J. Electrochem. Soc. (**2020**), 167, 6, p. 064507, DOI: 10.1149/1945-7111/ab7f87.

[125] Zhenye Kang, Shaun M. Alia, Marcelo Carmo, and Guido Bender, Journal of Power Sources, (**2021**), 481, DOI: 10.1016/j.jpowsour.2020.229012.

[126] Olha Panchenko, Marcelo Carmo, Marcin Rasinski, Tobias Arlt, Ingo Manke, Martin Müller, and Werner Lehnert, Materials Today Energy, (**2020**), 16, DOI: 10.1016/j.mtener.2020.100394.

[127] Andrea Burdzik, Markus Stähler, Irene Friedrich, Marcelo Carmo, and Detlef Stolten, J Coat Technol Res, (**2018**), 15, 6, pp. 1423–1432, DOI: 10.1007/s11998-018-0074-3.

[128] Fabian Scheepers, Andrea Stähler, Markus Stähler, Marcelo Carmo, Werner Lehnert, and Detlef Stolten, Coatings, (**2018**), 8, 12, DOI: 10.3390/coatings8120450.

[129] C. Liu, K. Wippermann, M. Rasinski, Y. Suo, M. Shviro, M. Carmo, and W. Lehnert, ACS Appl Mater Interfaces, (**2021**), 13, 14, pp. 16182–16196, DOI: 10.1021/acsami.0c20690.

[130] Shaun M. Alia, Sarah Stariha, and Rod L. Borup, J. Electrochem. Soc. (**2019**), 166, 15, F1164–F1172, DOI: 10.1149/2.0231915jes.

[131] G. Bender, M. Carmo, T. Smolinka, A. Gago, N. Danilovic, M. Mueller, F. Ganci, A. Fallisch, P. Lettenmeier, K. A. Friedrich, K. Ayers, B. Pivovar, J. Mergel, and D. Stolten, Int J Hydrogen Energ, (**2019**), 44, 18, pp. 9174–9187, DOI: 10.1016/j.ijhydene.2019.02.074.

[132] Thomas Lickert, Stefanie Fischer, James L. Young, Selina Klose, Irene Franzetti, Daniel Hahn, Zhenye Kang, Meital Shviro, Fabian Scheepers, Marcelo Carmo, Tom Smolinka, Guido Bender, and Sebastian Metz, Applied Energy, (**2023**), 352, p. 121898, DOI: 10.1016/j.apenergy.2023.121898.

[133] Luca Bohn, Miriam von Holst, Edgar Cruz Ortiz, Matthias Breitwieser, Severin Vierrath, and Carolin Klose, Journal of The Electrochemical Society, (**2022**), 169, 5, DOI: 10.1149/1945-7111/ac6e09.

[134] Robin Girod, Timon Lazaridis, Hubert A. Gasteiger, and Vasiliki Tileli, Nat Catal, (**2023**), DOI: 10.1038/s41929-023-00947-y.

[135] Arafeh Bigdeli, Mohammad Reza Hormozi-Nezhad, Mehdi Jalali-Heravi, Mohammad Reza Abedini, and Farzad Sharif-Bakhtiar, RSC Adv. (**2014**), 4, 104, pp. 60135–60143, DOI: 10.1039/C4RA10375K.

[136] B.K. Kakati, V.K. Yamsani, K.S. Dhathathreyan, D. Sathiyamoorthy, and A. Verma, Carbon, (**2009**), 47, 10, pp. 2413–2418, DOI: 10.1016/j.carbon.2009.04.034.

[137] Andrea Lanzini, Pierluigi Leone, and Pietro Asinari, Journal of Power Sources, (**2009**), 194, 1, pp. 408–422, DOI: 10.1016/j.jpowsour.2009.04.062.

[138] William D. Pyrz and Douglas J. Buttrey, Langmuir, (**2008**), 24, 20, pp. 11350–11360, DOI: 10.1021/la801367j.

[139] M C Pravin, S Karthikeyan, B Sathyabama, and D Synthiya Vinothini, INDIAN J. ENG. MATER. SCI. (**2017**), 24, pp. 261–269.

[140] L. Cervera Gontard, D. Ozkaya, and R. E. Dunin-Borkowski, Ultramicroscopy, (**2011**), 111, 2, pp. 101–6, DOI: 10.1016/j.ultramic.2010.10.011.

[141] Yen-Chun Chen, Chrysoula Karageorgiou, Jens Eller, Thomas J. Schmidt, and Felix N. Büchi, Journal of Power Sources, (**2022**), 539, p. 231612, DOI: 10.1016/j.jpowsour.2022.231612.

[142] Johnathon Farmer, Binh Duong, Supapan Seraphin, Sirivatch Shimpalee, Michael J. Martínez-Rodríguez, and John W. Van Zee, Journal of Power Sources, (**2012**), 197, pp. 1–11, DOI: 10.1016/j.jpowsour.2011.08.064.

[143] D. Itzhak, I. Dinstein, and T. Zilberberg, Corrosion Science, (**1981**), 21, 1, pp. 17–22, DOI: 10.1016/0010-938X(81)90059-7.

[144] E.N Codaro, R.Z Nakazato, A.L Horovistiz, L.M.F Ribeiro, R.B Ribeiro, and L.R.O Hein, Materials Science and Engineering: A, (**2002**), 334, 1, pp. 298–306, DOI: 10.1016/S0921-5093(01)01892-5.

[145] Da-Hai Xia, Shizhe Song, Lei Tao, Zhenbo Qin, Zhong Wu, Zhiming Gao, Jihui Wang, Wenbin Hu, Yashar Behnamian, and Jing-Li Luo, Journal of Materials Science & Technology, (**2020**), 53, pp. 146–162, DOI: 10.1016/j.jmst.2020.04.033.

[146] Renate Hiesgen, Tobias Morawietz, Michael Handl, Martina Corasaniti, and K. Andreas Friedrich, Electrochimica Acta, (**2015**), 162, pp. 86–99, DOI: 10.1016/j.electacta.2014.11.122.

[147] Velislava Yonkova, Nikolai Utsch, Julian Borowec, Rüdiger-A. Eichel, Florian Hausen, Fabian Scheepers, Steffen Brinckmann, and Ruth Schwaiger, JOM, (**2024**), 76, 5, pp. 2315–2325, DOI: 10.1007/s11837-024-06485-7.

[148] Julian Borowec, Jean-Pierre Poc, Shibabrata Basak, Ladislaus Dobrenizki, Günter Schmid, Eva Jodat, André Karl, Rüdiger-A. Eichel, and Florian Hausen, J. Electrochem. Soc. (**2025**), 172, 5, p. 054511, DOI: 10.1149/1945-7111/add213.

[149] Adarsh Jain, Vineetha Vinayakumar, André Olean-Oliveira, Christian Marcks, Mohit Chatwani, Anna K. Mechler, Corina Andronescu, and Doris Segets, ChemCatChem, (**2024**), 16, 5, e202301461, DOI: 10.1002/cctc.202301461.

[150] Mohammad J. Eslamibidgoli, Fabian P. Tipp, Jenia Jitsev, Jasna Jankovic, Michael H. Eikerling, and Kourosh Malek, RSC Adv. (**2021**), 11, 51, pp. 32126–32134, DOI: 10.1039/D1RA05324H.

[151] Kevin P. Treder, Chen Huang, Cameron G. Bell, Thomas J. A. Slater, Manfred E. Schuster, Doğan Özkaya, Judy S. Kim, and Angus I. Kirkland, npj Comput Mater, (**2023**), 9, 1, p. 18, DOI: 10.1038/s41524-022-00949-7.

[152] Rajneesh Kumar, P. Kulashekar, B. Dhanasekar, and B. Ramamoorthy, International Journal of Machine Tools and Manufacture, (**2005**), 45, 2, pp. 228–234, DOI: 10.1016/j.ijmachtools.2004.07.001.

[153] G. Bradski, Dr. Dobb's Journal of Software Tools, (**2000**), 120, pp. 122–125.

[154] Olaf Ronneberger, Philipp Fischer, and Thomas Brox. *U-Net: Convolutional Networks for Biomedical Image Segmentation*. May 18, 2015. DOI: 10.48550/arXiv.1505.04597. arXiv: 1505.04597[cs].

[155] Uwe Schmidt, Martin Weigert, Coleman Broaddus, and Gene Myers. "Cell Detection with Star-Convex Polygons". In: *Medical Image Computing and Computer Assisted Intervention – MICCAI 2018*. Ed. by Alejandro F. Frangi, Julia A. Schnabel, Christos Davatzikos, Carlos Alberola-López, and Gabor Fichtinger. Vol. 11071. Series Title: Lecture Notes in Computer Science. Cham: Springer International Publishing, 2018, pp. 265–273. ISBN: 978-3-030-00933-5 978-3-030-00934-2. DOI: 10.1007/978-3-030-00934-2_30.

[156] Stefan Neumann, Azita Rezvani, Matthäus Barasinski, Georg Garnweitner, Doris Segets, and David Rafaja, Microscopy and Microanalysis, (**2023**), 29, 1, pp. 118–130, DOI: 10.1093/micmic/ozac027.

[157] A Gebejes and R. Huertas. "Texture Characterization based on Grey-Level Co-occurrence Matrix". In: *ICTIC 2013*. Conference of Informatics and Management Sciences. 2nd International Conference. 2013.

[158] L.D. Todhunter, R.K. Leach, S.D.A. Lawes, and F. Blateyron, CIRP Journal of Manufacturing Science and Technology, (**2017**), 19, pp. 84–92, DOI: 10.1016/j.cirpj.2017.06.001.

[159] Markus Stöckl, Christin Schlegel, Anne Sydow, Dirk Holtmann, Roland Ulber, and Klaus-Michael Mangold, Electrochimica Acta, (**2016**), 220, pp. 444–452, DOI: 10.1016/j.electacta.2016.10.057.

[160] Sam Slegers, Mathias Linzas, Jeroen Drijkoningen, Jan D'Haen, Naveen Reddy, and Wim Deferme, Coatings, (**2017**), 7, 12, p. 208, DOI: 10.3390/coatings7120208.

[161] Maznah Iliyas Ahmad, Yusri Yusof, Md Elias Daud, Kamran Latiff, Aini Zuhra Abdul Kadir, and Yazid Saif, Int J Adv Manuf Technol, (**2020**), 108, 11, pp. 3645–3659, DOI: 10.1007/s00170-020-05620-3.

[162] A. Townsend, N. Senin, L. Blunt, R.K. Leach, and J.S. Taylor, Precision Engineering, (**2016**), 46, pp. 34–47, DOI: 10.1016/j.precisioneng.2016.06.001.

[163] K.K. Manesh, B. Ramamoorthy, and M. Singaperumal, Wear, (**2010**), 268, 11, pp. 1371–1379, DOI: 10.1016/j.wear.2010.02.005.

[164] Quanren Zeng, Yi Qin, Wenlong Chang, and Xichun Luo, International Journal of Mechanical Sciences, (**2018**), 149, pp. 62–72, DOI: 10.1016/j.ijmecsci.2018.09.044.

[165] Namita Aggarwal and R. K. Agrawal, JSIP, (**2012**), 03, 2, pp. 146–153, DOI: 10.4236/jsip.2012.32019.

[166] Tommy Löfstedt, Patrik Brynolfsson, Thomas Asklund, Tufve Nyholm, and Anders Garpebring, PLoS ONE, (**2019**), 14, 2, e0212110, DOI: 10.1371/journal.pone.0212110.

[167] Nai-Ming Cheng, Yu-Hua Dean Fang, and Tzu-Chen Yen, Ann Nucl Med, (**2013**), 27, 9, pp. 867–869, DOI: 10.1007/s12149-013-0759-8.

[168] Robert M. Haralick, K. Shanmugam, and Its'Hak Dinstein, IEEE Trans. Syst., Man, Cybern. (**1973**), SMC-3, 6, pp. 610–621, DOI: 10.1109/TSMC.1973.4309314.

[169] Mary M. Galloway, Computer Graphics and Image Processing, (**1975**), 4, 2, pp. 172–179, DOI: 10.1016/S0146-664X(75)80008-6.

[170] Guillaume Thibault, Jesus Angulo, and Fernand Meyer, IEEE Trans. Biomed. Eng. (**2014**), 61, 3, pp. 630–637, DOI: 10.1109/TBME.2013.2284600.

[171] M. Amadasun and R. King, IEEE Trans. Syst., Man, Cybern. (**1989**), 19, 5, pp. 1264–1274, DOI: 10.1109/21.44046.

[172] Chengjun Sun and William G Wee, Computer Vision, Graphics, and Image Processing, (**1983**), 23, 3, pp. 341–352, DOI: 10.1016/0734-189X(83)90032-4.

[173] Patrik Brynolfsson, David Nilsson, Turid Torheim, Thomas Asklund, Camilla Thellenberg Karlsson, Johan Trygg, Tufve Nyholm, and Anders Garpebring, Sci Rep, (**2017**), 7, 1, p. 4041, DOI: 10.1038/s41598-017-04151-4.

[174] Camilla Scapicchio, Michela Gabelloni, Andrea Barucci, Dania Cioni, Luca Saba, and Emanuele Neri, Radiol med, (**2021**), 126, 10, pp. 1296–1311, DOI: 10.1007/s11547-021-01389-x.

[175] J. J. M. van Griethuysen, A. Fedorov, C. Parmar, A. Hosny, N. Aucoin, V. Narayan, R. G. H. Beets-Tan, J. C. Fillion-Robin, S. Pieper, and Hjwl Aerts, Cancer Res, (**2017**), 77, 21, e104–e107, DOI: 10.1158/0008-5472.CAN-17-0339.

[176] Marius E. Mayerhoefer, Andrzej Materka, Georg Langs, Ida Häggström, Piotr Szczypiński, Peter Gibbs, and Gary Cook, J Nucl Med, (**2020**), 61, 4, pp. 488–495, DOI: 10.2967/jnumed.118.222893.

[177] Stefan Leger, Alex Zwanenburg, Karoline Pilz, Fabian Lohaus, Annett Linge, Klaus Zöphel, Jörg Kotzerke, Andreas Schreiber, Inge Tinhofer, Volker Budach, Ali Sak, Martin Stuschke, Panagiotis Balermpas, Claus Rödel, Ute Ganswindt, Claus Belka, Steffi Pigorsch, Stephanie E. Combs, David Mönnich, Daniel Zips, Mechthild Krause, Michael Baumann, Esther G. C. Troost, Steffen Löck, and Christian Richter, Sci Rep, (**2017**), 7, 1, p. 13206, DOI: 10.1038/s41598-017-13448-3.

[178] Chintan Parmar, Patrick Grossmann, Johan Bussink, Philippe Lambin, and Hugo J. W. L. Aerts, Sci Rep, (**2015**), 5, 1, p. 13087, DOI: 10.1038/srep13087.

[179] Ksh. Robert Singh, Saurabh Chaudhury, Subir Datta, and Subhasish Deb, Int J Syst Assur Eng Manag, (**2022**), 13, 5, pp. 2683–2697, DOI: 10.1007/s13198-022-01739-6.

[180] Ahmed Hosny, Chintan Parmar, John Quackenbush, Lawrence H. Schwartz, and Hugo J. W. L. Aerts, Nat Rev Cancer, (**2018**), 18, 8, pp. 500–510, DOI: 10.1038/s41568-018-0016-5.

[181] M. G. Poirot, M. W. A. Caan, H. G. Ruhe, A. Bjørnerud, I. Groote, L. Reneman, and H. A. Marquering, Sci Rep, (**2022**), 12, 1, p. 16712, DOI: 10.1038/s41598-022-20703-9.

[182] Rebecka Ericsson-Szecsenyi, Geoffrey Zhang, Gage Redler, Vladimir Feygelman, Stephen Rosenberg, Kujtim Latifi, Crister Ceberg, and Eduardo G. Moros, Technol Cancer Res Treat, (**2022**), 21, p. 15330338221099113, DOI: 10.1177/15330338221099113.

[183] Morgan Michalet, Gladis Valenzuela, Pierre Debuire, Olivier Riou, David Azria, Stéphanie Nougaret, and Marion Tardieu, Physics and Imaging in Radiation Oncology, (**2024**), 31, p. 100613, DOI: 10.1016/j.phro.2024.100613.

[184] Kateryna Artyushkova, Svitlana Pylypenko, Madhu Dowlapalli, and Plamen Atanassov, RSC Adv. (**2012**), 2, 10, p. 4304, DOI: 10.1039/c2ra00574c.

[185] Kateryna Artyushkova, Svitlana Pylypenko, Madhu Dowlapalli, and Plamen Atanassov, Journal of Power Sources, (**2012**), 214, pp. 303–313, DOI: 10.1016/j.jpowsour.2012.04.095.

[186] W. H. Nisbett, A. Kavuri, and M. Das, Sci Rep, (**2020**), 10, 1, p. 13510, DOI: 10.1038/s41598-020-69816-z.

[187] Li Liu, Jie Chen, Paul Fieguth, Guoying Zhao, Rama Chellappa, and Matti Pietikäinen, Int J Comput Vis, (**2019**), 127, 1, pp. 74–109, DOI: 10.1007/s11263-018-1125-z.

[188] Robert J. Gillies, Paul E. Kinahan, and Hedvig Hricak, Radiology, (**2016**), 278, 2, pp. 563–577, DOI: 10.1148/radiol.2015151169.

[189] Fawwaz Ulaby, F. Kouyate, B. Brisco, and T. H. Williams, IEEE Trans. Geosci. Remote Sensing, (**1986**), GE-24, 2, pp. 235–245, DOI: 10.1109/TGRS.1986.289643.

[190] Michael P. Bishop, John F. Shroder, Betty L. Hickman, and Luke Copland, Geomorphology, (**1998**), 21, 3, pp. 217–232, DOI: 10.1016/S0169-555X(97)00061-5.

[191] C. A. Coburn and A. C. B. Roberts, International Journal of Remote Sensing, (**2004**), 25, 20, pp. 4287–4308, DOI: 10.1080/0143116042000192367.

[192] Pasquale Foggia, Gennaro Percannella, Paolo Soda, and Mario Vento, IEEE Trans. Med. Imaging, (**2013**), 32, 10, pp. 1878–1889, DOI: 10.1109/TMI.2013.2268163.

[193] Nickolas Fularczyk, Jessica Di Re, Laura Stertz, Consuelo Walss-Bass, Fernanda Laezza, and Demetrio Labate, Neuroinform, (**2022**), 20, 2, pp. 513–523, DOI: 10.1007/s12021-022-09561-y.

[194] Bela Julesz, Trends in Neurosciences, (**1984**), 7, 2, pp. 41–45, DOI: 10.1016/S0166-2236(84)80275-1.

[195] Bela Julesz, Nature, (**1981**), 290, 5802, pp. 91–97, DOI: 10.1038/290091a0.

[196] Ashima Tyagi, Vibhav Prakash Singh, and Manoj Madhava Gore, Multimed Tools Appl, (**2023**), 82, 13, pp. 20343–20405, DOI: 10.1007/s11042-022-13809-9.

[197] I. Moalla, F. Lebourgeois, H. Emptoz, and A.M. Alimi. "Image analysis for palaeography inspection". In: *Second International Conference on Document Image Analysis for Libraries (DIAL'06)*. Second International Conference on Document Image Analysis for Libraries. Lyon: IEEE, 2006, 8 pp.–311. ISBN: 978-0-7695-2531-0. DOI: 10.1109/DIAL.2006.20.

[198] Itay Bar-Yosef, Isaac Beckman, Klara Kedem, and Itshak Dinstein, IJDAR, (**2007**), 9, 2, pp. 89–99, DOI: 10.1007/s10032-007-0041-5.

[199] S. Dutta, S.K. Pal, S. Mukhopadhyay, and R. Sen, CIRP Journal of Manufacturing Science and Technology, (**2013**), 6, 3, pp. 212–232, DOI: 10.1016/j.cirpj.2013.02.005.

[200] Ritendra Datta, Dhiraj Joshi, Jia Li, and James Z. Wang, ACM Comput. Surv. (**2008**), 40, 2, pp. 1–60, DOI: 10.1145/1348246.1348248.

[201] A.A. Kassim, M.A. Mannan, and Zhu Mian, Image and Vision Computing, (**2007**), 25, 7, pp. 1080–1090, DOI: 10.1016/j.imavis.2006.05.024.

[202] Philippe Lambin, Emmanuel Rios-Velazquez, Ralph Leijenaar, Sara Carvalho, Ruud G.P.M. van Stiphout, Patrick Granton, Catharina M.L. Zegers, Robert Gillies, Ronald Boellard, André Dekker, and Hugo J.W.L. Aerts, European Journal of Cancer, (**2012**), 48, 4, pp. 441–446, DOI: 10.1016/j.ejca.2011.11.036.

[203] Philippe Lambin, Ralph T.H. Leijenaar, Timo M. Deist, Jurgen Peerlings, Evelyn E.C. De Jong, Janita Van Timmeren, Sebastian Sanduleanu, Ruben T.H.M. Larue, Aniek J.G. Even, Arthur Jochems, Yvonka Van Wijk, Henry Woodruff, Johan Van Soest, Tim Lustberg, Erik Roelofs, Wouter Van Elmpt, Andre Dekker, Felix M. Mottaghy, Joachim E. Wildberger, and Sean Walsh, Nat Rev Clin Oncol, (**2017**), 14, 12, pp. 749–762, DOI: 10.1038/nrclinonc.2017.141.

[204] Xueyi Zheng, Zhao Yao, Yini Huang, Yanyan Yu, Yun Wang, Yubo Liu, Rushuang Mao, Fei Li, Yang Xiao, Yuanyuan Wang, Yixin Hu, Jinhua Yu, and Jianhua Zhou, Nat Commun, (**2020**), 11, 1, p. 1236, DOI: 10.1038/s41467-020-15027-z.

[205] Kaustav Bera, Nathaniel Braman, Amit Gupta, Vamsidhar Velcheti, and Anant Madabhushi, Nat Rev Clin Oncol, (**2022**), 19, 2, pp. 132–146, DOI: 10.1038/s41571-021-00560-7.

[206] Song Chen, Stephanie Harmon, Timothy Perk, Xuena Li, Meijie Chen, Yaming Li, and Robert Jeraj, Cancer Imaging, (**2019**), 19, 1, p. 56, DOI: 10.1186/s40644-019-0243-3.

[207] Niels W. Schurink, Simon R. Van Kranen, Sander Roberti, Joost J. M. Van Griethuysen, Nino Bogveradze, Francesca Castagnoli, Najim El Khababi, Frans C. H. Bakers, Shira H. De Bie, Gerlof P. T. Bosma, Vincent C. Cappendijk, Remy W. F. Geenen, Peter A. Neijenhuis, Gerald M. Peterson, Cornelis J. Veeken, Roy F. A. Vliegen, Regina G. H. Beets-Tan, and Doenja M. J. Lambregts, Eur Radiol, (**2022**), 32, 3, pp. 1506–1516, DOI: 10.1007/s00330-021-08251-8.

[208] A. Zwanenburg, M. Vallieres, M. A. Abdalah, Hjwl Aerts, V. Andrearczyk, A. Apte, S. Ashrafinia, S. Bakas, R. J. Beukinga, R. Boellaard, M. Bogowicz, L. Boldrini, I. Buvat, G. J. R. Cook, C. Davatzikos, A. Depeursinge, M. C. Desseroit, N. Dinapoli, C. V. Dinh, S. Echegaray, I. El Naqa, A. Y. Fedorov, R. Gatta, R. J. Gillies, V. Goh, M. Gotz, M. Guckenberger, S. M. Ha, M. Hatt, F. Isensee, P. Lambin, S. Leger, R. T. H. Leijenaar, J. Lenkowicz, F. Lippert, A. Losnegard, K. H. Maier-Hein, O. Morin, H. Muller, S. Napel, C. Nioche, F. Orlhac, S. Pati, E. A. G. Pfaehler, A. Rahmim, A. U. K. Rao, J. Scherer, M. M. Siddique, N. M. Sijtsema, J. Socarras Fernandez, E. Spezi, Rjhm Steenbakkers,

S. Tanadini-Lang, D. Thorwarth, E. G. C. Troost, T. Upadhaya, V. Valentini, L. V. van Dijk, J. van Griethuysen, F. H. P. van Velden, P. Whybra, C. Richter, and S. Lock, Radiology, (**2020**), 295, 2, pp. 328–338, DOI: 10.1148/radiol.2020191145.

[209] Marcin Kozak, Teaching Statistics, (**2009**), 31, 3, pp. 85–86, DOI: 10.1111/j.1467-9639.2009.00387.x.

[210] Roemer J Janse, Tiny Hoekstra, Kitty J Jager, Carmine Zoccali, Giovanni Tripepi, Friedo W Dekker, and Merel Van Diepen, Clinical Kidney Journal, (**2021**), 14, 11, pp. 2332–2337, DOI: 10.1093/ckj/sfab085.

[211] F. J. Anscombe, The American Statistician, (**1973**), 27, 1, pp. 17–21, DOI: 10.1080/00031305.1973.10478966.

[212] Yeu Wen Mak, (**2023**), 349848 Bytes, DOI: 10.6084/M9.FIGSHARE.23730699.

[213] Aylin Alin, WIREs Computational Stats, (**2010**), 2, 2, pp. 247–250, DOI: 10.1002/wics.72.

[214] Justin Matejka and George Fitzmaurice. "Same Stats, Different Graphs: Generating Datasets with Varied Appearance and Identical Statistics through Simulated Annealing". In: *Proceedings of the 2017 CHI Conference on Human Factors in Computing Systems*. CHI '17: CHI Conference on Human Factors in Computing Systems. Denver Colorado USA: ACM, May 2, 2017, pp. 1290–1294. ISBN: 978-1-4503-4655-9. DOI: 10.1145/3025453.3025912.

[215] Alberto Cairo. *The Functional Art: An Introduction to Information Graphics and Visualization: Download the Datasaurus: Never trust summary statistics alone; always visualize your data*. The Functional Art. Aug. 29, 2016. URL: https://thefunctionalart.blogspot.com/2016/08/download-datasaurus-never-trust-summary.html (visited on 08/08/2025).

[216] I. Miccoli, F. Edler, H. Pfnur, and C. Tegenkamp, J Phys Condens Matter, (**2015**), 27, 22, p. 223201, DOI: 10.1088/0953-8984/27/22/223201.

[217] Hamidreza Sadeghifar, Energy Conversion and Management, (**2017**), 154, pp. 191–202, DOI: https://doi.org/10.1016/j.enconman.2017.10.060.

[218] M. Mandal, M. Moore, and M. Secanell, ACS Appl Mater Interfaces, (**2020**), 12, 44, pp. 49549–49562, DOI: 10.1021/acsami.0c12111.

[219] Chuan Liu, Yong Xu, and Yong-Young Noh, Materials Today, (**2015**), 18, 2, pp. 79–96, DOI: 10.1016/j.mattod.2014.08.037.

[220] Edgar Cruz Ortiz, Friedemann Hegge, Matthias Breitwieser, and Severin Vierrath, RSC Advances, (**2020**), 10, 62, pp. 37923–37927, DOI: 10.1039/d0ra06714h.

[221] Friedemann Hegge, Florian Lombeck, Edgar Cruz Ortiz, Luca Bohn, Miriam von Holst, Matthias Kroschel, Jessica Hübner, Matthias Breitwieser, Peter Strasser, and Severin Vierrath, ACS Applied Energy Materials, (**2020**), 3, 9, pp. 8276–8284, DOI: 10.1021/acsaem.0c00735.

[222] Tobias Schuler, Joseph M. Ciccone, Bernd Krentscher, Federica Marone, Christian Peter, Thomas J. Schmidt, and Felix N. Büchi, Advanced Energy Materials, (**2019**), 10, 2, DOI: 10.1002/aenm.201903216.

[223] X. Peng, P. Satjaritanun, Z. Taie, L. Wiles, A. Keane, C. Capuano, I. V. Zenyuk, and N. Danilovic, Adv Sci (Weinh), (**2021**), 8, 21, e2102950, DOI: 10.1002/advs.202102950.

[224] A. Weiß, A. Siebel, M. Bernt, T. H. Shen, V. Tileli, and H. A. Gasteiger, Journal of The Electrochemical Society, (**2019**), 166, 8, F487–F497, DOI: 10.1149/2.0421908jes.

[225] M. Shayesteh, C. Ll. M. Daunt, D. O'Connell, V. Djara, M. White, B. Long, and R. Duffy. "N-type doped germanium contact resistance extraction and evaluation for advanced devices". In: *2011 Proceedings of the European Solid-State Device Research Conference (ESSDERC)*. ESSDERC 2011 - 41st European Solid State Device Research Conference. Helsinki: IEEE, Sept. 2011, pp. 235–238. ISBN: 978-1-4577-0707-0 978-1-4577-0708-7. DOI: 10.1109/ESSDERC.2011.6044191.

[226] Joshua D. Flygare, Adriaan A. Riet, Brian A. Mazzeo, and Dean R. Wheeler, Journal of The Electrochemical Society, (**2015**), 162, 10, A2136–A2144, DOI: 10.1149/2.0571510jes.

[227] Bryson J. Lanterman, Adriaan A. Riet, Nathaniel S. Gates, Joshua D. Flygare, Andrew D. Cutler, John E. Vogel, Dean R. Wheeler, and Brian A. Mazzeo, Journal of The Electrochemical Society, (**2015**), 162, 10, A2145–A2151, DOI: 10.1149/2.0581510jes.

[228] H.H. Berger, Journal of The Electrochemical Society, (**1972**), 119, 4, DOI: 10.1149/1.2404240.

[229] Alexandros Ch. Lazanas and Mamas I. Prodromidis, ACS Meas. Sci. Au, (**2023**), 3, 3, pp. 162–193, DOI: 10.1021/acsmeasuresciau.2c00070.

[230] R. Achanta, A. Shaji, K. Smith, A. Lucchi, P. Fua, and Sabine Süsstrunk, IEEE Trans. Pattern Anal. Mach. Intell. (**2012**), 34, 11, pp. 2274–2282, DOI: 10.1109/TPAMI.2012.120.

[231] Xinlin Xie, Gang Xie, and Xinying Xu, Multimed Tools Appl, (**2018**), 77, 24, pp. 31525–31543, DOI: 10.1007/s11042-018-6150-y.

[232] Peer Neubert and Peter Protzel. "Compact Watershed and Preemptive SLIC: On Improving Trade-offs of Superpixel Segmentation Algorithms". In: *2014 22nd International Conference on Pattern Recognition*. 2014 22nd International Conference on Pattern Recognition (ICPR). Stockholm, Sweden: IEEE, Aug. 2014, pp. 996–1001. ISBN: 978-1-4799-5209-0. DOI: 10.1109/ICPR.2014.181.

[233] Christian A. Combs and Hari Shroff, CP Neuroscience, (**2017**), 79, 1, DOI: 10.1002/cpns.29.

[234] Amicia D. Elliott, Current Protocols in Cytometry, (**2020**), 92, 1, DOI: 10.1002/cpcy.68.

[235] Vishal Panchal, Yanfei Yang, Guangjun Cheng, Jiuning Hu, Mattias Kruskopf, Chieh-I. Liu, Albert F. Rigosi, Christos Melios, Angela R. Hight Walker, David B. Newell, Olga Kazakova, and Randolph E. Elmquist, Commun Phys, (**2018**), 1, 1, p. 83, DOI: 10.1038/s42005-018-0084-6.

[236] Markus Fabich, Optik & Photonik, (**2009**), 4, 2, pp. 40–43, DOI: 10.1002/opph.201190025.

[237] The pandas development team. *pandas-dev/pandas: Pandas*. 2020. DOI: 10.5281/zenodo.3509134.

[238] Wes McKinney. "Data Structures for Statistical Computing in Python". In: Python in Science Conference. Austin, Texas, 2010, pp. 56–61. DOI: 10.25080/Majora-92bf1922-00a.

[239] J. D. Hunter, Computing in Science & Engineering, (**2007**), 9, 3, pp. 90–95, DOI: 10.1109/MCSE.2007.55.

[240] Pauli Virtanen, Ralf Gommers, Travis E. Oliphant, Matt Haberland, Tyler Reddy, David Cournapeau, Evgeni Burovski, Pearu Peterson, Warren Weckesser, Jonathan Bright, St'efan J. van der Walt, Matthew Brett, Joshua Wilson, K. Jarrod Millman, Nikolay Mayorov, Andrew R. J. Nelson, Eric Jones, Robert Kern, Eric Larson, C J Carey, .Ilhan Polat, Yu Feng, Eric W. Moore, Jake VanderPlas, Denis Laxalde, Josef Perktold,

Robert Cimrman, Ian Henriksen, E. A. Quintero, Charles R. Harris, Anne M. Archibald, Ant^onio H. Ribeiro, Fabian Pedregosa, Paul van Mulbregt, and SciPy 1.0 Contributors, Nature Methods, (**2020**), 17, pp. 261–272, DOI: 10.1038s41592-019-0686-2.

[241] Michael Waskom, JOSS, (**2021**), 6, 60, p. 3021, DOI: 10.21105/joss.03021.

[242] Gunnar Taraldsen, (**2020**), DOI: 10.13140/RG.2.2.23673.49769.

[243] Anwar Ul-Hamid. *A Beginners' Guide to Scanning Electron Microscopy*. Cham: Springer International Publishing, 2018. ISBN: 978-3-319-98481-0 978-3-319-98482-7. DOI: 10.1007/978-3-319-98482-7.

[244] Max Frei and Frank Einar Kruis, Powder Technology, (**2018**), 332, pp. 120–130, DOI: 10.1016/j.powtec.2018.03.032.

[245] J. Meija, M. Bushell, M. Couillard, S. Beck, J. Bonevich, K. Cui, J. Foster, J. Will, D. Fox, W. Cho, M. Heidelmann, B. C. Park, Y. C. Park, L. Ren, L. Xu, A. B. Stefaniak, A. K. Knepp, R. Theissmann, H. Purwin, Z. Wang, N. de Val, and L. J. Johnston, Anal Chem, (**2020**), 92, 19, pp. 13434–13442, DOI: 10.1021/acs.analchem.0c02805.

[246] Alida Mazzoli and Orlando Favoni, Powder Technology, (**2012**), 225, pp. 65–71, DOI: 10.1016/j.powtec.2012.03.033.

[247] Ahmed Mahgoub Ahmed Talab, Zhangcan Huang, Fan Xi, and Liu HaiMing, Optik, (**2016**), 127, 3, pp. 1030–1033, DOI: 10.1016/j.ijleo.2015.09.147.

[248] Stéfan Van Der Walt, Johannes L. Schönberger, Juan Nunez-Iglesias, François Boulogne, Joshua D. Warner, Neil Yager, Emmanuelle Gouillart, and Tony Yu, PeerJ, (**2014**), 2, e453, DOI: 10.7717/peerj.453.

[249] Ping-Sung; Liao, Tse-Sheng; Chen, and Pau-Choo Chung, Journal of Information Science and Engineering, (**2001**), 17, pp. 713–721.

[250] Tereza Bautkinova, Nikolai Utsch, Tomas Bystron, Miloslav Lhotka, Martina Kohoutkova, Meital Shviro, and Karel Bouzek, Journal of Power Sources, (**2023**), 565, p. 232913, DOI: 10.1016/j.jpowsour.2023.232913.

[251] Nikolai Utsch, Florian Berg, Fabian Scheepers, Sebastian Holtwerth, Meital Shviro, Werner Lehnert, and Anna K. Mechler, Small Methods, (**2025**), p. 2401842, DOI: 10.1002/smtd.202401842.

[252] A.K. Kulkarni, Kirk H. Schulz, T.S. Lim, and M. Khan, Thin Solid Films, (**1999**), 345, p. 4, DOI: https://doi.org/10.1016/S0040-6090(98)01430-8.

[253] J. S. Kim, F. Cacialli, M. Granstrom, R. H. Friend, N. Johansson, W. R. Salaneck, R. Daik, and W. J. Feast, Synthetic Metals, (**1999**), 101, 111, p. 2, DOI: https://doi.org/10.1016/S0379-6779(98)01127-8.

[254] Scott H. Brewer and Stefan Franzen, J. Phys. Chem. B, (**2002**), 106, pp. 12986–12992, DOI: https://doi.org/10.1021/jp026600x.

[255] Yilei Zhang and Sriram Sundararajan, Journal of Applied Physics, (**2005**), 97, 10, p. 103526, DOI: 10.1063/1.1914947.

[256] Alexander Davis, Yong Han Yeong, Adam Steele, Ilker S. Bayer, and Eric Loth, ACS Appl. Mater. Interfaces, (**2014**), 6, 12, pp. 9272–9279, DOI: 10.1021/am501640h.

[257] Cyril R. Pernet, Rand Wilcox, and Guillaume A. Rousselet, Front. Psychology, (**2013**), 3, DOI: 10.3389/fpsyg.2012.00606.

[258] Cliffton Wang, Keonhag Lee, Christopher Pantayatiwong Liu, Devashish Kulkarni, Plamen Atanassov, Xiong Peng, and Iryna V. Zenyuk, International Materials Reviews, (**2024**), 69, 1, pp. 3–18, DOI: 10.1177/09506608231216665.

[259] Yanqin Chen, Chao Jiang, and Chongdu Cho, Energies, (**2019**), 13, 1, DOI: 10.3390/en13010145.

Appendix

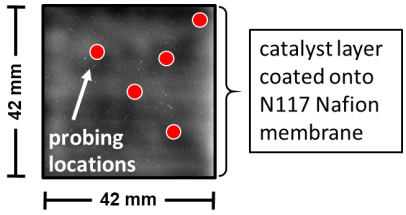

Figure AF.1. Schematic of the CL and the probing locations marked as red dots.

Table AT.1. Overview of the configuration that can be utilized to determine resistance. The two outer traces (P+, P-) were used to apply the current/potential, and the inner traces monitored the response. The number in the gray shaded background is the sum of the number of possible measurements per distance.

P+	S+	S-	P-	d / µm	P+	S+	S-	P-	d / µm	P+	S+	S-	P-	d / µm	P+	S+	S-	P-	d / µm	P+	S+	S-	P-	d / µm	P+	S+	S-	P-	d / µm	P+	S+	S-	P-	d / µm
1	2	3	4	250	1	3	5	7	500	1	4	7	10	750	1	5	9	13	1000	1	6	11	16	1250	1	7	13	19	1500	1	8	15	22	1750	1	9	17	25	2000	1	10	19	28	2250	1	11	21	31	2500
2	3	4	5	250	2	4	6	8	500	2	5	8	11	750	2	6	10	14	1000	2	7	12	17	1250	2	8	14	20	1500	2	9	16	23	1750	2	10	18	26	2000	2	11	20	29	2250	2	12	22	32	2500
3	4	5	6	250	3	5	7	9	500	3	6	9	12	750	3	7	11	15	1000	3	8	13	18	1250	3	9	15	21	1500	3	10	17	24	1750	3	11	19	27	2000	3	12	21	30	2250					
4	5	6	7	250	4	6	8	10	500	4	7	10	13	750	4	8	12	16	1000	4	9	14	19	1250	4	10	16	22	1500	4	11	18	25	1750	4	12	20	28	2000	4	13	22	31	2250					
5	6	7	8	250	5	7	9	11	500	5	8	11	14	750	5	9	13	17	1000	5	10	15	20	1250	5	11	17	23	1500	5	12	19	26	1750	5	13	21	29	2000	5	14	23	32	2250					
6	7	8	9	250	6	8	10	12	500	6	9	12	15	750	6	10	14	18	1000	6	11	16	21	1250	6	12	18	24	1500	6	13	20	27	1750	6	14	22	30	2000										
7	8	9	10	250	7	9	11	13	500	7	10	13	16	750	7	11	15	19	1000	7	12	17	22	1250	7	13	19	25	1500	7	14	21	28	1750	7	15	23	31	2000										
8	9	10	11	250	8	10	12	14	500	8	11	14	17	750	8	12	16	20	1000	8	13	18	23	1250	8	14	20	26	1500	8	15	22	29	1750	8	16	24	32	2000										
9	10	11	12	250	9	11	13	15	500	9	12	15	18	750	9	13	17	21	1000	9	14	19	24	1250	9	15	21	27	1500	9	16	23	30	1750																
10	11	12	13	250	10	12	14	16	500	10	13	16	19	750	10	14	18	22	1000	10	15	20	25	1250	10	16	22	28	1500	10	17	24	31	1750																
11	12	13	14	250	11	13	15	17	500	11	14	17	20	750	11	15	19	23	1000	11	16	21	26	1250	11	17	23	29	1500	11	18	25	32	1750																
12	13	14	15	250	12	14	16	18	500	12	15	18	21	750	12	16	20	24	1000	12	17	22	27	1250	12	18	24	30	1500																						
13	14	15	16	250	13	15	17	19	500	13	16	19	22	750	13	17	21	25	1000	13	18	23	28	1250	13	19	25	31	1500																						
14	15	16	17	250	14	16	18	20	500	14	17	20	23	750	14	18	22	26	1000	14	19	24	29	1250	14	20	26	32	1500																						
15	16	17	18	250	15	17	19	21	500	15	18	21	24	750	15	19	23	27	1000	15	20	25	30	1250																										
16	17	18	19	250	16	18	20	22	500	16	19	22	25	750	16	20	24	28	1000	16	21	26	31	1250																										
17	18	19	20	250	17	19	21	23	500	17	20	23	26	750	17	21	25	29	1000	17	22	27	32	1250																										
18	19	20	21	250	18	20	22	24	500	18	21	24	27	750	18	22	26	30	1000																														
19	20	21	22	250	19	21	23	25	500	19	22	25	28	750	19	23	27	31	1000																														
20	21	22	23	250	20	22	24	26	500	20	23	26	29	750	20	24	28	32	1000																														
21	22	23	24	250	21	23	25	27	500	21	24	27	30	750																																		
22	23	24	25	250	22	24	26	28	500	22	25	28	31	750																																		
23	24	25	26	250	23	25	27	29	500	23	26	29	32	750																																		
24	25	26	27	250	24	26	28	30	500																																					
25	26	27	28	250	25	27	29	31	500																																					
26	27	28	29	250	26	28	30	32	500																																					
27	28	29	30	250																																										
28	29	30	31	250																																										
29	30	31	32	250																																										
				29					26					23					20					17					14					11					8					5					2

Table AT.2. List of surface texture parameters calculated by the LEXT software.

classification	symbol	unit	definition
height parameters	S_q	µm	root mean square height
	S_{sk}	-	skewness
	S_{ku}	-	kurtosis
	S_p	µm	maximum peak height
	S_v	µm	maximum pit depth
	S_z	µm	maximum height
	S_a	µm	arithmetical mean height
space parameters	S_{al}	µm	autocorrelation length
	S_{tr}	-	texture aspect ratio
functional parameters	S_k	µm	core height
	S_{pk}	µm	reduced peak height
	S_{vk}	µm	reduced valley height
	S_{Mr1}	%	material ratio in peak
	S_{Mr2}	%	material ratio in valley
	S_{xp}	µm	peak extreme height
volume parameters	V_{mp}	$\mu m^3/\mu m^2$	peak material volume
	V_{mc}	$\mu m^3/\mu m^2$	core material volume
	V_{vv}	$\mu m^3/\mu m^2$	core void volume
	V_{vc}	$\mu m^3/\mu m^2$	dale void volume

Table AT.3. List of acronyms and corresponding image features.

acronym	**image feature**
FO13	robust mean absolute deviation
FO14	root mean squared
FO5	interquartile range
FO6	kurtosis
FO8	mean absolute deviation
FO9	mean
GLCM13	idn
GLCM14	imc1
GLCM16	inverse variance
GLCM19	joint entropy
GLCM2	cluster prominence
GLCM21	maximum probability
GLCM5	contrast
GLDM1	dependence entropy
GLDM10	large dependence low gray level emphasis
GLDM13	small dependence high gray level emphasis
GLDM2	dependence non uniformity
GLDM3	dependence non uniformity normalized
GLDM7	high gray level emphasis
GLDM8	large dependence emphasis
GLDM9	large dependence high gray level emphasis
GLRLM12	run percentage
GLRLM15	short run high gray level emphasis
GLRLM5	long run emphasis
GLRLM6	long run high gray level emphasis
GLRLM7	long run low gray level emphasis
GLRLM8	low gray level run emphasis
GLSZM10	size zone non uniformity normalized
GLSZM12	small area high gray level emphasis
GLSZM13	small area low gray level emphasis
GLSZM15	zone percentage
GLSZM4	high gray level zone emphasis
GLSZM5	large area emphasis
GLSZM6	large area high gray level emphasis
GLSZM7	large area low gray level emphasis
GLSZM9	size zone non uniformity
NGTDM1	busyness
NGTDM4	contrast

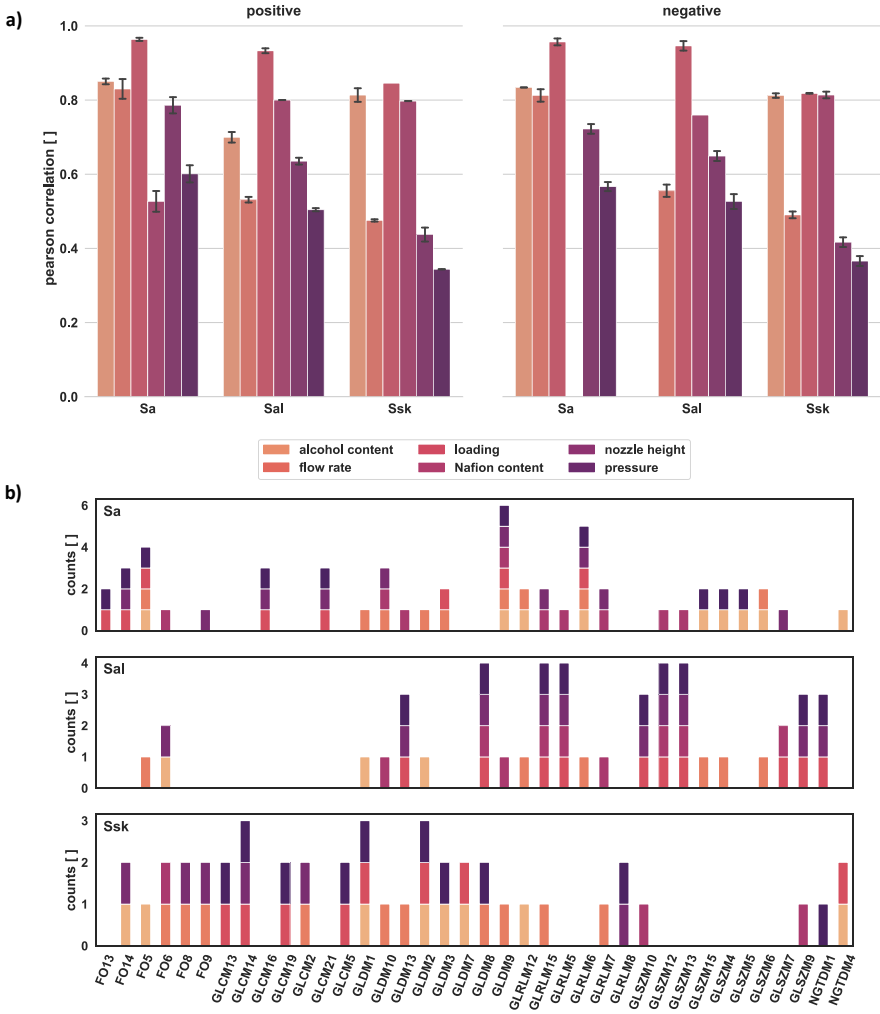

Figure AF.2. Results of the first two steps of the parameter space reduction (a) selecting the ten strongest correlation for each dataset and (b) checking the redundancy of the prioritized IFs. The acronyms referring to the respective IFs calculated by the different matrices, such as the gray-level co-occurrence matrix (GLCM), gray-level run length matrix (GLRLM), gray level size zone matrix (GLSZM), neighboring gray tone difference matrix (NGTDM), gray level dependency matrix (GLDM), and the first-order texture parameter. The exact definition of the parameters can be found in Table AT.3

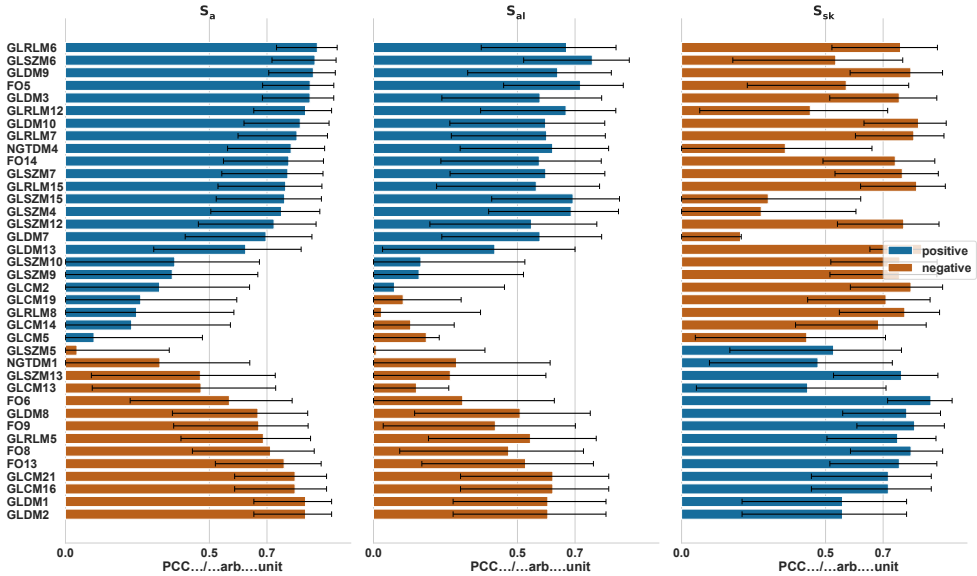

Figure AF.3. Evaluation of the correlation strength between STPs and IFs for the "alcohol content" dataset and the previously reduced IF parameter set.

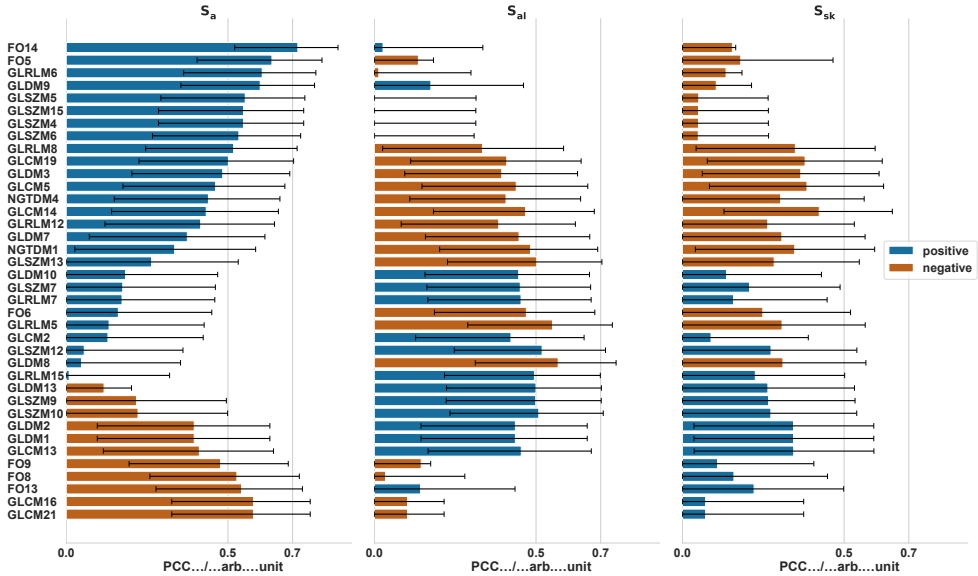

Figure AF.4. Evaluation of the correlation strength between STPs and IFs for the "gas pressure" dataset and the previously reduced IF parameter set.

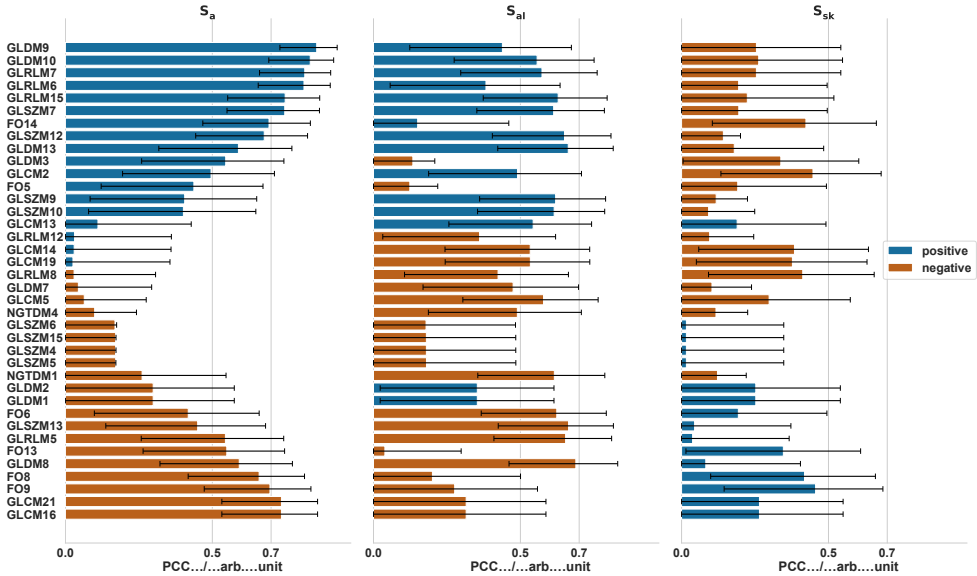

Figure AF.5. Evaluation of the correlation strength between STPs and IFs for the “nozzle height" dataset and the previously reduced IF parameter set.

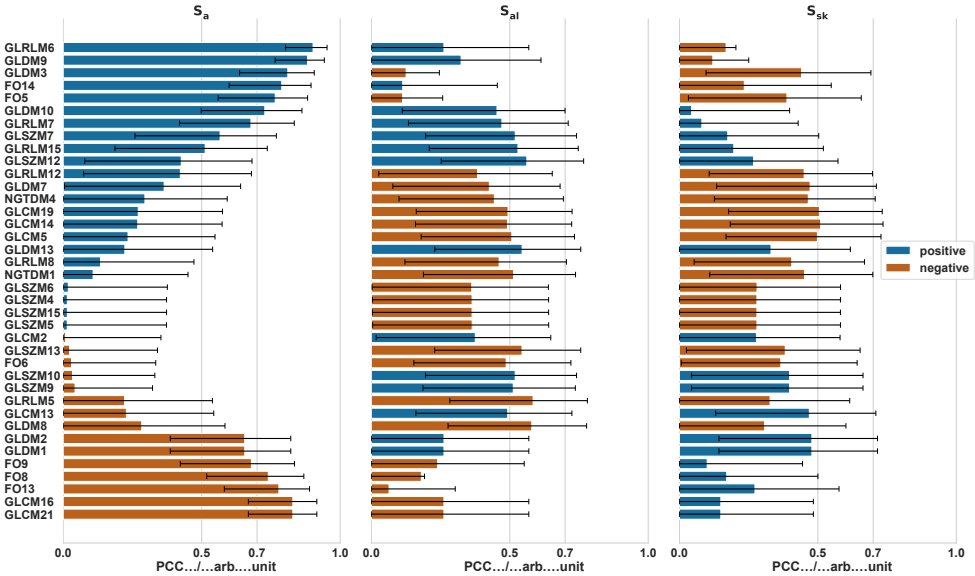

Figure AF.6. Evaluation of the correlation strength between STPs and IFs for the “flow rate" dataset and the previously reduced IF parameter set.

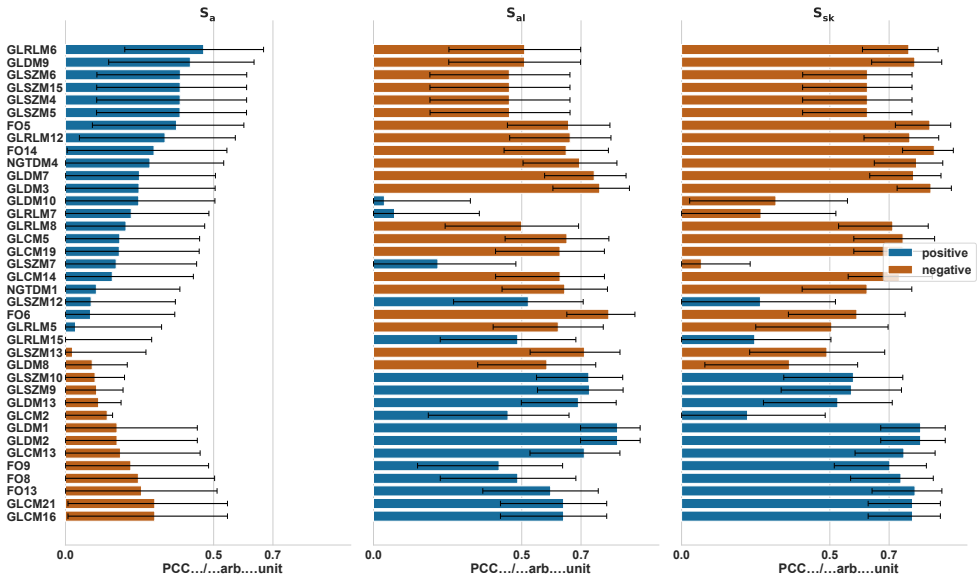

Figure AF.7. Evaluation of the correlation strength between STPs and IFs for the "Nafion content" dataset and the previously reduced IF parameter set.

Table AT.4. Exact definition of the selected parameters presented in Figure 7.7

	definition	equation
surface texture parameter	arithmetical mean height	$S_a = \frac{1}{A}\iint_A \lvert z(x,y)\rvert \, dx \, dy$
	skewness	$S_{sk} = \frac{1}{S_q^3}\left(\frac{1}{A}\iint_A z^3(x,y) \, dx \, dy\right)$
	autocorrelation length	$S_{al} = \min_{(t_x, t_y) \in R} \sqrt{t_x^2 + t_y^2}$ $R = \{(t_x, t_y): f_{ACF}(t_x, t_y) \leq s\}$ $0 \leq s < 1$ $f_{ACF}(t_x, t_y) = \frac{\iint_A z(x,y) z(x - t_x, y - t_y) \, dx \, dy}{\iint_A z(x,y) z(x,y) \, dx \, dy}$
image features	small area high gray level emphasis	$GLSZM12 = \frac{\sum_{i=1}^{N_a} \sum_{j=1}^{N_s} \frac{P(i,j)}{i^2 j^2}}{N_z}$
	long run emphasis	$GLRLM5 = \frac{\sum_{i=1}^{N_a} \sum_{j=1}^{N_r} P(i,j\lvert\theta) j^2}{N_r(\theta)}$
	long run high gray level emphasis	$GLRLM6 = \frac{\sum_{i=1}^{N_a} \sum_{j=1}^{N_r} P(i,j\lvert\theta) i^2 j^2}{N_r(\theta)}$
	short run high gray level emphasis	$GLRLM15 = \frac{\sum_{i=1}^{N_a} \sum_{j=1}^{N_r} \frac{P(i,j\lvert\theta) i^2}{j^2}}{N_r(\theta)}$
	dependence entropy	$GLDM1 = -\sum_{i=1}^{N_a} \sum_{j=1}^{N_d} p(i,j) \log_2(p(i,j) + \epsilon)$
	dependence non-uniformity	$GLDM2 = \frac{\sum_{i=1}^{N_d} \left(\sum_{j=1}^{N_a} P(i,j)\right)^2}{N_z}$
	large dependence emphasis	$GLDM8 = \frac{\sum_{i=1}^{N_a} \sum_{j=1}^{N_d} P(i,j) j^2}{N_z}$
	large dependence high gray level emphasis	$GLDM9 = \frac{\sum_{i=1}^{N_a} \sum_{j=1}^{N_d} P(i,j) i^2 j^2}{N_z}$

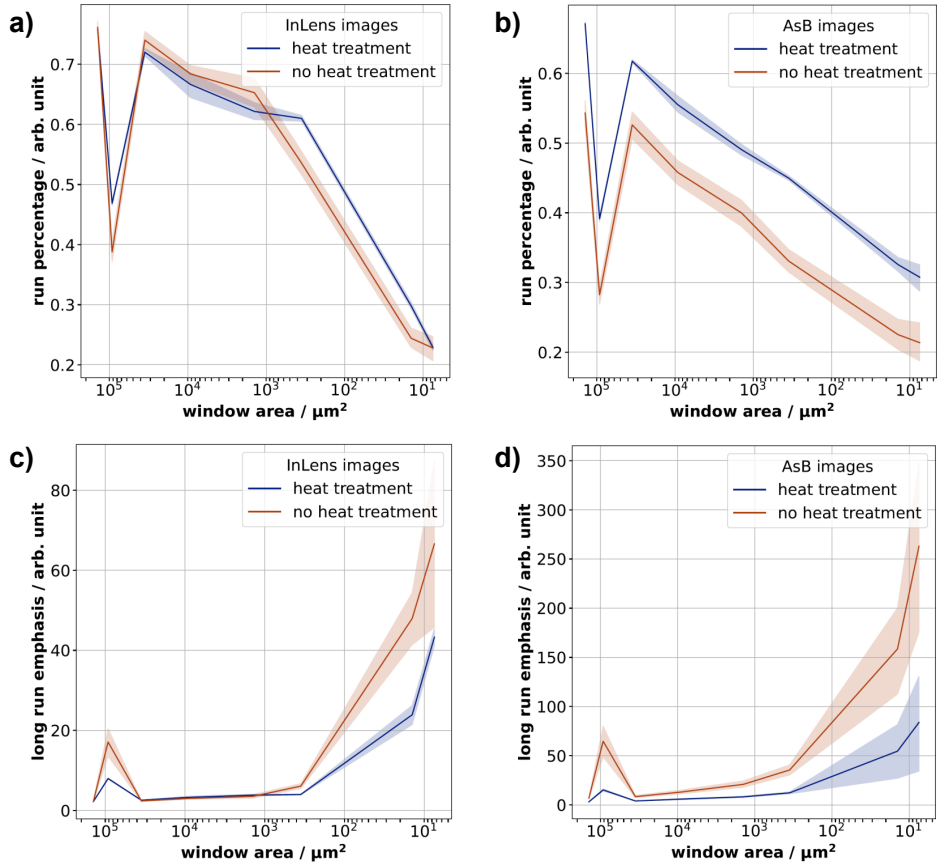

Figure AF.8. Analysis of microstructural changes induced by the heat treatment of the CL at 150°C. While in a and c the inlens images are used to calculate the run percentage and long run emphasis. In b and d the AsB images are used instead.

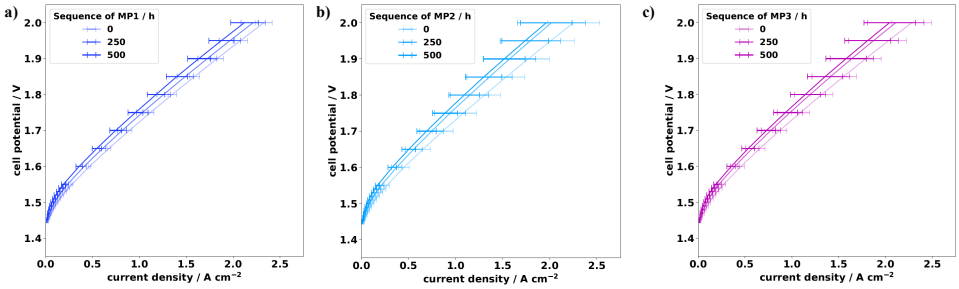

Figure AF.9. Polarization curves recorded during the initial performance assessment and durability testing for MP1 to MP3.

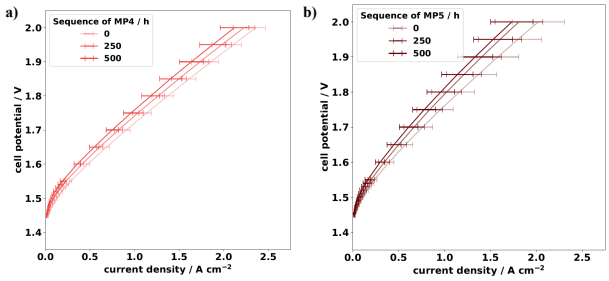

Figure AF.10. Polarization curves recorded during the initial performance assessment and durability testing for MP4 and MP5.

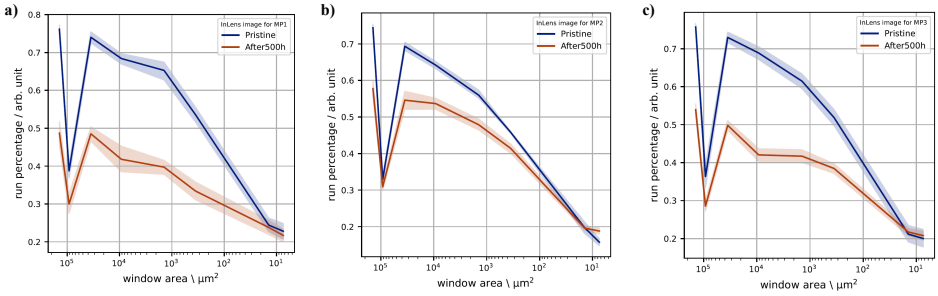

Figure AF.11. Analysis of the structural changes for MP1, MP2, and MP3 during durability testing using the run percentage.

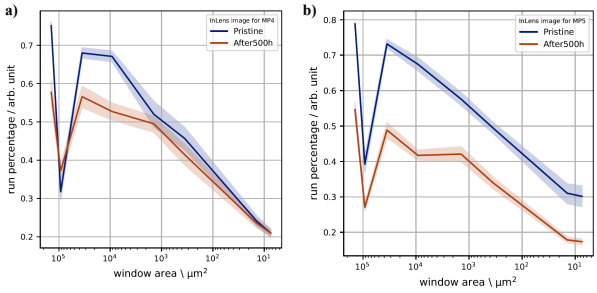

Figure AF.12. Analysis of the structural changes for the more heterogeneous MP4 and MP5 during durability testing using the run percentage.

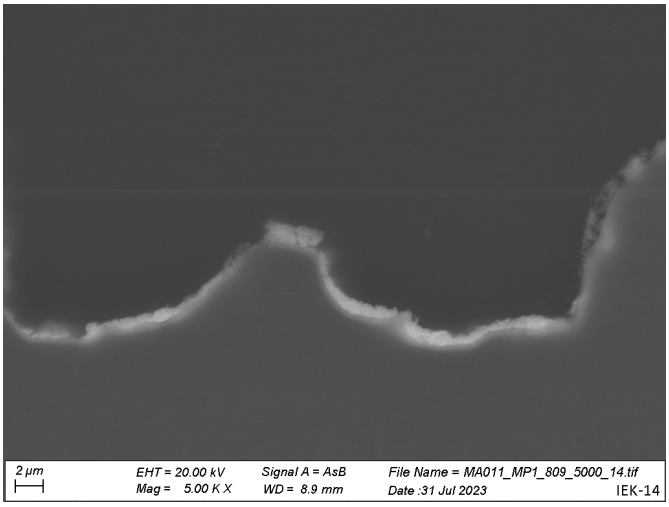

Figure AF.13. Post-Mortem analysis of MP1 by cross-section. Iridium band formation below the CL was observed.

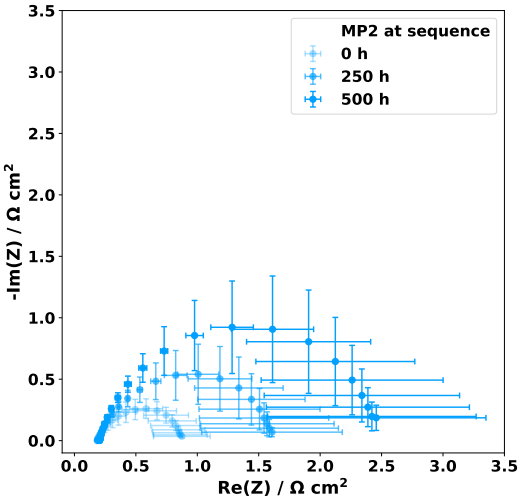

Figure AF.14. -Nyquist plots for MP1 recorded during the durability testing at 1.45 V.

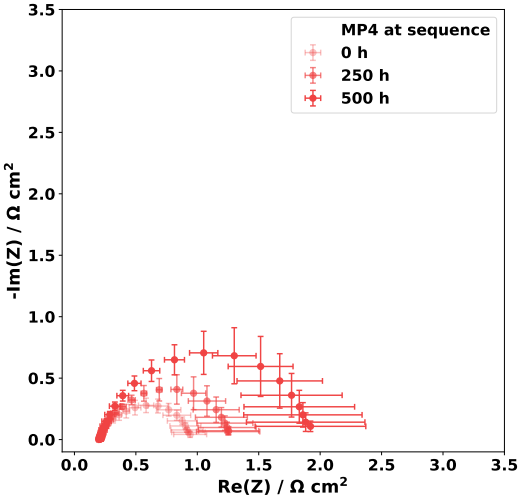

Figure AF.15. -Nyquist plots for MP1 recorded during the durability testing at 1.45 V.

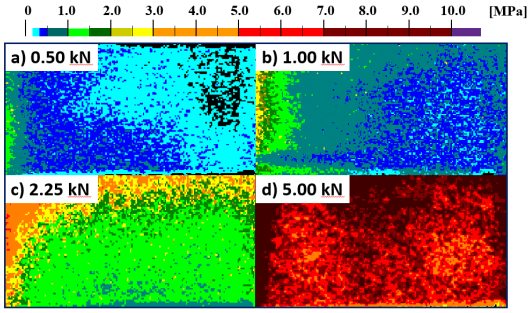

Figure AF.16. Distribution of the compression onto the measuring field. The compression force was adjusted to (a) 0.50 kN, (b) 1.00 kN, (c) 2.25 kN, and (d) 5.00 kN.

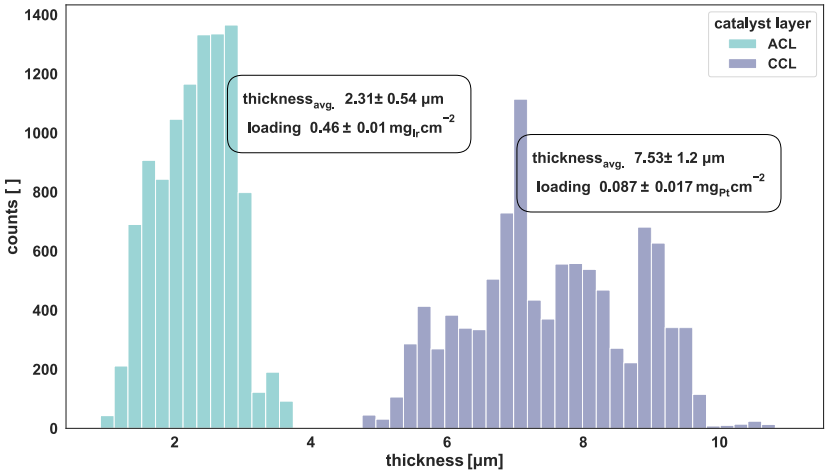

Figure AF.17. Obtained thickness distribution for CLs by cross-sectional analysis of AsB images. CCL denotes a PEM water electrolyzer cathode characterized by low metal loading but a high carbon fraction. The ACL represents optimized anode loading for the PEMWE.

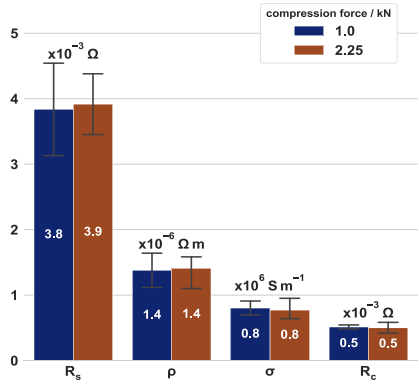

Figure AF.18. Determined sheet resistance of the titanium-based PTL and in-plane electrical resistivity/conductivity with typical values for metals.

Figure AF.19. Result of the spatially-resolved resistance for both CLs studied in this work. The two chosen distances were 0.25mm (a) and 2.25mm (b).

List of Figures

List of Tables

Glossary of Acronyms and Symbols

List of Acronyms

ACL anodic catalyst layer

AFM atomic force microscopy

AsB angle-selective backscattered electron

CCL cathodic catalyst layer

CL catalyst layer

CLSM confocal laser scanning microscope

CRM critical raw material

ECHA European Chemicals Agency

EDX energy dispersive X-ray spectroscopy

EIS electrochemical impedance spectroscopy

EPDM ethylene propylene diene monomer rubber

FO first-order

GDL gas diffusion layer

GLCM gray-level co-occurrence matrix

GLDM gray level dependency matrix

GLRLM gray-level run length matrix

GLSZM gray level size zone matrix

HER hydrogen evolution reaction

HFR high frequency resistance

IEA International Energy Agency

IF image feature

IRENA International Renewable Energy Agency

ITO indium tin oxide

MEA membrane electrode assemblies

MPL microporous layer

NGTDM neighboring gray tone difference matrix

NREL National Renewable Energy Laboratory

OCV open circuit voltage

OER oxygen evolution reaction

OLED organic light-emitting diode

PCB printed circuit boards

PCC Pearson correlation coefficient

PEM proton exchange membrane

PEMFC proton exchange membrane fuel cell

PEMWE proton exchange membrane water electrolyzer

PET polyethylene terephthalate

PFAS per- and polyfluorinated alkyl substance

PGM platinum group metals

PSPT production-structure-property triangle

PTFE polytetrafluorethylen

PTL porous transport layer

Glossary

ROI regions of interest

RSD relative standard deviation

SEM scanning electron microscopy

SLIC simple linear iterative clustering

STP surface texture parameter

TEM transmission electron microscopy

tif tagged image file

List of Symbols

ΔG°	change of Gibbs free energy
e^-	electron
$\mathrm{H_2O}$	water
$\mathrm{H_2}$	hydrogen
$\mathrm{H^+}$	hydrogen proton
$\mathrm{O_2}$	oxygen
η	overpotential
η_e	ohmic overpotential
η_i	ionic overpotential
η_{anode}	anode overpotential
$\eta_{cathode}$	cathode overpotential
η_k	activation overpotential
λ	decay constant
ρ	in-plane electrical resistivity
$\rho_{A,m}$	material resistivity
σ	in-plane electrical conductivity
φ_{ox}	driving force of the OER
φ_{red}	driving force of the ORR
A_i	initial value of the exponential decay curve
d_m	distance between the traces
d_t	trace width
E°_{anode}	anodic electrode potential
$E^\circ_{cathode}$	cathodic electrode potential
E°_{cell}	cell potential
E_F	Fermi levels
E_q	equilibrium potential
F	Faraday's constant ($96\,485\,\mathrm{C\,mol^{-1}}$)
h_{ox}	barrier of the oxidation
h_{red}	barrier of the reduction
J	current densities
j_0	exchange current density
n	number of electrons
R_0	y-axis intercept
R_c	contact resistance
R_i	current supply
R_m	sample resistance
R_s	sheet resistance
R_t	trace resistance
R_{ct}	charge-transfer resistance

Glossary

R_{HFR}	high frequency resistance
R_{su}	peripheral resistance
R_{theo}	theoretical resistance
S_a	arithmetical mean height
S_k	core height
S_p	maximum peak height
S_q	root mean square height
S_v	maximum pit depth
S_z	maximum height
S_{al}	autocorrelation length
S_{ku}	kurtosis
S_{ox}	oxidized species
S_{pk}	reduced peak height
S_{red}	reduced species
S_{sk}	skewness
S_{tr}	texture aspect ratio
S_{vk}	reduced valley height
S_{xp}	peak extreme height
t	thickness
T_g	glass temperature
U_{cell}	cell voltage
V_{mc}	core material volume
V_{mp}	peak material volume
V_{vc}	dale void volume
V_{vv}	core void volume
x_t	time variable
A	cross-sectional area
C	current density at the end of testing
d	distance
E	thermodynamic voltage
l	total length
N	number of traces
PEDOT-PSS	poly(3,4-ethylenedioxythiophene) polystyrene sulfonate
R	resistance
SMr1	material ratio in peak
SMr2	material ratio in valley
w	length of the traces

Band / Volume 690
Design of Local Multi-Energy Systems: Impact of Coupled Energy Vector Integration and Grid Service Participation
P. S. Glücker (2026), xxviii, 145 pp
ISBN: 978-3-95806-880-3

Band / Volume 691
A Parallel-in-Space Simulator for Accelerating Power System Simulation on Graphics Processing Units
J. Zhang (2026), 112 pp
ISBN: 978-3-95806-882-7

Band / Volume 692
Entwicklung von Reparaturmethoden für einkristalline Bauteile mittels thermischer Spritzverfahren
M. L. Létang (2026), X, 211 pp
ISBN: 978-3-95806-883-4

Band / Volume 693
Assessing the Environmental Implications of Offshore Wind Energy Advancements on the Future German Electricity Sector
A. Benitez (2026), xi, 176 pp
ISBN: 978-3-95806-885-8

Band / Volume 694
Entwicklung von Korrosionsschutzschichten für Protonen-Austausch-Membran-Wasserelektrolyseure
T. Sievert (2026), 201 pp
ISBN: 978-3-95806-888-9

Band / Volume 695
Hierarchical Modeling of Electrocatalytic Reactions from a Local Perspective
X. Zhu (2026), ix, 121 pp
ISBN: 978-3-95806-889-6

Band / Volume 696
Nanocrystalline Silicon Carbide in Transparent Passivating Contact Solar Cells
A. Eberst (2026), xiii, 225 pp
ISBN: 978-3-95806-891-9

Band / Volume 697
Theory of Electronic and Ionic Perturbations at Supported Electrocatalyst Nanoparticles
Y. Zhang (2026), XI, 131 pp
ISBN: 978-3-95806-896-4

Band / Volume 698
Aufbau und Einsatz eines on-board Messsystems zur Untersuchung der Abgaszusammensetzung von Fahrzeugen betrieben mit konventionellen und alternativen Kraftstoffen
V. Polinowski (2026), VIII, 269 pp
ISBN: 978-3-95806-897-1

Band / Volume 699
Ab Initio-based large-scale Atomistic Simulations of Cathode Materials for Secondary Batteries: From Computational Methodologies to Applications towards improved Structural and Chemical Stability
K. Köster (2026), x, 204, x pp
ISBN: 978-3-95806-898-8

Band / Volume 700
Materials Design, Processing and Application of Proton-Conducting Oxides for Electrochemical Energy Conversion
Y. Zeng (2026), vii, 117 pp
ISBN: 978-3-95806-899-5

Band / Volume 701
Accelerating the discovery of alkaline-stable anion exchange membrane materials via computational exploration
F. P. Tipp (2026), xii, 135 pp
ISBN: 978-3-95806-900-8

Band / Volume 702
Methods for Investigating the Structure-Performance Correlation in Membrane Electrode Assemblies
N. Utsch (2026), XIII, 138, LXVII pp
ISBN: 978-3-95806-901-5

Weitere ***Schriften des Verlags im Forschungszentrum Jülich*** unter
http://wwwzb1.fz-juelich.de/verlagextern1/index.asp

Energie & Umwelt / Energy & Environment
Band / Volume 702
ISBN 978-3-95806-901-5

Mitglied der Helmholtz-Gemeinschaft

JÜLICH
Forschungszentrum